UNIVERSITY OF SOUTHAMPTON

A Semi-Empirical Jet-Surface Interaction Noise Model

by

Martin Dawson

A thesis submitted for the degree of
Doctor of Philosophy

in the
Faculty of Engineering and Physical Sciences
Institute of Sound and Vibration Research

April 2022

UNIVERSITY OF SOUTHAMPTON

ABSTRACT

FACULTY OF ENGINEERING AND PHYSICAL SCIENCES
INSTITUTE OF SOUND AND VIBRATION RESEARCH

Doctor of Philosophy

A SEMI-EMPIRICAL JET-SURFACE INTERACTION NOISE MODEL

by Martin Dawson

The bypass ratio of modern turbofan engines continues to increase in order to improve propulsive efficiency and to reduce the amount of fuel burned by aeroplanes. However, the increase in bypass ratio has reduced the distance between jet and wing, increasing jet-surface interaction noise. It is, therefore, important for the next generation of 'Ultra-High-Bypass' turbofan engines that the level of jet-surface interaction noise can be predicted and mitigated during the preliminary design process.

In this thesis, a semi-analytical jet-surface interaction noise model has been created. The model scales a database of experimentally measured isolated jet near-field pressure spectra with jet velocity, flight velocity, core nozzle area and secondary nozzle area. The near-field pressure is then propagated onto the surface using cylindrical harmonics, whereupon Amiet's theory is used to calculate the far-field noise scattered by the surface trailing edge. The model has been validated against small scale laboratory measurements of installed jet noise for flight Mach numbers less than 0.2. The scattering solution has been further extended with back-scattering theory, improving the prediction of the spectral shape for surfaces with chord to jet nozzle diameter ratios of 2.5 or less. However, at these chord to diameter ratios the amplitude of the laboratory measurements are overpredicted at mid and rear polar angles, most noticeably for jet Mach number of 0.6 or greater. Strip theory has also been used to model the cranked planforms of modern airliners, accounting for the swept and unswept portions of more realistic wing trailing edges. Finally, comparisons to measurements of large model-scale installed jets have demonstrated that the model can scale to larger jet diameters.

"Don't Panic."

Douglas Adams, The Hitchhiker's Guide to the Galaxy

Contents

List of Figures

List of Tables

Nomenclature

A	Area	m^2
a	Speed of sound	m/s
b	Semi-chord	m
C	Coefficient	
c	Chord	m
d	Span	m
D	Jet Nozzle Diameter	m
f	Frequency	Hz
G	Greens Function	
H	Hankel function	
h	Shortest distance from jet axis to trailing edge	m
I	Intensity	W/m^2
J	Bessel function of the first kind	
K	Modified Bessel function of the second kind	
k	Wave number	rad/m
l	Axial distance from nozzle to trailing edge	m
M	Mach number	
m	Mode order	
p	Pressure	N/m^2
r	Distance from source to observer	m
S	Surface Area	m^2
s	Entropy	kg $m^2/(s^2K)$
St	Strouhal number	
T	Lighthill's Stress Tensor	kg/(m s^2)
t	Time	s
U	Mean velocity	m/s
u	Instantaneous velocity	m/s
V	Volume	m^3
W	Spectral Shape Function	
x	Observer location	
y	Source location	

Greek Symbols

β	Flap angle	$^\circ$ or rad
γ	Ratio of specific heats	
δ	Kronecker or Dirac delta	
ϵ	Turbulent dissipation rate	W/(s kg)
Θ	Temperature	K
θ	Polar angle	$^\circ$ or rad
ι	Positive real wave number component	
κ	Turbulent kinetic energy	W/kg
λ	Wavelength	m
μ	Dynamic viscosity	kg/(s m)
ρ	Density	kg/m^3
σ	Viscous stress tensor	kg/(m s^2)
τ	Delay time	(s)
ϕ	Azimuthal angle	$^\circ$ or rad
Ψ	Trailing edge sweep angle	$^\circ$ or rad
ψ	Phase angle	rad
ω	Angular frequency	rad/s

Subscripts

0	Ambient condition
$1, 2, 3$	Coordinate vectors
a	Acoustic
c	Centroid location
c	Convective velocity
f	Flight-stream condition
s	Secondary (Bypass) jet condition
p	Primary (Core) jet condition
j	Single-stream jet condition
e	Effective jet
ref	Reference jet
i, j, k	Coordinate vectors
I	Incident
S	Scattered
P	Pressure
V	Volume

Diacritics

$'$	Fluctuating component
$\hat{}$	Fourier transformed variable
$\tilde{}$	Moving reference frame

*	Complex Conjugate

Acronyms & Abbreviations

BEM	Boundary Element Method
BPR	Bypass Ratio
CFD	Computational Fluid Dynamics
CPSD	Cross Power Spectral Density
EIS	Entry Into Service
EPN	Effective Perceived Noise
FAA	Federal Aviation Administration
FWH	Ffowcs-William Hawking
HARMONY	wHole AiRcraft Multidisciplinary nOise desigN sYstem
ICAO	International Civil Aviation Organisation
JFI	Jet-Flap Impingement
JM	Jet Mixing
JSI	Jet-Surface Interaction
JSR	Jet-Surface Reflection
LES	Large-Eddy Simulation
LSAF	Low-Speed Aeroacoustic Facility
NASA	National Aeronautics and Space Administration
NTF	Noise Test Facility
OASPL	OverAll Sound Pressure Level
PIV	Particle Image Velocimetry
PNL	Perceived Noise Level
PSD	Power Spectral Density
QC	Quota Count
RANS	Reynolds Averaged Navier-Stokes
RDT	Rapid Distortion Theory
SPL	Sound Pressure Level
SYMPHONY	SYstem Manufacturing and Product design tHrough cOmponent Noise technologY
TDR	Turbulent Dissipation Rate
TKE	Turbulent Kinetic Energy

Coordinate System

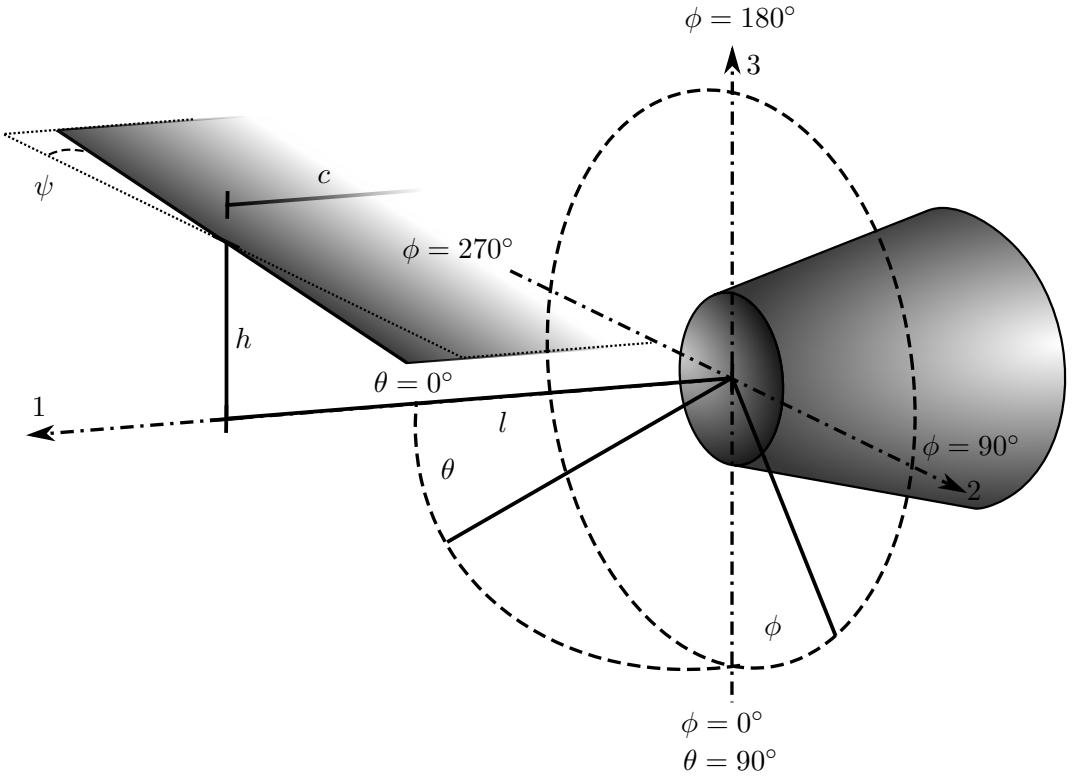

FIGURE 1: Orientation of the spherical coordinate system relative to jet and wing

Declaration of Authorship

I, Martin Dawson, declare that this thesis entitled A Semi-Empirical Jet-Surface Interaction Noise Model and the work presented in it are my own and has been generated by me as the result of my own original research.

I confirm that:

1. This work was done wholly or mainly while in candidature for a research degree at this University;
2. Where any part of this thesis has previously been submitted for a degree or any other qualification at this University or any other institution, this has been clearly stated;
3. Where I have consulted the published work of others, this is always clearly attributed;
4. Where I have quoted from the work of others, the source is always given. With the exception of such quotations, this thesis is entirely my own work;
5. I have acknowledged all main sources of help;
6. Where the thesis is based on work done by myself jointly with others, I have made clear exactly what was done by others and what I have contributed myself;
7. Either none of this work has been published before submission, or parts of this work have been published as: Dawson et al. 2019 (AIAA 2019-2432), Dawson et al. 2020 (AIAA 2020-2550, AIAA 2020-2551, AIAA Journal 2020 58:3 pp. 1130-1139).

Signed:

Date:

Acknowledgements

I would like to acknowledge the financial support of the EPSRC through award 1790095 - *Installed Jet Noise Modelling* and the support of Rolls-Royce plc, especially that of Dr Peer Böhning, through the Rolls-Royce University Technology Centre in Gas Turbine Noise at the University of Southampton's Institute of Sound and Vibration Research, including providing HARMONY (Innovate UK reference number 101367) and SYMPHONY (Innovate UK reference number 100539) geometry and data.

My heart felt thanks go out to my supervisors Prof Rod Self and Dr Jack Lawrence for guiding me through this Ph.D. process, providing feedback on my work, overseeing my time spent in the lab and teaching me so much. A big thanks also to Dr Mike Kingan for proof reading papers, checking mathematical derivations and not least for agreeing to meetings late in the evening.

I am indebted to Dr Anderson Proença for the helping and supervising me in the lab. Also to Dr Zhong-Nan Wang, at the University of Cambridge, for supplying the LES data that has been used in this thesis and for advice on how to process the data.

To my parents, thank you for all the love, encouragement and support, I would not have made it this far without you.

To all the friends I have made while in Southampton, in the UTC (especially Alex James and Sergi Pallejà-Cabré), various societies and elsewhere: Thanks for putting up with me!

Chapter 1

Introduction

1.1 The Aircraft Noise Problem

Millions of people worldwide are exposed to aeroplane noise. For instance, approximately 260,000 people live within the 57 dBA (the onset Leq of significant community annoyance) contour around Heathrow airport.[1] This noise can cause significant irritation to those exposed. Studies have also shown that aeroplane noise can have a negative effect on health; with correlations between increased noise levels and rates of hypertension and cardiovascular disease, amongst other problems.[2] Aeroplane noise can also affect children's learning, for example, a 5 dB increase in aircraft noise exposure can result in a 1-2 month delay in reading age.[2] In response the ICAO (International Civil Aviation Organization) developed the EPNdB (Effective Perceived Noise) metric, in order to characterise the annoyance of aeroplane noise to humans, accounting for the human perception of tones and noise duration.[3]

1.1.1 Control Measures

Beginning with the FAA (Federal Aviation Administration) in 1972, aviation authorities have implemented measures to limit aircraft noise, specifing noise limits that must be met for aircraft types to be certified. For civil airliners, three noise measurements are taken during the certification process. Two are taken during take-off: one along the sideline, 450 m from the runway axis; and the other 6.5 km from the brake release point. The third measurement is taken 2 km before the runway threshold during approach (see Figure 1.1). The ICAO specifies limits for each measurement and for the sum of all three, based on maximum take-off weight and number of engines.[3] Since their inception the ICAO has lowered the limit values in a series of 'chapters',[4] the latest of which (Chapter 14) came into effect on the 31st of December 2017 for aircraft with a

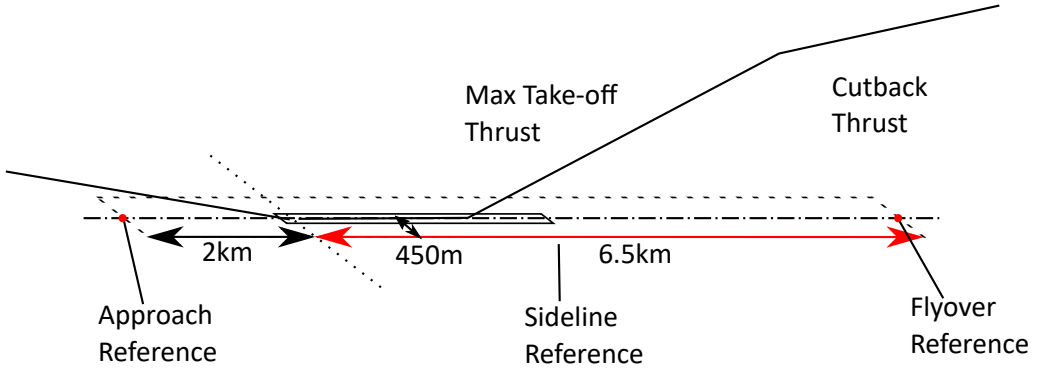

FIGURE 1.1: Noise certification measurement locations

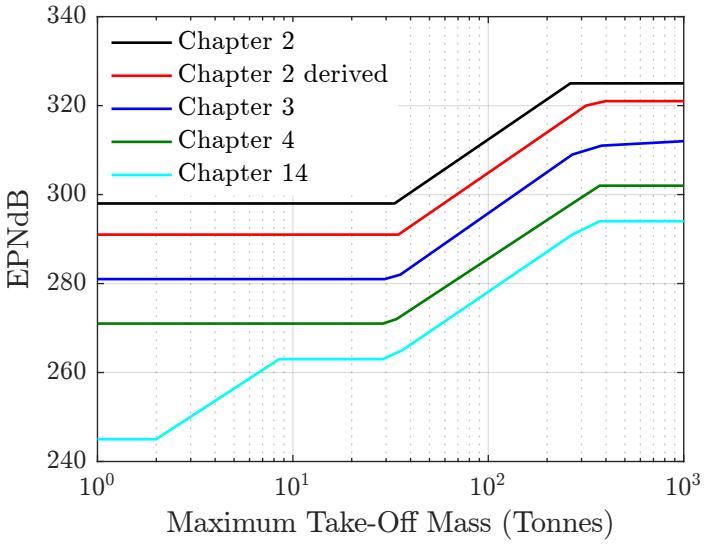

FIGURE 1.2: ICAO cumulative noise limits[4]

maximum take-off mass greater than 55 tonnes[5] (see Figure 1.2). This puts the onus directly on the manufacturers to make their aeroplanes quieter.

In order to combat the effect of aeroplane noise on local communities, some governments and airports have taken further steps to reduce operational noise at airports in built up areas. For instance, the UK government regulates noise at the London Airports (Heathrow, Gatwick and Stansted), assigning Quota Counts (QC) to aeroplanes based on their certificated noise levels (for both take off and landing)(see Table 1.1).[6] The government then assigns a night noise quota to each airport (see Table 1.2), and bans QC4 and above aeroplanes from taking off or landing between 23:30 and 06:00.[6] In order to meet these quotas, increase capacity and reduce noise, these airports charge landing fees based on aeroplane noise relative to Chapter 3 certification levels. At Heathrow this leads to the noisiest aeroplanes paying more than ten times that of the quietest, and charges increase by more than double at night.[7] This creates a monetary incentive for airlines to buy and operate quieter aeroplanes.

TABLE 1.1: Aeroplane Quota Count Classification[6]

Noise Level (dB)	QC
>101.9	16
99-101.9	8
96-98.9	4
93-95.9	2
90-92.9	1
87-89.9	0.5
84-86.9	0.25

TABLE 1.2: London Airport Quota Count and Movement Limits[8]

Airport	Heathrow		Gatwick		Stansted	
Season	Summer	Winter	Summer	Winter	Summer	Winter
Movements	3250	2550	11200	3250	7000	5000
Quota Counts	5100	4080	6200	2000	4650	3310

Additionally, public bodies have set strategic targets for the aviation industry. As part of Flightpath 2050, the European Commission have set the target of reducing the perceived noise level due to aviation by 65%[9] (relative to new aircraft in 2000), which they plan to achieve by funding research within industry and universities. NASA has also set noise reduction targets, in order to focus research, with the more ambitious goal of reducing perceived noise level by 75%[10] by 2035.

1.1.2 Aeroplane Noise Sources

Aeroplane noise can be split, at the highest level, into that created by the engines (here turbofans are considered) and the airframe. Historically, the engines have been the dominant source of noise from aeroplanes. However, increasing bypass ratio, combined with noise reduction technologies, has reduced engine noise and increased the importance of airframe noise, especially during approach/landing where the engine produces low thrust.[11] Airframe noise is generated predominantly by the wing and surface discontinuities in the 'clean' condition and by the landing gear, slats and flaps in the 'dirty' configuration.[3] The primary sources of engine noise are the fan, jet, compressors, turbines and combustion. An example of the relative source levels is presented in Figure 1.3 for a chapter 4 aircraft with high-bypass-ratio engines. It can be seen that the jet is a major contributor to departure noise, and should be decreased to ensure the continuing reduction of aeroplane noise.

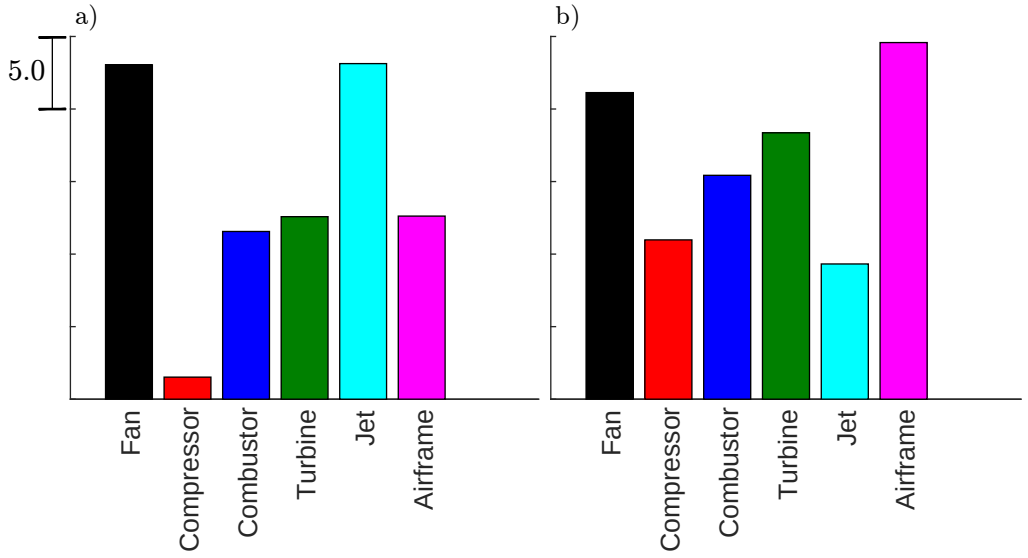

FIGURE 1.3: Comparison of relative engine noise source levels at a) departures, and, b) arrivals, for a Chapter 4 type aircraft (relative source levels courtesy of Rolls-Royce).

1.1.3 Jet Noise

A gas turbine engine generates thrust by accelerating air through a propelling nozzle, producing a jet.[12] Figure 1.4 displays the development of a jet from a conical nozzle. Downstream of a conical jet nozzle an annular mixing layer (or shear layer) forms around a region of approximately uniform velocity, called the potential core. As the jet mixes with the surrounding air the shear layer grows in thickness, while the potential core reduces in diameter and disappears after approximately four to five jet diameters.[13] Within the shear layer, the high vorticity drives instabilities and turbulent eddies that generate acoustic waves[14, 15] that propagate away from the jet, creating jet-mixing noise. Additionally, an irrotational hydrodynamic pressure field, made up of evanescent pressure fluctuations that decay exponentially with distance, is generated in a region close to the jet.[16]

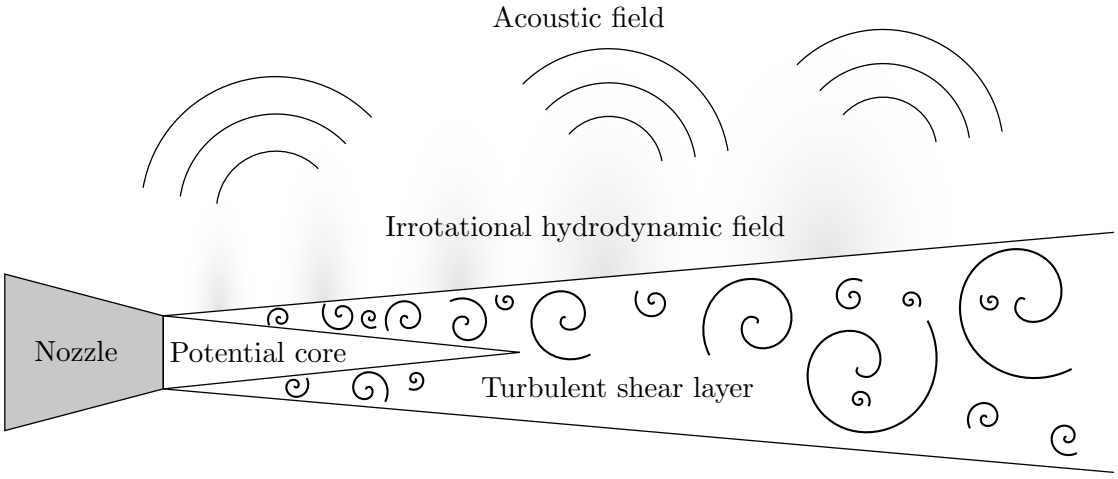

FIGURE 1.4: Illustration of the regions of a subsonic single-stream round jet

Starting in the 1950s, the use of turbojet engines, with their very high exhaust velocities, to power commercial airliners meant that jet-mixing noise, which scales as jet velocity to the eighth power,[15] was the dominant noise source.[3] During this time, much research was conducted on the use of suppressors, which increased the mixing of the jet with the surrounding air, to reduce mixing noise.[3] This method was used to some success,[17] and is still used within small, low-bypass, turbofans. However, the introduction of turbofans, to increase propulsive efficiency, is the reason that jet-mixing is no longer the dominant noise source.[11] This is because turbofans divert some of the air through the first compressor stage (the 'fan') such that it bypasses the core of the engine, allowing for an increased mass flow rate and a reduction in jet velocity for a given thrust. However, as engine bypass ratio (ratio of air bypassing to entering the core) has increased (see Figure 1.5), the distance between jet and wing has been reduced, increasing the importance of installation effects on jet noise.[18]

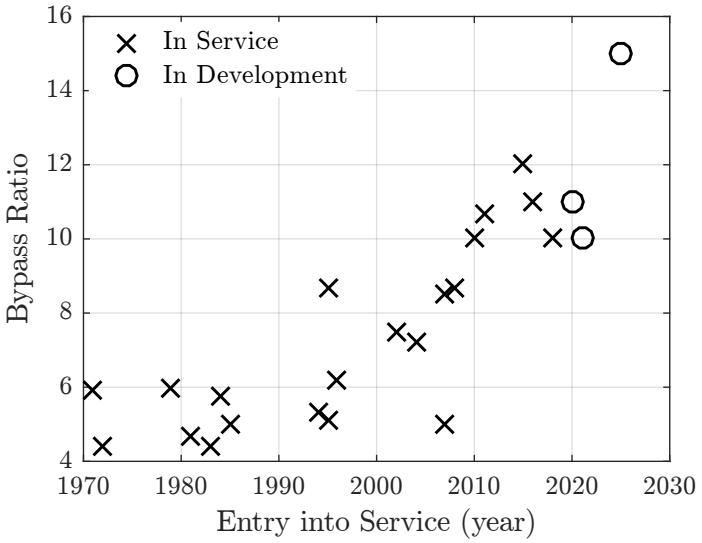

FIGURE 1.5: Civil large and medium engine bypass ratio. Based on data from Jane's Aero-Engines[19]

.

When a gas turbine engine in installed beneath a wing, the jet noise heard by an observer in the far field is modified (see Figure 1.6) compared to a jet in isolation. For observers on the same side of the wing as the jet, high frequency jet-mixing noise is increased by reflection from the wing. For observers on the opposite side of the wing, high frequency jet-mixing noise is reduced by the wing shielding the observer from the high frequency noise sources (see Figure 1.7). If the wing is positioned very close to the jet, the jet can be distorted, changing the jet-mixing noise produced. The trailing edge of the wing can also scatter the non-propagating hydrodynamic pressure field of the jet into a propagating acoustic field, creating jet-surface interaction noise.

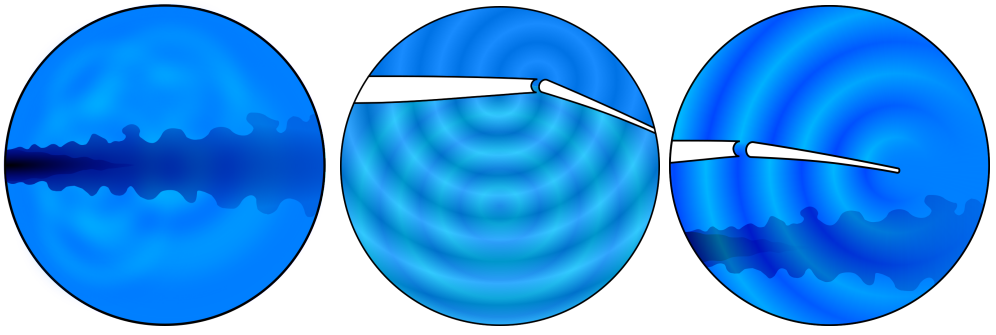

FIGURE 1.6: Illustrations of jet-mixing noise (left), jet-surface reflection (centre) and jet-surface interaction noise (right)

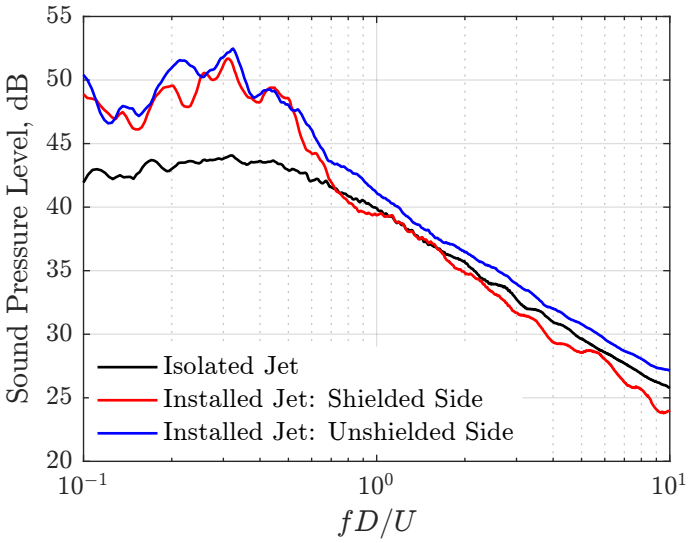

FIGURE 1.7: Example of isolated and installed jet noise spectra. Jet-surface interaction noise is apparent at low Strouhal numbers, while reflection/shielding is apparent at high Strouhal numbers

Model-scale laboratory experiments have shown that jet-surface interaction noise is a large component of low frequency jet noise in the forward arc,[20–23] and that its prominence increases at approach conditions and when flaps are deployed.[22,24] Measurements have also shown that it scales with jet velocity to the fifth power.[18,21,25] This means that as bypass ratio continues to increase, and jet velocity decreases, jet-surface interaction noise could become an increasingly large component of jet noise. It is important, therefore, for the development of future ultra-high-bypass turbofan engines that the mechanism that produces jet-surface interaction noise is understood and tools developed to predict that produced by a given engine-wing configuration.

1.2 Contributions of the Thesis

This thesis aims to further jet-surface interaction noise modelling towards producing a semi-empirical model that could be used by industry. To this end, empirical scaling methods have been produced for the hydrodynamic pressure field of jets created by axisymmetric nozzles, extending existing methods to include the effect of nozzle diameter, bullet diameter and flight velocity. This required taking near-field unsteady pressure measurements within the flow of a co-flowing 'flight stream', which simulates the effect of flight on a laboratory jet. Using these in-flow near-field pressure measurements as the input, the jet-surface interaction model of Lyu & Dowling has been validated in flight. The model has then been extended with Roger & Moreau's back-scattering theory and strip theory to model more realistic scattering surface planform geometries. Finally, these models are combined to produce a semi-empirical jet-surface interaction noise prediction tool. This tool is compared to large-model-scale measurements of installed jet noise using realistic airframe and jet-nozzle geometries.

1.3 Thesis Outline

The following chapter, Chapter 2, presents a review of the relevant literature. This begins with an introduction to jet noise modelling with Lighthill's equation. The trailing-edge scattering models of Ffowcs-Williams & Hall and Amiet are then introduced, both fundamental to the jet-surface interaction noise models that are subsequently discussed. Finally, several methods for modelling the unsteady hydrodynamic pressure field produced by a jet are introduced.

Next in Chapter 3 experiments are described to measure the near-field pressure and far-field jet-surface interaction noise of a jet in simulated flight. These measurements are used in the subsequent chapters to explore changes to the near-field pressure spectra in flight, and to assess a jet-surface interaction noise model.

In Chapter 4 an empirical model is developed for the hydrodynamic pressure field of a jet. At first, more evidence is presented for the pressure squared scaling of the hydrodynamic field presented by various authors. This is then extended to include the effect of jet diameter, including a bullet, and flight velocity. A comparison is then made of the axial wavenumbers of the hydrodynamic field calculated using the method of Lyu & Dowling and from $k-\omega$ decomposition. This is then used to develop an empirical model for the axial wavenumber of the hydrodynamic pressure field of a jet.

Chapter 5 concerns jet-surface interaction noise. Firstly, the jet-surface interaction noise model of Lyu & Dowling is validated against laboratory measurements utilising a co-flowing 'flight stream' to simulate the effect of forward motion on jet-surface interaction

noise. The model is then compared with measurements utilising scattering surfaces with more realistic chords. Finally, the problems of modelling jet-airliner wing geometries analytically are discussed, including the possible use of strip theory.

Within Chapter 6 the results of the previous two chapters are brought together, and a semi-empirical tool for predicting jet-surface interaction noise is presented. This tool is then compared against large-scale laboratory measurements of installed jet noise. These measurements were taken with a model airframe representative of modern 150-seat airliners, and nozzles with increasing realism, starting from a simple axisymmetric un-bulleted nozzle up to a nozzle that matches the airframe. This is used to demonstrate the areas in which the prediction tool works well, and its current limitations.

Finally, Chapter 7 draws together the conclusions of the thesis, including a discussion of further work which could improve the prediction tool.

Chapter 2

Literature Review

In this chapter the literature on installed jet noise is explored, examining methods that have been used to calculate jet-surface interaction (JSI) noise analytically, numerically and experimentally. This is followed by a review of the literature on jet near-field pressure spectra.

2.1 Isolated Jet Noise

Before looking at installed jet noise, it is useful to first introduce Lighthill's equation, being the first attempt to analytically describe jet noise and starting the field of aeroacoustics.

2.1.1 Lighthill

Lighthill,[14]in 1952, was the first to produce an analogy describing the aerodynamic generation of sound. Starting with the continuity equation,

$$\frac{\partial \rho}{\partial t} + \frac{\partial \rho u_i}{\partial y_i} = 0 \tag{2.1}$$

and the momentum equation,

$$\frac{\partial \rho u_i}{\partial t} + \frac{\partial}{\partial y_j}(\rho u_i u_j) + \frac{\partial p}{\partial y_i} - \frac{\partial \sigma_{ij}}{\partial y_j} = 0, \tag{2.2}$$

Lighthill combined and rearranged them in such a manner as to produce a non-homogeneous wave equation,

$$\frac{\partial^2 \rho}{\partial t^2} - a_0^2 \frac{\partial^2 \rho}{\partial y_i^2} = \frac{\partial^2}{\partial y_i \partial y_j}(\rho u_i u_j - \sigma_{ij}) + \frac{\partial^2}{\partial y_i^2}(p - a_0^2 \rho). \tag{2.3}$$

This equation demonstrates how turbulence, viscous stress and enthalpy fluctuations can produce noise with a quadrupole nature. However, by arbitrarily splitting the equation into terms representing the wave equation and sources, the effect of the flow field on wave propagation is ignored. The flow field is effectively replaced by a distribution of quadrupoles, hence why Lighthill's equation is an analogy.

Using the method of Stratton,[26] Lighthill's equation can be cast into a general integral form,

$$\rho' = \frac{1}{4\pi a_0^2} \int_V \frac{1}{r} \frac{\partial^2 T_{ij}}{\partial y_i \partial y_j} |_{\tau = t - r/a_0} \, \mathrm{d}y + \frac{1}{4\pi} \int_S \left[\frac{1}{r} \frac{\partial \rho}{\partial n} + \frac{1}{r^2} \frac{\partial r}{\partial n} \rho + \frac{1}{r a_0} \frac{\partial r}{\partial n} \frac{\partial \rho}{\partial \tau} \right]_{\tau = t - r/a_0} \mathrm{d}S, \tag{2.4}$$

where

$$T_{ij} = \rho u_i u_j - \sigma_{ij} + (p - a_0^2 \rho) \delta_{ij} \tag{2.5}$$

is the Lighthill stress tensor and

$$\sigma_{ij} = -\frac{2}{3} \mu \frac{\partial u_k}{\partial x_k} \delta_{ji} + \mu \left(\frac{\partial u_j}{\partial y_i} + \frac{\partial u_i}{\partial y_j} \right) \tag{2.6}$$

is the viscous stress tensor for a Stokesian gas.[27] By casting Lighthill's equation into integral form, solutions and scaling laws can be found for a known source strength. If the flow field is unbounded then the surface integral term disappears, leaving the volume integral of the Lighthill stress tensor,

$$\rho' = \frac{1}{4\pi a_0^2} \int_V \frac{1}{r} \frac{\partial^2 T_{ij}}{\partial y_i \partial y_j} |_{\tau = t - r/a_0} \, \mathrm{d}y. \tag{2.7}$$

Currently the divergence of the stress tensor is evaluated at a time dependent on the time at the observer and the time required to travel from the source to the observer, which is itself a function of the source location. The decay of the acoustic field is also dependent on the distance from source to observer. It will become more convenient if the entire term within the integral is also within the derivatives. Using the chain rule this becomes

$$\rho' = \frac{1}{4\pi a_0^2}\int_V \frac{\partial^2}{\partial y_i \partial y_j}\frac{T_{ij}}{r}\,\mathrm{d}y + 2\frac{1}{4\pi a_0^2}\frac{\partial}{\partial x_j}\int_V \frac{\partial}{\partial y_i}\frac{T_{ij}}{r}\,\mathrm{d}y + \frac{1}{4\pi a_0^2}\frac{\partial^2}{\partial x_i \partial x_j}\int_V \frac{T_{ij}}{r}\,\mathrm{d}y. \quad (2.8)$$

By encapsulating the entire term within the integral within the derivatives the first two integrals can be re-expressed using the divergence theorem as surface integrals, and in our unbounded flow go to zero. In the final integral the derivatives are in terms of observer position only, and hence can be removed from within the integral. This leaves the integral form of Lighthill's equation as derived by Lighthill,

$$\rho' = \frac{1}{4\pi a_0^2}\frac{\partial^2}{\partial x_i \partial x_j}\int_V \frac{T_{ij}}{r}\,\mathrm{d}y \quad (2.9)$$

whereby, for an observer in the far-field, the differential can be transformed into one with respect to time,

$$\rho' = \frac{x_i x_j}{4\pi a_0^4 x^3}\frac{\partial^2}{\partial t^2}\int_V T_{ij}\,\mathrm{d}y. \quad (2.10)$$

The source term, T_{ij}, is comprised of three components: a Reynolds stress term, $\rho U_i U_j$; a viscous stress term, σ_{ij}; and a term, $(p - a_0^2\rho)\delta_{ij}$, related to fluctuations in entropy. For jet flows of large Reynolds number there exists a region, called the shear layer, where the Reynolds stress terms are significantly larger than the viscous stress terms. Outside this region both the Reynolds stress terms and the viscous stress terms will be small relative to those in the shear layer, and hence the viscous term can be ignored. If the jet is also subsonic and isothermal then temperature fluctuations, and hence entropy fluctuations, will also be small, allowing T_{ij} to be simplified to $\rho_0 u_i u_j$.

In the form of Equation 2.10, and using the simplified stress tensor, dimensional analysis can be used to estimate the noise produced by a jet. If one assumes that length scales are proportional to jet diameter, D_j, and time scales are proportional to $D_\mathrm{j}/U_\mathrm{j}$, then

$$\rho' \propto \frac{\rho_0 U_\mathrm{j}^4 D_\mathrm{j}}{a_0^4 x}. \quad (2.11)$$

As pressure fluctuations are related to density fluctuations via the square of the speed of sound, and intensity is pressure squared divided by the specific acoustic impedance of air, then total acoustic intensity scales with

$$I \propto \frac{\rho_0 D_\mathrm{j}^2 U_\mathrm{j}^8}{x^2 a_0^5}. \quad (2.12)$$

This expression shows how the acoustic intensity of a jet is proportional to jet velocity to the 8th power and jet diameter to the 2nd power. This has been confirmed experimentally for subsonic, cold jets at a polar angle, θ, of 90°.[13, 28–31]

Lighthill's Analogy has proved fundamental to the prediction of jet noise. It explains why increasing bypass ratio, and hence decreasing jet velocity, reduces jet noise. It has formed the basis of methods for scaling jet noise measurements from one condition to another. Also, its simplicity, in relation to other acoustic analogies, has meant it sees continued usage and success in the development of RANS based jet noise prediction tools.[32–34]

2.2 Trailing-Edge Scattering

Several methods have been published for calculating the far-field noise scattered from the trailing edge of a surface. In this section two of the most commonly used trailing-edge scattering theories, at least for calculating jet-surface interaction noise, will be described.

2.2.1 Ffowcs-Williams and Hall

Ffowcs Williams & Hall[35] derived an equation that describes the far-field acoustic intensity produced by an eddy positioned very close to the edge of a half plane in a turbulent fluid. Starting with Lighthill's equation Equation 2.3, and assuming that variations in density are due to variations in pressure, a Fourier transform is taken with respect to time to produce an inhomogeneous Helmholtz equation,

$$\frac{\partial^2 \hat{p}}{\partial y_i^2} + \frac{\omega^2}{a_0^2}\hat{p} = -\frac{\partial^2 \widehat{T_{ij}}}{\partial y_i \partial y_j}. \tag{2.13}$$

A solution to this equation is then sought using the Greens function method,

$$-\int_V \hat{p}\left(\frac{\partial^2 G}{\partial y_i^2} + k^2 G\right) \mathrm{d}y = \int_V G\frac{\partial^2 \widehat{T_{ij}}}{\partial y_i \partial y_j}\,\mathrm{d}y + \int_S \left(G\frac{\partial \hat{p}}{\partial y_i} - \frac{\partial G}{\partial y_j}\hat{p}\right)\cdot n\,\mathrm{d}s, \tag{2.14}$$

where the Greens function is found from the solution to

$$\frac{\partial^2 G}{\partial y_i^2} + k^2 G = -4\pi\delta(x-y) \tag{2.15}$$

with the boundary conditions on the surface

$$\frac{\partial \hat{p}}{\partial y_i} \cdot n = 0 \tag{2.16}$$

and

$$\frac{\partial G}{\partial y_i} \cdot n = 0. \tag{2.17}$$

Application of the boundary conditions and Greens function definition reduces the solution to

$$\hat{p} = \frac{1}{4\pi} \int_V G \frac{\partial^2 \widehat{T_{ij}}}{\partial y_i \partial y_j} \, \mathrm{d}y. \tag{2.18}$$

The divergences can be applied to the Greens function, rather than the stress tensor, by repeated application of integration by parts

$$\hat{p} = \frac{1}{4\pi} \int_S \left(G \frac{\partial \widehat{T_{ij}}}{\partial y_j} - \frac{\partial G}{\partial y_i} \widehat{T_{ij}} \right) \cdot n \, \mathrm{d}s + \frac{1}{4\pi} \int_V \frac{\partial^2 G}{\partial y_i \partial y_j} \widehat{T_{ij}} \, \mathrm{d}y. \tag{2.19}$$

If the Lighthill stress tensor is then approximated by only the turbulent stress term $\rho u_i u_j$, then the boundary conditions are such that the surface integral disappears. This leaves Ffowcs-Williams & Hall's equation

$$\hat{p} = \frac{1}{4\pi} \int_V \frac{\partial^2 G}{\partial y_i \partial y_j} \widehat{\rho u_i u_j} \, \mathrm{d}y. \tag{2.20}$$

The Greens function for this problem has been solved for an observer in the far-field by MacDonald[36] in cylindrical coordinates and is given by

$$G = \frac{\mathrm{e}^{\frac{1}{4}\mathrm{i}\pi}}{\sqrt{\pi}} \left(\frac{\mathrm{e}^{-\mathrm{i}kr}}{r} \int_{-\infty}^{U_r} \mathrm{e}^{-\mathrm{i}u^2} \, \mathrm{d}u + \frac{\mathrm{e}^{-\mathrm{i}kr'}}{r'} \int_{-\infty}^{U_{r'}} \mathrm{e}^{-\mathrm{i}u^2} \, \mathrm{d}u \right). \tag{2.21}$$

The limits of the integrals are given by

$$U_r = \pm[k(D - r)] \tag{2.22}$$

and

$$U_{r'} = \pm[k(D - r')], \tag{2.23}$$

where r' is the distance from the image source in the half plane to the observer position, and D is the shortest distance from source to observer position via the edge of the half plane.

Ffowcs William & Hall have compared their solution with that of the unbounded solution of Lighthill by sending the infinite half plane off to infinity. In this case r remains constant while U_r and r' also go to infinity. Thus the second term in the Greens function goes to zero, while

$$\frac{\mathrm{e}^{\frac{1}{4}\,\mathrm{i}\pi}}{\sqrt{\pi}} \int_{-\infty}^{\infty} \mathrm{e}^{-\,\mathrm{i}u^2}\,\mathrm{d}u \to 1. \tag{2.24}$$

Thus the Greens function becomes

$$G = \frac{\mathrm{e}^{-\,\mathrm{i}kr}}{r}, \tag{2.25}$$

which if substituted into Equation 2.18 and the inverse Fourier transform taken, leads to

$$p' = \frac{1}{4\pi} \int_V \frac{1}{r} \left[\frac{\partial^2 T_{ij}}{\partial y_i \partial y_j} \right]_{t - r/a_0} \mathrm{d}y \tag{2.26}$$

which is identical to Equation 2.7. This demonstrates the equivalence of the solutions by Ffowcs Williams & Hall and Lighthill for unbounded domains.

From Equation 2.20 Ffowcs Williams & Hall have demonstrated that the far-field noise produced by an eddy positioned much less than a wavelength from the trailing edge scales as

$$I = \frac{k^4 \cos(\phi) \sin^2(\theta/2) \rho_0 U^4 \sin^2(\psi) (\cos^2 \text{or} \sin^2)(\Omega^2/2) \nu^2}{\pi^3 a_0 R^2 (k\bar{r})^3}, \tag{2.27}$$

where the cosine is chosen for longitudinal quadrupoles and the sine for lateral quadrupoles. It is found that maximum PSD scales as the 4th power of velocity, and intensity to the 5th power, lower than that predicted by Curle[37] for the sound produced by a surface in a fluid. The polar directivity is seen to be a cardioid in shape, unlike the dipole shape of an acoustically compact surface, but the azimuthal directivity still retains the dipole form. Finally, the intensity of the noise produced is seen to depend on the orientation of

the eddy relative to the edge. Those eddies aligned with the edge producing no sound at all.

The equation developed by Ffowcs Williams & Hall does not include the Kutta condition, which would prevent a singularity occurring at the trailing edge of the plate and thus could significantly affect the scattered field. Jones[38] has derived a modification to the 2D edge diffraction problem to include a Kutta condition. The modification introduces a wake, which travels downstream with the speed of the ambient flow, that removes the trailing edge singularity. With fluctuations in the wake travelling slower than the speed of sound, the wake does not contribute directly to the sound field; however, the creation of vorticity in the wake draws energy from the acoustic field, while the interaction of the vorticity with the edge can scatter an acoustic field.[39] Jones has demonstrated that for an observer in the far field and in the limits as $kr \to 0$ and $R \to \infty$ the contribution of the Kutta correction is proportional to M/kr. The Kutta correction could therefore be important for JSI noise, being a low frequency phenomena, especially when flaps are deployed, reducing the distance between the trailing edge and the shear layer.

Ffowcs Williams & Halls equation demonstrates how a surface with a sharp edge can create an acoustic field from the pressure field of turbulent eddies. This is particularly important for modern commercial airliners, where wings with sharp trailing edges are positioned very close to the jet flow-field of their gas turbine engines.

2.2.2 Amiet

In 1976 Amiet[40] developed an analytical solution for the scattered pressure field generated by turbulence convecting past a trailing edge in uniform flow. This solution was based on linearised acoustics and made use of Schwarzchild's solution,[41] which states that for a problem defined by the 2D Helmholtz equation

$$k^2 p' + \frac{\partial^2 p'}{\partial x_1^2} + \frac{\partial^2 p'}{\partial x_3^2} = 0, \tag{2.28}$$

with boundary conditions

$$\frac{\partial p'}{\partial x_3} = 0, x_1 < 0 \tag{2.29}$$

and

$$p' = f(x_1), x_1 \geq 0, \tag{2.30}$$

the scattered pressure field on the surface of the plate ($x_1 \leq 0$, $x_3 = 0$) is given by

$$p' = \frac{1}{\pi} \int_0^\infty \sqrt{-\frac{x_1}{\xi}} \frac{\mathrm{e}^{-\mathrm{i}k(\xi - x_1)}}{\xi - x_1} f(\xi) d\xi. \tag{2.31}$$

Amiet formulated the problem as one in which a rigid, infinitesimally thick and semi-infinite, extending from $y_1 = -\infty$ to 0, plate is positioned in the $y_3 = 0$ plane with a uniform flow in the x_1 direction. A fluctuating pressure is incident on the lower surface of the plate, with one component of the pressure in the plane of the plate described by

$$p'_{\mathrm{I}}(\omega, y_1, y_2) = p'_{\mathrm{I}}(\omega, k_1, k_2)\,\mathrm{e}^{-\,\mathrm{i}(y_1 k_1 + y_2 k_2)}, \tag{2.32}$$

assuming that the incident pressure is unaffected by the presence of the trailing edge. As this fluctuating pressure convects past the trailing edge the sudden change in boundary conditions causes an acoustic pressure to be scattered, which propagates according to the convected Helmholtz equation,

$$k^2 p' - 2\,\mathrm{i}kM\frac{\partial p'}{\partial y_1} + (1 - M^2)\frac{\partial^2 p'}{\partial y_1^2} + \frac{\partial^2 p'}{\partial y_2^2} + \frac{\partial^2 p'}{\partial y_3^2} = 0. \tag{2.33}$$

and satisfies the non-penetration boundary condition,

$$\frac{\partial p'}{\partial y_3} = 0, \tag{2.34}$$

on the surface of the rigid plate.

In order to make use of Schwarzchild's solution to solve the scattering problem defined by Amiet, the 3D convected Helmholtz equation needs transforming into a static 2D form. Firstly the convected Helmholtz equation is transformed with

$$\tilde{y}_1 = y_1, \tilde{y}_2 = y_2 \,\text{and}\, \tilde{y}_3 = \beta y_3, \tag{2.35}$$

where $\beta = \sqrt{1 - M^2}$, into

$$k^2 p' - 2\,\mathrm{i}kM\frac{\partial p'}{\partial \tilde{y}_1} + \beta^2\frac{\partial^2 p'}{\partial \tilde{y}_1^2} + \frac{\partial^2 p'}{\partial \tilde{y}_2^2} + \beta^2\frac{\partial^2 p'}{\partial \tilde{y}_3^2} = 0. \tag{2.36}$$

Next the acoustic pressure, p', has to be transformed so as to remove the first order differentials, $\frac{\partial p'}{\partial \tilde{y}_1}$ and $\frac{\partial^2 p'}{\partial \tilde{y}_2^2}$, this can be accomplished with

$$p' = \tilde{p}'\,\mathrm{e}^{\,\mathrm{i}kM\tilde{y}_1/\beta^2 - \,\mathrm{i}k_2\tilde{y}_2}, \tag{2.37}$$

to give

$$\tilde{k}^2\tilde{p}' + \frac{\partial^2 \tilde{p}'}{\partial \tilde{y}_1^2} + \frac{\partial^2 \tilde{p}'}{\partial \tilde{y}_3^2} = 0, \tag{2.38}$$

a static 2D form the Helmholtz equation, where

$$\tilde{k} = \frac{\sqrt{k^2 - \beta^2 k_2^2}}{\beta^2} \tag{2.39}$$

To transform the boundary conditions, the solution for the scattered surface pressure is split into two parts, $p_S = p_{S1} + p_{S2}$. For the first solution, the plate is extended to infinity downstream of the trailing edge. Then, using the method of images,

$$p_{S1} = p'_I(\omega, k_1, k_2)\, e^{-ik_1 y_1 - ik_2 y_2}. \tag{2.40}$$

This first solution satisfies the boundary condition of no flow through the plate, but introduces a discontinuity in pressure across the trailing edge and imaginary downstream extension. According to the Kutta condition the pressure at the trailing edge must be finite and continuous, nor can the wake sustain a discontinuity in pressure. Hence the second solution must fulfil the boundary conditions

$$\frac{\partial \tilde{p}'_{S2}}{\partial \tilde{y}_3} = 0, \tilde{y}_1 < 0 \tag{2.41}$$

and

$$\tilde{p}'_{S2} = -p'_I\, e^{-ik_1\tilde{y}_1 - ikM\tilde{y}_1/\beta^2}, \tilde{y}_1 \geq 0. \tag{2.42}$$

With these boundary conditions $\tilde{p}_{S2}$ on the lower surface of the plate, $\tilde{y} \leq 0$, can be found using the Schwarzchild solution,

$$\tilde{p}'_{S2} = -\frac{p'_I\, e^{i\tilde{k}\tilde{y}_1}}{\pi} \int_0^\infty \sqrt{-\frac{\tilde{y}_1}{\xi}} \frac{e^{-i\xi(\tilde{k}+k_1+kM/\beta^2)}}{\xi - \tilde{y}_1}\, d\xi. \tag{2.43}$$

This can then be simplified to

$$p'_{S2} = p'_I\, e^{-ik_1 y_1 - ik_2 y_2}[(1+i)\, E(-y_1[k_1 + \tilde{k} + kM/\beta^2]) - 1], \tag{2.44}$$

where

$$E = \int_0^x \frac{e^{-it}}{\sqrt{2\pi t}}\, dt \tag{2.45}$$

is a combination of Fresnel integrals. Combining p_{S1} and p_{S2} gives the full solution for the scattered pressure on the lower surface of the plate to be

$$p'_S = p'_I\, e^{-ik_1 y_1 - ik_2 y_2}(1+i)\, E(-y_1[k_1 + \tilde{k} + kM/\beta^2]). \tag{2.46}$$

In order to come to this solution it has been assumed that the incident pressure at the trailing edge extends over the entire domain. For the pressure induced by boundary layer turbulence (as modelled by Amiet), the change in boundary layer characteristics along the plate means that this is not the case, with the pressure spectra changing with y_1. To compensate for this, Amiet[42] includes a small real component, ε, in p'_{S1}, effectively allowing the strength of the incident pressure component to vary with chord-wise location

(y_1), thus

$$p'_{\mathrm{S}} = p'_{\mathrm{I}}\,\mathrm{e}^{-\,\mathrm{i}k_1y_1-\,\mathrm{i}k_2y_2}[(1+\,\mathrm{i})\,\mathrm{E}(-y_1[k_1+\sqrt{k^2-(\beta k_2)^2}/\beta^2+kM/\beta^2])-1] + p'_{\mathrm{I}}\,\mathrm{e}^{k_1y_1(-\,\mathrm{i}+\varepsilon)-\,\mathrm{i}k_2y_2} \quad (2.47)$$

To calculate the scattered pressure in the far-field Curle's/Kirchoff's theory is applied to the scatted surface pressure,

$$p' = \int_{\mathrm{S}} p' \frac{\partial G}{\partial n}\,\mathrm{d}S, \quad (2.48)$$

where G is the free-field acoustic Greens function in a uniform flow. Given the anti-symmetric nature of the scattered surface pressure and the negligible thickness of the plate, it is possible to integrate the pressure difference across the plate

$$p'_{\mathrm{S}x} = \int_{-c}^{0}\int_{-d/2}^{d/2} 2p'_{\mathrm{S}}\frac{\partial G}{\partial y_3}\,\mathrm{d}y_2\,\mathrm{d}y_1, \quad (2.49)$$

where c is the chord of the plate and d is the span. The scattered surface pressure, p_{S}, has been calculated for a plate with semi-infinite chord, however, completing the far-field integral over a finite chord length has been shown by Roger & Moreau[43] to accurately approximate the effect of finite chord lengths for $kc > 1$. In the frequency domain the free-field Greens function in a uniform flow is given by

$$G = \frac{\mathrm{e}^{-\,\mathrm{i}k\tilde{r}_{x-y}/\beta+\,\mathrm{i}kM(x_1-y_1)/\beta^2}}{4\pi\beta\tilde{r}_{x-y}}, \quad (2.50)$$

where

$$\tilde{r}_{x-y} = \sqrt{(x_1-y_1)^2/\beta^2+(x_2-y_2)^2+(x_3-y_3)^2}, \quad (2.51)$$

the derivative of the Greens function with respect to the surface normal is then

$$\frac{\partial G}{\partial y_3} = \frac{-(x_3-y_3)\,\mathrm{e}^{-\,\mathrm{i}k\tilde{r}_{x-y}/\beta+ikM(x_1-y_1)/\beta^2}}{4\pi\beta\tilde{r}_{x-y}^2}\left[-\mathrm{i}\frac{k}{\beta}-\frac{1}{\tilde{r}_{x-y}}\right]. \quad (2.52)$$

Assuming that the observer is in the geometric far field, $|x| >> |y|$, and given that $y_3 = 0$ on the plate, several approximations can be made

$$\tilde{r}_{x-y} \approx \tilde{r}_x - \frac{y_1x_1}{\beta^2\tilde{r}_x} - \frac{y_2x_2}{\tilde{r}_x} \quad (2.53)$$

and

$$\frac{1}{\tilde{r}_{x-y}^2} \approx \frac{1}{\tilde{r}_x^2}, \quad (2.54)$$

so the derivative of the Greens function simplifies to

$$\frac{\partial G}{\partial y_3} \approx \frac{\mathrm{i}kx_3}{4\pi\beta^2\tilde{r}_x^2}\,\mathrm{e}^{-\mathrm{i}k(\tilde{r}_x - y_1x_1/\tilde{r}_x\beta^2 - y_2x_2/\tilde{r}_x)/\beta + \mathrm{i}kM(x_1-y_1)/\beta^2}, \tag{2.55}$$

with which the integrals with respect to y_1 and y_2 in Equation 2.49 are separable. First, the integral over the spanwise direction is

$$\int_{-d/2}^{d/2} \mathrm{e}^{-\mathrm{i}y_2(k_2 - kx_2/\beta\tilde{r}_x)}\,\mathrm{d}y_2 = 2\frac{\sin([k_2 - kx_2/\beta\tilde{r}_x]d/2)}{k_2 - kx_2/\beta\tilde{r}_x}. \tag{2.56}$$

In the limit of the plate span, d, extending from $-\infty$ to ∞ this function simplifies to

$$\lim_{d/2\to\infty} 2\frac{\sin([k_2 - kx_2/\beta\tilde{r}_x]d/2)}{k_2 - kx_2/\beta\tilde{r}_x} = 2\pi\delta(k_2 - kx_2/\beta\tilde{r}_x), \tag{2.57}$$

which demonstrates that a single spanwise wavenumber propagates to each azimuthal location in the far-field, due to interference between the sources along the span. Next, the integration is performed along the chord

$$\begin{aligned}\int_{-c}^{0} (\,\mathrm{E}(-y_1C_1) - 1/(1+i))\,\mathrm{e}^{-\mathrm{i}y_1C_2} + \frac{1}{1+\mathrm{i}}\,\mathrm{e}^{-\mathrm{i}y_1(C_2 - \varepsilon k_1/\mathrm{i})}\,\mathrm{d}y_1 = \\ \frac{1}{\mathrm{i}C_2}\left[\mathrm{e}^{\mathrm{i}C_2c}\,\mathrm{E}(C_1c) - \sqrt{\frac{C_1}{C_1 - C_2}}\,\mathrm{E}(c[C_1 - C_2]) + \frac{1 - \mathrm{e}^{\mathrm{i}C_2c}}{1+\mathrm{i}}\right] \\ - \frac{1 - \mathrm{e}^{\mathrm{i}c_2c - \varepsilon k_1c}}{(1+\mathrm{i})(\,\mathrm{i}C_2 - \varepsilon k_1)} = \Gamma(c, C_1, C_2),\end{aligned} \tag{2.58}$$

where $C_1 = k_1 + \tilde{k} + kM/\beta^2$ and $C_2 = k_1 - kx_1/\beta^3\tilde{r}_x + kM/\beta^2$. In the limits that $kc \to \infty$ and $\varepsilon \to 0$, the last factor becomes

$$\frac{1 - \mathrm{e}^{\mathrm{i}c_2c - \varepsilon k_1c}}{(1+\mathrm{i})(\,\mathrm{i}C_2 - \varepsilon k_1)} \to \frac{1}{\mathrm{i}C_2(1+\mathrm{i})} \tag{2.59}$$

and so

$$\Gamma(c, C_1, C_2) = \mathrm{e}^{\mathrm{i}C_2c}\,\mathrm{E}(C_1c) - \sqrt{\frac{C_1}{C_1 - C_2}}\,\mathrm{E}(c[C_1 - C_2]) - \frac{\mathrm{e}^{\mathrm{i}C_2c}}{1+\mathrm{i}}. \tag{2.60}$$

Combining these results gives the scattered pressure in the far-field as

$$p'_{\mathrm{S}x}(\omega) = (1+\mathrm{i})\frac{kx_3\,\mathrm{e}^{-\mathrm{i}k(\tilde{r}_x - Mx_1/\beta)/\beta}}{C_2\beta^2\tilde{r}_x^2}\int\int p'_{\mathrm{I}}\delta(k_2 - kx_2/\beta\tilde{r}_x)\Gamma(c, C_1, C_2)\,\mathrm{d}k_2\,\mathrm{d}k_1. \tag{2.61}$$

Finally, completing the integral with respect to the spanwise wavenumber and assuming the axial-wavenumber components are uncorrelated, the PSD in the far-field can be found,

$$\mathrm{PSD}_{\mathrm{S}x}(\omega) = \left[\frac{kx_3}{C_2\beta^2\tilde{r}_x^2}\right]^2 \int \mathrm{PSD}_{\mathrm{I}}(\omega, k_1, k_2)\,|\Gamma(c, C_1, C_2)|^2\,\mathrm{d}k_1, \tag{2.62}$$

where $k_2 = kx_2/\beta\tilde{r}_x$.

Using the equation for far-field PSD and making some simplifications Amiet[40] draws some conclusions on the directivity of the scattered acoustic field. Setting M equal to zero, $k_2 = kx_2/r_x = k\sin(\theta)\sin(\phi)$, $C_1 = k_1 + k\sqrt{1-\sin^2(\theta)\sin^2(\phi)}$ and $C_2 = k_1 - kx_1/r_x = k_1 - k\cos(\theta)$. If then $kc \to \infty$, $\mathrm{E}(C_1 c)$ & $\mathrm{E}(c(C_1 - C_2)) \to 0.5(1 - \mathrm{i})$. In these limits far-field PSD becomes a proportional to

$$\mathrm{PSD}_{Sx} \propto \frac{k^2\sin^2(\theta)\cos^2(\phi)}{r_x^2[k_1 - k\cos(\theta)]^2}\frac{k_1 + k\sqrt{1-\sin^2(\theta)\sin^2(\phi)}}{k[\cos(\theta) + \sqrt{1-\sin^2(\theta)\sin^2(\phi)}]}, \tag{2.63}$$

the first thing to notice is that PSD is proportional to $1/r_x^2$ as is expected when the observer is in the geometric far field. Next, to look at azimuthal directivity, the polar angle, θ, is set to $\pi/2$, then

$$\mathrm{PSD}_{Sx} \propto \frac{k^2\cos^2(\phi)}{r_x^2 k_1^2}\frac{k_1 + k\cos(\phi)}{k\cos(\phi)}, \tag{2.64}$$

which demonstrates the directivity, approximately, of a dipole. The dipole directivity comes from the fluctuating pressure on either side of the plate, which with opposing phase leads to cancellation at angles close to the plane of the surface. However, the azimuthal directivity displayed above differs from a true dipole due to the infinite span of the surface which reduces the cancellation from opposing sides of the surface. The directivity can also differ from a dipole if the amplitude of the incident pressure varies with spanwise wavenumber, because only one wavenumber component propagates to each azimuthal angle (for a surface of infinite span).

If instead the azimuthal angle, ϕ, is set to zero or π, the polar directivity can be assessed. In this case

$$\mathrm{PSD}_{Sx} \propto \frac{k^2\sin^2(\theta/2)}{r_x^2[k_1 - k\cos(\theta)]^2}\frac{k_1 + k}{k}, \tag{2.65}$$

displaying the cardioid directivity that has been seen in experiments[18] and shown analytically by other methods.[35]

In order to make use of Schwarzchild's solution Amiet has extended the turbulent pressure spectra immediately adjacent to the trailing edge across the entire domain. Instead the boundary layers modelled by Amiet, and their pressure fields, will grow from the leading edge and continue to change in the wake of the aerofoil. The pressure field of a jet originates in the shear layer, which grows from the lip line. The source strength of each frequency component grows and decays[44,45] across the finite extent of the jet, with the frequency components peaking at different axial locations.[18,44–46] Therefore the incident pressure from a jet onto a closely positioned surface will also not be stationary, but vary along the surface.

To correct for the assumption that the incident pressure is stationary, Amiet includes a small real component in the incident pressure field. Instead, a more precise method would be to decompose the entire pressure field into axial wavenumber components, which would then be said to extend over the entire domain. This is the approach taken by Bychkov & Faranosov[47][48] for calculating JSI noise, and is possible due to the relative ease of measuring the near-field pressure of jets, as well as the growth and decay of each frequency component of the hydrodynamic field over a limited axial distance. However, near-field measurements are taken on a cone about the jet, so some method is required to get the pressure onto a cylinder to allow a spatial Fourier transform to be taken along the jet axis. Many microphones are also required, currently limiting the practicality of this method. In the future models for the jet hydrodynamic field may be available that make the axial wavenumber decomposition of the jet near-field more practical.

2.2.2.1 Roger & Moreau

If the scattering surface is not semi-infinite, i.e. it does not extend to $y_1 = -\infty$, then Amiet's theory leads to an, unphysical, pressure difference across $y_1 = \pm 0$ upstream of the leading edge of the surface. To remove this pressure difference, Schwarzchild's solution can be applied iteratively,[49,50] removing the pressure difference created ahead of the leading edge/aft of the trailing edge by each previous iteration. Roger & Moreau[43][51] have calculated the first leading-edge correction for Amiet's trailing-edge theory, showing that it has the largest effect for $kc < 1$ where it reduces the amplitude of the scattered noise.

JSI occurs at low frequencies, and therefore the backscattering correction could be important. Assuming a 4 m chord for a generic modern 150-seater airliner[18] and a speed of sound of 340 m/s, $kc = 1$ occurs at a frequency of approximately 15 Hz, below the lower limit of frequencies used to calculate EPNL.[52] For the experiments described in Chapter 5, $kc = 1$ occurs at a frequency of approximately 540 Hz for the mid-sized chord, equivalent to a Strouhal number of 0.2 for the lowest jet velocity. While the effect of backscattering is most pronounced for $kc < 1$ it can still affect directivity and, hence, the spectral shape at higher values of kc. It could therefore be beneficial to include Roger & Moreau's backscattering correction when comparing Amiet's theory with laboratory measurements of JSI noise.

With the inclusion of a leading edge scattered term, p'_{S3}, the solution for the scattered pressure on the surface of the plate becomes, $p'_{\mathrm{S}} = p'_{\mathrm{S1}} + p'_{\mathrm{S2}} + p'_{\mathrm{S3}}$. p'_{S3} can then be found using the Schwarzchild solution. Upstream of the leading edge the boundary condition for the scattered field is[43,49,53]

$$\Phi = 0, \tag{2.66}$$

where Φ is velocity potential. This boundary condition has been variously described as: 1) stating that only the surface of the aerofoil can support lift;[49] 2) a simplification of the Sommerfield condition;[43] or 3) ensuring the scattered field cannot produce noise sources upstream of the surface. With the pressure on one side of the plane $y_3 = 0$ for $y_1 < 0$ given by 2.44, then using

$$p' = \rho_0 \left(\frac{\partial \Phi}{\partial t} + U_0 \frac{\partial \Phi}{\partial x_1} \right) \tag{2.67}$$

the velocity potential that needs to be removed upstream of the trailing edge is

$$\Phi_{S2} = \frac{p'_I \, \mathrm{e}^{-\mathrm{i}y_1\omega/U_0 - \mathrm{i}y_2 k_2}}{\mathrm{i}\rho_0 U_0(\omega/U_0 - k_1)} \left\{ \mathrm{e}^{\mathrm{i}y_1(\omega/U_0 - k_1)}[(1+\mathrm{i})\,\mathrm{E}(-y_1 C_1) - 1] \right.$$
$$\left. - \sqrt{\frac{C_1}{C_1 + \omega/U_0 - k_1}}[(1+\mathrm{i})\,\mathrm{E}(-y_1[C_1 + \omega/U_0 - k_1]) - 1] \right\} \tag{2.68}$$

In order to apply Schwarzchild's solution, the variables need to be transformed using

$$\breve{y}_1 = -(y_1 + c) \tag{2.69}$$

and

$$\Phi' = \tilde{\Phi}' \, \mathrm{e}^{-\mathrm{i}k_2 y_2 - \mathrm{i}(\breve{y}_1 + c)kM/\beta^2}. \tag{2.70}$$

Which leads to

$$\tilde{\Phi}'_{S3} = -\frac{p'_I \, \mathrm{e}^{\mathrm{i}(\breve{y}_1 + c)\omega/U_0 + \mathrm{i}(\breve{y}_1 + c)kM/\beta^2}}{\mathrm{i}\rho_0 U_0(\omega/U_0 - k_1)} \left\{ \mathrm{e}^{-\mathrm{i}(\breve{y}_1 + c)(\omega/U_0 - k_1)}[(1+\mathrm{i})\,\mathrm{E}([\breve{y}_1 + c]C_1) - 1] \right.$$
$$\left. - \sqrt{\frac{C_1}{C_1 + \omega/U_0 - k_1}}[(1+\mathrm{i})\,\mathrm{E}([\breve{y}_1 + c][C_1 + \omega/U_0 - k_1]) - 1] \right\}$$
$$\breve{y}_1 \geq 0 \tag{2.71}$$

and

$$\frac{\partial \tilde{\Phi}'_{S3}}{\partial y_3} = 0 \qquad \breve{y}_1 \leq 0 \tag{2.72}$$

In order to get an analytical solution using Schwarzchild's solution, Amiet's Error function is transformed into an Error function and replaced with the asymptotic expansion

$$(1+\mathrm{i})\,\mathrm{E}(t) - 1 = \mathrm{Erf}(\sqrt{\mathrm{i}t}) - 1 \sim -\frac{\mathrm{e}^{-\mathrm{i}t}}{\sqrt{\mathrm{i}\pi t}}. \tag{2.73}$$

Further, the potential at the trailing edge is assumed to be stationary, leaving the potential upstream of the leading edge as

$$\tilde{\Phi}_{S3} = \frac{p'_I \, \mathrm{e}^{-\mathrm{i}\tilde{k}(\breve{y}_1 + c)}}{i\rho_0 U_0(\omega/U_0 - k_1)\sqrt{\mathrm{i}\pi C_1 c}} \left[1 - \frac{C_1}{C_1 + \omega/U_0 - k_1} \right] \qquad \breve{y}_1 \geq 0. \tag{2.74}$$

Applying Schwarzchild's solution, the scattered potential becomes

$$\tilde{\Phi}_{\mathrm{S3}} = \frac{p'_{\mathrm{I}}\,\mathrm{e}^{-\,\mathrm{i}\tilde{k}c+\,\mathrm{i}\tilde{k}\breve{y}_1}}{\mathrm{i}\rho_0 U_0(\omega/U_0-k_1)\sqrt{\mathrm{i}\pi C_1 c}}\left[1-\frac{C_1}{C_1+\omega/U_0-k_1}\right]\left\{\mathrm{e}^{-2\,\mathrm{i}\tilde{k}\breve{y}_1}\left[1-(1+\,\mathrm{i})\,\mathrm{E}(-2\tilde{k}\breve{y}_1)\right]\right\}^{\mathrm{c}}, \tag{2.75}$$

where the imaginary component of the function surrounded by $\{\}^{\,\mathrm{c}}$ is multiplied by the correction factor $\varepsilon = \left(1+\frac{1}{2\tilde{k}c}\right)^{-1/2}$. This correction was derived by a comparison to a numerical calculation of Schwarzchild's integral that did not assume that the velocity potential incident on the leading edge is stationary.

Using Equation 2.67 the scattered pressure on the plate is calculated from the potential

$$\begin{aligned} p'_{\mathrm{S3}} = {} & \frac{p'_{\mathrm{I}}\,\mathrm{e}^{-\,\mathrm{i}c(\tilde{k}+kM/\beta^2)-ik_2y_2}}{\mathrm{i}U_0(\omega/U_0-k_1)\sqrt{\mathrm{i}\pi C_1 c}}\left[1-\frac{C_1}{C_1+\omega/U_0-k_1}\right] \\ & \left(\mathrm{i}[\omega+U_0kM/\beta^2-U_0\tilde{k}]\,\mathrm{e}^{-\,\mathrm{i}\breve{y}_1(kM/\beta^2-\tilde{k})}\left\{\mathrm{e}^{-2\,\mathrm{i}\tilde{k}\breve{y}_1}\left[1-(1+\,\mathrm{i})\,\mathrm{E}(-2\tilde{k}\breve{y}_1)\right]\right\}^{\mathrm{c}}\right. \\ & \left. -U_0\,\mathrm{e}^{-\,\mathrm{i}\breve{y}_1(kM/\beta^2-\tilde{k})}\frac{\partial}{\partial\breve{y}_1}\left\{\mathrm{e}^{-2\,\mathrm{i}\tilde{k}\breve{y}_1}\left[1-(1+\,\mathrm{i})\,\mathrm{E}(-2\tilde{k}\breve{y}_1)\right]\right\}^{\mathrm{c}}\right). \end{aligned} \tag{2.76}$$

Once again applying Curle's theory to find the far-field pressure, if the span of the plate is infinite, the integral over the span again leads to a delta function

$$\delta(k_2 - kx_2/\beta\tilde{r}_x). \tag{2.77}$$

The integral over the chord-wise dimension is complicated by the correction factor. In order to include the correction, if the plate has infinite span, and hence $\tilde{k}$ remains real, the corrected term can be rewritten as

$$\begin{aligned} \left\{\mathrm{e}^{-2\,\mathrm{i}\tilde{k}\breve{y}_1}\left[1-(1+\,\mathrm{i})\,\mathrm{E}(-2\tilde{k}\breve{y}_1)\right]\right\}^{\mathrm{c}} = {} & \cos(2\tilde{k}\breve{y}_1) - \,\mathrm{i}\varepsilon\sin(2\tilde{k}\breve{y}_1) \\ & -\frac{1}{2}(1+\varepsilon)(1+\,\mathrm{i})\,\mathrm{e}^{-2\,\mathrm{i}\tilde{k}\breve{y}_1}\,\mathrm{E}(-2\tilde{k}\breve{y}_1) \\ & -\frac{1}{2}(1-\varepsilon)(1-\,\mathrm{i})\,\mathrm{e}^{2\,\mathrm{i}\tilde{k}\breve{y}_1}\,\mathrm{E}^*(-2\tilde{k}\breve{y}_1), \end{aligned} \tag{2.78}$$

where

$$\mathrm{E}^* = \int_0^x \frac{\mathrm{e}^{\,\mathrm{i}t}}{\sqrt{2\pi t}}\,\mathrm{d}t. \tag{2.79}$$

Completing the integral over $\breve{y}_1$, the scattered far-field pressure becomes

$$p'_{\mathrm{S}x3} = \frac{p'_{\mathrm{I}} k x_3 \,\mathrm{e}^{-\,\mathrm{i}k(\tilde{r}_x - Mx_1/\beta)/\beta - 2\,\mathrm{i}c\tilde{k}}}{\beta^2 \tilde{r}_x^2 (k - Mk_1)\sqrt{\mathrm{i}\pi C_1 c}} \left[1 - \frac{MC_1}{MC_1 + k - Mk_1}\right]$$
$$\left[M\left\{\mathrm{e}^{2\,\mathrm{i}\tilde{k}c}\left[1 - (1+\mathrm{i})\,\mathrm{E}(2\tilde{k}c)\right]\right\}^{\mathrm{c}} - M\,\mathrm{e}^{\,\mathrm{i}cC_3} + \mathrm{i}\left\{k + kM^2/\beta^2 - M\tilde{k} + MC_3\right\}\left\{\right.\right.$$
$$\frac{1+\varepsilon}{C_3 - 2\tilde{k}}\,\mathrm{e}^{\,\mathrm{i}c[2\tilde{k}+C_3]/2}\sin(c[C_3 - 2\tilde{k}]/2) + \frac{1-\varepsilon}{C_3 + 2\tilde{k}}\,\mathrm{e}^{\,\mathrm{i}c[C_3 - 2\tilde{k}]/2}\sin(c[C_3 + 2\tilde{k}]/2)$$
$$+ \frac{(1-\mathrm{i})(1+\varepsilon)}{2(C_3 - 2\tilde{k})}\,\mathrm{e}^{2\,\mathrm{i}c\tilde{k}}\,\mathrm{E}(2\tilde{k}c) - \frac{(1+\mathrm{i})(1-\varepsilon)}{2(C_3 + 2\tilde{k})}\,\mathrm{e}^{-2\,\mathrm{i}c\tilde{k}}\,\mathrm{E}^*(2\tilde{k}c)$$
$$\left.\left. + \frac{1}{2}\,\mathrm{e}^{\,\mathrm{i}cC_3}\sqrt{\frac{2\tilde{k}}{C_3}}\,\mathrm{E}(cC_3)\left[\frac{(1+\mathrm{i})(1-\varepsilon)}{C_3 + 2\tilde{k}} - \frac{(1-\mathrm{i})(1+\varepsilon)}{C_3 - 2\tilde{k}}\right]\right\}\right] \tag{2.80}$$

with

$$C_3 = \tilde{k} - \frac{kx_1}{\beta^3 \tilde{r}_x} \tag{2.81}$$

$$k_2 = kx_2/\beta\tilde{r}_x. \tag{2.82}$$

When applying the above back-scattering theory it is important that the pressures are summed with Amiet's original theory, and not the PSDs, as the two are coherent.

2.3 Jet-Surface Interaction Noise

In this section different jet-surface interaction noise models are discussed; starting with a model for the directivity of JSI noise and continuing on to discuss different semi-analytical JSI noise models.

2.3.1 Miller

In 1983, Miller[54] presented a semi-empirical model for jet-airframe interaction noise, developed from the theory of Curle,[37] Yildiz & Mawardi[55] and Ffowcs-Williams & Hall,[35] together with laboratory measurements of installed jet noise.

First, Miller defines a peak Strouhal number for jet airframe interaction noise, based on the shear layer width at the trailing edge, rather than jet diameter (Equation 2.83). As the shear layer width isn't known Miller suggests it scales with the distance of the trailing edge from the nozzle and the change in potential core length with flight.

$$\mathrm{St} = \frac{fl}{3U_{\mathrm{j}}}\left(\frac{U_{\mathrm{j}} - U_{\mathrm{f}}}{U_{\mathrm{j}}}\right)^{C_1} \tag{2.83}$$

To scale the magnitude of the far-field acoustic pressure Miller uses the equation developed by Curle for the far-field acoustic pressure created by a fluctuating pressure on a rigid surface. This involves first scaling the dynamic pressure on the surface near the jet using Equation 2.84 and then inserting this into Curle's equation to give Equation 2.85, where K is the acoustic pressure coefficient.

$$C_p = \frac{P}{0.5\gamma P_0 M_\mathrm{j}^2} = M_\mathrm{j}^{C_4}\left(1 - \frac{U_\mathrm{f}}{U_\mathrm{j}}\right)^{C_2} C_3 K \tag{2.84}$$

$$p = C_5 M_\mathrm{j}^{3+C_4}\left(1 - \frac{U_\mathrm{f}}{U_\mathrm{j}}\right)^{C_6} \int K(y1, t - r/a_0)\frac{r_j n_j}{r^2}\,\mathrm{d}S \tag{2.85}$$

To derive a directivity Miller starts with the cardioid shape for sound produced by a semi-infinite surface in a turbulent flow as derived by Yildiz & Mawardi and Ffowcs-Willams & Hall, among others. This is then extended to account for the interference of sound waves diffracted at the leading edge of a finite chord wing. Miller's directivity is given by

$$p \propto \sqrt{1 - (C_7\cos(\pi C_8))^2}\cos\left(\frac{\theta + \beta}{2}\right) \tag{2.86}$$

where

$$C_7 = \left(1 - \frac{\theta}{\pi}\right)^{0.25} \exp[-\frac{c}{2\pi\lambda}(\theta + \beta)], \tag{2.87}$$

$$C_8 = \frac{\left(r_\mathrm{TE} - r_\mathrm{LE} - \frac{c}{1-M_\mathrm{f}}\right)}{\lambda}, \tag{2.88}$$

θ is measured to the upstream axis, and r_LE and r_TE are the distances from leading edge and trailing edge, respectively, to the observer. Additionally, a $(1 - M\cos(\theta))^4$ dipole Doppler amplification factor is assumed for sound pressure level.

The measurements of installed jet noise used by Miller were taken of an $1/13^\mathrm{th}$-scale half-body 757 model within an acoustic wind tunnel. The measurements were taken with surface pressure transducers on the flaps in the cut-out region, while acoustic measurements were taken with two microphones 3 ft from the model. The microphones were protected from the flow using nose cones and their position along the wing tunnel could be varied using a linear traverse. The microphone and surface pressure measurements were used to determine the proportion of far-field power radiated form each surface pressure location.

Using these measurements, Miller found the overall directivity of the jet-surface interaction noise from the main flap to appear as a half baffled dipole in the rear arc, but to deviate from this in the forward arc. The directivity of a specific third octave band was found to be dependent on flight speed, which was attributed to the change in phase speed with flow speed and emission angle in a moving medium. The effect of leading edge diffraction and flight speed are captured in Miller's directivity model, which was demonstrated to match well with the measured JSI noise from the main flap. Other experiments have also shown good agreement between Miller's directivity and JSI noise.[18]

Using the measurements Miller found found values of C_1 between 0.1 and 0.6 a value of approximately 2 for C_2, and found C_4 to vary between -0.3 and 0.25 depending on the surface location

2.3.2 Cavalieri et al.

In 2014 Cavalieri et al. published[56] a method for calculating JSI noise using the Tailored Greens Function (TGF) method of Ffowcs-Williams & Hall[35] in combination with a wavepacket source model. The solution for the far-field pressure due to scattering from the trailing edge of a semi-infinite surface is given by Ffowcs-William & Hall as

$$\hat{p} = \frac{1}{4\pi} \int_V G \frac{\partial^2 \hat{T}_{ij}}{\partial y_i \partial y_j} \, \mathrm{d}y, \tag{2.89}$$

where the Greens function, G, is specific to the trailing-edge scattering problem. Cavalieri et al. model the Lighthill stress tensor using a wavepacket model[57]

$$\hat{T}_{ij} = 2\rho_0 U_1(r) u_1'(r, m, \omega) \, \mathrm{e}^{-\mathrm{i}k_1 y_1 - y_1^2/L_{corr}^2}, \tag{2.90}$$

where the stress tensor has been simplified to contain only the axial velocity components. For this model, U_1 is found from velocity profile measurements at the axial location of interest. Using this profile, instability analysis is used to find k_1 and u_1', leaving a constant in the solution of u_1' and L_{corr} to be found. These are found by comparison of isolated jet noise measurements, at polar angles far into the rear arc, with wavepacket predictions.

The edge-scattering method of Ffowcs-Williams & Hall assumes a semi-infinite plate. In reality there will be conditions where the assumption of a semi-infinite plate does not provide a good approximation for the scattered field, such as when the chord and span is not large relative to the wavelength. Therefore, Cavalieri et al.[56] have produced a numerical solution, accounting for finite span and chord, using the Boundary Element Method (BEM). This method is found to converge on the analytical solution as the chord and span go to infinity.[56] For scattering surfaces of finite chord and span, a lobed polar directivity is found, with a change in chord affecting the number, position and strength

of the lobes, while increasing the span for a given chord suppresses the peaks and troughs of the lobes. For each of the different spans used in the BEM calculations the azimuthal directivity remains similar to that of a dipole.

Piantanida et al.[58,59] have compared the directivity predicted with the TGF and BEM models to laboratory measurements of installed jet noise, using surfaces with varying degrees of trailing-edge sweep. The BEM model directivity is shown to be in good agreement with the experimental measurements, capturing lobes that the TGF does not.

Additionally, the measurements, and models, of Piantanida et al. show that as sweep increases the peak angle of JSI noise shifts towards the sideline. Nogueira et al.[60,61] have shown, using the TGF model, that this is because the spanwise wavenumber distribution of the pressure incident on the plate forms a Gaussian, and, as sweep angle increases, the peak spanwise wavenumber shifts from $k_2 = 0$, with an increasing amount of the distribution falling into the non-propagating region. Nogueira et al. have also used this model to demonstrate the rotation of the cardioid directivity pattern of JSI noise as the scattering surface is inclined.

Huber et al.[62] have used this model to try to deduce the effect of flight on JSI noise. This was achieved via the inclusion of ambient flow velocity in the TGF, and via the stretching of the wave packet source using

$$1 + 0.4\frac{U_\mathrm{f}}{U_\mathrm{j} - U_\mathrm{f}}, \tag{2.91}$$

where 0.4 has been found from measurements. They conclude that the effect of flight on jet noise is to reduce rear arc wavepacket noise much more than the JSI noise. With reported reductions of 25 dB and 7 dB respectively for $M_\mathrm{f} = 0.3$. However, no comparison is made with experimental measurements, to validate the model and predictions in flight.

2.3.3 Vera

Vera[63–65] has used the Wiener-Hopf method to calculate far-field scattered noise produced by a pressure field convecting past the trailing edge of a static semi-infinite surface. Vera has shown that the solution generated using the Wiener-Hopf method is equivalent, in the far-field, to that of Amiet's theory, and so will not be discussed further here.

To calculate the incident pressure along the trailing edge of the plate, Vera starts with the near-field pressure about an isolated jet calculated by LES. The pressure data is taken from the LES in cones of probes about the jet, to which the Ffowcs-William Hawking (FWH) equation would otherwise be applied to calculate the far-field noise created by

the jet. To calculate the incident pressure on the surface, the free-field conical Greens function of Reba et al.[66] is applied

$$G_m = \frac{\mathrm{i}}{4\sqrt{r_y r_x}} \sum_{\mu} \frac{1}{A_\mu} \mathrm{H}_{\mu+0.5}(kr_x)\, \mathrm{J}_{\mu+0.5}(kr_y)\, \mathrm{P}_\mu^m(\cos(\theta_x))\, \mathrm{P}_\mu^m(\cos(\theta_y)), \tag{2.92}$$

where P_μ^m is the Lengendre polynomial of order m and degree μ, m is the azimuthal mode, and A_μ is the integral of the Lengendre function

$$A_\mu = \int_0^{\theta_0} |\, \mathrm{P}_\mu^m(cos(\theta))|^2 \sin(\theta)\, \mathrm{d}\theta. \tag{2.93}$$

The CPSD between the incident pressures at two points on the plate is then given by integrating over the cone

$$\mathrm{CPSD}(x_1, x_2) = 4\pi^2 \sin^2(\alpha) \sum_m \mathrm{e}^{\,\mathrm{i}m(\phi_{y1}-\phi_{y2})} \int\int \mathrm{CPSD}_y \frac{\partial G_m}{\partial \theta}_{r_{y1}} \frac{\partial G_m}{\partial \theta}_{r_{y2}} \mathrm{d}r_{y1}\, \mathrm{d}r_{y2}. \tag{2.94}$$

Once the CPSD between points along the span of the trailing edge has been found, a Fourier transform is taken along the span so as to give spanwise-wavenumber spectra at each frequency. The Wiener-Hopf solution also requires the axial wavenumber of the incident pressure; this is calculated using a convection velocity of $0.6U_j$.

Comparison of the calculated far-field JSI noise with measurements show good agreement. The advantages to this method are: Firstly, no assumptions have been made concerning the properties of the near-field pressure of jets, keeping the solution quite general, and bypassing the debate on the source of the incident pressure field; secondly, by using a solution equivalent to Amiet's theory, the effect of finite chord can be approximated; thirdly, the method could be extended to more realistic geometries, such as swept wings, by continuing to calculate the wavenumber components perpendicular and parallel to the trailing edge; and, fourthly, for additional computational cost, the axial wavenumber could be calculated by propagating the near-field pressure to various chordwise locations along the plate and taking a Fourier transform along the chord. However, the disadvantages to the method are: Firstly, the prediction is dependent on having an LES solution for the near-field pressure of an isolated jet; secondly, the frequency resolution is limited by the LES, which usually has limited resolution (compared to experiment) by the run time required; thirdly, the conical propagation method is quite slow and it takes a significant amount of time to calculate the eigenvalues required for a new FWH surface with a new cone angle; and, fourthly, the conical Greens function used requires the plate to be situated outside the conical FWH surface, with empirical corrections required for surfaces positioned closer to the jet.

In order to reduce the dependency on LES, Vera has created an semi-empirical model for the near-field pressure along a cone, based on that of Reba et al.,[66]

$$\mathrm{CPSD}(r_{y1}, r_{y1}, \omega, m) = \sqrt{\mathrm{PSD}_{r_{y1},\omega,m}\,\mathrm{PSD}_{r_{y2},\omega,m}}\,\mathrm{e}^{-(\frac{r_{y1}-r_{y2}}{2L_{\mathrm{cor}}})^2}\,\mathrm{e}^{-\mathrm{i}k(r_{y1}-r_{y2})}, \tag{2.95}$$

where k is the axial wavenumber and L_{cor} is the correlation length, both defined at the midpoint between y_1 and y_2. L_{cor} is found with a simple linear model,

$$L_{\mathrm{cor}} = C_1 y + C_2, \tag{2.96}$$

and the PSD along the cone is modelled using a Glegg[45] style distribution,

$$\mathrm{PSD}(y) = C_3 \left(\frac{y}{\lambda}\right)^{C_4-1} \exp(-2\pi C_5 \frac{y}{\lambda}). \tag{2.97}$$

Then, to run cases in which the jet parameters do not match the LES, the near-field pressure amplitude is scaled by $(D/D_{\mathrm{ref}})^2(M/M_{\mathrm{ref}})^{3.5}$ and the frequency with Strouhal number $St = fD/(U_{\mathrm{j}} - U_{\mathrm{f}})$. If the plate is positioned within the FWH surface, then the solution is calculated with the plate positioned just outside the surface, with the far-field scattered pressure scaled to account for the actual plate locations using $(h/h_{\mathrm{ref}})^6$. In flight the Strouhal number $St = fD/(U_{\mathrm{j}} - U_{\mathrm{f}})$ and amplitude scaling, $\left(\frac{U_{\mathrm{j}}}{U_{\mathrm{j}}-U_{\mathrm{f}}}\right)^{-4-l/D}$, are used. These scaling methods go some way to extending the model beyond its initial capabilities, however, further work is needed to extend the propagation and Wiener-Hopf solution used to include ambient flow, decrease the reliance on LES and to allow the plate to be positioned within the FWH surface.

2.3.4 Lyu & Dowling

Lyu[67][68][69][70][71] has used Amiet's theory to calculate the JSI noise produced by the interaction of the evanescent hydrodynamic pressure field of a jet with the trailing edge of a plate.

Lyu suggests that, as the hydrodynamic field is coherent and slowly varying over a large length of the jet axis, the evanescent hydrodynamic field can be decomposed into modes and axial wavenumber components to be propagated using cylindrical harmonics

$$p'_{\mathrm{I}}(\omega, y_1, r, \phi) = \sum_{m=-\infty}^{\infty} \mathrm{e}^{\mathrm{i}m\phi} \int_{-\infty}^{\infty} p'(\omega, k_1, m)\,\mathrm{H}_m^2(k_r r)\,\mathrm{e}^{-\mathrm{i}k_1 y_1}\,\mathrm{d}k_1, \tag{2.98}$$

where $k_r = \sqrt{k^2 - (k_1\beta^2 + kM)^2}/\beta$. For an evanescent decay k_r is imaginary, so $\mathrm{H}_m^2(k_r r)$ can instead be replaced with $\mathrm{K}_m(\iota_r r)$, where $\iota_r = \sqrt{(k_1\beta^2 + kM)^2 - k^2}/\beta$. Lyu assumes that at each frequency and axial location the hydrodynamic pressure is

dominated by a single convection velocity, and hence axial wavenumber, which simplifies 2.98 to

$$p'_{\mathrm{I}}(\omega, y_1, r, \phi) = \sum_{m=-\infty}^{\infty} \mathrm{e}^{\,\mathrm{i}m\phi} p'(\omega, m)\, \mathrm{K}_m(\iota_r r)\, \mathrm{e}^{-\,\mathrm{i}k_1 y_1}. \tag{2.99}$$

The validity of this assumption is demonstrated by Lyu with LES by plotting wavenumber versus frequency about a given axial location. With this assumption, measurements of the spectra of the hydrodynamic field at two different radial locations can be collapsed using

$$\frac{\mathrm{PSD}(\omega, m)}{\mathrm{K}_m^2(\iota_r r)} \tag{2.100}$$

from which the axial wavenumber for each frequency can be found. This removes the reliance on costly LES, allowing the input to come from experimental measurements using few microphones. Also, the plate is no longer required to remain outside an arbitrarily positioned FWH surface, allowing the plate to be positioned closer to the jet. However, the propagation method is not valid if the plate is within the flow field of the isolated jet from which the near-field pressure measurements were taken.

For a plate positioned in a plane parallel to and a distance h above the jet axis, the position of a point on the span is given in cylindrical coordinates by

$$r = \sqrt{h^2 + y_2^2}, \cos(\phi) = \frac{h}{\sqrt{h^2 + y_2^2}}, \sin(\phi) = \frac{y_2}{\sqrt{h^2 + y_2^2}}, \tag{2.101}$$

where the coordinate system of Lyu & Dowling has been used ($\phi = 0°$ is in the direction of y_1 and $\phi = 90°$ in the direction of y_2). Using De Moivre's and Euler's formulae, the pressure at a point on the span is given by 2.99 with

$$\begin{aligned} \mathrm{e}^{\,\mathrm{i}m\phi} = \Bigg(& \sum_{n=0}^{\lfloor |m|/2 \rfloor} (-1)^n \binom{|m|}{2n} \frac{h^{|m|-2n} y_2^{2n}}{(h^2 + y_2^2)^{|m|/2}} \\ & + \mathrm{i} \sum_{n=0}^{\lfloor (|m|-1)/2 \rfloor} (-1)^n \binom{|m|}{2n+1} \frac{m}{|m|} \frac{h^{|m|-(2n+1)} y_2^{2n+1}}{(h^2 + y_2^2)^{|m|/2}} \Bigg). \end{aligned} \tag{2.102}$$

In order to utilise Amiet's theory the incident pressure on the plate needs to be decomposed into axial and spanwise wavenumbers. Therefore, a Fourier transform is taken

with respect to y_2,

$$p'_{\mathrm{I}}(\omega, m, k_2) = \frac{p'(\omega, m)}{2\pi} \int_{-\infty}^{\infty} \mathrm{K}_m\left(\iota_r \sqrt{h^2 + y_2^2}\right) \mathrm{e}^{\mathrm{i}m\phi}\, \mathrm{e}^{\mathrm{i}k_2 y_2}\, \mathrm{d}y_2 =$$
$$\frac{p'(\omega, m)}{\sqrt{2\pi}} \left(\sum_{n=0}^{\lfloor |m|/2 \rfloor} \binom{|m|}{2n} h^{-2n+1/2} \iota_r^{-|m|} \frac{\mathrm{d}^{2n}}{\mathrm{d}k_2^{2n}} \left[(\iota_r^2 + k_2^2)^{|m|/2 - 1/4}\, \mathrm{K}_{|m|-1/2}\left(h\sqrt{\iota_r^2 + k_2^2}\right)\right] \right.$$
$$\left. - \frac{m}{|m|} \sum_{n=0}^{\lfloor (|m|-1)/2 \rfloor} \binom{|m|}{2n+1} h^{-2n+1/2} \iota_r^{-|m|} \frac{\mathrm{d}^{2n}}{\mathrm{d}k_2^{2n}} \left[k_2 (\iota_r^2 + k_2^2)^{|m|/2 - 3/4}\, \mathrm{K}_{|m|-3/2}\left(h\sqrt{\iota_r^2 + k_2^2}\right)\right] \right) \tag{2.103}$$

(see Appendix A for the full derivation). The pressure along the span of the plate can then be written as

$$p'_{\mathrm{I}}(\omega, y_1, y_2) = \sum_{m=-\infty}^{\infty} \int_{-\infty}^{\infty} p'_I(\omega, m, k_2)\, \mathrm{e}^{-\mathrm{i}k_1 y_1 - ik_2 y_2}\, \mathrm{d}k_2. \tag{2.104}$$

Lyu & Dowling have then extended Amiet's theory to account for a swept trailing edge using the transforms of Roger & Carazo.[72]

Starting with the convected Helmholtz equation

$$k^2 p' - 2\,\mathrm{i}kM \frac{\partial p'}{\partial y_1} + (1 - M^2) \frac{\partial^2 p'}{\partial y_1^2} + \frac{\partial^2 p'}{\partial y_2^2} + \frac{\partial^2 p'}{\partial y_3^2} = 0, \tag{2.105}$$

the first part of the solution for the scattered surface pressure is, as before,

$$p'_{\mathrm{S1}} = p'_{\mathrm{I}}(\omega, k_1, k_2)\, \mathrm{e}^{-\mathrm{i}k_1 y_1 - \mathrm{i}k_2 y_2}. \tag{2.106}$$

However, the boundary conditions for the second part of the solution are now given by

$$\frac{\partial p'_{\mathrm{S2}}}{\partial y_3} = 0, y_1 < y_2 \tan(\psi) \tag{2.107}$$

and

$$p'_{\mathrm{S2}} = -p'_I\, \mathrm{e}^{-ik_1 y_1 - \mathrm{i}k_2 y_2}, y_1 \geq y_2 \tan(\psi). \tag{2.108}$$

The boundary conditions and Helmholtz equation are then transformed using the transformations[72]

$$\tilde{y}_1 = y_1 - y_2 \tan(\psi), \tag{2.109}$$

$$\tilde{y}_2 = y_2, \tag{2.110}$$

$$\tilde{y}_3 = \sqrt{\beta^2 + \tan^2(\psi)}\, y_3 \tag{2.111}$$

and

$$p = \tilde{p}\, \mathrm{e}^{-\mathrm{i}\tilde{k}_2 \tilde{y}_2 - \mathrm{i}(\tilde{k}_2 \tan(\psi) - kM)/(\beta^2 + \tan^2(\psi)))\tilde{y}_1}, \tag{2.112}$$

where

$$\tilde{k}_2 = k_2 + k_1 \tan(\psi). \tag{2.113}$$

This gives a static form of the Helmholtz equation

$$\tilde{k}^2 \tilde{p}' + \frac{\partial^2 \tilde{p}'}{\partial \tilde{y}_2^2} + \frac{\partial^2 \tilde{p}'}{\partial \tilde{y}_3^2} = 0, \tag{2.114}$$

where

$$\tilde{k} = \frac{\sqrt{k^2 - \tilde{k}_2^2 + [\tilde{k}_2 M - k \tan(\psi)]^2}}{\beta^2 + \tan^2(\psi)}, \tag{2.115}$$

along with the boundary conditions

$$\frac{\partial \tilde{p}'_{\mathrm{S2}}}{\partial \tilde{y}_3} = 0, \tilde{y}_1 < 0 \tag{2.116}$$

and

$$\tilde{p}'_{\mathrm{S2}} = -p'_{\mathrm{I}} \, \mathrm{e}^{-\mathrm{i}(k_1 - (\tilde{k}_2 \tan(\psi) - kM)/(\beta^2 - \tan^2(\psi)))\tilde{y}_1}, \tilde{y}_1 \geq 0. \tag{2.117}$$

Applying Schwarzchild's solution

$$p'_{\mathrm{S2}} = \mathrm{e}^{-\mathrm{i}k_2 y_2 - \mathrm{i}k_1 y_1}[(1 + \mathrm{i})\,\mathrm{E}(-[y_1 - y_2 \tan(\psi)]C_1) - 1], \tag{2.118}$$

where

$$C_1 = \tilde{k} + k_1 - \frac{\tilde{k}_2 \tan(\psi) - kM}{\beta^2 + \tan^2(\psi)}. \tag{2.119}$$

The far-field pressure is given by Curle's theory

$$p'_{\mathrm{S}x} = \int_{-d/2}^{d/2} \int_{y_2 \tan(\psi) - c}^{y_2 \tan(\psi)} 2p'_{\mathrm{S2}} \frac{\partial G}{\partial y_3} \, \mathrm{d}y_1 \, \mathrm{d}y_2. \tag{2.120}$$

It is more convenient to complete this integral in the transformed coordinates, therefore,

$$\frac{\partial G}{\partial y_3} \approx \frac{\mathrm{i}kx_3}{4\pi\beta^2 \tilde{r}_x} \, \mathrm{e}^{-\mathrm{i}k/\beta(\tilde{r}_x - Mx_1/\beta) - \mathrm{i}(k/\beta)(\tilde{y}_1[M/\beta - x_1/(\beta^2 \tilde{r}_x)] + \tilde{y}_2[\tan(\psi)M/\beta - x_2/\tilde{r}_x - x_1 \tan(\psi)/(\beta^2 \tilde{r}_x])}. \tag{2.121}$$

Completing the integral along the spanwise direction

$$\int_{-d/2}^{d/2} \mathrm{e}^{-\mathrm{i}\tilde{y}_2 C_2} d\tilde{y}_2 = 2\frac{\sin(C_2 d/2)}{C_2}, \tag{2.122}$$

which in the limit $d/2 \to \infty$ becomes

$$2\frac{\sin(C_2 d/2)}{C_2} \to 2\pi\delta(C_2) \tag{2.123}$$

where

$$C_2 = \tilde{k}_2 + \frac{k}{\beta}\left(\tan(\psi)\left[\frac{M}{\beta} - \frac{x_1}{\beta^2 \tilde{r}_x}\right] - \frac{x_2}{\tilde{r}_x}\right). \tag{2.124}$$

Next, integrating along the chordwise direction

$$\int_{-c}^{0} \mathrm{e}^{-\mathrm{i}\tilde{y}_1 C_3}[\,\mathrm{E}(-\tilde{y}_1 C_1) - 1/(1+\mathrm{i})]\,\mathrm{d}\tilde{y}_1 = \frac{1}{\mathrm{i}C_3}\left[\mathrm{e}^{\mathrm{i}C_3 c}\,\mathrm{E}(C_1 c) - \sqrt{\frac{C_1}{C_1 - C_3}}\,\mathrm{E}(c[C_1 - C_3]) + \frac{1-\mathrm{e}^{\mathrm{i}C_3}}{1+\mathrm{i}}\right], \quad (2.125)$$

where

$$C_3 = k_1 + (k/\beta^2)(M - x_1/\beta\tilde{r}_x). \quad (2.126)$$

Applying Amiet's correction,

$$\Gamma(c, C_1, C_3) = \mathrm{e}^{\mathrm{i}C_3 c}\,\mathrm{E}(C_1 c) - \sqrt{\frac{C_1}{C_1 - C_3}}\,\mathrm{E}(c[C_1 - C_3]) - \frac{\mathrm{e}^{\mathrm{i}C_3}}{1+\mathrm{i}}, \quad (2.127)$$

the solution for the scattered far-field pressure becomes

$$p'_{\mathrm{S}x} = (1+\mathrm{i})\frac{k x_3\,\mathrm{e}^{-\mathrm{i}(k/\beta)(\tilde{r}_x - M x_1/\beta)}}{\beta^2 \tilde{r}_x^2 C_3} p'_{\mathrm{I}}\Gamma(c, C_1, C_3), \quad (2.128)$$

where

$$k_2 = -k_1\tan(\psi) - (k/\beta)(\tan(\psi)[M/\beta - x_1/(\beta^2\tilde{r}_x)] - x_2/\tilde{r}_x). \quad (2.129)$$

For JSI noise it is more convenient to work in terms of the statistical quantity power spectral density. Combining the equations for the spanwise wavenumber spectrum and the far-field trailing-edge-scattered noise, and assuming that the different near-field modes are independent, the far-field PSD becomes

$$\mathrm{PSD}_x(\omega) = \frac{2k^2 x_3^2}{\beta^4 C_2^2 \tilde{r}_x^4}\sum_{m=0}^{\infty}\mathrm{PSD}(\omega, m, \tilde{k}\tilde{x}_2/\tilde{r}_x)\left|\Gamma(c, C_1, C_2|_{k_2=\tilde{k}\tilde{x}_2/\tilde{r}_x})\right|^2, \quad (2.130)$$

where

$$\mathrm{PSD}(\omega, m, k_2) = \frac{\mathrm{PSD}(\omega, m)}{2\pi}\left\{\left(\sum_{n=0}^{\lfloor |m|/2\rfloor}\binom{|m|}{2n}h^{-2n+1/2}\iota_r^{-|m|}\frac{\mathrm{d}^{2n}}{\mathrm{d}k_2^{2n}}\left[(\iota_r^2+k_2^2)^{|m|/2-1/4}\,\mathrm{K}_{|m|-1/2}\left(h\sqrt{\iota_r^2+k_2^2}\right)\right]\right)^2 + \left(\sum_{n=0}^{\lfloor (|m|-1)/2\rfloor}\binom{|m|}{2n+1}h^{-2n+1/2}\iota_r^{-|m|}\frac{\mathrm{d}^{2n}}{\mathrm{d}k_2^{2n}}\left[k_2(\iota_r^2+k_2^2)^{|m|/2-3/4}\,\mathrm{K}_{|m|-3/2}\left(h\sqrt{\iota_r^2+k_2^2}\right)\right]\right)^2\right\} \quad (2.131)$$

and $\mathrm{PSD}(\omega, m)$ is a one-sided PSD of the jet near-field pressure.

In the case where no modal information is available for the near-field spectrum (such

as where near-field pressure measurements were taken with a single microphone), the solution can be approximated by computing that for mode 0 only, but with $\mathrm{PSD}(\omega, m)$ and k_1 based on the total PSD

$$\mathrm{PSD}_x(\omega) = \frac{2k^2 x_3^2}{\beta^4 C_2^2 \tilde{r}_x^4} \mathrm{PSD}(\omega, \tilde{k}\tilde{x}_2/\tilde{r}_x) \left|\Gamma(c, C_1, C_2|_{k_2=\tilde{k}\tilde{x}_2/\tilde{r}_x})\right|^2, \tag{2.132}$$

with

$$\mathrm{PSD}(\omega, k_2) = \frac{\mathrm{PSD}(\omega)}{2\pi} \frac{h}{\sqrt{\iota_r^2 + k_2^2}} \mathrm{K}_{-1/2}^2 \left(h\sqrt{\iota_r^2 + k_2^2}\right) \tag{2.133}$$

This approximation is possible because, for axi-symmetric jets, modes 0 and 1 dominate the hydrodynamic spectra. These modes have similar axial wavenumbers, and propagate in a similar manner over the small distance from jet to surface.

Lyu & Dowling's method for calculating JSI noise is relatively quick and simple. The input comes from jet near-field pressure measurements using single rings of microphones. With access to a laboratory with a jet, these measurements can be very quick to take. Once these measurements have been taken, and the axial wavenumber found, the solution is fully analytic. However, this method currently assumes that the incident pressure is stationary. This may be a pitfall when the scattering surface has a very short chord and/or a swept trailing edge. However, it could become the basis of a quick JSI noise prediction tool useful for industry.

2.3.5 Bychkov & Faranosov

Bychkov & Faranosov[47, 48, 73] have produced a model for JSI noise incorporating the change in amplitude of the jet hydrodynamic pressure field along the jet axis.

In order to account for the variation in amplitude along the jet, near-field measurements are taken, either experimentally or with LES, on a cone about the jet. At each axial location the measured hydrodynamic pressure is decomposed into frequency and mode and propagated onto a cylinder using a similar method to Lyu & Dowling. A Gaussian distribution is then fitted to the amplitude of the hydrodynamic field along the cylinder,

$$p'(\omega, m, x_1) = \frac{p'(\omega, m)}{C_1\sqrt{\pi}} \mathrm{e}^{-(x_1 - C_2)^2/C_1^2 + \mathrm{i}\omega(x_1 - C_2)/U_\mathrm{j}}, \tag{2.134}$$

where C_1 defines the width of the distribution and C_2 the centre. Finally, a Fourier transform is taken of the Gaussian distribution, giving axial wavenumber spectra that describe the variation in amplitude.

Once the axial wavenumber spectra have been found, each component of the pressure field can be propagated on to the surface of the plate using cylindrical harmonics. Using the Wiener-Hopf method, the far-field scattered pressure is then calculated from the incident surface pressure. The results have been validated against installed jet noise

measurements taken at TsAGI, with a flat plate positioned in close proximity to the laboratory jet.

Not assuming the pressure incident on the trailing edge could improve the predictions. However, the choice of distribution could be improve; as pointed out by Bychkov, the Gaussian distribution does not fit the measured amplitudes very well. A Glegg distribution could perhaps have been used instead, as has already been used by Vera to model the hydrodynamic field. The axial wavenumber is also assumed to be constant, while Vera's results also show that the axial wavenumber of the hydrodynamic field does slowly vary along the jet axis. Unfortunately, by propagating the each axial measurement independently from the cone onto a cylinder the phase between the axial locations is lost. This method of propagating from the cone to a cylinder does at least mean that the measurements at the different axial locations do not need to be taken synchronously. Finally, comparison to calculations where the incident pressure on the trailing edge is assumed to be stationary has shown that the assumption of a Gaussian wavepacket is unnecessary, with both methods giving the same result.[48]

2.3.6 Afsar

Another model is that presented by Afsar,[74, 75] for calculating the scattered pressure created by the interaction of a planar jet with a trailing edge.

The pressure generated on the trailing edge due to this interaction is calculated using Rapid-Distortion Theory (RDT), which requires the trailing edge to be positioned well inside the jet flow field, due to the assumptions that $u' << \bar{U}$. This, however, means that it is not well applicable to configurations where the plate is positioned outside or on the edge of the jet flow-field, where it is possible that $u' > \bar{U}$, which may be more closely related to current aeroplane configurations. One advantage, though, is that the model is able to use RANS solutions for turbulent kinetic energy and dissipation, along with empirical models relating these values to turbulent length scales, as an input. This allows the model to be used for more general cases than those previously mentioned.

To calculate the scattered pressure due to the trailing edge the Wiener-Hopf method is again used. However, while the model results follow the general spectral shapes seen in experiment, it does not capture the interference patterns typically found using the Wiener-Hopf method, or Amiet's theory, and in the experimental measurements. Several of the cases used also display large differences in the measured and calculated peak amplitudes. This method may, therefore, be useful for extreme cases in which the scattering surface is heavily wetted, such as for strongly deployed flaps, but less so for un- or lightly-wetted cases.

2.3.7 Summary

Five published models for predicting JSI noise have been reviewed. Four of these use the Wiener-Hopf technique, or equivalent theory of Amiet, for calculating the trailing-edge scattering. The other uses both the Green's function of Ffowcs-Williams & Hall and BEM. These methods have been shown by the authors to be capable of predicting the directivity of JSI noise for static jets with straight and swept wings. Of these methods the Wiener-Hopf technique/ Amiet's theory appears the most suitable for a theoretical scattering model, as, unlike the TGF, it can approximate the effect of finite chord length and span. For more complicated geometries, the numerical BEM may be more suitable, however, the time and effort required to mesh/run a solution may make this impractical for industry.

The majority of the authors consider plate locations outside the flow-field of the equivalent isolated jet, with an apparent consensus that the irrotational hydrodynamic pressure field of the jet is the source of JSI noise, and is comprised of coherent structures that can be described either by wavepackets or cylindrical harmonics. These two descriptions are essentially the same, for example the models of Bychkov and Cavalieri both assume a Gaussian wave envelope. The difference is that the wavepacket model is propagated using a point Green's function, and is based on far-field data, while the other is propagated with cylindrical harmonics and based on near-field measurements. There are, however, exceptions: the model of Afsar, which considers a plate within the jet flow field, uses RDT; and the model of Vera, which makes no assumptions about the hydrodynamic pressure field, relying solely on LES data.

Discounting the model of Afsar, as it is solely for a plate which greatly distorts the jet flow and so will not be considered further. The models of Vera, Bychkov and Lyu have been shown by the authors to accurately predict the spectra of JSI noise for static jets. However, they all require jet hydrodynamic pressure spectra, either from experiment or numerical calculation, as an input. They have also not been validated against installed jet noise measurements either in flight (except for that of Bychkov & Faranosov[76]), or using realistic wing geometries. As for the model of Cavalieri et al., the amplitude and directivity have been well validated at a several Strouhal numbers, and has already been used to estimate possible changes to JSI noise in flight. It can also be calibrated using far-field data, which may be advantageous, as it removes the need for separate near-field measurements. However, it still has to overcome the same issues as the other models, and no comparisons of frequency spectra been published.

Of the four methods for predicting JSI noise, that of Lyu & Dowling appears most suited towards producing a method for calculating JSI noise that can be used by industry. However, before it can be used some of the aforementioned short comings need to be addressed.

2.4 Jet Near-Field Modelling

In the previous section methods were presented for calculating JSI noise. One of the limitations of these methods were that they relied on LES or experimental measurements of the near-field pressure of jets. In this section published work is presented that aims to understand the near-field pressure of isolated jets, the source of the JSI noise.

2.4.1 Harper-Bourne

Harper-Bourne[46, 77–79] has created a semi-empirical model for the near-field spectra of isolated jets. The model was based on measurements taken of the near-field unsteady pressure of isolated jets within QinetiQ's Noise Test Facility (NTF), with the aim of improving acoustic fatigue prediction capability for modern fast jets.

The model consists of a shape function describing the spectral shape, with the parameters varying with location and jet velocity, and semi-empirical equations for the peak amplitude and frequency.

The shape function is described by Equation 2.135, with C_1 and C_2 based on fits to measured spectra. This shape factor is similar in form to that developed by Tam[80] for the far-field noise generated by large scale structures for which there is growing evidence that they are the source of the hydrodynamic pressure field.

$$W = \frac{\frac{C_2}{C_2 - C_1}\left(\frac{f}{f_{\text{peak}}}\right)^{C_1}}{1 + \left(\frac{C_1}{C_2 - C_1}\right)\left(\frac{f}{f_{\text{peak}}}\right)^{C_2}} \tag{2.135}$$

The peak frequency of the hydrodynamic pressure spectra was found to vary with Strouhal number and an inverse power of the radial distance from the jet axis. The power with which the peak frequency varies along the jet axis and the characteristic Strouhal number were both found to be dependent on axial position.

Finally, the peak amplitude of the near-field third-octave-band spectra was found to scale with jet velocity between the fourth and fifth power, and decay with distance from the edge of the shear layer as a power law. At a distance greater than 0.5 jet diameters from the shear layer the amplitude decayed as radial distance to the power of -3.7, very similar to the decay of the mid-field of a quadrupole.

The model of Harper-Bourne provides a simple manner in which to describe the unsteady near-field pressure of the jet, in a not dissimilar manner to how semi-empirical models are used for far-field jet noise prediction. Very good agreement was found when validated against measurements of a full-scale jet.

2.4.2 Lawrence

A parametric study of the near-field pressure of an isolated jet has also been undertaken by Lawrence[18] in the University of Southampton's Doak Laboratory. The study assessed changes with jet velocity and microphone location, both radial and axial.

Analysing the peak frequency of the jet's hydrodynamic field, Lawrence found that, for a given axial microphone location, peak frequencies could be collapsed using a Strouhal number based on jet velocity and radial microphone location, relative to the jet lip line. For a constant radial location and jet velocity, the peak Strouhal number was found to decrease with the log of axial position.

For peak SPL, Lawrence found it to scale with jet velocity to a power between 3.5 and 4.4, dependent on axial and radial location. The peak SPL was also found to increase with the log of axial position, while it was found to reduce as radial location to the power of -0.13. This radial decay is similar to the linear decay that would be expected of an exponentially decaying hydrodynamic field. Combining the measured spectra at varying radial locations, the envelope of all the spectra displays the $(fr/U_\mathrm{j})^{20/6}$ and $(fr/U_\mathrm{j})^2$ decay predicted for the hydrodynamic pressure and acoustic fields, respectively, by Arndt.[81]

Another parametric study was conducted on the effects of jet velocity and trailing-edge location on far-field installed jet noise. Far-field noise measurements were then taken on flyover and azimuthal arrays. The results display a U_j^5 relationship for the JSI noise OASPL, and U_j^4 relationship for the peak amplitude. Logarithmic relationships are found between the peak SPL and both radial and axial trailing-edge positions. Miller's directivity is shown to be in very good agreement with that measured on the flyover array. Finally, while the resolution is insufficient to give a good comparison, the OASPL measured on the azimuthal array appears to be consistent with the dipole suggested by theory.

Additionally, the installed jet noise study included unsteady surface pressure measurements on the plate. At a constant transducer location, the peak frequency of the surface pressure was found to scale with U_j and the peak amplitude with U_j^3. This is at odds to the isolated near-field pressure measurements, but agrees with other measurements in the literature.[82]

2.4.3 Vera

Vera,[65] starting from the work of Miller,[83] has extended Lighthill's model to produce an analytical model for the cross power spectral density of the near-, mid- and far-fields of an isolated jet. With the aim being to be able to remove the dependence on LES from the JSI noise model.

Starting from Lighthill's equation in integral form,

$$\rho' = \frac{1}{4\pi a_0^2} \frac{\partial^2}{\partial x_i \partial x_j} \int_V \frac{T_{ij}|_{\tau=t-r/a_0}}{r} \, \mathrm{d}y \tag{2.136}$$

the derivatives are then expanded without the use of the far-field approximation,

$$p' = \frac{1}{4\pi} \int_V \frac{r_i r_j}{a_0^2 r^2} \left[\frac{1}{r} \frac{\partial^2 T_{ij}}{\partial t^2} + \left(\frac{3a_0}{r^2} - \frac{a_0 \delta_{ij}}{r_i r_j} \right) \frac{\partial T_{ij}}{\partial t} + \left(\frac{3a_0^2}{r^3} - \frac{a_0^2 \delta_{ij}}{r r_i r_j} \right) T_{ij} \right] \mathrm{d}y \tag{2.137}$$

(where $r_i = x_i - y_i$), which is Equation 2.10 with the near-field terms included. The three terms are the same as for a quadrupole, representing the far, mid and near fields respectively. The first term is the usual solution to Lighthill's equation, it is the propagating acoustic field in which pressure and velocity are in phase. The last term represents the hydrodynamic component of the pressure field, which is the solution to the incompressible component of the wave equation, which can be demonstrated by setting $a_0 = \infty$.

Next, a cross correlation is then taken between two observer locations (a and b) and times (t and $t + \tau$), which is indicative of acoustic power,

$$\overline{p(x_a, t) p(x_b, t+\tau)} = \int \int \frac{r_i r_j r_l r_m}{r_{(ij)} r_{(lm)}} \overline{\left[C_{1a} \frac{\partial^2 T_{ij}}{\partial t^2} + C_{2a} \frac{\partial T_{ij}}{\partial t} + C_{3a} T_{ij} \right] \left[C_{1b} \frac{\partial^2 T_{lm}}{\partial t^2} + C_{2b} \frac{\partial T_{lm}}{\partial t} + C_{3b} T_{lm} \right]} \, \mathrm{d}y_a \, \mathrm{d}y_b \tag{2.138}$$

As $\overline{\frac{\partial^2 T}{\partial t^2} \frac{\partial T}{\partial t}} = \overline{\frac{\partial}{\partial t} T} = 0$ and $\overline{\frac{\partial T_{ij}}{\partial t} \frac{\partial T_{lm}}{\partial t}} = \frac{\partial^2}{\partial \tau^2} \overline{T_{ij} T_{lm}}$, this equation then becomes

$$\overline{p(x_a, t) p(x_b, t+\tau)} = \int \int \frac{r_i r_j r_l r_m}{r_a r_b} \left[C_{1a} C_{1b} \frac{\partial^4}{\partial \tau^4} + (C_{1a} C_{3b} + C_{2a} C_{2b} + C_{3a} C_{1b}) \frac{\partial^2}{\partial \tau^2} + C_{1a} C_{1b} \right] \overline{T_{ij} T_{lm}} \, \mathrm{d}y_a \, \mathrm{d}y_b. \tag{2.139}$$

Finally the cross power spectral density is calculated as

$$\mathrm{CPSD} = \int_{-\infty}^{\infty} \overline{p(x_a, t) p(x_b, t+\tau)} \exp(-i\omega\tau + \frac{r_a - r_b}{a_0}) \, \mathrm{d}\tau, \tag{2.140}$$

which reverts to the auto power spectral density when $x_a = x_b$.

From Equation 2.140 dimensional analysis is used to generate scaling laws for the power spectral density of the near field,

$$\mathrm{PSD}_{\mathrm{NF}} \sim \frac{U_{\mathrm{j}}^3 D_{\mathrm{j}}^7}{r^6}, \tag{2.141}$$

mid field,

$$\mathrm{PSD}_{\mathrm{MF}} \sim \frac{U_{\mathrm{j}}^5 D_{\mathrm{j}}^5}{a_0^2 r^4}, \tag{2.142}$$

and far field,

$$\mathrm{PSD}_{\mathrm{FF}} \sim \frac{U_{\mathrm{j}}^7 D_{\mathrm{j}}^3}{a_0^4 r^2}, \tag{2.143}$$

of an isolated jet. It can be seen that each component of the pressure field decays as a power law. This contradicts two of the JSI noise models, which use Hankel functions for the propagation, as well as experimental results[84] that show an exponential decay of the near-field. Although, it is feasible that over a short distance a power law decay and an exponential decay could appear similar. Additionally, individual coherent sources could combine to give an exponential decay; however, this would require knowing the phase difference between the sources, something that would have to be modelled separately.

A comparison of far-field installed jet noise measurements by Lawrence suggest with two different nozzle diameters suggests the amplitude of JSI noise scales with D^2, which is also used by Vera's JSI noise model. Rather the near-field is found by Vera to scale with D^7; measurements should therefore be taken to determine whether this is correct.

In order to predict the spectra of the near, mid and far fields of a jet from RANS data, the cross-correlation of the Lighthill stress tensor is modelled using a method proposed by Ribner, which has been used successfully in far-field models. The RANS model is then compared with near-field measurements taken in the Doak Laboratory. The empirical coefficients were set by matching the predicted far-field spectrum with measured data at a polar angle of 90°. The calculated near-field spectra compares very well with the measured spectra with the microphone at an axial location of 4 - 5D, but less well elsewhere. This could be due to the length scale coefficients being dependent on location in the jet. This model could therefore be improved by trying to account for these changes, and further still if it could be made to predict the phase along the jet, which, for the near-field, has been shown to be coherent over a large distance along the jet axis.

2.4.4 Stability Analysis

Measurements taken in the near field of jets, starting back in the 1960s,[85] have shown that the near-field pressure can be coherent over large distances along the jet axis. Not only was the pressure coherent over a large distance but it also showed alternating phase, suggesting that the pressure field is created by a train of structures in the velocity field of the jet, not simply a large eddy. More recently, measurements of the near-field pressure on cones about jets, both from experiment and LES, have shown the amplitude of these structures to behave like a Glegg style distribution along the jet axis,[64–66] with phase speeds $\approx 0.6U_\mathrm{j}$. Despite the subsonic phase speeds of these 'large coherent structures', and therefore evanescent decay perpendicular to the jet axis, they play an important role in jet noise at low polar angles, as shown for instance by the results of Reba.[66] This is because a Fourier transform taken of the entire envelope results in a wavenumber spectrum, a proportion of which falls in the region which allows acoustic propagation.[16] The pressure field of these large coherent structures are also likely to be important for JSI noise, which, as shown in the previous section, is created by the scattering of a non-propagating pressure field into an acoustic field by a trailing edge.

Due to the importance of these structures to noise at low polar angles and near-field pressure, much work has been focussed on trying to model them. The velocity and pressure fields of these large coherent structures can be captured using LES. However, as with jet noise, the large amount of time required to mesh a geometry, and the huge amount of computing power required to calculate a solution, makes this method unsuitable for general engineering problems. Attempts to produce simpler models have focussed on stability analysis of jets. Initially Linearised Stability Equations (LSE) were used, starting with a cylindrical vortex sheet description of the jet,[86] but extended to later to include more realistic shear layer profiles[87] and spreading jets.[88] Later, the introduction of the Parabolic Stability Equations (PSE) allowed for the inclusion of non-linear effects.

Stability analysis has been shown to be capable of predicting the amplification and attenuation of instability waves of low Strouhal numbers over the length of the potential core of the jet (for example[89]). However, there are several problems with their use. For one thing, the amplitudes calculated by linear stability analysis are highly dependent on the amplitude of the initial disturbance, and so the initial conditions are usually calibrated against experimental data. Also, if the amplitude of the instability wave is too high then non-linear effects, not included in linear-stability analysis, will dominate. Experiments have shown that for low Reynolds number jets the instability waves quickly form into eddies that interact with one another, rolling around each other or breaking apart.[90] For high Reynolds number jets the spreading rate is assumed to be great enough that the instability waves grow and decay with negligible non-linearity.[16] Finally, for this discussion, a base flow is required as an input to the LSE/PSE. This base flow will likely

come from RANS calculations, as it is much quicker than LES but can still be used for general geometries. However, RANS tends to underestimate the spreading rate of jets, which, as previously mentioned, is an important factor in stability analysis.

2.4.5 Summary

Ideally, a jet near-field pressure model would be generic enough that it would be able to predict the amplitude and wavenumbers of the near-field pressure of a jet for any nozzle geometry, jet velocity, temperature and flight velocity. If that were the case then a true prediction could be made for JSI noise. Stability models and near-field Lighthill extensions come some way to achieving this, however, they still need to be calibrated against experimental data to get the correct amplitudes. Even LES should be validated against experimental measurements, often with hot-wire or PIV measurements of the flow field. Even for far-field Jet Mixing (JM) noise such a generic model does not yet exist. Current RANS based models for JM noise still need parameters, describing the structure of the turbulence, to be calibrated using LES or measured data and are in any case considered too complex for industrial use. Therefore, industry standards for JM noise tend to be methods which scale databases of measured jet noise to the required parameters,[91] such as those by ESDU,[92,93] SAE[94] and Stone,[95,96] for example. It therefore seems logical to try to extend the near-field scaling models of Harper-Bourne and Lawrence to include the effects of flight and different nozzle geometries. Combining such an empirical model with an analytical scattering model could generate reasonable predictions useful to industry.

Chapter 3

Experimental Methodology

This chapter describes the measurements of the jet near-field unsteady pressure, far-field isolated jet noise and far-field installed-jet noise that will be used in subsequent chapters. It begins with a description of the laboratory facility in which the experiments were conducted. The experiments themselves are then described, first the near-field pressure measurements, and secondly the far-field jet-mixing and jet-surface interaction noise measurements. Finally, the procedure used to process the measured time series signals is outlined.

3.1 Facility

The experiments described in this chapter were conducted in the University of Southampton's Doak Laboratory - an anechoic chamber for the measurement of the noise produced by jets and handling bleed valves. The anechoic chamber is 15 m long, by 7 m wide and 5 m high, and is anechoic down to approximately 400 Hz. For the measurement of jet noise, the chamber contains a jet nozzle with a diameter of 40 mm fed by compressed air, and a co-axial 'flight-stream' nozzle with a diameter of 300 mm, fed by a fan, for simulating the effect of forward engine motion on installed jet noise. To ensure stable propagation paths, by reducing flow recirculation within the chamber, the exhaust air from the two jets pass through a collector before being passively vented outside the building via a series of louvres.

FIGURE 3.1: Doak Laboratory with jet and flight stream. Also shown is the aerofoil support structure and, at the top of the figure, the flyover microphone array used to measure far-field jet noise

The flight stream in the Doak laboratory is sized for the simulation of forward-flight effects on installed jet noise. As such, the size of the flight-stream minimises the effect of the flight-stream shear layer on the development of the jet across axial trailing-edge positions of interest. The size of the flight-stream also ensure that a spanwise portion of the aerofoil/plate is within the potential core of the flight-stream at trailing-edge positions of interest.

A boundary layer will form on the outside of the jet pipe and nozzle when the flight-stream is active. To prevent the separation of this boundary layer, the jet nozzle, and pipework immediately upstream of the nozzle, has a shallow conical angle of 3°.

3.2 Near-field Measurements

Near-field pressure measurements of static jets have been made multiple times in the past, however, several complications occur when performing similar measurements in flight: 1) the microphone diaphragm needs to be protected from the flow when positioned within the flow field of the flight stream; 2) the microphone will generate self-noise; and 3) the microphone will measure the near-field pressure of both the jet and the flight stream. These problems are common to all in-flow pressure measurements in open-jet wind tunnels, and are overcome by: 1) protecting the microphone diaphragm with a nose cone, here a G.R.A.S. RA0022 nose cone was used (see Figure 3.2); 2) align the microphone with the flow to minimise separation around the microphone, this was

done in conjunction with a thin B & K Type 2670 pre-amplifier; and, 3) tailoring the microphone location, as well as the jet and flight stream velocities, to ensure that the hydrodynamic pressure spectra of the jet is apparent over the near-field pressure of the flight stream.

FIGURE 3.2: Jet near-field pressure measurements were taken using a microphone protected by a nose cone (left) and positioned using a three axis traverse (right)

Microphones measure the change in position, relative to a backing plate, of a diaphragm due to the pressure difference across it. The pressure difference should be due to the unsteady pressure being measured, with a steady difference in pressure causing an offset in initial diaphragm position and affecting the sensitivity of the microphone. To equalize the steady pressure across the diaphragm the cavity behind the diaphragm is vented, either from the rear, front or side. The position of the vent could, therefore, be important when taking measurements within a flow with a nose cone, as the static pressure varies around the nose cone.

For the near-field pressure measurements a G.R.A.S. 40BF rear-vented microphone capsule was used. The rear vent being located away from the nose cone inlet screens could cause a pressure difference across the diaphragm. However, the G.R.A.S. RA0022 is based on the NLR-DNW AMF[97] (Aerodynamic Microphone Forebody) which has been designed using panel methods to have zero pressure gradient at the screen position, with static pressure at the start of the screen equal to ambient. This would help prevent a steady pressure difference across the diaphragm, though a vent closer to the nose cone screen (front or side) would increase confidence that this is the case.

To locate and support the microphone within the flow of the flight stream, a three-axis traverse was used (see Figure 3.2). To ensure accurate positioning of the microphone, the traverse had to be aligned with the jet axis and a reference location set.

To align the near-field microphone with the jet axis, first the traverse was positioned on and aligned with beams on the floor of the chamber running parallel to the jet axis. Next, a laser level was positioned downstream of the nozzle point towards the jet along the jet axis (Figure 3.3). Linear scales were then attached to the microphone and centred on the

laser beam. The microphone was then traversed along the traverse axis set nominally parallel to the jet axis, during which time any movement of the microphone relative to the laser beam could be measured. Corrections could then be derived to apply to the other traverse axes to keep the microphone traversing parallel to the jet axis.

To ensure that the microphone was positioned correctly relative to the nozzle a paper target was affixed to the nozzle, and the microphone traversed such that the tip of the nose cone was touching the centre of the paper target. At the end of each set of measurements the traverse instructions were reversed to ensure the microphone returned to this reference location. When taking measurements the microphone was positioned such that the centre of the diaphragm was in the desired measurement location.

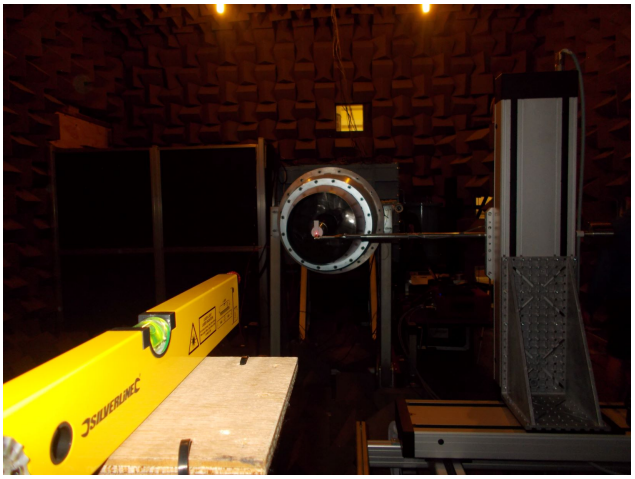

FIGURE 3.3: Traverse is aligned with the jet axis using a laser

Prior to the installation of the flight stream within the Doak laboratory, an experimental campaign was conducted by Lawrence in which the near-field pressure of a static jet was measured. This involved spacing eight microphones equidistantly around the circumference of a steel-ring array, the axis of which was aligned with that of the jet nozzle (Figure 3.4). The array was then traversed along the jet axis, and the radii of the microphones varied such that the near-field pressure was measured on two virtual cones spaced one jet diameter apart (Table 3.1). At each measurement location, the jet was run at the following acoustic Mach numbers: $M_j = 0.3,\ 0.4,\ 0.5,\ 0.6,\ 0.7,\ 0.75,\ 0.8$ & 0.9. Each measurement was taken over a ten second interval with a sampling frequency of 100 kHz.

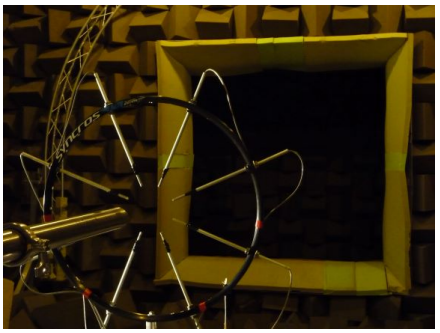

FIGURE 3.4: The azimuthal near-field measurement campaign of Lawrence placed eight microphones in a ring surrounding the jet

TABLE 3.1: Axial and radial measurement locations in the azimuthal near-field pressure measurement campaign of Lawrence

x/D	0	1	2	3	4	5	6	7
r/D	0.75	0.91	1.06	1.22	1.38	1.53	1.69	1.85
	1.75	1.91	2.06	2.22	2.38	2.53	2.69	2.85

With the installation of the new flight stream rig, the jet diameter increased from 38.1 to 40 mm, and the cone angle changed from 14° to 2.3°. However, these changes were considered small enough that a comparison of measurements could be used to validate the use of the nose cones and the alignment of the traverse, by comparing trends in amplitude and spectral shape with microphone radial and axial position. Therefore, the first measurements were taken at some of the same axial locations as Lawrence (x/D = 3, 4, 5 & 6) with jet acoustic Mach numbers of 0.3 and 0.6.

It was hypothesised that the jet hydrodynamic pressure spectra would display similarity when the microphone axial location was scaled with potential core length. To test this hypothesis, measurements were taken of the near-field pressure over a range of flight velocities with the axial position relative to the potential core length of the jet, x/x_{p}, with the radial position, r, kept constant. The potential core length of the 40 mm Doak laboratory jet has been measured by Proenca,[98] and is defined empirically as

$$\frac{x_{\mathrm{p}}}{D_{\mathrm{j}}} = 16M_{\mathrm{f}} + 4.6. \tag{3.1}$$

Using this equation, the axial locations for each flight velocity were chosen as shown in Table 3.2. At each axial location, measurements were taken at radial locations $r/D_{\mathrm{j}} =$ 1.22, 1.72 & 2.22.

TABLE 3.2: Axial measurement locations for velocity scaling

M_{f}	0.0	0.1	0.2	0.3
x/D	3	4	5	6

Next, unsteady pressure measurements were taken to assess the effect of jet diameter the on the hydrodynamic pressure spectra. This involved placing the microphone at x/D = 2 and r/D = 1.1 relative to the jet nozzle and then the flight stream nozzle. This location was chosen as it was the only location the traverse could reach, due to the placement of the traverse, that matched measurement locations used with the previous, 38.1 mm, jet nozzle. At these locations the jet/ flight stream was run at acoustic Mach numbers of M_j = 0.1, 0.2 & 0.3. When taking the flight-stream measurements, the jet was run at the same velocity as the flight stream to prevent separation of the flight stream flow around the jet nozzle.

Finally, measurements were taken to be used as inputs to the scattering model. This required the microphone to be placed at x/D = 3 (the axial location of the trailing edge in Chapter 5) and measurements taken with a range of jet velocities, flight velocities and radial locations. The radial locations used are given in Table 3.3. The static locations are the same as that used in the near-field measurements of Lawrence, with an additional location at $r/D = 1.72$. This point was added to ensure that, at high jet Mach numbers, the jet hydrodynamic pressure would dominate the jet acoustic pressure at more than one radial location. With the flight stream active, the flight stream shear layer also generates noise, which contaminates the measurement of the jet near-field pressure. The flight stream also reduces the shear on the jet, which serves both to stretch the jet, increasing the distance of the microphone from the edge of the shear layer, and to reduce the amplitude of the noise created by the jet. Taking this into consideration, the microphone radial distances were reduced, ensuring though that the microphone did not enter the jet flow field, and reducing the radial interval between measurements.

Table 3.3: Radial near-field measurement locations

M_f	0.0	0.1	0.2	0.3
r/D	1.22	1.15	1.11	0.98
	1.72	1.65	1.36	1.08
	2.22	2.15	1.61	1.33

3.3 Far-field Measurements

Two experimental campaigns were undertaken to measure installation noise in the far field. The first, aimed to validate the model of Lyu in flight and to assess the effect of chord on JSI noise. The second aimed to repeat the validation of Lyu & Dowling's extension of Amiet's theory to swept wings, using both near-field and far-field data from the same jet, and to assess the effect of finite span.

During the first campaign, measurements were taken with 10 1/4" free-field B & K Type 4939 microphones positioned on a linear fly-over array, parallel to the jet axis

(Figure 3.5), at a distance of approximately 50 jet diameters from the axis. The microphones were spaced approximately 10° apart at polar angles from 40° to 130°. The fly-over array consists of a quad truss that can be winched up into position. To minimise any reflections from the truss, the microphones were placed at a distance of 250 mm from the structure.

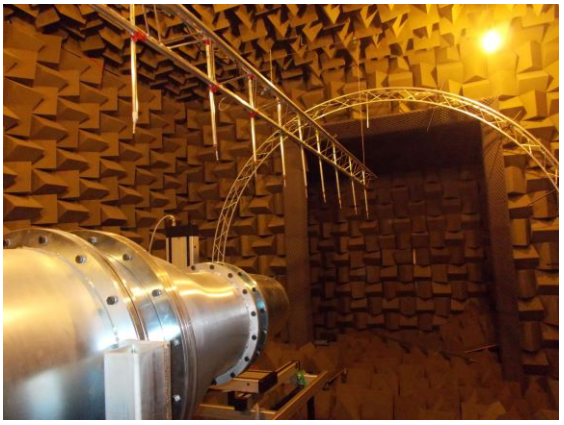

FIGURE 3.5: Fly over array before being winched into position

To start the campaign, far-field pressure measurements were taken of the jet in isolation both statically and in flight. The jet was run at acoustic Mach numbers of $M_\mathrm{j} = U_\mathrm{j}/a_0 =$ 0.3, 0.4, 0.5, 0.6, 0.7, 0.75, 0.8, 0.875 & 0.9, while the flight-stream was run at acoustic Mach numbers of $M_\mathrm{f} =$ 0, 0.1, 0.2 & 0.3. Before each set of static jet measurements an electronic background noise measurement was taken. For in-flight cases, background measurements were taken with the jet and flight-stream velocities matched at the desired flight velocity. The purpose of taking isolated jet noise measurements was to compare with the installed measurements, thus making the installation effects discernible.

Far-field pressure measurements were then taken with flat plates positioned parallel to the jet axis. Three plates were already available for installed jet noise measurements in the Doak laboratory, with chords of 300 mm, 200 mm and 100 mm, or $c/D =$ 7.5, 5.0 & 2.5 respectively. The $c/D = 7.5$ and $c/D = 2.5$ were chosen for the installed jet noise measurements; the $c/D = 7.5$ plate as it gave the longest chord against which to compare the trailing-edge scattering theory, which assumes a semi-infinite chord; and the $c/D = 2.5$ plate as it is at the lower end of the range of commercial airliner jet-diameter to crank-chord ratios. Additionally, a rule with $c/D = 0.7$ was used to give a very short c/D against which to compare. The rule could also be considered to represent a wing tip, or flap, though it is possibly also on the short side of either of these.

Each of the plates had a thickness of $0.03D$, the trailing edges were un-tapered, and each had a span of $d/D = 15$. The trailing edge of each flat plate was located at $l/D = 3$ and $h/D = 1$, measured to the surface of the plate facing the jet. The radial location was set just outside the flow field of the isolated jet since the model of Lyu & Dowling assumes that the jets hydrodynamic pressure spectra is unaffected by the presence of

the plate. This location has also been used previously, as part of the SYMPHONY (SYstem Manufacturing and Product design tHrough cOmponent Noise technologY) project, in measurements taken both in the Doak Laboratory[18] and in QinetiQ's Noise Test Facility (NTF),[137] allowing for direct comparison between several test campaigns.

Using flat plates means that the thickness is constant across the chord, there is no camber, and no lift is generated (at zero incidence), in contrast to aerofoil sections that would expected for an aeroplane wing. For jet-surface interaction noise, the low frequencies, and hence low thickness-to-wavelength ratio, mean that differences in thickness and camber are unlikely to have a significant effect. In flight, the change in thickness of an aerofoil will cause the local velocity around the aerofoil to vary, and lift, caused by incidence or camber, will cause the local velocity to vary between the upper and lower aerofoil surfaces. This could potentially affect the far-field interference pattern, in comparison to a flat plate at zero incidence, by changing the phase and amplitude relationship between the trailing-edge scattered wave and leading-edge diffracted waves. The far-field interference pattern may then not be symmetric for observers above and below the wing.

To enable the accurate positioning of the plates, they are attached to a support structure (Figure 3.6) that could be traversed parallel to the jet and positioned vertically using spacers. The flat plates with chords $c/D = 7.5$ & 2.5(Figure 3.6a) were connected to the structure via a mounting that includes tension bolts to prevent excessive bending or vibration of the plates. The $c/D = 0.7$ plate was an aluminium metre rule which was clamped in place between the spacers used to set vertical position (Figure 3.6b). This proved to be adequate in the static case, when there is no flight-stream flow. However, with the flight stream active, the rule bent towards the jet, reducing the distance from trailing edge to the jet axis by an unknown amount. Therefore, in-flight measurements with the metre rule were discounted, and have not been subject to any further analysis.

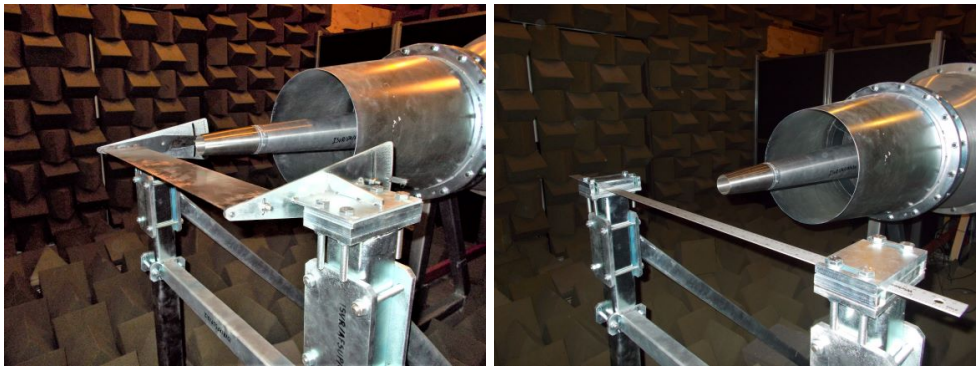

FIGURE 3.6: Far-field jet-surface interaction noise measurements were acquired by positioning a plate next to the jet and within the nominally laminar potential core of a flight stream. Left) $c/D = 2.5$ plate, and, right) $c/D = 0.7$ metre rule

With the flat plates installed, the jet was run at acoustic Mach numbers $M_j = 0.3$, 0.6, 0.75, 0.8, 0.875 & 0.9. These jet velocities were chosen to cover the typical range of approach, cut-back and take-off jet velocities; and to match those used within previous installed jet noise measurement campaigns.

The aim of the second campaign was to provide further validation evidence for the swept wing model of Lyu & Dowling, with matched near-field and far-field measurements. For this reason, ten microphones were placed on an azimuthal array at a distance of 45 jet diameters from the jet axis (Figure 3.7). Seven microphones were positioned between $\phi = -67.5°$ and 67.5° at 22.5° intervals, with the remainder were placed at 80°, −60° and 34°. These locations were chosen to give good resolution around the peak azimuthal angles of the unswept and swept plates. The array was kept at a polar angle $\theta = 90°$, as the model of Lyu & Dowling predicted the biggest difference between the swept and unswept plates at this angle. As with the fly-over array, the microphones were positioned approximately 250 mm from the supporting structure to prevent excessive reflections in the measured spectra.

FIGURE 3.7: Azimuthal array positioned at a polar angle of 90° to the jet nozzle exit

With the microphones and plate support structure in place, isolated jet noise measurements were taken at jet acoustic Mach numbers $M_j = 0.5$, 0.6, 0.75, 0.8 & 0.9, and at flight acoustic Mach numbers $M_f = 0$, 0.1, 0.2 & 0.3. Again, background noise measurements were taken at each flight-stream velocity with a matched jet velocity.

In the second campaign, three plates were again used: 1) the $c/D = 7.5$ plate, to assess the effect of finite span; 2) a swept plate, with $c/D = 2.5$ and sweep angle $\psi = 20°$; and, 3) the $c/D = 2.5$ plate to compare with the swept plate. The planform of the swept plate (Figure 3.8) was chosen to allow direct comparison with the unswept $c/D = 2.5$ plate, and to fit within the constraints of the support structure. The trailing edge of each plate was positioned at $l/D = 3$ and $h/D = 1$, so as to allow comparison with the measurements taken in the previous campaign. With the plates installed, the jet and flight stream were run at acoustic Mach numbers matching the isolated measurements.

FIGURE 3.8: Swept plate with a chord of 2.5D and sweep angle of 20°

Lastly, a series of installed jet noise measurements were taken to demonstrate the effect of a nozzle centre body ("bullet") on JSI noise. To do so, a plate with chord $c/D = 5$ was placed at $l/D = 3$ and $h/D = 1$ relative to the 40 mm metal nozzle used thus far. The location of the plate was then held constant while the nozzle was replaced, with far-field measurements taken with each nozzle at an acoustic Mach number $M_j = 0.3$. In total, four nozzles were used: 1) the standard 40 mm nozzle; 2) a 40 mm nozzle with bullet; 3) a 36 mm nozzle with bullet; and, 4) a 32 mm nozzle without a bullet (nozzles courtesy of Proenca and Lawrence[99]). Despite the different diameters, all but the original 40 mm nozzle had the same nozzle-exit flow area.

FIGURE 3.9: Left) Three nozzles of constant flow area were used to demonstrate the effect of a bullet. Right) The 40 mm nozzle with bullet installed

3.4 Signal Processing

All microphone pressure measurements were recorded using a 24-bit National Instruments PXIe-4497, with the signals first passed through GRAS 12AQ amplifiers. A sample frequency of 100 kHz was used for the near-field measurements and 200 kHz for the far-field measurements. Each recording was taken for 10 s, with the 10 far-field microphones recorded simultaneously.

Prior and subsequent to the test campaigns the microphones were calibrated using a pistonphone-type calibrator. The calibration sensitivities and amplifier gains were used to convert the recorded signal from Volts to Pascals.

After converting the time series from Volts to Pascals, the spectral density of the measured data has been estimated using Welch's[100] modified periodogram method. This method splits the signal into segments, computes the periodogram of each segment and then averages the periodograms, reducing the variance of the final spectra. The computation of a periodogram requires taking the Discrete Fourier Transform (DFT), or FFT, of the measured signal, or segment thereof. Due to the finite length of the signal, and the DFT assuming the signal is periodic, spectral leakage can occur. Therefore, a window whose amplitude reduces towards each end of the signal is typically applied to the segments, reducing the discontinuity between the ends of the signal.[101] As the application of a window effectively reduces the contribution of each end of the signal segment to the periodogram, the segments can be overlapped. For both the near-field and far-field measurements a bandwidth of 10 Hz has been used along with the Hamming window with 50% overlap.

The presence of the microphone distorts the pressure field about the microphone. Therefore, free-field corrections are applied as a function of frequency and incidence angle. For the far-field microphones, which were attached perpendicular to the fly-over array, the incidence angle was calculated from the jet nozzle to the microphone, and varied from approximately 0° to 50°. While for the near-field microphone, with attached nose cone, the pressure is incident at approximately 90° due to the microphone axis being parallel to the jet axis. The individual microphone capsules have also been calibrated for their frequency sensitivity, and these calibrations have been applied to the measured spectra.

At the start of each set of measurements a background noise measurement was taken. This was especially important for in-flight cases, where the flight stream, being a large jet, can contribute significantly to the measured spectra. Background noise measurements with the flight stream were taken with the velocity of the jet and flight stream matched. Matching the jet and flight velocity prevents recirculation around the jet nozzle distorting the flight stream and the noise it produces. For a flight-stream acoustic Mach number of 0.1 a jet Mach number of 0.15 was used, due to limitations in the jet valve control systems preventing a lower jet Mach number. The impact of this discrepancy on the background noise measurement was deemed insignificant due to the much larger size of the flight stream. The background measurements were then subtracted from the test cases, with any test points less than 1 dB greater than the background spectra removed.

Finally, the far-field spectra have been corrected to 'loss less' by correcting for atmospheric attenuation and spherical spreading. The spherical spreading correction simply requires the addition of $20\log_{10}(r/r_{\text{ref}})$, where in this case $r_{\text{ref}} = 1$ m. To correct for

the atmospheric attenuation of air the method of Bass et al.[102] has been used. For the microphone-source distances used (≈2-3 m), frequencies of interest and ambient conditions the atmospheric attenuation corrections are less than 1 dB.

Using a flight stream to simulate flight introduces a shear layer between the noise source and the microphones. This shear layer can refract the acoustic waves, changing the amplitude and spectral shape of the noise measured by the microphones relative to the case of a homogenous flow. Therefore, a correction is commonly applied to the measured spectra to counteract the effect of the shear layer, with the angle and amplitude corrections calculated with geometrical acoustics.[103–105]

The vorticity thickness of the flight-stream shear layer above the trailing edge of the plate was estimated from LES[106, 107] of the Doak laboratory jet, scaling to the diameter of the flight stream. This vorticity thickness was found to be the same length as the shortest peak wavelength of the measured JSI noise spectra, with $M_\mathrm{j} = 0.9$ and $M_\mathrm{f} = 0.3$. Geometrical acoustics is applicable when the properties of the medium through which the sound waves are propagating vary slowly over a wavelength. Therefore, a shear layer correction has not been applied.

The analytical trailing-edge scattering model assumes that the surface and observer are within a homogeneous flow. Therefore, to compare the analytical solution with the measured spectra, the observer is positioned in the analytical solution such that the emission angle and propagation distance (θ and R respectively in Figure 3.10) match the experimental case. The reception angle and distance (θ_R and R_R respectively in Figure 3.10), which define the observer position in the analytical solution, are calculated from the emission angle and distance using[108, 109]

$$\tan(\theta_R) = \sin(\theta)/[M_\mathrm{f} + \cos(\theta)] \tag{3.2}$$

and the reception distance from

$$R_R = R\sqrt{1 + M_\mathrm{f}^2 + 2M_\mathrm{f}\cos(\theta)}. \tag{3.3}$$

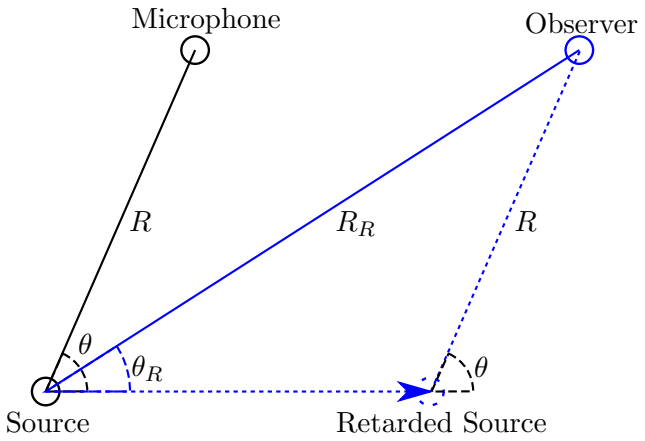

FIGURE 3.10: The position of the observer in the model needs to be chosen such that the emission angle and distance match the position of the microphone relative to the source in the experiment

Examples of the measured far-field spectra are displayed in Figure 3.11 along with the estimated Signal-to-Noise Ratio (SNR). The test cases are those as measured, without background noise subtracted, and the estimated SNR is the ratio of the test spectra, minus background noise, to the background spectra. Statically, with the flight stream off, the background noise in the anechoic chamber is very low and contributes negligibly to the measured jet spectra. With the addition of a flight-stream flow, the flight stream essentially being a second larger-diameter jet, the background noise increases significantly, especially in the installed case where leading and trailing-edge noise will also be generated. As the flight-stream velocity increases the flight-stream spectra comes to dominate the test spectra at low frequencies, and the SNR becomes very low by a flight Mach number of 0.3. The separation between the jet and flight-stream noise levels can be increased by increasing the jet velocity, which increases the amplitude of the jet noise, but also increases the peak frequency. Decreasing the distance between the plate and the jet centreline as the flight velocity is increased could also help in increasing the amplitude of the jet installation noise. If the plate were also moved closer to the jet nozzle, then the peak frequency of the JSI noise would be increased, also helping to separate it from the background noise - though one would still have to contend with the low SNR of the isolated jet noise when trying to discern the JSI noise from jet-mixing noise.

Figure 3.12 displays a similar comparison for the measured spectra for the near-field microphone. As with the far-field measurements the background flight-stream noise increases as the flight-stream velocity is increased, reducing the estimated signal-to-noise ratio. The sharpness of the peaks in the spectra and the separation between the jet and flight stream leads to a rapid increase in SNR from low frequencies and a higher SNR at the highest flight-stream velocity than for the far-field case.

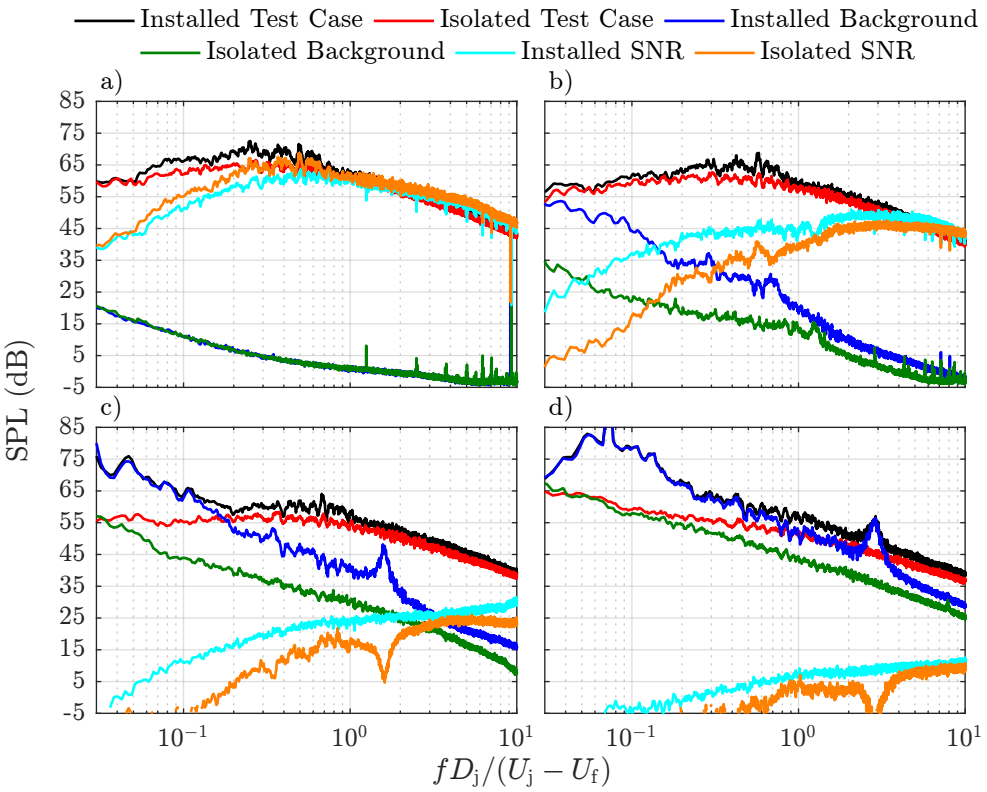

FIGURE 3.11: Examples of measured far-field spectra - test cases are the measured jet noise uncorrected for background levels. $c/D = 7.5$, $l/D = 3$, $h/D = 1$ and $M_j = 0.75$. a) $M_f = 0.0$; b) $M_f = 0.1$; c) $M_f = 0.2$; and, d) $M_f = 0.3$.

For both the near-field and far-field cases using a separation of 1 dB leads to a large amount of uncertainty/large confidence limits at low frequencies. This will decrease with increasing frequency as SNR increases, as displayed in Figure 3.11 and Figure 3.12. Using a value greater than 1 dB would have helped improve the interpretation and confidence in the measured jet near-field and far-field spectra.

In Figure 3.11a JSI noise is still just apparent above the isolated jet noise below the laboratory's anechoic limit of $\approx$ 400 Hz ($fD_j/U_j \approx 0.06$). In Chapter 5 a jet Mach number of $M_j = 0.3$ will be used extensively, due to the increased separation between JSI and JM noise, with a greater amount of JSI noise apparent below the anechoic limit ($fD_j/U_j \approx 0.16$). Below the anechoic limit of the laboratory the sound field will depart from the free-space spherical spreading rule. Hence, the amplitudes of the spectra below the anechoic limit can no longer be directly compared to the model, which assumes free-field conditions, or to frequencies above the anechoic limit. However, by first comparing trends with frequency between the installed and isolated spectra, trends with changing plate dimensions/flight velocity/etc in this frequency range can be deduced.

In Figure 3.12a the hydrodynamic field of the jet is also apparent above the background noise below the anechoic limit of the chamber. As these measurements aim to measure

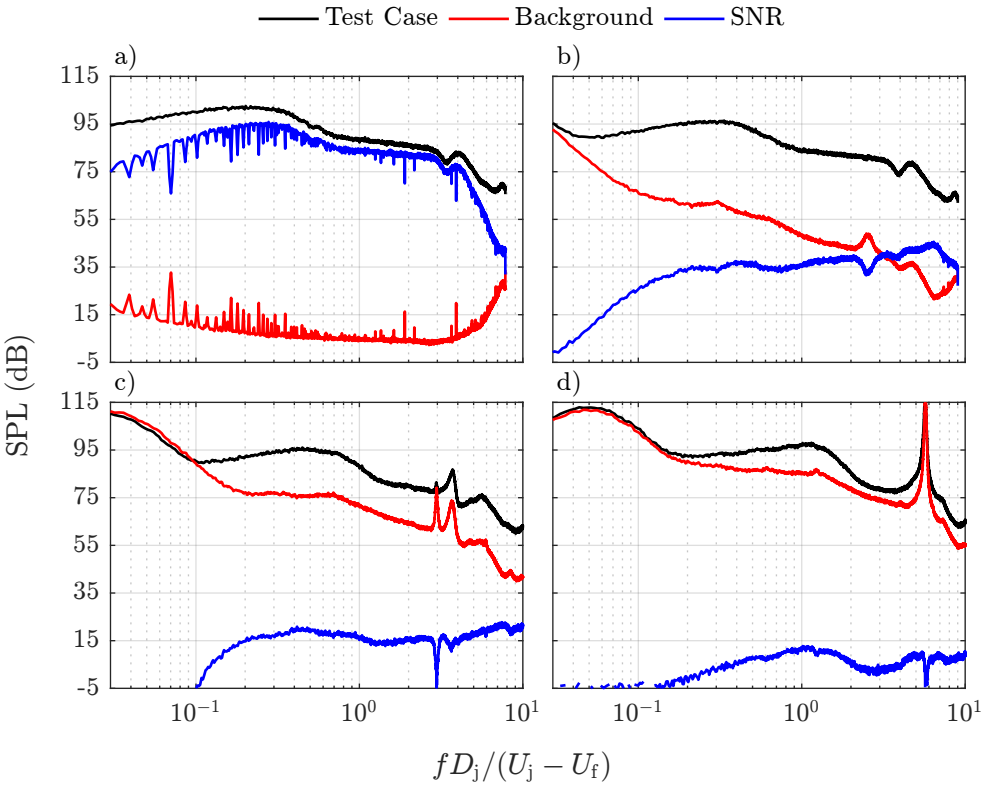

FIGURE 3.12: Examples of measured near-field spectra - test cases are the measured jet noise uncorrected for background levels.$x/D = 3$ and $M_j = 0.75$. a) $M_f = 0.0$ & $r/D = 1.72$; b) $M_f = 0.1$ & $r/D = 1.65$; c) $M_f = 0.2$ & $r/D = 1.36$; and, d) $M_f = 0.3$ & $r/D = 1.08$.

the amplitude of the hydrodynamic field of the jet, which decays exponentially with distance, and is positioned very close to the source, the anechoic limit is less of a constraint than in the far field.

Chapter 4

Scattered Source

Jet-surface interaction noise is created by the scattering of the non-propagating component of the pressure field surrounding a jet by the trailing edge of a surface positioned close to the jet. Therefore, to correctly predict the amplitude and spectral shape of far-field JSI noise it is important that the amplitude and spectrum of the non-propagating pressure field of the jet is known.

As has been discussed in Chapter 2, semi-empirical models have been created for the irrotational hydrodynamic field of a jet, by placing microphones in close proximity to static laboratory jets. These measurements have, mainly, shown peak PSD to scale as jet velocity to the third power, in line with theory. Additionally, while JSI noise measurements between different facilities have been used to determine that the amplitude of JSI noise scales with jet diameter squared, it appears that no direct comparison has been made of the hydrodynamic fields of jets of different diameters. Knowing how the hydrodynamic pressure, both the frequency and amplitude, scales with diameter is important to producing semi-empirical JSI noise models, with the hydrodynamic pressure as the input. Similarly, with current models limited to static jets, near-field pressure measurements are required of jets in flight. Extending the scaling laws/hydrodynamic pressure models to include the effect of flight will be important to understanding how flight effects JSI noise.

In this chapter, near-field isolated jet pressure measurements will be taken for a laboratory jet, including a flight stream to simulate the effect of flight on a jet. The measurements are then used to generate scaling laws for the hydrodynamic pressure spectra of a jet, including the effects of flight, nozzle diameter and jet velocity. The measurements will also be used as the input to trailing-edge scattering predictions in subsequent chapters.

4.1 Data Quality

Measurements of the near-field pressure of static jets have previously been taken using arrays of microphones perpendicular (i.e. at 0° incidence to) the jet axis. This microphone orientation is used to ensure maximum dynamic range/sensitivity of the microphone. However, to take measurements in flight a nose cone was attached to the microphone, which was then oriented parallel to the jet axis. To ensure that the addition of the nose cone and change in orientation did not adversely affect the accuracy of the location of the microphone and the pressure reading, a comparison was made with previous near-field measurements (Figure 4.1). The measurements used for comparison come are those taken by Lawrence using the ring array. There is, therefore, a slight difference in the nozzle diameter, 40 mm versus 38.1 mm, however it is small enough that any large errors due to the nose cone or microphone placement should be apparent. In Figure 4.1, there is a very good agreement in the sur-peak spectra, giving confident in the equivalence of the two measurement techniques. There is some disagreement with the sub-peak spectra, maybe due to differences in the upstream boundary conditions, which could perhaps be the subject of further research. The sudden decrease in the amplitude of the 40 mm nozzle below 20 Hz comes from the subtraction of the background noise, as this frequency is well below the anechoic limit of the chamber.

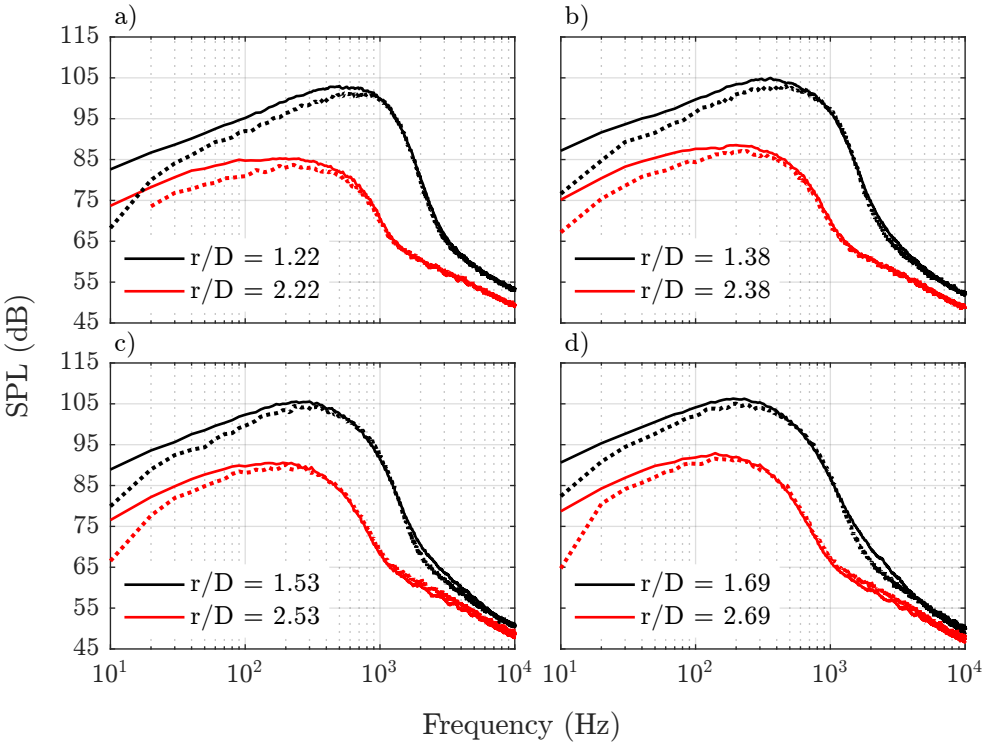

FIGURE 4.1: Comparison of measured near-field spectra between the 38.1 mm Doak jet nozzle (solid lines) and the 40 mm Doak nozzle (dotted lines). $M_j = 0.3$. a) x/D = 3; b) x/D = 4; c) x/D = 5; and, d) x/D = 6.

Figure 4.2 demonstrates the effect of the flight stream on the near-field pressure spectra. The microphone has been held at the same location and the jet velocity is also constant at an acoustic Mach number of $M_\mathrm{j} = 0.6$. At $M_\mathrm{f} = 0$, there is a single broadband hump with its peak at a frequency of ≈1.5 kHz, which is the hydrodynamic field of the jet. At frequencies above the peak, the amplitude decays rapidly until the acoustic field of the jet dominates the near field of the jet, at which point the rate of decay reduces significantly. When the flight stream is turned on, it makes several changes to the spectra. Firstly, a new broadband hump appears, with a peak initially at ≈ 40 Hz. This is the hydrodynamic field of the flight stream, which is essentially just a larger jet. This increases significantly in amplitude and peak frequency as the flight stream velocity increases. Secondly, the amplitude of the jet hydrodynamic pressure spectra reduces in amplitude with flight stream velocity. This is due to both the reduction in shear across the jet shear layer, and the accompanying stretching of the jet, which increases the distance from the edge of the shear layer to the microphone. This change in shear also causes a slight change increase in the peak frequency. Finally, at the high frequency end of the spectrum the acoustic pressure of the jet is also shown to reduce with the addition of the flight stream. However, the reduction is less than for the hydrodynamic pressure. This is in part because the evanescent hydrodynamic pressure is much more sensitive to the microphone distance from the jet shear layer.

The rapid increase in peak amplitude and frequency of the flight stream hydrodynamic field combined with the reduction in amplitude of the jet hydrodynamic field creates a problem for taking jet hydrodynamic pressure measurements in flight. This is because the hydrodynamic pressure spectra of the jet can be masked by that of the flight stream either if the microphone is too far from the jet or if the jet velocity is too low relative to the flight-stream velocity. Furthermore, if the microphone is too far from the jet or if the jet velocity too high, the acoustic field of the jet can also dominate. This is why the position of the microphone and the jet and flight stream velocities need to be carefully chosen. More specifically, as the flight velocity increases the microphone has to move closer to the jet axis. The velocity of the jet also needs to be increased, both to increase the amplitude of the jet hydrodynamic field and to increase the frequency separation between the two hydrodynamic fields of the jet and flight stream.

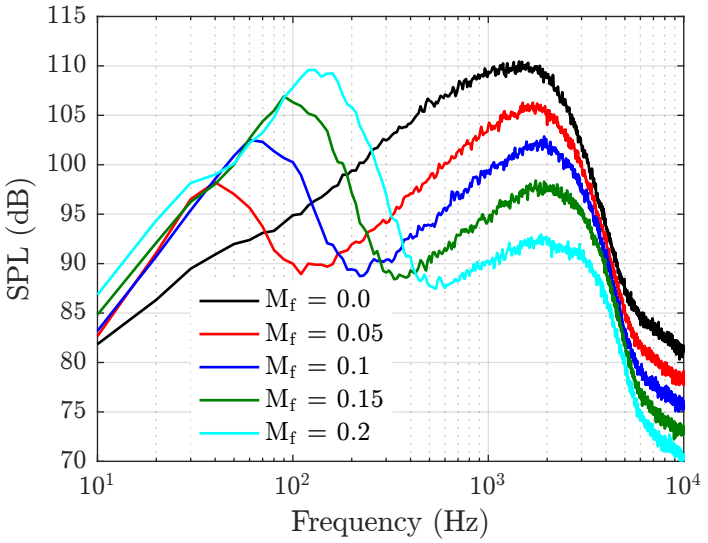

FIGURE 4.2: Comparison of near-field pressure spectra as flight velocity is increased, keeping jet velocity and microphone location constant. $M_j = 0.6$, $x/D = 3$ and $r/D = 1.22$.

At a flight Mach number of $M_f = 0.3$, two very large tones appear in the near-field pressure spectrum (Figure 4.3), at frequencies of 22.28 kHz and 44.59 kHz. Given that the frequency of the second tone is almost exactly double that of the first, it would appear that they both have a common origin. Using a shedding Strouhal number of 0.2, the length dimension of the first tone is 1 mm. This is much smaller than the diameter of the rods making up the support arm and the diameter of the cable, therefore they are unlikely to be the source. Further testing ruled out the possibility of any cavities in the supporting rods and clamps. Another possibility is that the flow over the nose cone, which consists of a series of small openings, with an aspect ratio of approximately three, into an approximately cylindrical cavity, is generating cavity noise. These tones are at frequencies above that of interest for the jet hydrodynamic field, however, the tonal frequency that may be produced was estimated quickly using Rossiter modes; in which the downstream travelling disturbance in the shear layer interacts with the edge of the cavity to produce an upstream travelling acoustic wave that interacts with the upstream edge to produce a disturbance in the shear layer. This gave a frequency of 23.8 kHz, not far from the measured 22.28 kHz of the fundamental tone, and remains a possible mechanism for its generation.

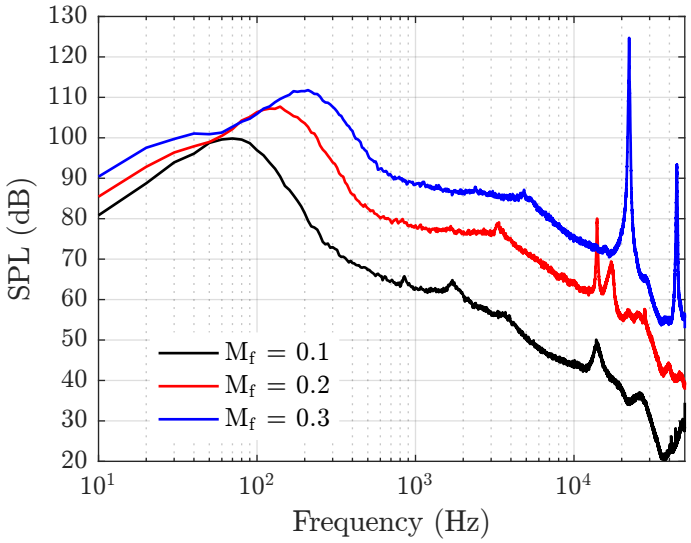

FIGURE 4.3: Flight-stream spectra captured with the inflow microphone inside the flight-stream potential core, very high amplitude tones appear when $M_f = 0.3$

A similar tone was also seen during the design and testing of the NLR-DNW Aerodynamic Microphone Forebody[97] (on which the G.R.A.S. RA0022 is based). Theoretical and experimental investigations of the tones did not conclusive determine the origin. However, evidence pointed to cavity shear layer oscillations across the openings in the nose cone. The tone was not detected with far-field microphones, suggesting that they are not due to acoustic cavity resonances.

4.2 Scaling with Velocity

Both experiments[18,65,66,82] and theoretical models[35,65] have suggested that jet hydrodynamic spectra scale according to either jet velocity to the 3rd or 4th power. Figure 4.4 demonstrates the hydrodynamic spectra collapsing with jet velocity to the 3rd power, matching the theory of Vera,[65] the surface pressure measurements of Lawrence[18] and the isolated near-field pressure measurements of Guitton.[82] This does not necessarily contradict the scaling with jet velocity to the fourth power, which is seen for OASPL, found by integrating over the frequency range dominated by the hydrodynamic pressure (see Figure 4.5), and has also been found when looking at the peak along the length of the jet.[66]

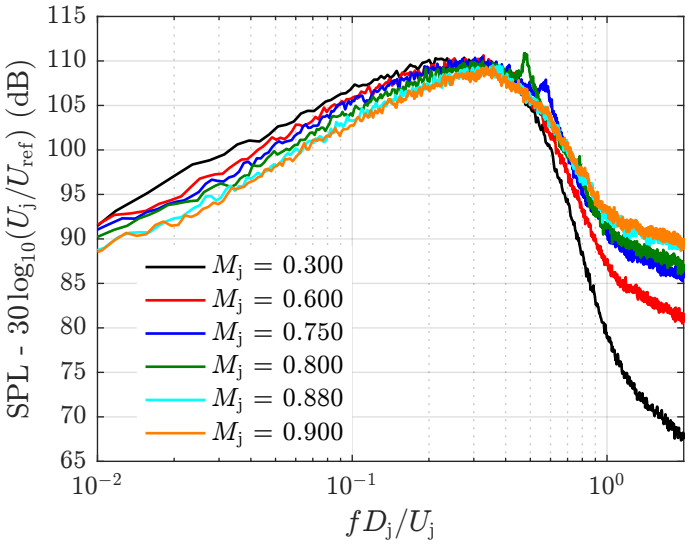

FIGURE 4.4: Comparison of near-field spectra at x/D = 3, r/D = 1.22 over a range of jet acoustic Mach numbers. $M_f = 0$.

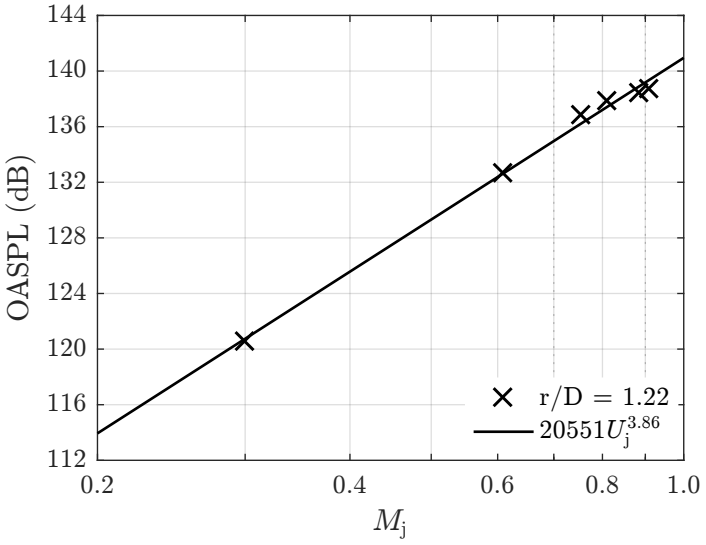

FIGURE 4.5: Scaling of the hydrodynamic pressure spectra at x/D = 3. A Strouhal number cut-off of 0.9 has been used for computing the OASPL. $M_f = 0$.

Figure 4.6 displays the collapse of the measured spectra from a single microphone on the array over a range of axial and radial locations, providing further evidence for the scaling of the hydrodynamic pressure field. Likewise, Figure 4.7 displays the relationship between jet velocity and the OASPL of the hydrodynamic pressure field over the range of axial locations measured. This clearly shows OASPL scaling with approximately U_j^4, as expected.

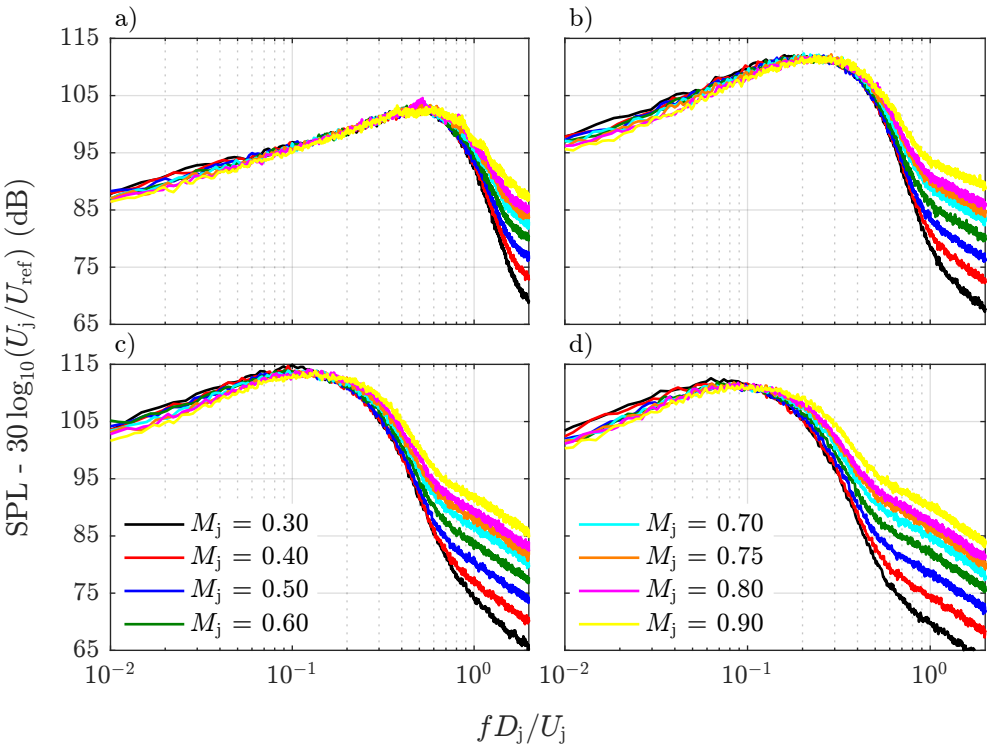

FIGURE 4.6: Scaling of the narrow band spectra of the hydrodynamic field measured in Lawrence's ring-array measurements. a) l/D = 1, r/D = 0.91; b) l/D = 3, r/D = 1.22; c) l/D = 5, r/D = 1.53; d) l/D = 7, r/D = 1.85.

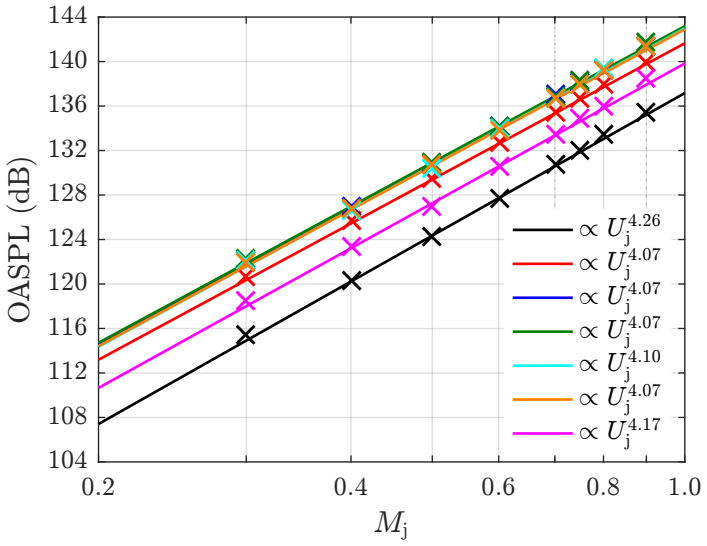

FIGURE 4.7: Scaling of the OASPL of the hydrodynamic pressure at a range of axial locations. Black: $l/D = 1$, $r/D = 0.91$, $St_{\text{cutoff}} = 1.5$; Black: $l/D = 1$, $r/D = 0.91$, $St_{\text{cutoff}} = 1.5$; Red: $l/D = 2$, $r/D = 1.06$, $\text{St}_{\text{cutoff}} = 1.0$; Blue: $l/D = 3$, $r/D = 1.22$, $\text{St}_{\text{cutoff}} = 0.9$; Green: $l/D = 4$, $r/D = 1.38$, $\text{St}_{\text{cutoff}} = 0.6$; Cyan: $l/D = 5$, $r/D = 1.53$, $\text{St}_{\text{cutoff}} = 0.5$; Orange: $l/D = 6$, $r/D = 1.69$, $\text{St}_{\text{cutoff}} = 0.4$; Fuchsia: $l/D = 7$, $r/D = 1.85$, $\text{St}_{\text{cutoff}} = 0.4$.

In Figure 4.4 and Figure 4.6 the acoustic component of the measured pressured comes to dominate the spectra at the upper end of the Strouhal number range. This is demonstrated by the sudden reduction in gradient of the spectra; however, the acoustic component likely still contributes to the spectra at lower Strouhal numbers. This would explain, at least in part, the divergence of the different velocity spectra for Strouhal numbers greater the peak value.

There is also a spread in the amplitudes of the different jet velocities at Strouhal numbers below the peak in Figure 4.6 and particularly for Figure 4.4. The reason for this difference has not been determined. Possibly it is affected by the condition of the boundary layer at the nozzle exit. The 40 mm nozzle from which Figure 4.4 is produced, has a relatively low convergence angle that leads to a thick boundary layer[98] relative to that of the 38.1 mm nozzle. Additionally, there appears to be increasing differences in the peak Strouhal numbers of the different jet velocities with increasing axial microphone location in Figure 4.6, which contributes to the spread in amplitude at low Strouhal numbers. The measurements were taken for a fixed microphone location, while Witze[110] derived a semi-empirical equation showing that potential core length increases with jet velocity; the resulting decrease in the axial position of the microphone relative of the potential core length, and, hence, decrease in shear layer thickness below the microphone, could explain the increase in peak Strouhal number. However, this is in contrast to the surface pressure measurements of Lawrence,[18] using the same jet, and the measurements of Guitton,[82] both of which show an excellent collapse of the measured spectra.

The effect of flight on a jet is to reduce the velocity difference across the shear layer and to stretch the jet, reducing the shear layer thickness at a given axial location. Miller[54] hypothesised that the peak frequency of the hydrodynamic field would scale relative to the shear layer thickness and jet velocity. The shear-layer thickness was in turn assumed to depend linearly on the potential-core length, and the potential core-length on $U_\mathrm{j} - U_\mathrm{f}$ to the power of an experimentally determined exponent. The pressure amplitude was also hypothesised to scale with the velocity difference $(U_\mathrm{j} - U_\mathrm{f})$, again, to an experimentally determined exponent. Such a velocity difference relationship is also found for far-field jet-mixing noise, at a polar observer angle of $\theta = 90°$ and a given flight velocity. Using surface pressure data on a wing positioned close to a laboratory jet, Miller found the scaling methods to work well, with carefully chosen empirical constants.

Miller tested the scaling methods against surface pressure measurements on a model 757 wing within an acoustic wind tunnel. Statically it is possible that the jet may wet the surface, and with the wind-tunnel operational the wing may produce lift, distorting the jet. The wing position was also not modified to account for the reduction in shear-layer width in flight. Finally, the shear-layer width/potential-core length was not known, requiring extra empirical constants to make up for this. Using the flight stream in the Doak laboratory it is possible to measure the near-field pressure of the isolated jet simulating the effect of flight. Additionally, hot wire measurements of Proenca[98] mean

that the near-field measurements can be made keeping the axial microphone location constant relative to the potential-core length.

Figure 4.8 to Figure 4.10 display comparisons of the measured near-field spectra at three different radial locations. In each, the axial microphone location relative to the potential-core length, and the velocity difference, has been kept constant. The spectra appear to collapse very well, when using a Strouhal number based on jet velocity, as predicted by Miller. There appears to be a discrepancy between the sub-peak spectra for the static and in-flight cases. Further work is required to determine if this is an effect of the interaction between the nozzle and flight stream boundary layers.

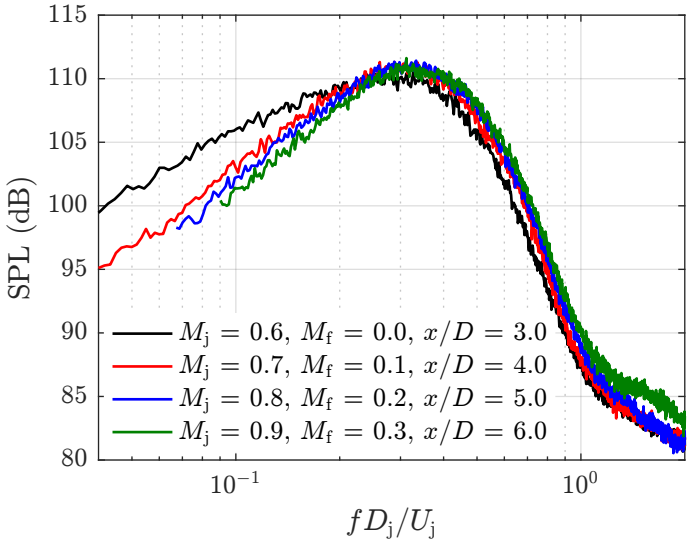

FIGURE 4.8: Comparison of near-field spectra at r/D = 1.22. $M_j - M_f = 0.6$ and $x/x_p = 0.65$.

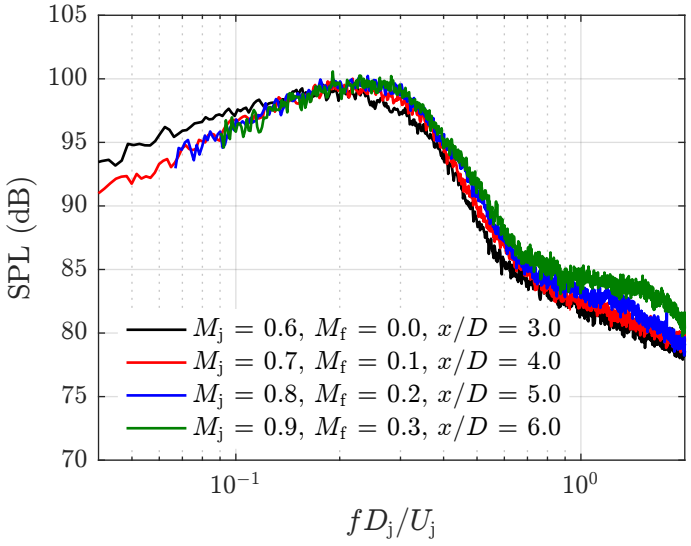

FIGURE 4.9: Comparison of near-field spectra at r/D = 1.72. $M_j - M_f = 0.6$ and $x/x_p = 0.65$.

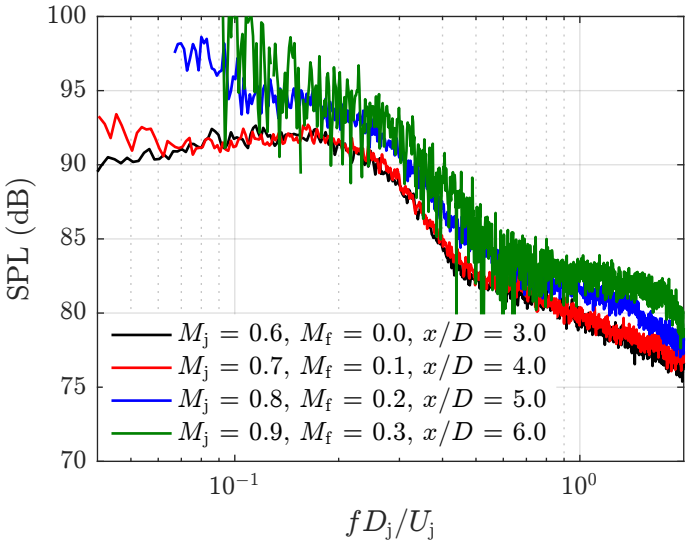

FIGURE 4.10: Comparison of near-field spectra at r/D = 2.22. $M_j - M_f = 0.6$ and $x/x_p = 0.65$.

For the static jet, the amplitude of the hydrodynamic pressure spectra at different jet velocities is collapsed using jet Strouhal number and jet velocity to the third power (Figure 4.4). In flight, one would expect the amplitude to scale as $(U_j - U_f)^3$. This is demonstrated in Figure 4.11 for a range of flight velocities and microphone locations. Unfortunately, the range of jet velocities is limited to $M_j = 0.75,\ 0.8$ & 0.9, however the excellent collapse of the spectra gives strong evidence for this method of amplitude scaling.

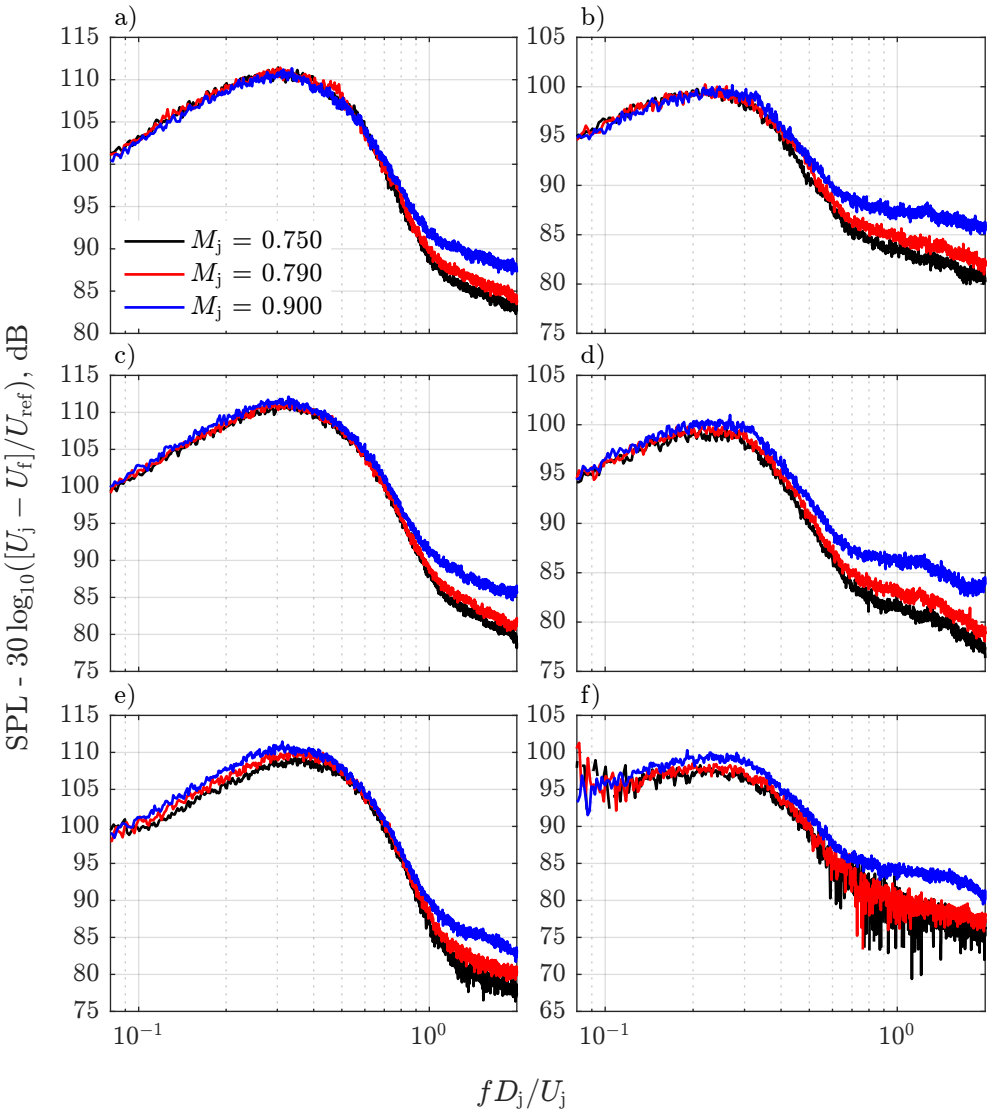

FIGURE 4.11: Scaling of near-field spectra in-flight. a) x/D = 4, r/D = 1.22, M_f = 0.1; b) x/D = 4, r/D = 1.72, M_f = 0.1; c) x/D = 5, r/D = 1.22, M_f = 0.2; d) x/D = 5, r/D = 1.72, M_f = 0.2; e) x/D = 6, r/D = 1.22, M_f = 0.3; f) x/D = 6, r/D = 1.72, M_f = 0.3;

4.3 Scaling with Jet Diameter

Comparisons of far-field JSI noise measurements, taken with jet nozzles with different diameters, have suggested that the frequency scales as $1/D_j$ and amplitude with D_j^2, as with jet-mixing noise. To determine whether these scaling methods also apply to the jet hydrodynamic pressure spectra, near-field pressure measurements were also taken of the flight stream, which is essentially just a bigger jet. A comparison of the jet and flight stream spectra in presented in Figure 4.12. The spectra have been scaled for jet velocity, further demonstrating the scaling of the hydrodynamic pressure spectra of static jets;

although only a small range of jet velocities are used, which is down to the operating range of the flight stream. Unsurprisingly, the flight stream is significantly louder than the jet, being 7.5 times greater in diameter. Attempting to scale the amplitude and frequency to account for the difference in diameter, it appears that the amplitude scales with the diameter and the frequency with Strouhal number (see Figure 4.13).

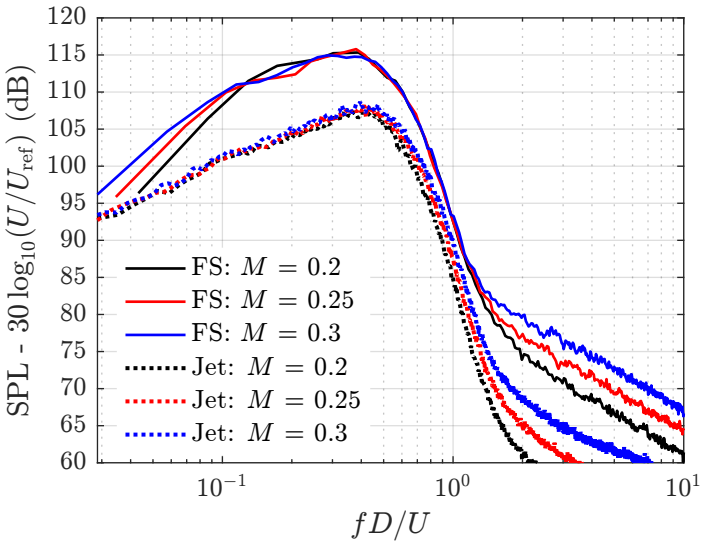

FIGURE 4.12: Comparison of near-field spectral measurements taken relative to the jet and flight-stream. $x/D = 2$ and $r/D = 1.06$

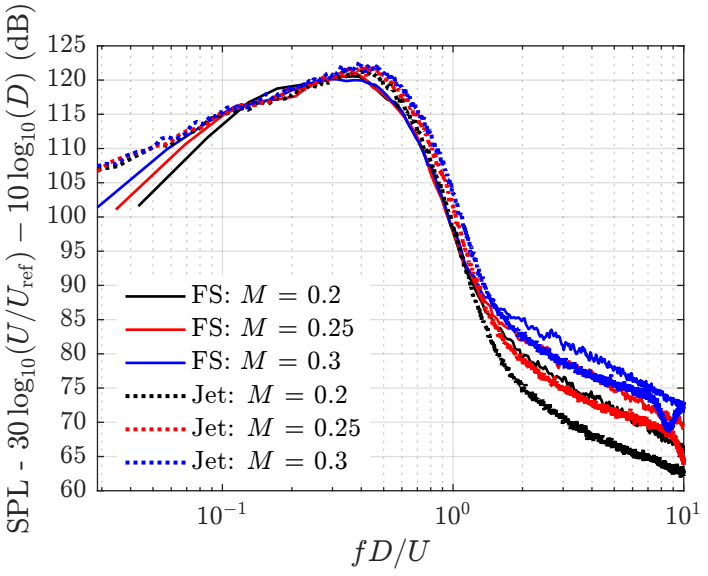

FIGURE 4.13: Near-field spectral measurements of the flight-stream and jet with amplitude scaled with diameter. $x/D = 2$ and $r/D = 1.06$

4.4 Axial Wavenumber

When calculating JSI noise it is important to know the axial wavenumber, as well as the spectrum, of the hydrodynamic pressure field. This is because the radial decay of the hydrodynamic pressure field and the polar directivity of JSI noise are related to the axial wavenumber.

Lyu[68,111] used LES data of an isolated jet to complete an $k-\omega$ decomposition of the near-field pressure. Using this decomposition, Lyu demonstrates that the convection velocity is frequency dependent, showing that at low frequencies the convection velocity is significantly below the $0.6U_\mathrm{j}$ which is often assumed for fluctuations in the shear layer.

Figure 4.14 and Figure 4.15 show $k-\omega$ decompositions of the near-field pressure in two LES. The two LES come from the University of Cambridge, the first as part of the HARMONY (wHole AiRcraft Multidisciplinary nOise desigN sYstem) project,[112] the second is of the Doak Laboratory's 38.1 mm jet[106,107] (see Appendix B for further information). The decompositions have been created by Fourier transforming the pressure time series around each ring of the FWH surfaces positioned within the near-fields of the jets. The CPSD is then calculated between each ring for each mode. Finally, a Fourier transform is performed along axial locations, giving PSD as a function of frequency, mode, axial wavenumber and axial position. Also shown in Figure 4.14 and Figure 4.15 are lines (in black) denoting waves travelling along the cones at the speed of sound, $k_1 = 2\pi f/a_0$, and waves travelling at $0.6U_\mathrm{j}$ (in red).

The decomposition in Figure 4.14 uses 41 probes spaced $0.25D$ apart, to give a resolution of $k_1 D_\mathrm{j}/2\pi = 0.1$. The CPSD between rings has been computed using seven averages with 50% overlap with a Strouhal number resolution of 0.085. Figure 4.15 has been calculated using 106 rings of probes spaced $0.2D$ apart to give a resolution of $k_1 D_\mathrm{j}/2\pi = 0.048$. In the frequency domain thirteen averages have been used with a Strouhal number resolution of 0.037.

These $k-\omega$ decompositions only approximate the axial decomposition, because the FWH surfaces are in fact conical rather than cylindrical. However, there is a clear distinction between the acoustic, as outlined by the black lines, and hydrodynamic components. As has been shown from modal decompositions of near-field spectra, Figure 4.14 and Figure 4.15 show that modes 0 and 1 dominate the hydrodynamic spectra and that the acoustic component increasingly dominates the near-field spectra of the higher order modes.

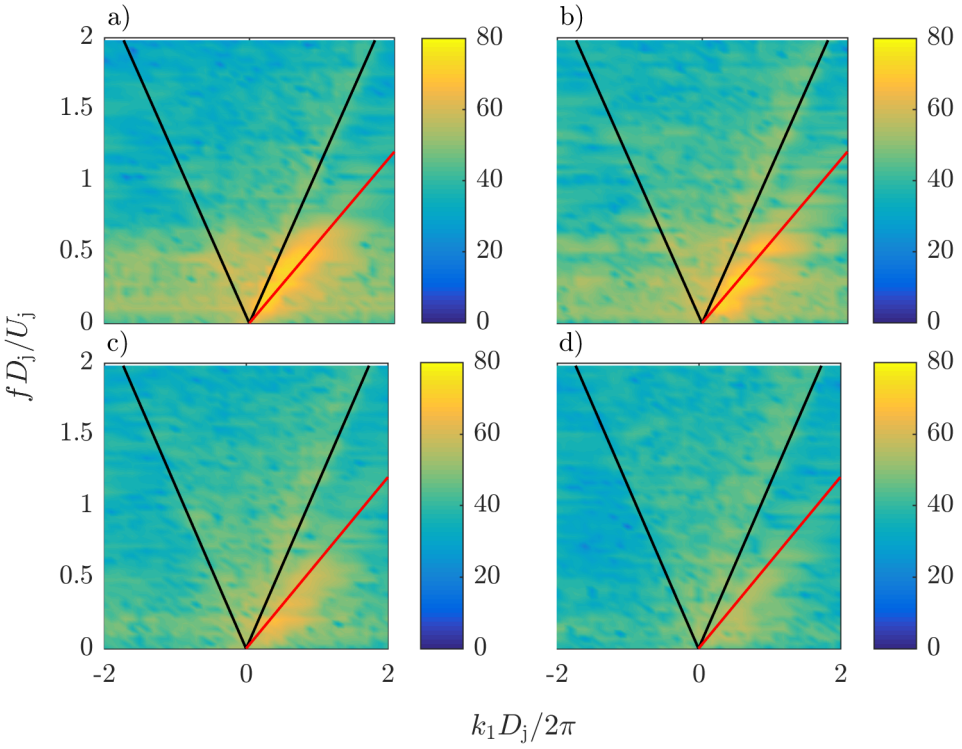

FIGURE 4.14: k-ω decomposition of a jet near-field pressure using HARMONY jet LES[112] data. a) mode 0; b) mode 1; c) mode 2; d) mode 3. $M_j = 0.875$, $x/D = 3$ & $r/D = 1.28$

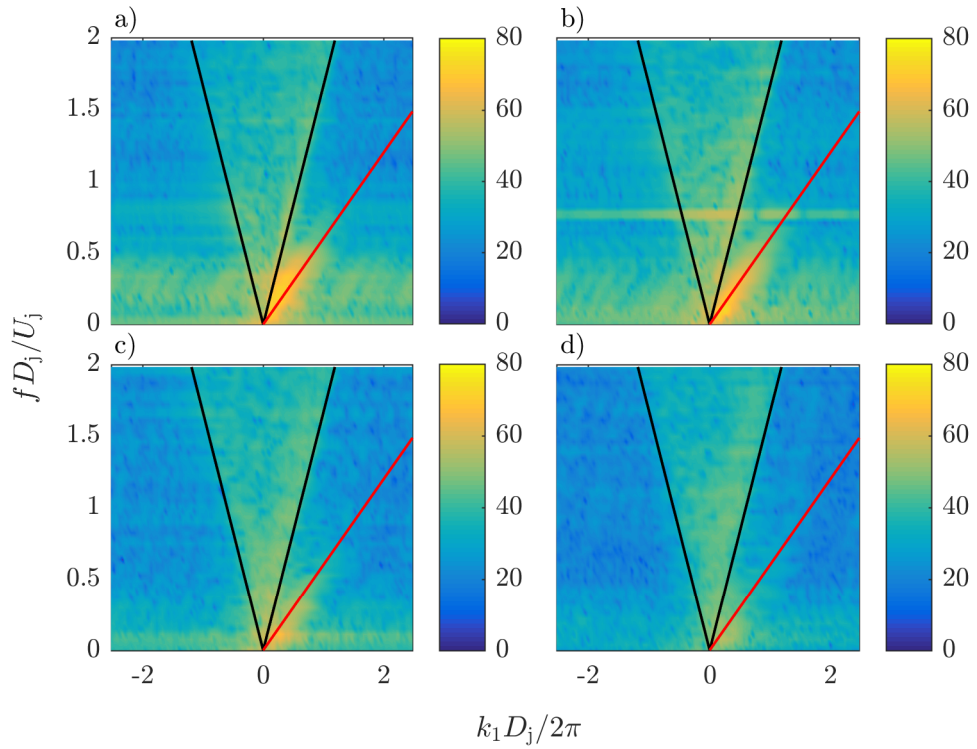

FIGURE 4.15: k-ω decomposition of a jet near-field pressure using Doak jet LES[106, 107] data. a) mode 0; b) mode 1; c) mode 2; d) mode 3. $M_j = 0.6$, $x/D = 3$ & $r/D = 1.75$

In order to create modal and $k - \omega$ decompositions, a significant number of microphones are required to get good k_1 resolution in the low frequency region where the hydrodynamic pressure field is present (Figure 4.14 and Figure 4.15 use ≈1300 & 13000 probes respectively). Therefore, during an experiment it may not be possible to take synchronous measurements over a sufficient number of microphones to find the axial wavenumber using $k - \omega$ decomposition. Therefore, Lyu has developed a method to calculate the axial wavenumber that uses a single ring of microphones if modal decomposition is required, or a single microphone otherwise.

Using the assumption that the propagation of the hydrodynamic pressure can be described by cylindrical harmonics, Lyu suggests calculating the axial wavenumber at a given axial location by taking near-field measurements at several radial locations (the measurements are not required to be taken synchronously). Then, a value for ι_r is found as a function of frequency such that the spectra across the different radial location can be collapsed using a modified Bessel function of the second kind, $\mathrm{K}_m^2(r\iota_r)$. From ι_r it is then possible to find a value for the axial wavenumber, k_1.

The LES data used to produce Figure 4.15 uses the same nozzle used in the near-field measurements of Lawrence, and uses a jet Mach number also used in the experimental campaign. This means a comparison can be made between the calculation method of Lyu and the $k - \omega$ decomposition. In Figure 4.16, the peak axial wavenumber, k_1, is

plotted as a function of frequency. This allows a comparison with the axial wavenumber calculated with Lyu's method, which will only return a single value. At modes 0 and 1 the peak axial wavenumber increases approximately linearly until St = 0.5, beyond which the maximum PSD corresponds to the acoustic component. In the region corresponding to the hydrodynamic pressure, the axial wavenumber calculated with Lyu's method compares very well up to St ≈ 0.9 & 0.25 (modes 0 and 1 respectively). Above these Strouhal numbers the near-field spectra at the upper radial measurement location is increasingly dominated by the acoustic rather than hydrodynamic field (Figure 4.17). Therefore, the calculated wavenumber converges on the wavenumber associated with the maximum PSD of the acoustic component. At this point, however, the calculation method of Lyu & Dowling fails, because acoustic propagation is not described by $\mathrm{K}_m^2(r\iota_r)$.

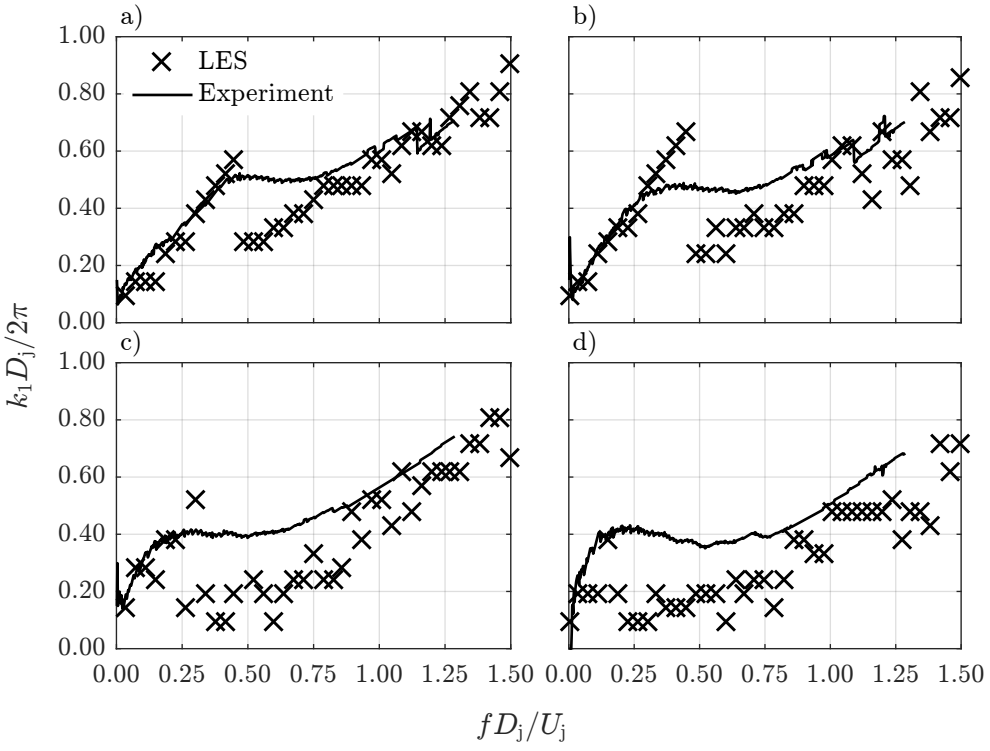

FIGURE 4.16: Comparison of the axial wavenumber calculated using the method of Lyu with the axial wavenumber corresponding to the peak of the k-ω spectra from the LES and Doak jets (X). a) mode 0; b) mode 1; c) mode 2; and, d) mode 3. $x/D_\mathrm{j} = 3$

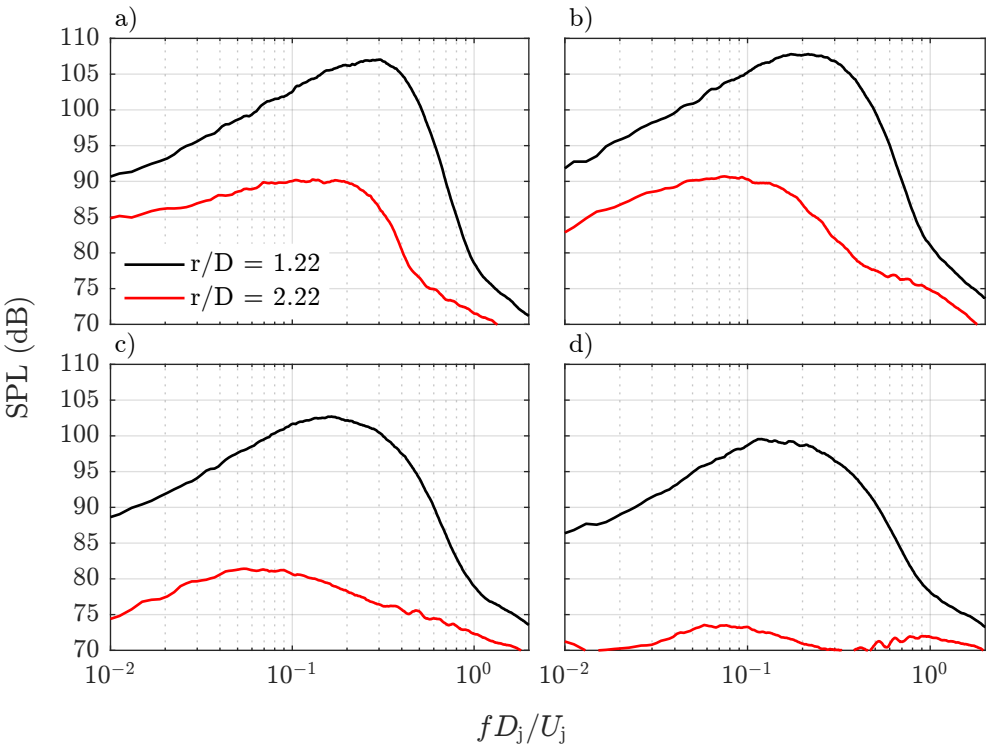

FIGURE 4.17: Modal decomposition of the near-field pressure measurements of Lawrence. a) mode 0; b) mode 1; c) mode 2; and, d) mode 3. $x/D_j = 3$, $M_j = 0.6$.

At modes 2 and 3 a comparison between the wavenumbers found from the method of Lyu & Dowling and the $k - \omega$ decomposition (Figure 4.16) is more difficult, because the amplitude of the acoustic component dominates the hydrodynamic component in the LES data for most frequencies. The comparison can be improved both by using the HARMONY LES data (Figure 4.14), as the FWH surface is half a jet diameter closer to the jet, and finding the maximum over the range of PSD values for which $k_1 > 1.1k$, thus excluding the acoustic component (see Figure 4.18). Now the hydrodynamic wave number is apparent over a larger range of Strouhal numbers and at mode 2. At some Strouhal numbers the amplitude of the hydrodynamic component drops below the noise in the decomposition, at which point the maximum $k_1 = 1.1k$. It is apparent from Figure 4.18 that the non-dimensional values plotted in Figure 4.18 collapse the results from the two different jets. This is in agreement with the measurements of Bychkov & Faranosov,[48] which show the convection velocity to scale with Strouhal number. This could therefore be incorporated into a semi-empirical JSI noise prediction model. It is now even more apparent that the axial wavenumbers of the hydrodynamic field increase linearly, and are very similar for the 4 different modes plotted. This knowledge could be used to extrapolate the initial values calculated using Lyu & Dowling's method linearly into the frequency range where the lower measurement location is still dominated by the hydrodynamic pressure field of the jet.

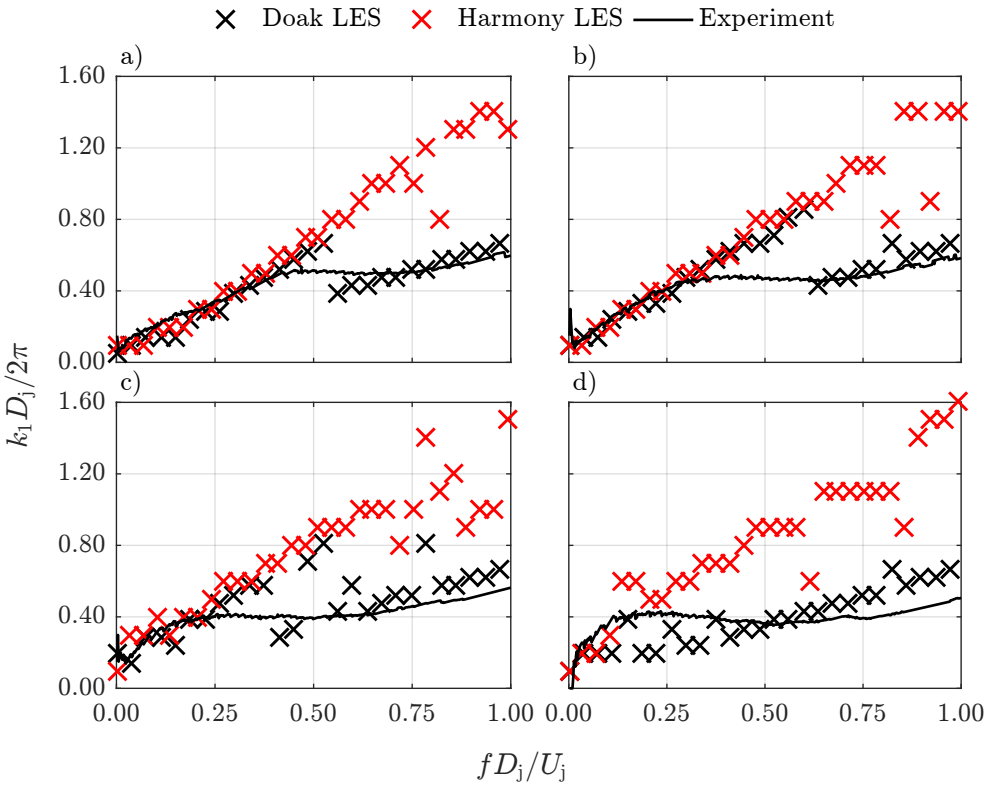

FIGURE 4.18: Comparison of the axial wavenumber calculated using the method of Lyu with the axial wavenumber corresponding to the peak of the k-ω spectra from the LES HARMONY and Doak jets. a) mode 0; b) mode 1; c) mode 2; d) mode 3. $x/D = 3$

The effect of axial location on the axial wavenumber is explored in Figure 4.19. Over the axial locations plotted the peak axial wavenumber does not appear to vary significantly. Why this is the case is not immediately obvious. Upstream of the potential core, the convection velocity may be fairly constant; however, beyond the end of the potential core the jet velocity decays, and the convection velocity would then also be expected to decrease. One possible problem may be that the resolution of the $k - \omega$ decomposition is not sufficient in either frequency or wavenumber to show the variation in convection velocity.

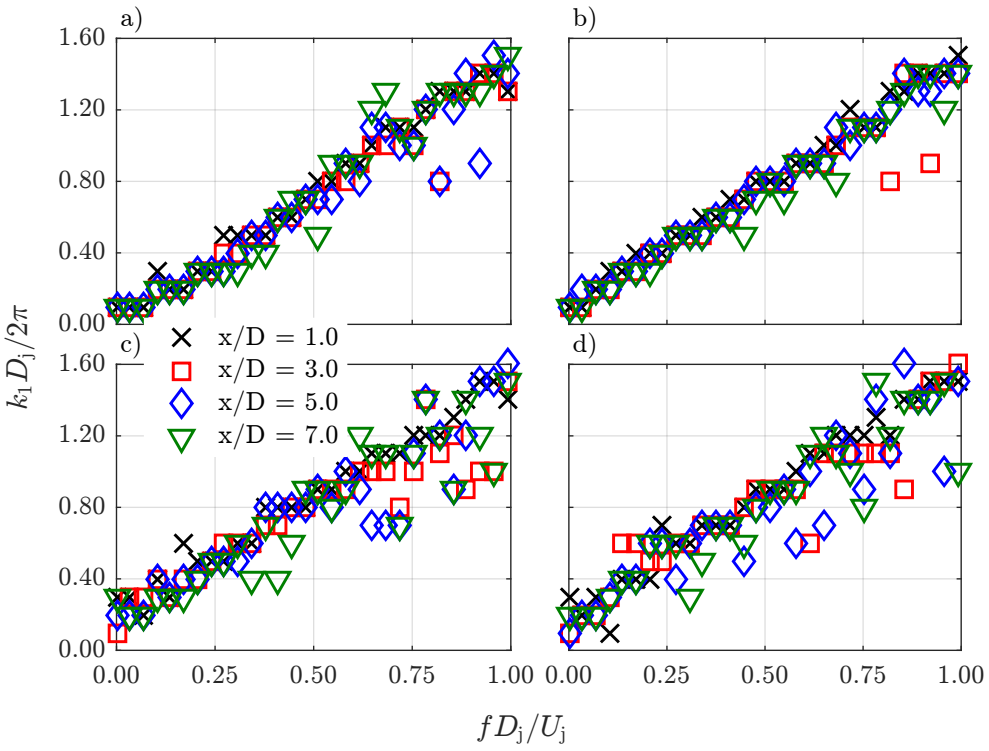

FIGURE 4.19: Axial wavenumber associated with the maximum PSD of the $k-\omega$ decomposition of the HARMONY LES FWH surface. a) mode 0; b) mode 1; c) mode 2; and, d) mode 3.

The measurements of the near-field pressure of the 40 mm Doak jet can be used to assess the effect of flight on the axial wavenumber of the hydrodynamic pressure. Figure 4.20 and Figure 4.21 compare the axial wavenumbers calculated using the method of Lyu & Dowling from the near-field pressure measurements at $x/x_{\mathrm{p}} = 0.65$ and $r/D = 1.22$ & 1.72. Because of the need to keep the jet hydrodynamic pressure spectra above the noise of the flight stream, only a few jet velocities are used. Additionally, as only one microphone was used, it is not possible to decompose the pressure spectra into azimuthal modes.

Figure 4.20 demonstrates that the axial wavenumber remains a function of the jet Strouhal number even in flight. This is somewhat surprising, as one may expect that the convection velocity of the jet hydrodynamic pressure would be modified by the presence of the flight stream. There are some differences between the axial wavenumbers at different flight velocities. There appears to be an increase in the gradient of axial wavenumber with respect to Strouhal number as flight stream velocity increases. This made more clear in Figure 4.21, which compares axial wavenumbers at different flight-stream velocities for a given jet velocity. Over the limited Strouhal number range, this would appear to be due to a reduction in axial wavenumber at Strouhal numbers below 0.25. The gradient of the $M_{\mathrm{f}} = 0$ curve is actually lower than that found for the LES

and 38.1 mm Doak nozzle, which is closer to $M_\mathrm{f} = 0.1$ and $M_\mathrm{f} = 0.2$. Before it is possible make any conclusions about changes to axial wavenumber with flight, it will be necessary to take measurements in a manner which allows azimuthal modal decomposition. It would also be beneficial to have measurements for different nozzles, or even LES, as before, if possible.

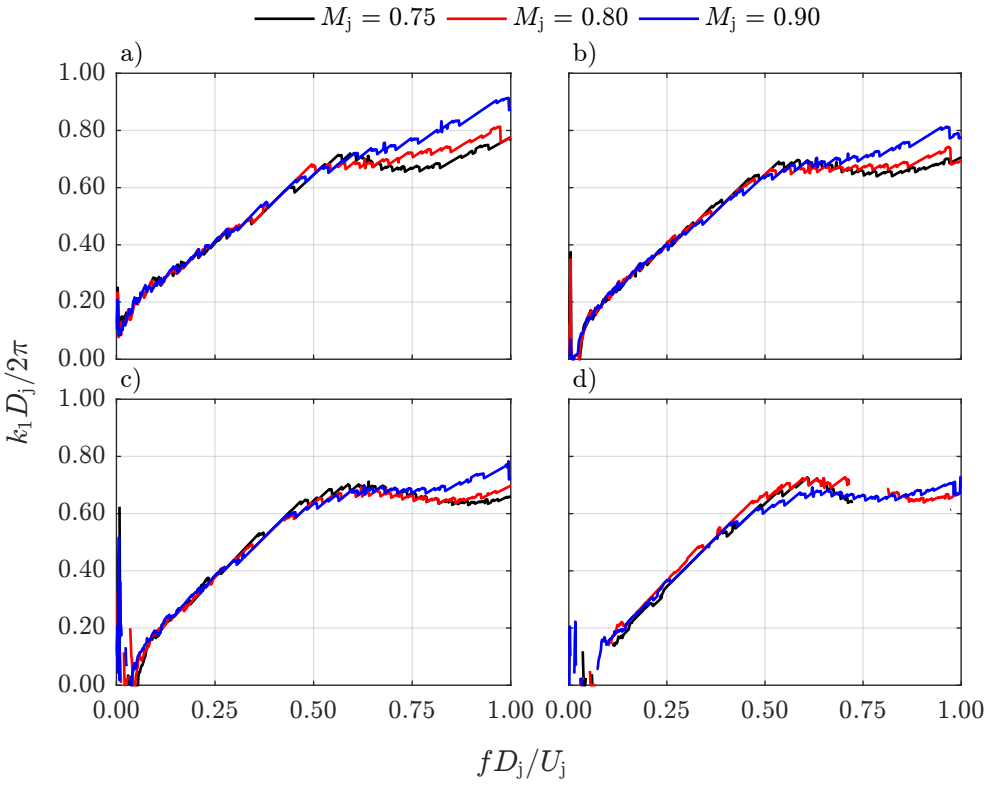

FIGURE 4.20: Axial wavenumber calculated using Lyu's method at different jet and flight velocities. $x/x_\mathrm{p} = 0.65$. a) $M_\mathrm{f} = 0$; b) $M_\mathrm{f} = 0.1$; c)$M_\mathrm{f} = 0.2$; and, d)$M_\mathrm{f} = 0.3$.

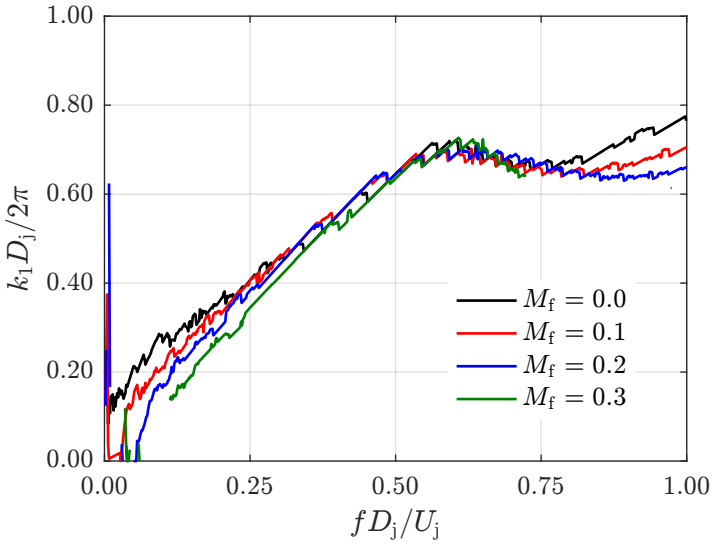

FIGURE 4.21: $M_\mathrm{j} = 0.75$ and $x/x_\mathrm{p} = 0.65$.

4.5 Bulleted Nozzles

In order for jet noise to be studied in isolation in a repeatable manner and in laboratories, laboratory jets are fed from a compressor far upstream of the nozzle, and separated by settling chambers and baffles. This, combined with the need to study the fundamentals of jets, leads for the most part to simple axisymmetric jet nozzles, such as used so far. On gas turbine engines there is a centre portion reserved for all the turbo-machinery required to power the engine, with the 'gas' travelling in annular ducts around the core. Therefore, to prevent separation and the resulting loss of thrust, there is a 'bullet' at the end of the core that draws the inner diameter of the air stream back to the centreline. In low bypass gas turbine engines, such as on business jets, where the primary jet produces a significant level of noise, this bullet is generally hidden in a combined nozzle, externally appearing as a circular nozzle. On high bypass ratio gas turbine engines, the primary jet produces little noise, so there is less need to mix the primary and secondary flows. The large diameter of these engines also means that extending the nacelle to create a combined nozzle would lead to a large increase in weight and drag. Therefore, the bullet is external to both primary and secondary nozzles. This causes the properties of the jet to change between the nozzle exit and the end of the bullet, affecting the noise produced.

The most obvious effect of the bullet is to reduce the outer radius of the jet, due to conservation of mass. Then, assuming the jet is fully expanded at the nozzle exit, an effective jet diameter can be defined past the end of the bullet

$$D_{\mathrm{e}} = \sqrt{\frac{4(A_{\mathrm{s}} + A_{\mathrm{p}})}{\pi}}, \tag{4.1}$$

where A_{p} and A_{s} are the primary and secondary nozzle exit areas respectively. Figure 4.22 shows the TKE predicted from a RANS calculation of a bulleted jet. If the radial position of the line of maximum TKE is used as an indication of the diameter of the jet close to the nozzle, then at the end of the bullet the effective jet diameter is $\approx 0.4D_{\mathrm{s}}$, very close to that predicted from Equation 4.1. The effect this effective diameter has on far-field jet-mixing noise is demonstrated in Figure 4.23, where the use of the effective diameter calculated with Equation 4.1 correctly collapses the spectra with the circular jets.

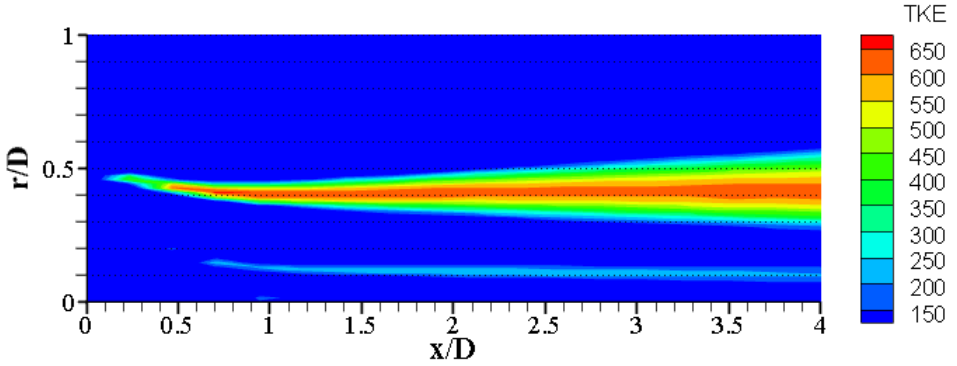

FIGURE 4.22: RANS solution for the turbulent kinetic energy of a dual-stream bulleted nozzle with matched jet velocities. $A_s + A_p = 0.5D_s^2$

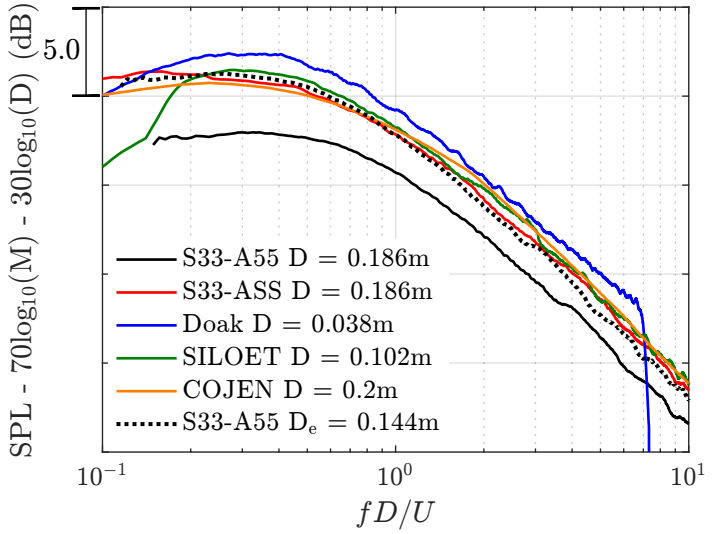

FIGURE 4.23: Collapse of far-field noise data ($\theta = 90°$) for jets of various diameters, showing the effect of the bullet on far-field jet-mixing noise

What is less clear is how the bullet effects the hydrodynamic field of the jet. If a near-field microphone is positioned beyond the bullet, it seems logical to scale the radial location by the effective diameter. However, an axial position scaling is less clear cut, as the shear layer is unlikely to develop in a similar manner along the bullet as for a circular jet. Also, disturbances originating at the trailing edge that are coherent over large axial distances will be subject to the reduction in diameter, and hence circumference of the jet. This could possibly change the amplitudes and frequencies with respect to a circular jet with the same effective diameter.

Ko et al. have studied the effect of the diameter of the bullet on near-field pressure of an annular jet[113] with outer diameter kept constant. There results show that at a given microphone location the diameter of the bullet had no effect on the measured spectral shape and peak frequency. However, increased bullet diameter was associated with spectra of lower amplitudes, possibly due to the decreased mass flow rate, or distance

from shear layer to microphone. These results may not be entirely representative of bulleted annular jets though, as the bullets aren't aligned with the jet streamlines, leading to separation from the bullet.[114] This may cause the jet near-field to develop in a manner closer to that of a plain jet.

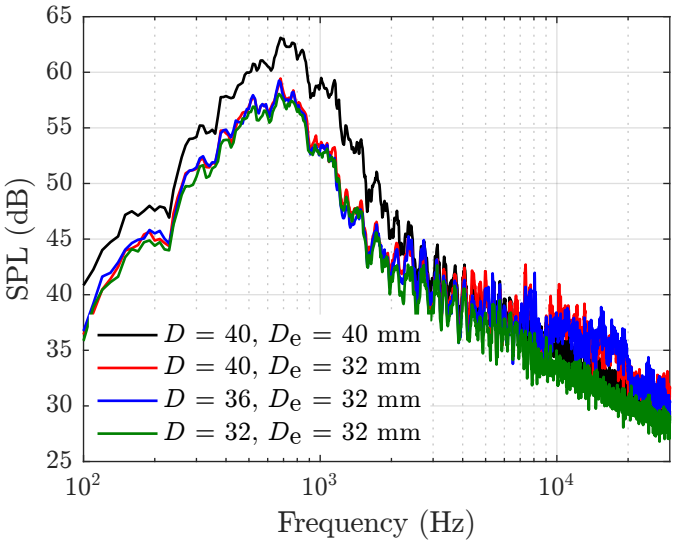

FIGURE 4.24: Comparison of the JSI noise produced by nozzles with and without bullets. $\theta = 90°$, $\phi = 0°$, l = 120 mm & h = 40 mm

Figure 4.24 gives a comparison of the JSI noise produced by two nozzles with ($D \neq D_e$) and two nozzles without ($D = D_e$) bullets. The trailing edge of the plate was positioned 120 mm downstream of the nozzle and 40 mm radially from the jet axis. It is readily apparent that the JSI noise produced is identical for the nozzles with matching effective diameters. This lends weight to the argument for using the effective diameter to calculate the amplitude of the hydrodynamic field. On the other hand, the spectral shape between the different nozzles is very similar, despite the different h/D and l/D locations of the plate, maybe suggesting that the absolute distance from nozzle to plate is a better indication of spectral shape. Or, possibly, this is just due to the difference between $l/D = 3$ and $l/D = 3.75$ being quite small.

4.6 Summary

The aim of this chapter was to demonstrate and develop scaling laws for the hydrodynamic pressure spectra of a jet. These scaling laws can then be used, along with measurements of jet hydrodynamic pressure spectra, to produce the input to a jet-surface interaction noise calculation.

Near-field unsteady-pressure measurements have been taken of the Doak laboratory jet with and without the presence of a coaxial 'flight stream' to simulate the effect of flight

on the jet. The measurements were taken with a single nose-cone-equipped microphone aligned with the jet axis and placed using a three-axis traverse, allowing the microphone to be placed quickly and accurately at many locations. Additionally, measurements were taken of the near-field of the flight stream, which is essentially just a larger jet.

The measured near-field spectra provide further evidence that the amplitude of the hydrodynamic pressure spectra scale with jet velocity to the third power. Comparing the measurements taken relative to the jet and flight stream suggests that the amplitude also scales with nozzle diameter. Further, comparison of installed jet noise measurements taken with nozzles of different diameter and flow area would suggest it is a diameter based on flow area against which the near-field pressure spectra scales (at least downstream of any bullet). The in-flight measurements would suggest that these scaling laws remain true in flight if the axial location of the microphone is held constant relative to the potential-core length of the jet.

In addition to the spectrum of the hydrodynamic pressure, it is also important that the axial wavenumber of the hydrodynamic pressure field is known for the calculation of jet-surface interaction noise. k-ω decomposition has been used to get the wavenumber spectra on FWH surfaces placed within the near-field of jets in LESs. This has shown the peak axial wavenumber of the hydrodynamic field to increase approximately linearly with Strouhal number, and to remain constant with axial position. Comparison with the method proposed by Lyu & Dowling to calculate the axial wavenumber from experimental data, showed that the method of Lyu & Dowling returned the peak axial wavenumber of the k-ω decomposition. Measurements showed small changes between axial wavenumbers at low Strouhal numbers in flight. However, in-flight measurements with multiple microphones (so the near-field pressure can be decomposed into azimuthal modes) will be required before further conclusions can be drawn.

Chapter 5

Trailing Edge Scattering

Several jet-surface interaction noise models have been published, based on analytical edge-scattering theories.[65][73][67] These models have been validated against small-scale laboratory measurements of installed jet noise. In this chapter, the jet-surface interaction noise model of Lyu & Dowling[67–69,71,115] will be validated against laboratory measurements of installed jet noise, where a co-axial 'flight stream' has been used to simulate the effect of forward motion on the jet. Additionally, comparisons have been made with installed jet noise measurements using plates with chord lengths more representative of airliner wings. Finally, the use of Roger & Moreau's back-scattering theory[43,51] and strip theory are discussed for modelling more realistic planform geometries.

5.1 Data Quality

Figure 5.1 shows far-field installed spectra at 90° with the flight-stream and the jet matched to the flight-stream the velocity. There is a broad tone, the frequency of which is dependent on the flight-stream velocity, between 5 and 15 kHz. Using a shedding Strouhal number of 0.22 leads to a length dimension between approximately 1.8 and 2 mm. This suggests that the source of this noise is vortex shedding from the trailing edge of the plate, which is approximately 1.2 mm thick, if one also includes the thickness of the boundary layer formed on the plate by the flight-stream flow.

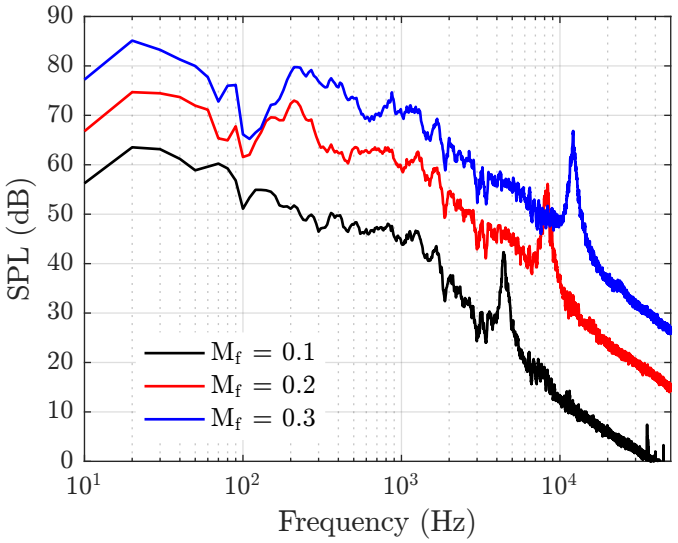

FIGURE 5.1: Far-field installed flight-stream background noise. Installed flat plate is located at $l/D = 3$ and $h/D = 1$, with $c/D = 7.5$

As several of the same plates and jet/flight acoustic Mach numbers were used in both the experiment campaigns, it is possible to compare the results of the two to ascertain the repeatability of measurements. A comparison of far-field installed spectra, using the $c/D = 7.5$ plate, between the two test campaigns is presented in Figure 5.2. The only noticeable differences are observed at high frequencies, well above the frequency range of the JSI noise. This difference is likely because microphone capsule frequency corrections were not available for the capsules used in the second campaign, and so have not been applied to these spectra. The measurements are, therefore, deemed to be suitably repeatable.

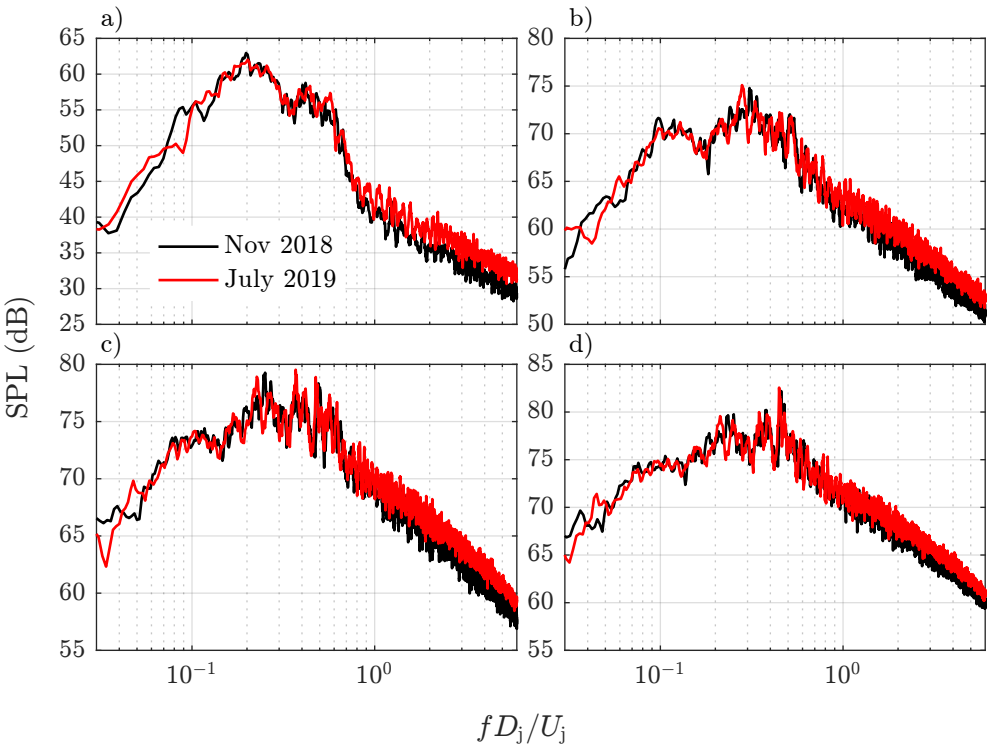

FIGURE 5.2: Comparison of installed far-field pressure measurements taken in the first and second measurement campaigns. $M_f = 0$, $\theta = 90°$ and $\phi = 0°$. a) $M_j = 0.3$; b) $M_j = 0.6$; c) $M_j = 0.75$; d) $M_j = 0.8$

After taking the installed measurements with the $c/D = 2.5$ plate during the first campaign, it was discovered that the plate was positioned closer to the jet than intended at $h/D = 0.9$ rather than $h/D = 1$. This was found to be due to a bow in the plate, which the tensioning bolts straightened out, reducing the distance to the jet. With the actual position of the plate now measured, only a few key jet and flight-stream velocities were repeated with the plate in the correct location. This difference is clearly noticeable in Figure 5.3. The repeats are much more comparable with the measurements in the second campaign, again considering the messy spectra and the lack of frequency response corrections. This again suggests a certain degree of repeatability, once one accounts for the bow in the plate.

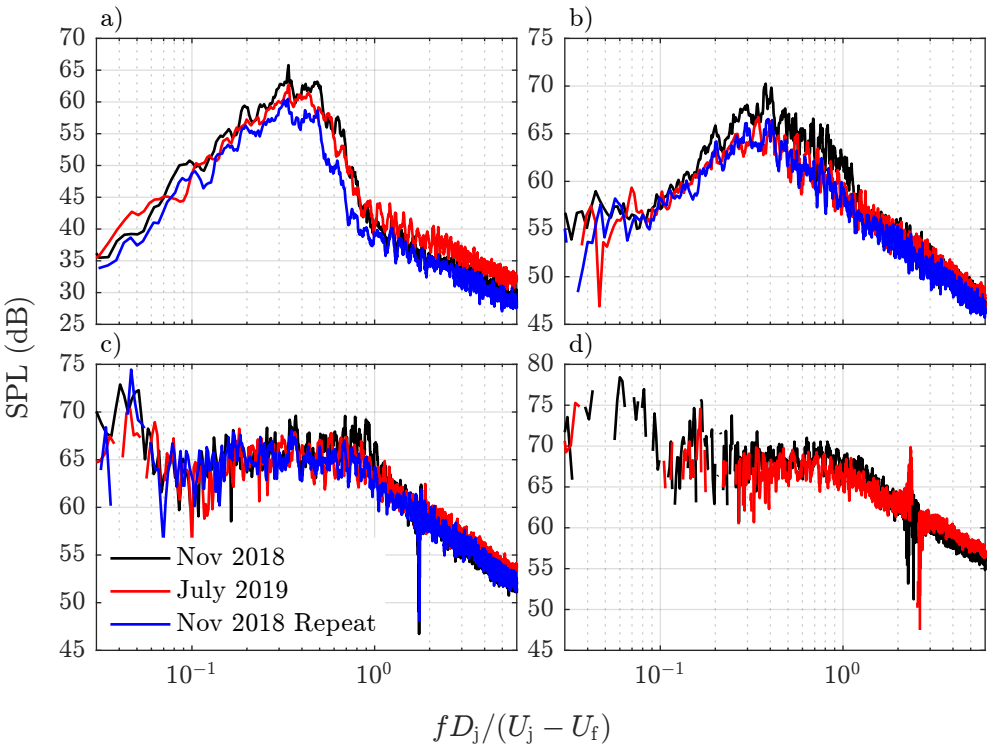

FIGURE 5.3: Comparison of installed far-field pressure measurements taken in the first and second measurement campaigns. $\theta = 90°$ and $\phi = 0°$. a) $M_j = 0.3$, $M_f = 0$; b) $M_j = 0.6$, $M_f = 0.1$; c) $M_j = 0.75$, $M_f = 0.2$; d) a)$M_j = 0.9$, $M_f = 0.3$

Figure 5.2 and Figure 5.3 suggest that the plates can be placed with some precision, but does not necessarily ensure that the plate is positioned with a high degree of accuracy. For instance, the plate has been positioned using a tape measure to measure the distance from the nozzle to the underside of the plate (side of the plate facing the jet). This means that the position of the plate can be measured to, at best, the nearest millimetre. In addition, the plates are approximately 1.2 mm thick and the nozzle thickness at the exit is 0.5 mm. This adds to the uncertainty over the value of h that is equivalent to that in a model that assumes negligible plate thickness.

5.2 Sources of Error

5.2.1 Modal Decomposition

In order to validate Lyu & Dowling's JSI noise model in flight, measurements are required of the jet near-field pressure within the flight stream. As discussed in Chapter 3, this requirement to have a microphone in the flow, plus the need to reposition the microphone regularly meant that only a single microphone was used. With only one microphone it is not possible to decompose the near-field pressure into modes. Far-field JSI noise

calculations can therefore only be made using Lyu & Dowling's simplified model. It would therefore be appropriate to try to understand what effect the use of the simplified model could have on the JSI noise calculations.

To demonstrate differences between the full and simplified models, the near-field ring-array measurements of Lawrence (described in Chapter 3 and Chapter 4) will be used. It should be noted, however, that these measurements were of a different nozzle to that used for the in-flight measurements, so the effect of a modal decomposition on calculations using the measurements of Lawrence may not be directly applicable to the in-flight calculations. Additionally, these near-field measurements were taken only for a static nozzle, the modal composition of the near-field could potentially change in flight.

Figure 5.4 displays modal decompositions of the near-field spectra at $x/D = 3$ and $M_\mathrm{j} = 0.3$. As has previously been shown, modes 0 and 1 dominate the hydrodynamic spectra, especially at the peak. At Strouhal numbers much higher than the peak, in this case around one, the acoustic field of the jet starts to dominate the spectra. The generation of the acoustic field by random turbulent fluctuations in the shear layer means that higher order modes become increasingly important.

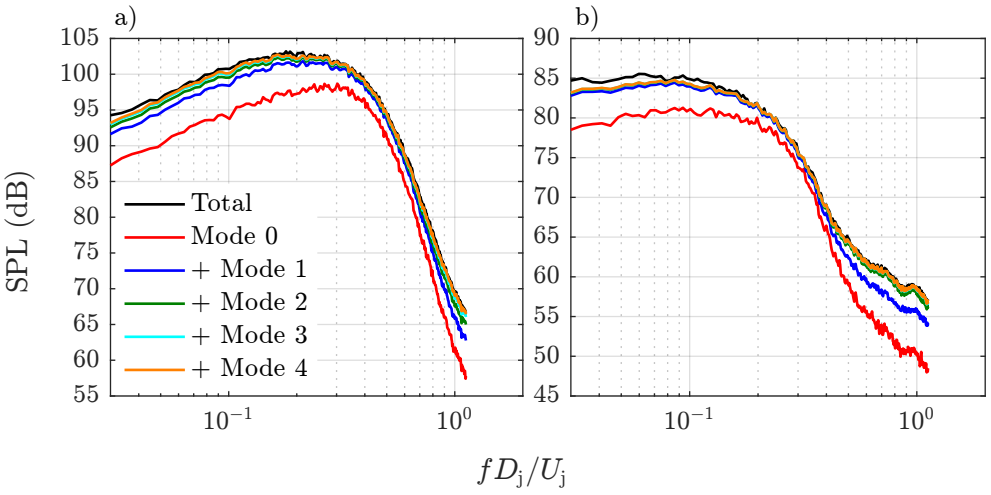

FIGURE 5.4: Modal decomposition of the near-field pressure of an isolated static axi-symmetric jet. $M_\mathrm{j} = 0.3$, $x/D = 3$. a) $r/D = 1.22$; b) $r/D = 2.22$

Using this modal decomposition, far-field predictions have been made using increasing numbers of modes, and compared with Lyu's simplified model (Figure 5.5). Unsurprisingly, given the previous results, there is a large difference in amplitude between predictions using mode 0 and modes 0 and 1. However, adding the remaining modes to the predictions has little effect. This is because the amplitude of these modes is low, and, when decomposed into spanwise components, their energy does not peak at $k_2 = 0$, which is the component that propagates to this location, at $\phi = 0$.

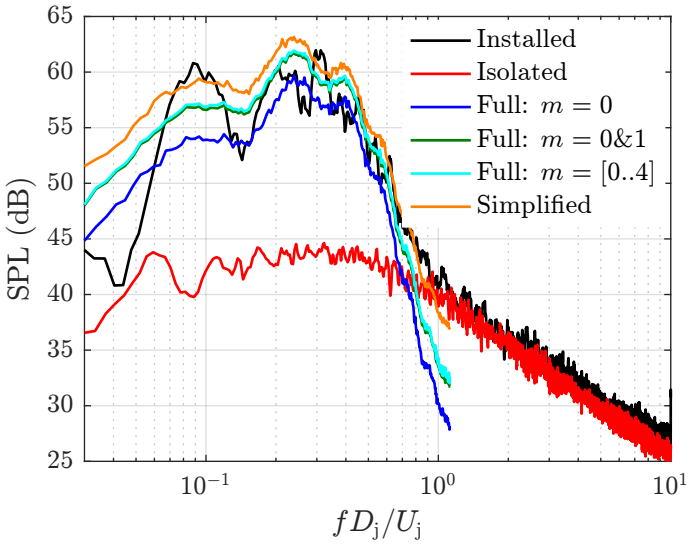

FIGURE 5.5: Comparison of far-field JSI noise calculated with Lyu's simplified method, using one microphone, and full method using modes $m = 0$, $m = 0$ & 1 and $m = 0,\ 1,\ 2,\ 3,$ & 4. $M_j = 0.30$, $c/D = 20$, $\theta = 90°$ and $\phi = 0°$.

Figure 5.5 shows that there is a difference of several decibels between the full model, using the modal decomposition of the near-field, and the simplified model. This difference is plotted in Figure 5.6, where it is compared with the difference in SPL between modes $m = 0$ & 1 and the near-field spectra on a single microphone. Clearly the majority of the increase with the simplified model is due to retaining the higher order modes, which would otherwise have an insignificant contribution to the JSI noise. The remainder likely comes from the difference in propagation and spanwise-wavenumber distribution between modes 0 and 1. This leads to an error of 1 dB at the peak, which increases to 2.5 dB at low frequencies and 5 dB at high frequencies, where the modes greater than 1 contribute most.

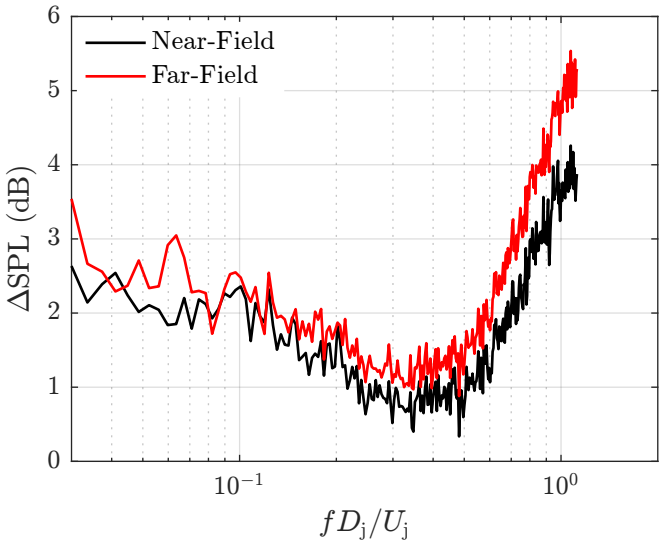

FIGURE 5.6: Difference in amplitude measured/calculated (near-field/far-field respectively) between the near-field measured with a single microphone and modes $m = 0$ & 1 of the near-field measured with multiple microphones. $M_j = 0.30$, $c/D = 20$, $\theta = 90°$.

This error does not appear to have a significant effect on the overall noise prediction because, firstly, the interference pattern remains unchanged, so the same directivity will be predicted, and, secondly, at the point when the error reaches 5 dB the spectrum is already 20 dB below the peak. Therefore, using near-field pressure measurements taken with a single microphone in conjunction with Lyu's simplified model is likely to be sufficient to create OASPL predictions for axisymmetric jets where the observer is positioned at $\phi = 0°$ or 180°.

5.2.2 Near-Field Microphone Position

The model predictions are sensitive to errors in the positioning of the microphones in two ways: 1) it can lead to the use of incorrect axial wavenumbers; and, 2) the incident pressure amplitude on the surface of the plate can be affected. The near-field pressure varies much more rapidly in the radial direction than the axial direction, so it is much more likely that any error is due to the radial placement of the microphone.

To calculate the axial wavenumber the hydrodynamic pressure spectra at two radial measurement locations are collapsed using modified Bessel functions of the second kind. Thus, if the microphones are not in the expected locations, either through a systematic error or otherwise, then the wrong wavenumber may be calculated. With a traverse resolution of 6.25 μm, the error in spacing between microphone locations will be negligible. A systematic error is, therefore, more likely, as the reference radius of the microphone was set by eye against a laser cast along the jet centreline. An estimate can be made of the effect of a systematic error using the ratio of spectral amplitudes at two radii with

a constant offset

$$\frac{\mathrm{PSD}_2}{\mathrm{PSD}_1} = \frac{\mathrm{K}_m^2([h_2+\epsilon]\iota_r)}{\mathrm{K}_m^2([h_1+\epsilon]\iota_r)}. \tag{5.1}$$

The first term of the Taylor expansion can be found by differentiating with respect to ϵ,

$$\frac{\mathrm{d}}{\mathrm{d}\epsilon}\left[\frac{\mathrm{K}_m^2(C_2)}{\mathrm{K}_m^2(C_1)}\right] = -\frac{\iota_r\,\mathrm{K}_m(C_2)}{\mathrm{K}_m^2(C_1)}\left[\mathrm{K}_{m-1}(C_2) + \mathrm{K}_{m+1}(C_2) - \frac{\mathrm{K}_m(C_1)[\mathrm{K}_{m-1}(C_1) + \mathrm{K}_{m+1}(C_1)]}{\mathrm{K}_m(C_1)}\right]. \tag{5.2}$$

If the asymptotic expansion of the Bessel function for large arguments is used,

$$\mathrm{K}_m(z) \sim \sqrt{\frac{\pi}{2z}}e^{-z}, \tag{5.3}$$

then the result of the differential simplifies to

$$-2\iota_r\frac{C_2}{C_1}e^{-2(C_1-C_2)} + 2\iota_r\frac{C_2}{C_1}e^{-2(C_1-C_2)} = 0. \tag{5.4}$$

This suggests that, if the systematic error is small, the effect it has on the calculated wavenumber, and thus on the model predictions, will be negligible.

The hydrodynamic pressure field is measured on a ring about the jet and then propagated onto the trailing edge of the scattering surface using a modified Bessel function of the second kind, hence

$$\mathrm{PSD} \propto \frac{1}{\mathrm{K}_m^2(\iota_r r_0)}. \tag{5.5}$$

Differentiating with respect to r_0 gives

$$\frac{\mathrm{d}}{\mathrm{d}r_0}\frac{1}{\mathrm{K}_m^2(r_0\iota_r)} = k_r\frac{\mathrm{K}_{m-1}(r_0\iota_r) + \mathrm{K}_{m+1}(r_0\iota_r)}{\mathrm{K}_m^3(r_0\iota_r)}. \tag{5.6}$$

Applying the Taylor series approximation, the PSD on the trailing edge, and therefore in the far-field, is proportional to

$$\mathrm{PSD} \propto \frac{1}{\mathrm{K}_m^2(\iota_r r_0)}\left[1 + \epsilon\iota_r\frac{\mathrm{K}_{m-1}(r_0\iota_r) + \mathrm{K}_{m+1}(r_0\iota_r)}{\mathrm{K}_m(r_0\iota_r)}\right]. \tag{5.7}$$

The first error term is proportional to ι_r, which is itself proportional to frequency. Therefore, an error in the placement of the microphone will more adversely affect the higher frequencies. In the rest of the chapter predictions will be made using mode 0 only.

5.3 Flight

The steps for calculating JSI noise with Lyu's model are demonstrated at a jet Mach number of 0.75. This jet Mach number has been chosen because, at this trailing-edge

location, JSI noise is apparent above the jet and flight-stream mixing noise at all flight-stream velocities and a polar angle of $\theta = 90°$.

Measured near-field spectra across the flight-stream Mach number range are displayed in Figure 5.7. As the flight-stream Mach number is increased, the hydrodynamic pressure spectra of the flight stream dominates that provided by the jet at increasing Strouhal numbers. The regions where the flight stream dominates are well below the peak Strouhal number of the jet hydrodynamic pressure spectra, so should have little effect on the JSI noise calculation, and have, therefore, been removed from the spectra.

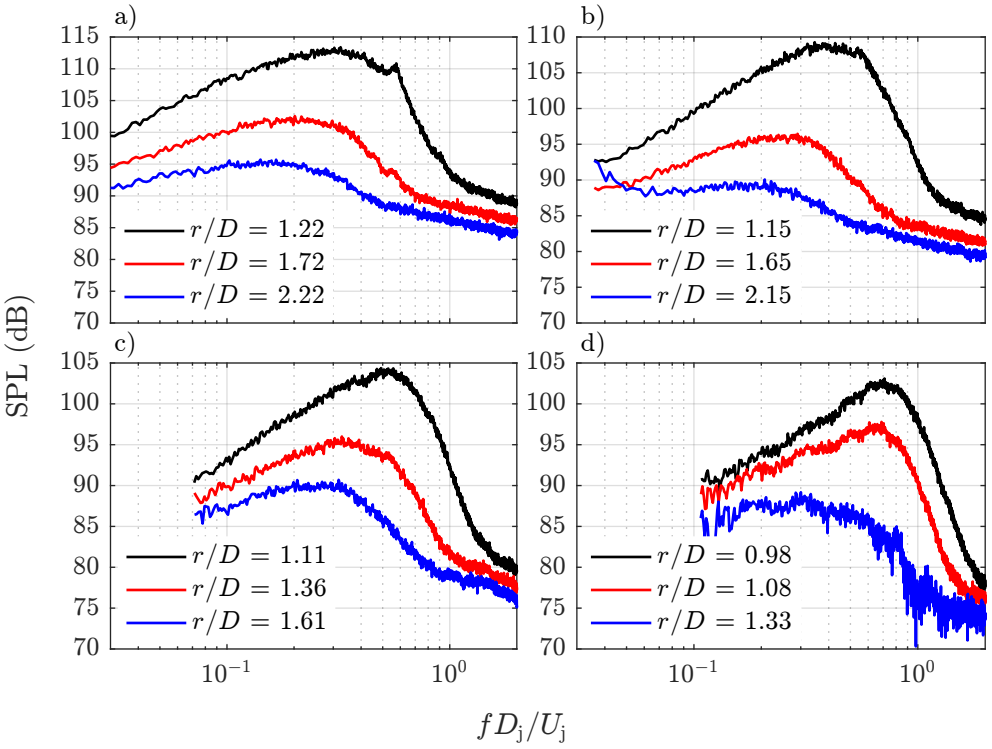

FIGURE 5.7: Jet Near-field spectra. $M_j = 0.75$, x/D = 3. a) $M_f = 0.0$; b) $M_f = 0.1$; c) $M_f = 0.2$; and, d) $M_f = 0.3$

The first step towards calculating JSI noise via Lyu & Dowling's method is to calculate the axial wavenumber of the hydrodynamic pressure field. This is accomplished via the method outlined by Lyu & Dowling, using modified Bessel functions of the second kind to collapse the red and black spectra in Figure 5.7. The resulting axial wavenumbers are shown in Figure 5.8. As was discussed in Chapter 4, the axial wavenumber of the jet hydrodynamic pressure field increases linearly with Strouhal number up until a local maximum. This maximum corresponds to the point at which the acoustic pressure begins to dominate the hydrodynamic pressure at the furthest radial measurement location (red lines in Figure 5.7). Above this Strouhal number, the calculated wavenumber tends to the acoustic wavenumber. $k - \omega$ decomposition of the near-field pressure of an isolated jet using LES data, in Chapter 4, suggested that the peak of the axial-wavenumber

distribution increases linearly. Thus, the initial linear region in Figure 5.8 has been extrapolated to higher Strouhal numbers.

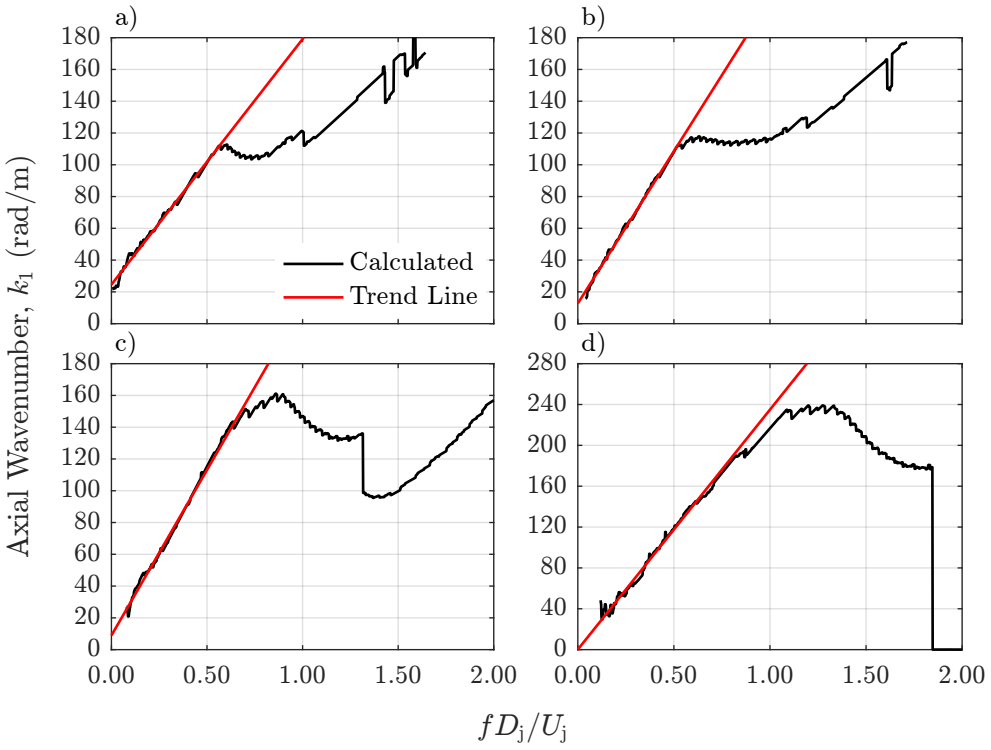

FIGURE 5.8: Wavenumbers calculated from the near-field spectra of a Mach 0.75 jet. a) $M_f = 0.0$; b) $M_f = 0.1$; c) $M_f = 0.2$; and, d) $M_f = 0.3$

Using the jet near-field spectra measured at the lowest radial location (Figure 5.7) and the calculated wavenumbers (Figure 5.8), JSI noise is then calculated using Lyu's method; propagating the pressure onto the plate using cylindrical harmonics, and using Amiet's theory to calculate the noise scattered to the far field. A comparison of the calculated and experimentally measured JSI noise is made in Fig. 5.9. For flight Mach numbers of $M_f = 0$ (Figure 5.9a) and $M_f = 0.1$ (Figure 5.9b), there is very good agreement between the calculated and measured results, both in amplitude and shape. The slight upturn in the JSI noise spectra between Strouhal numbers of 1 and 2 is caused by the acoustic field beginning to dominate the hydrodynamic field in the near-field spectra. At flight Mach numbers of 0.2 (Figure 5.9c) and 0.3 (Figure 5.9d), it is more difficult to make a comparison, as the installed level is close to the isolated level. However, the model appears to increasingly under-predict the measured spectra as flight velocity increases; though the spectral shapes still appear to be in good agreement.

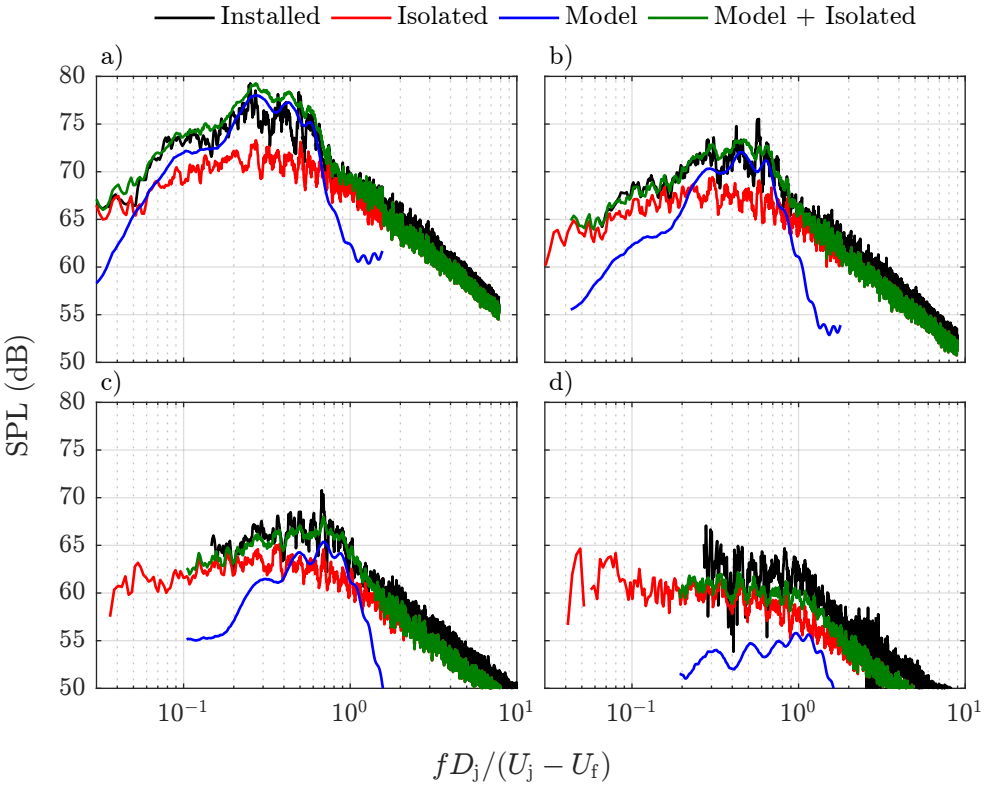

FIGURE 5.9: Comparison of far-field JSI noise calculated with Lyu's method with experimental measurements of installed and isolated jet noise. $M_j = 0.75$. a) $M_f = 0.0$; b) $M_f = 0.1$; c) $M_f = 0.2$; and, d) $M_f = 0.3$

Despite the under-prediction of the model at $M_f = 0.3$, both the model and the experimental measurements in Figure 5.9 serve to demonstrate the effect of flight in reducing jet noise (at a polar angle of 90°). Both the isolated and installed spectra can be seen to reduce as flight velocity increases, with the peak level reducing by approximately 10 dB for the isolated jet noise and the installed jet noise by 13 dB. With static jet noise and jet-surface interaction peak noise scaling as jet velocity to the seventh and fifth power respectively, it may be expected that the isolated jet noise would decay by the greater amount in flight. However, in flight the jet stretches so jet mixing noise scales with a velocity difference to an exponent less than seven, while the same stretching increases the distance from the edge of the shear layer to the trailing-edge of the wing, reducing JSI noise further than the velocity difference to the fifth power.

Another installation effect apparent from the experimental data in Figure 5.9 is reflection of the acoustic jet-mixing noise from the plate. This is apparent at high Strouhal numbers, where the installed jet noise remains higher than the isolated levels. This has been extensively covered in literature, and is not modelled here.

Further comparison is made between the model and the experimental data in Figure 5.10. The higher velocity Mach 0.9 jet is used as it gives the greatest separation from the noise produced by the flight stream, both in frequency and amplitude, at the flight Mach

number of 0.3. It is immediately apparent from Figure 5.10 that the under-prediction of the model at a flight Mach number of 0.3 (as seen in Figure 5.9) is true also for a jet Mach number of 0.9. Reasons for this under prediction could include: Firstly, a smaller radial separation between the near-field microphone locations was used to calculate the axial wavenumbers in this case. This could exacerbate any error in the positioning of the microphone and the effect it has on the calculation of the axial wavenumbers. Secondly, high frequency JSI noise is more sensitive to the positioning of both the near-field microphone and the plate. As the peak frequency increases in flight, this would also exacerbate any positioning error. Thirdly, the jet may experience a Coanda effect in flight, moving toward the plate and increasing the level of JSI noise. Finally, the decrease in amplitude and increase in peak frequency of the JSI noise may make the reflection of mixing noise significant over the same Strouhal number range. Another aspect that needs exploring, but is unlikely to contribute to the under-prediction, is the effect of flight on the relative amplitudes of the azimuthal modes, as this will affect the amplitude and azimuthal directivity of far-field JSI noise.

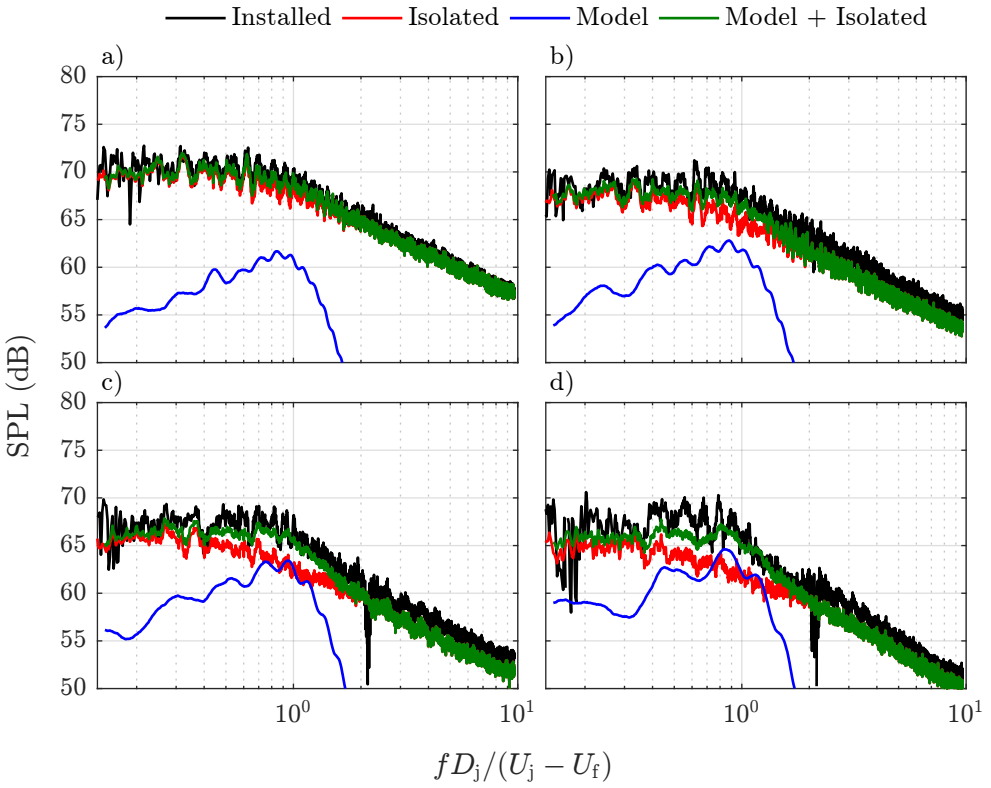

FIGURE 5.10: Comparison of far-field JSI noise calculated with Lyu's method with experimental measurements of installed and isolated jet noise. $M_j = 0.90$, $M_f = 0.3$, $h/D = 1$, $l/D = 3$ and $\phi = 0°$. a) $\theta = 71°$; b) $\theta = 90°$; c) $\theta = 109°$; d) $\theta = 129°$

Figure 5.11 displays a comparison between model and experimental measurements for the $M_j = 0.9$ jet, with $M_f = 0.2$. As for $M_j = 0.75$ at the same flight-stream velocity, both the amplitude and spectral shape compare very well with the model. It would appear, therefore, that the under-prediction is limited to $M_f > 0.2$.

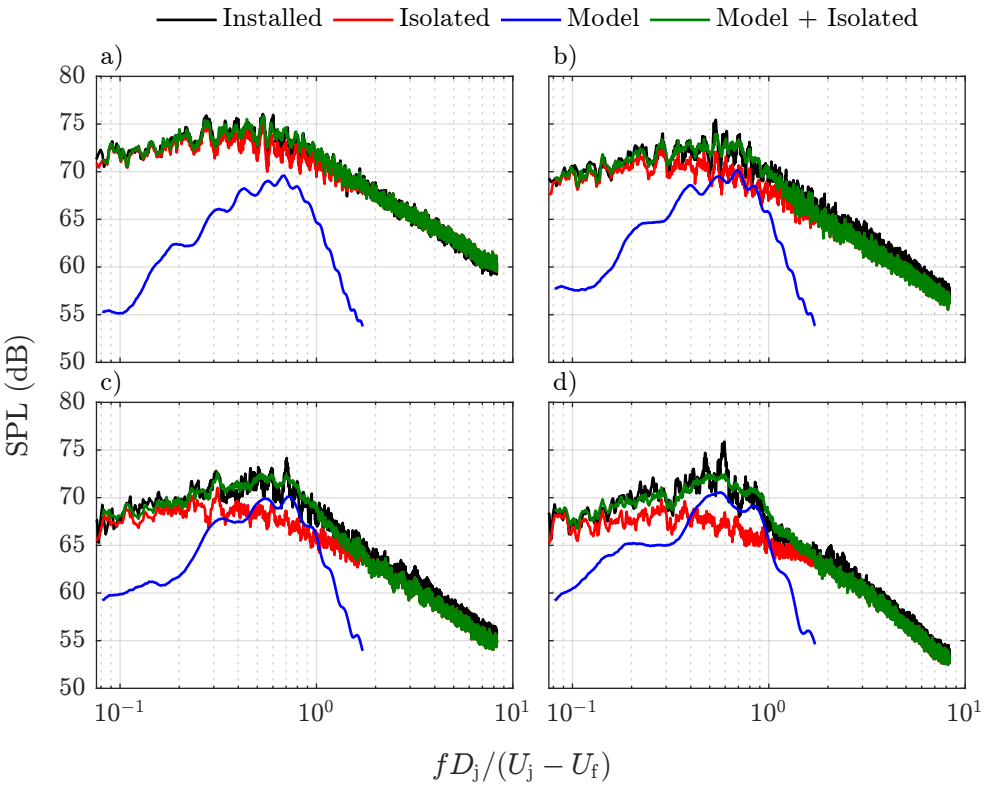

FIGURE 5.11: Comparison of far-field JSI noise calculated with Lyu's method with experimental measurements of installed and isolated jet noise. $M_j = 0.90$, $M_f = 0.2$, $h/D = 1$, $l/D = 3$ and $\phi = 0°$. a) $\theta = 71°$; b) $\theta = 90°$; c) $\theta = 109°$; d) $\theta = 129°$

5.4 Chord Length

Various previously published experiments[22] have shown how the chord of a plate positioned in proximity to a jet changes the spectral shape and amplitude of JSI noise. This is also demonstrated in Figure 5.12, which shows how the amplitude of the lower frequencies of JSI noise reduce as chord length decreases. This is because the reduction in chord: a) changes the phase of the incident pressure on the plate, which when scattered to the far-field interact to create angles where the sources are in phase and areas where the plate sources are out of phase; b) increases the strength of the trailing-edge scattered noise diffracted by the leading edge and interfering with the trailing-edge scattered noise in the far-field, as was modelled by Miller;[54] and, c) changes the phase angle and relative strengths of the leading-edge and trailing-edge scattered noise.

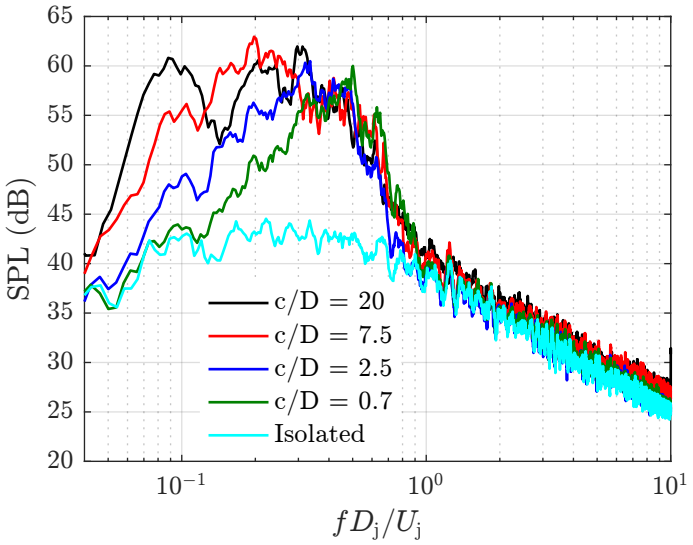

FIGURE 5.12: Measured far-field noise spectra with four different chord lengths. c/D = 20 comes from measurements with a 38.1 mm nozzle. $M_j = 0.3$, $M_f = 0$, $h/D = 1$, $l/D = 3$, $\theta = 90°$ and $\phi = 0°$

The effect of chord length on installed jet noise is further demonstrated in Figure 5.13. It is apparent in this figure that the directivity becomes less of a cardioid and more of a dipole as chord reduces, in agreement with edge-scattering theory. While this change has a large effect on the amplitude in the forward polar arc there is little change in the rear-arc, where jet noise is a large component of turbofan noise. The reason for the small change in OASPL in the mid and rear polar arcs is shown in Figure 5.12, where the biggest effect of the changing chord is on the low frequency end of the JSI noise spectra, and therefore does not have a strong effect on OASPL. At full scale and applying a weighting for the human response to frequency, the difference in PNL (Perceived Noise Level) in the mid and rear polar arcs would likely be even less.

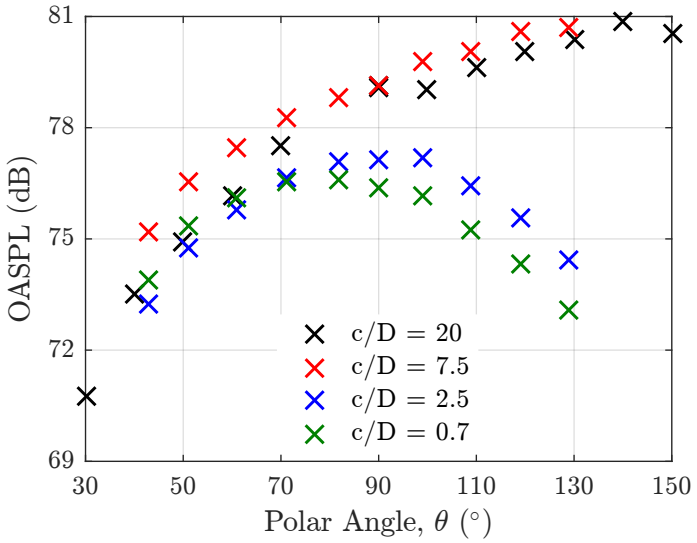

FIGURE 5.13: Comparison of measured far-field installed-jet OASPL directivity with four different chord lengths. c/D = 20 comes from measurements with a 38.1 mm nozzle. $M_j = 0.3$, $M_f = 0$ and $\phi = 0°$.

Amiet's theory (used by Lyu & Dowling) assumes that the chord of the surface is semi-infinite for calculating the scattered surface pressure. The effect of finite chord on the far-field scattered noise is approximated by limiting the surface area to which Curle's theory is applied. This ignores the diffraction of the trailing-edge-scattered noise by the leading edge, and any leading-edge scattering.

Most comparisons between JSI noise calculated with Amiet's theory and experiment have used plates with very large chords, in order to reduce the effects of the leading edge on the measured installed jet noise. Therefore, a comparison has been made with surfaces of differing chords, including cases closer in scale to realistic wing surfaces (2.5D - wing, 0.7D - single slotted flap).

In Figure 5.14 and Figure 5.15 JSI noise model predictions are compared with experimental measurements of installed jet noise. From these figures it would appear that the model has accurately calculated the spectra of the two largest plates ($c/D = 20$ and $c/D = 7.5$). There is a slight over-prediction of the peak SPL with $c/D = 7.5$ at $M_j = 0.75$. This is likely to be due to taking near-field pressure measurements with only one microphone, preventing the decomposition of the near-field pressure spectrum into azimuthal modes. This would allow modes of order $|m| > 1$ to contribute to the JSI noise prediction more than they should at this polar angle. To confirm this hypothesis near-field pressure measurements would need to be taken at the same axial and radial location, relative to the jet nozzle, and jet velocity, but with sufficient microphones to decompose the pressure into azimuthal modes and use the modal spectra to calculate the JSI noise.

Once the chord has been reduced to 2.5 jet diameters, the entire JSI noise spectra is overpredicted by approximately ≈ 5 dB. This suggests that the simplified model no longer captures the physics of the situation, as not decomposing the near-field into modes would show the same level of overprediction between different chord lengths. Reducing the chord further, to $c/D = 0.7$, the overprediction has increased further below the peak frequency. Although at frequencies at and above the peak the model and measured spectra compare very well. However, with the leading edge $2.3D$ downstream of the nozzle, a leading-edge-scattering source is likely to exist, which would further raise the calculated spectra.

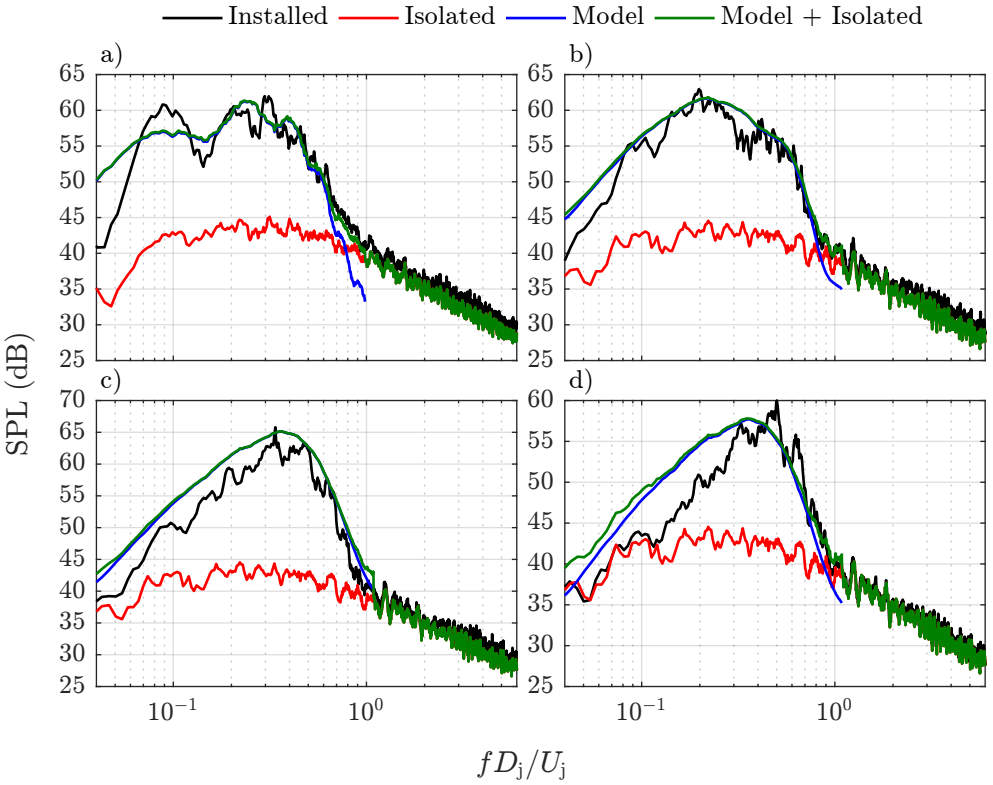

FIGURE 5.14: Comparison of model predictions and experimental installed jet noise measurements with different chord lengths. $M_j = 0.3$, $M_f = 0$, $l/D = 3$, $h/D = 1$, $\theta = 90°$ and $\phi = 0°$. a) $c/D = 20$; b) $c/D = 7.5$; c) $c/D = 2.5$ ($h/D = 0.9$); and, d) $c/D = 0.7$

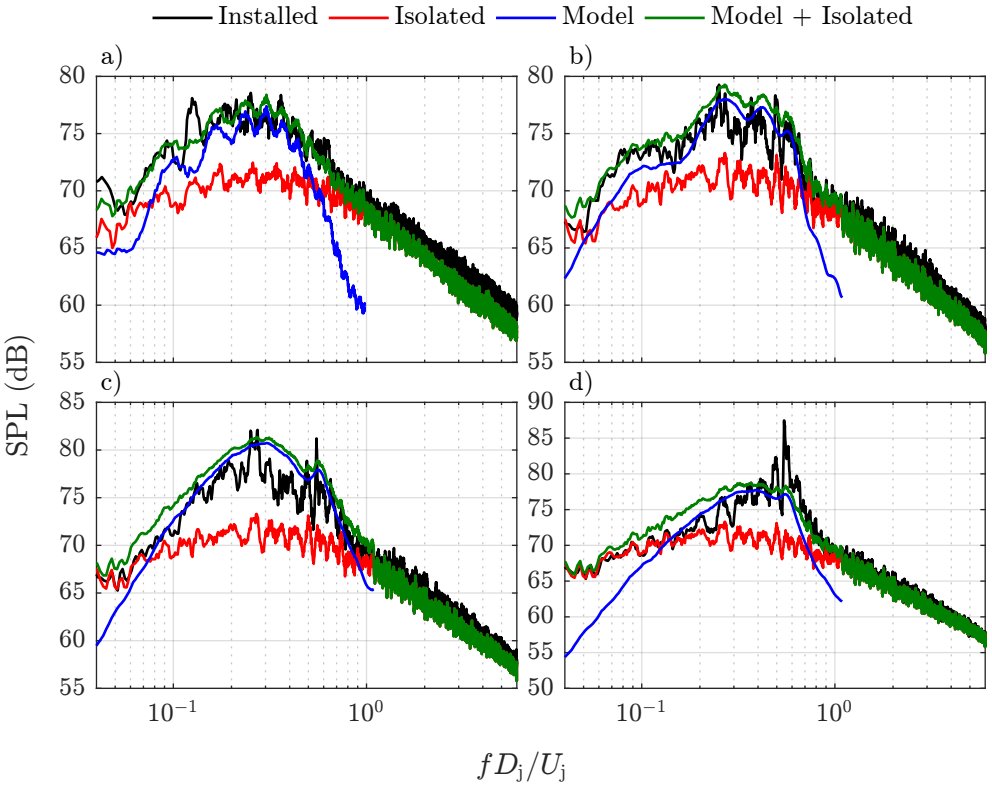

FIGURE 5.15: Comparison of model predictions and experimental installed jet noise measurements with different chord lengths. $M_j = 0.75$, $M_f = 0$, $l/D = 3$, $h/D = 1$, $\theta = 90°$ and $\phi = 0°$. a) $c/D = 20$; b) $c/D = 7.5$; c) $c/D = 2.5$ ($h/D = 0.9$); and, d) $c/D = 0.7$

As chord reduces, one expects the comparison to become less favourable because Amiet's theory does not account for the leading edge when calculating the scattered surface pressure. This can be corrected by applying Schwarzchild's solution iteratively to the leading and trailing edges. The first leading edge correction to Amiet's trailing edge scattering theory has been derived by Roger & Moreau.[43, 51]

In Figure 5.16 and Figure 5.17 Roger & Moreau's back-scattering correction has been applied to the calculation of the JSI noise from the $c/D = 2.5$ and 0.7 plates. Compared with Amiet's original theory, the largest effect of the back-scattering correction has been to reduce the amplitude of the JSI noise spectra at Strouhal numbers/frequencies, below the peak. Roger & Moreau have demonstrated that the back-scattering correction increasingly reduces the amplitude of the scattered far field noise as kc reduces below one. This explains why it is most noticeable at the lower jet velocity of $M_j = 0.3$ (see Figure 5.16).

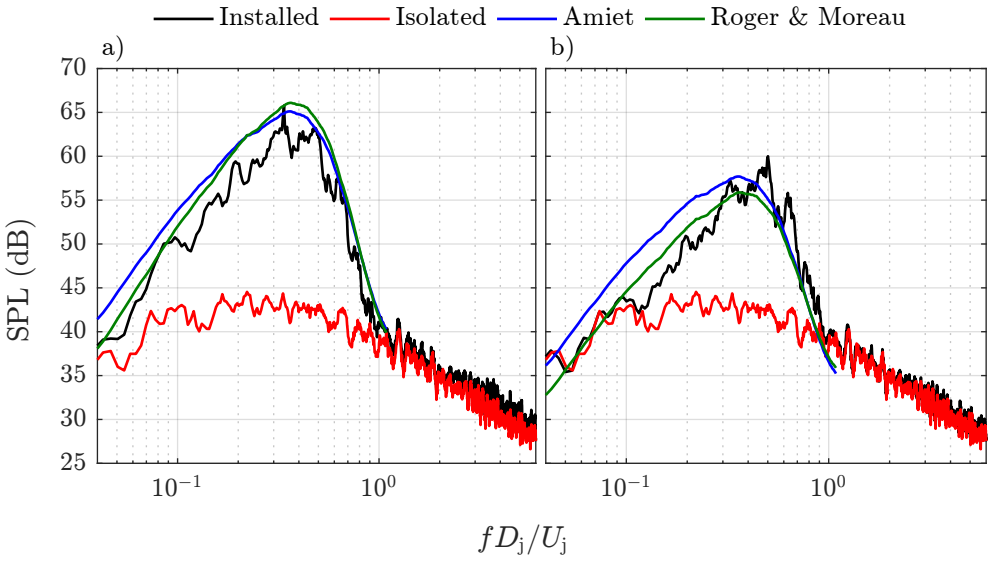

FIGURE 5.16: Comparison of JSI noise predictions using Amiet's theory without and with Roger & Moreau's back-scattering theory. $M_j = 0.3$, $M_f = 0$, $l/D = 3$, $h/D = 1$, $\theta = 90°$ and $\phi = 0°$. a) $c/D = 2.5$ ($h/D = 0.9$); b) $c/D = 0.7$

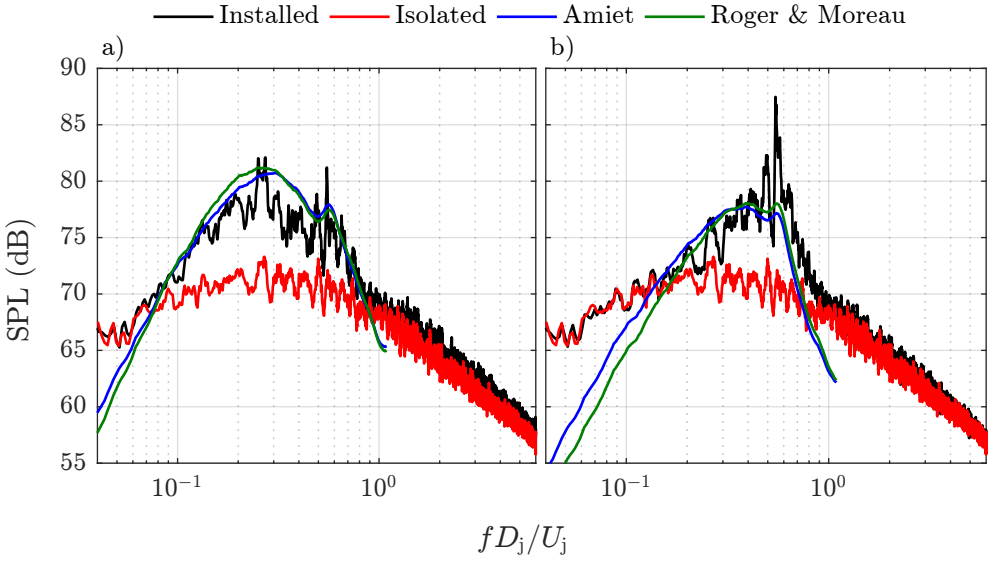

FIGURE 5.17: Comparison of JSI noise predictions using Amiet's theory without and with Roger & Moreau's back-scattering theory. $M_j = 0.75$, $M_f = 0$, $l/D = 3$, $h/D = 1$, $\theta = 90°$ and $\phi = 0°$. a) $c/D = 2.5$ ($h/D = 0.9$); b) $c/D = 0.7$

At higher frequencies the effect of the back-scattering correction is to modify the directivity and hence the spectral shape. This is demonstrated further in Figure 5.18 where the biggest change to spectral shape occurs in the rear arc. This is because the back-scattering correction is another edge scattering solution, and by itself has far-field directivity pattern that goes to zero in the forward arc. However, the effect has been to raise the peak amplitude further, not to lower it, increasing the discrepancy with the measured data.

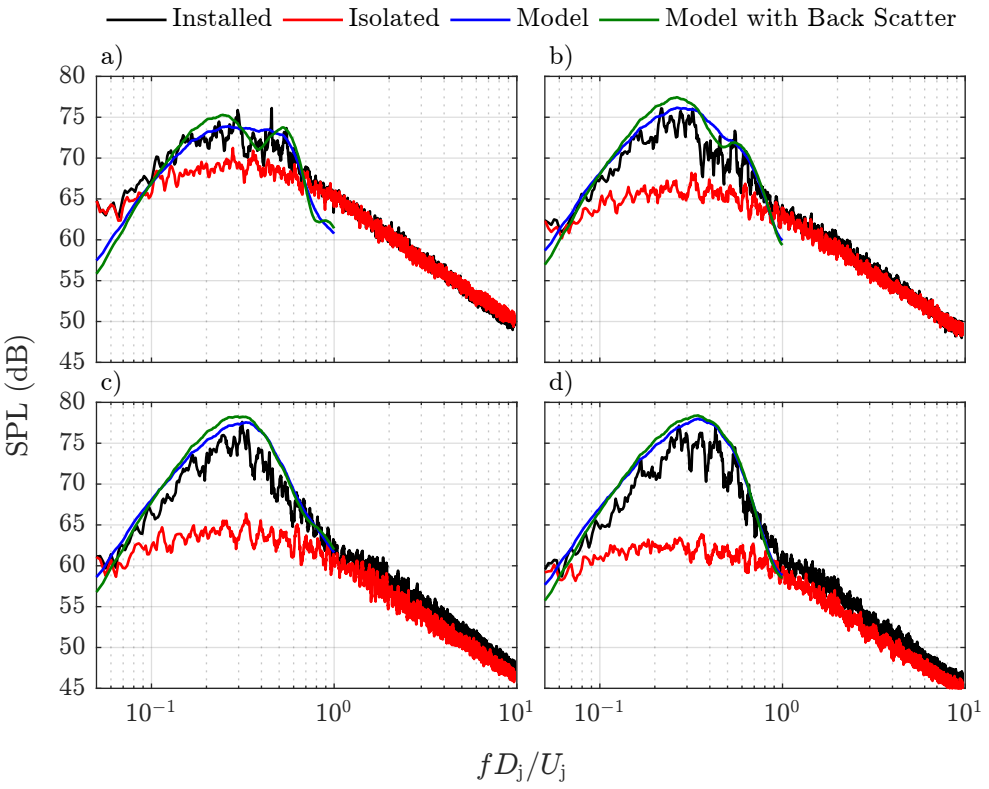

FIGURE 5.18: Comparison of far-field JSI noise predictions using Amiet's theory without and with Roger & Moreau's back-scattering theory. $M_j = 0.6$, $M_f = 0$, $l/D = 3$, $h/D = 0.9$ and $\phi = 0°$. a) $\theta = 50°$; b) $\theta = 70°$; c) $\theta = 90°$; and, d) $\theta = 110°$

In Figure 5.19 a comparison has been made between the experimentally measured JSI noise OASPL and that calculated with the method of Lyu & Dowling for the $c/D = 7.5$ plate. At the lowest Mach number ($M_j = 0.3$, Figure 5.19a), the shapes of the model and experimental directivities match very well. The amplitude of the model is approximately 1-2 dB greater than that of the experiment for this case, but, as previously mentioned, this is likely due to using the total near-field SPL rather than using a modal decomposition. Also included for comparison are dipole and cardioid directivity patterns, with the amplitude at 90° set to match that of the experimental data. At large chord lengths, and high frequencies, Amiet's theory suggests that the directivity should display a cardioid directivity pattern. In Figure 5.19a, there appears to be a cardioid directivity in the forward arc and a dipole directivity in the rear arc. As the jet velocity is increased, the directivity appears to 'flatten' in the forward arc. This trend is seen in both the experimental and model directivity patterns, though the model appears to be increasingly overpredicting in the forward arc, while maintaining the 1-2 dB offset in the rear arc.

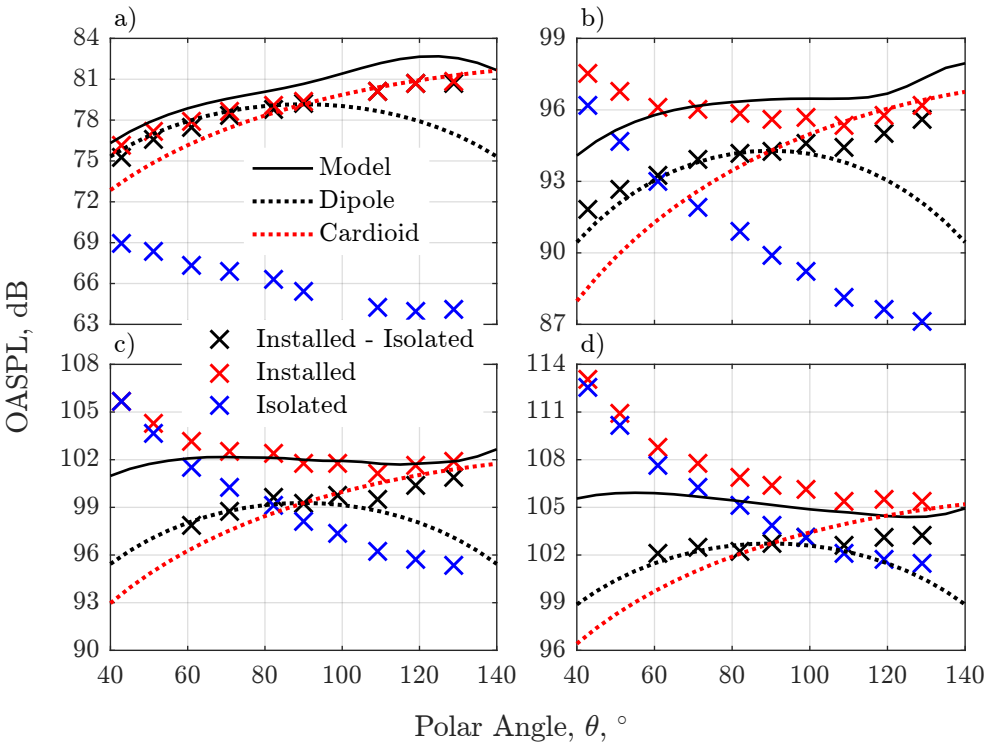

FIGURE 5.19: Comparison of model and experimental polar OASPL directivity. $l/D = 3$, $h/D = 1$, $c/D = 7.5$, $M_f = 0$ and $\phi = 0°$. a) $M_j = 0.3$; b) $M_j = 0.6$; c) $M_j = 0.75$; and, d) $M_j = 0.9$;

Polar directivity plots for $c/D = 2.5$ and $c/D = 0.7$ are displayed in Figure 5.20 and Figure 5.21 respectively. As in Figure 5.19, both plots display a good comparison between the model and experimental OASPL directivity patterns at the lowest jet velocity, while the OASPL in the rear arc is increasingly overpredicted by the model as jet velocity is increased. In addition, the overprediction of the OASPL within the forward arc has increased with the $c/D = 2.5$ plate. The forward arc OASPL of the $c/D = 0.7$ plate appears to be very well predicted, however the model OASPL would likely increase if leading-edge scattering were also included. For the $c/D = 0.7$ plate, the directivity at each jet velocity appears to be close to that of a dipole, which is to be expected as kc becomes small.

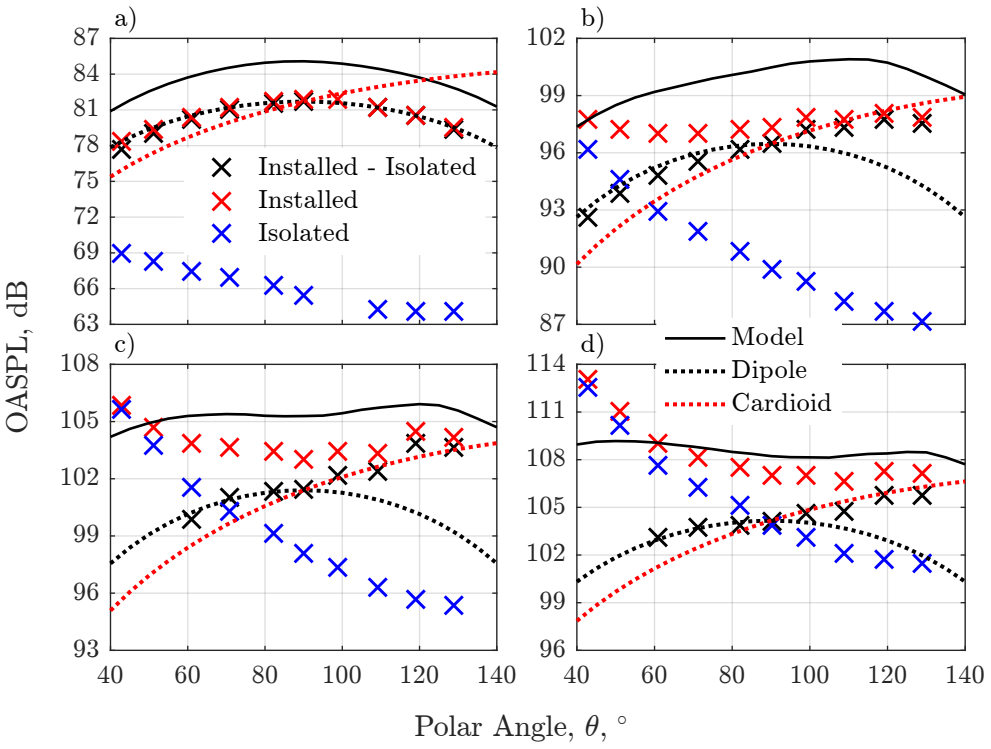

FIGURE 5.20: Comparison of model and experimental polar OASPL directivity. $l/D = 3$, $h/D = 0.9$, $c/D = 2.5$, $M_\mathrm{f} = 0$ and $\phi = 0°$. a) $M_\mathrm{j} = 0.3$; b) $M_\mathrm{j} = 0.6$; c) $M_\mathrm{j} = 0.75$; and, d) $M_\mathrm{j} = 0.9$;

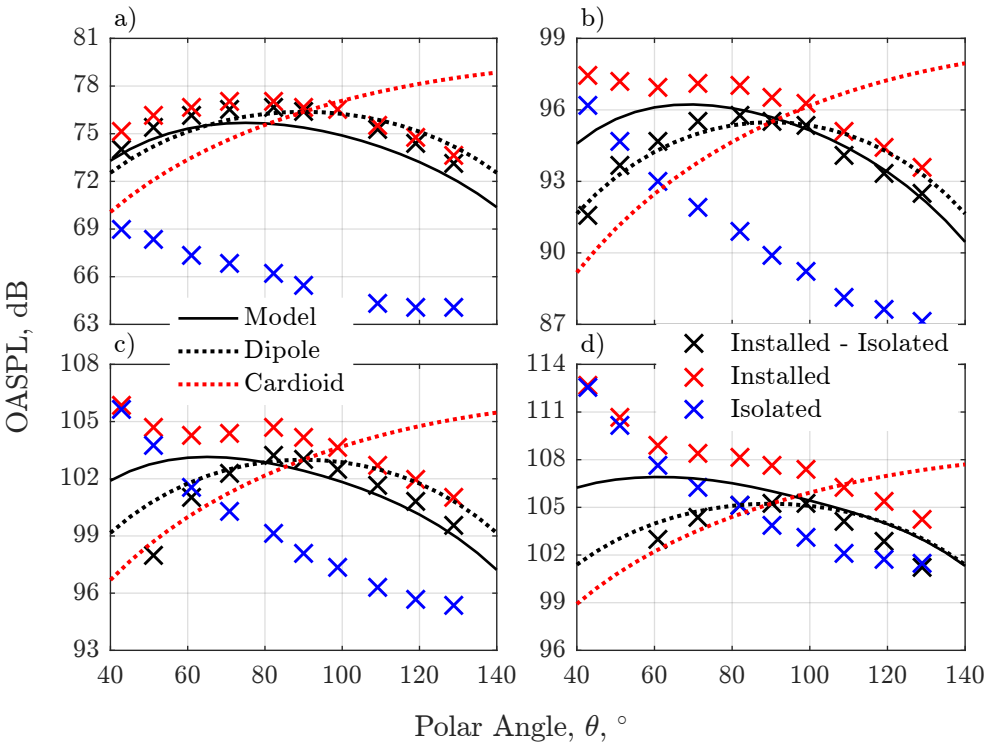

FIGURE 5.21: Comparison of model and experimental polar OASPL directivity. $l/D = 3$, $h/D = 1$, $c/D = 0.7$, $M_f = 0$ and $\phi = 0°$. a) $M_j = 0.3$; b) $M_j = 0.6$; c) $M_j = 0.75$; and, d) $M_j = 0.9$;

To calculate OASPL in Figures 5.19, 5.20 and 5.21, the measured spectra were integrated from 100 Hz up to a Strouhal number of one. This limited range has been used to try to capture the JSI noise, while minimising the contributions from the reflection of jet mixing noise. The isolated jet OASPL has then been subtracted from the installed OASPL, where the installed OASPL is greater one decibel above the isolated OASPL. Below one decibel of separation it becomes increasingly difficult to determine whether the difference between the installed and isolated level is due to JSI noise, other installation effects or differences in jet velocity (due to control system).

Further work is required to understand why the model increasingly overpredicts the JSI noise in the rear arc as jet velocity increases. One hypothesis concerns the assumption that the incident pressure, p'_{S1}, is stationary and takes the value at the trailing edge; as it has a greater amplitude in the rear arc than the trailing-edge scattered component, p'_{S2}, and is dependent on the pressure across the entire surface. This could be further explored using a near-field pressure model that includes the variation along the jet axis, such as the models of Bychkov & Faranosov[48] or Vera.[64]

5.5 Finite Span

So far it has been assumed, for the purpose of calculating the JSI noise analytically using Amiet's theory, that the span of the scattering surfaces are infinite. Amiet[40, 50] states that the infinite span assumption is valid when

$$Mk_1 d >> 1, \quad d/c >> 1, \quad k_1 d >> 1. \tag{5.8}$$

These conditions have not necessarily been met at all frequencies for the experimental data used. For instance the plate of Lawrence had an aspect ratio, d/c of 1.44 which is not much greater than 1. Therefore it may not always be possible to assume that the span is infinite.

It may also not be possible to assume the scattering surface has an infinite span if either the geometry of the scattering surface or the flow conditions vary along the span.[116–119] In such cases, the solution can be approximated by splitting the surface into strips of finite span, assuming the conditions are constant along each strip, and then applying Amiet's theory. However, when applying Amiet's theory to each strip, as the span is finite the sinc function does not become a delta function, and, therefore, the integral over k_2 cannot be so easily evaluated.

For aerofoil self-noise, the spanwise wavenumbers and the different strips are assumed to be incoherent. Thus, the scattered far-field noise due to each strip becomes

$$\mathrm{PSD}_{\mathrm{S}x}(\omega) = \left(\frac{kx_3}{\beta^2 \tilde{r}_x^2}\right)^2 \frac{d}{2} \int_{-\infty}^{\infty} \mathrm{PSD}_{\mathrm{I}}(\omega, k_2) |\Gamma(c, C_1, C_3)|^2 \frac{2\sin^2(C_2 d/2)}{\pi d |C_2|^2} \, \mathrm{d}k_2. \tag{5.9}$$

Summing the noise due to each strip incoherently works well if the spanwise extent of each strip is greater than the correlation length. If not, the amplitude and directivity will be incorrect. To correctly calculate the far-field noise in this situation, the noise from each strip should be summed coherently. However, the coherence of the boundary layer generated self-noise between strips is generally unknown. Therefore, an inverse strip theory has been suggested by Christophe & Anthoine,[116] whereby the noise from a large strip is subtracted from an infinite span calculation to effectively give the noise produced by a much smaller strip.

In the model of Lyu & Dowling, measurements of the jet near field are used to decompose the hydrodynamic pressure field into modes and axial wavenumber components (although only one axial wavenumber is assumed for each frequency and mode), which are incoherent. These modes are then propagated onto the scattering surface whereupon a Fourier transform is taken to get the spanwise wavenumber distribution. The components of the spanwise wavenumber distribution are therefore coherent, and therefore need to be summed in terms of pressure. The integral over k_2 is then calculated in terms

of pressure for each strip

$$p'_{\mathrm{S}x}(\omega) = (1+i)\frac{kx_3 e^{-i\tilde{k}\tilde{r}_x + \tilde{k}M\tilde{x}_1}}{\pi\beta^2\tilde{r}_x^2} \sum_{m=-\infty}^{\infty}\int_{-\infty}^{\infty}\hat{p}'_{\mathrm{I}}(\omega,m,k_2)\Gamma(c,C_1,C_3)\,\mathrm{e}^{-\,\mathrm{i}C_2y_{2c}}\frac{\sin(C_2d/2)}{C_2}\,\mathrm{d}k_2, \quad (5.10)$$

where y_{2c} is the location of the spanwise centre of the strip.

Since the incident pressure on each strip is due to the same source - the jet - the far-field noise from each strip should also be summed coherently. For N strips, and assuming the trailing edges of the strips are at the same axial location (l), the far-field noise is

$$p'_{\mathrm{S}x}(\omega) = (1+\,\mathrm{i})\frac{kx_3\,\mathrm{e}^{-\,\mathrm{i}k(\tilde{r}_x - Mx_1/\beta)/\beta}}{\pi\beta^2\tilde{r}_x^2} \sum_m\sum_{q=1}^{N}\int_{-\infty}^{\infty}p'(\omega,m)f(\iota_r,m,k_2,h)\Gamma(c_q,C_1,C_3)\,\mathrm{e}^{-\,\mathrm{i}C_2y_{2c,q}}\frac{\sin(C_2d_q/2)}{C_2}\,\mathrm{d}k_2, \quad (5.11)$$

where $f(\iota_r,m,k_2,h) = p'_{\mathrm{I}}(\omega,m,k_2)/p'(\omega,m)$.The far-field PSD can then be calculated using

$$\mathrm{PSD}_{\,\mathrm{S}x}(\omega) = \lim_{T\to\infty}\frac{\pi}{T}p'_{\mathrm{S}x}\bar{p}'^{*}_{\mathrm{S}x}. \quad (5.12)$$

The only stochastic variable in the calculation of $p'_{\mathrm{S}x}$ is $p'(\omega,m)$, which being independent of k_2 can be removed from the integral. Also, as the modes are incoherent, it is not necessary to calculate the CPSD between different modes. This then results in

$$\mathrm{PSD}_{\,\mathrm{S}x}(\omega) = \frac{2k^2x_3^2}{\pi^2\beta^4\tilde{r}_x^4} \sum_m\left|\sum_{q=1}^{N}\int_{-\infty}^{\infty}f(\iota_r,m,k_2,h)\Gamma(c_q,C_1,C_3)\,\mathrm{e}^{-\,\mathrm{i}C_2y_{2c,q}}\frac{\sin(C_2d_q/2)}{C_2}\,\mathrm{d}k_2\right|^2\mathrm{PSD}(\omega,m). \quad (5.13)$$

There are several points to note when completing the integrals in Equation 5.9 and Equation 5.10. Firstly, it may be necessary to integrate over super-critical wavenumbers, for which the transformed wavenumber $\tilde{k}$ is imaginary. In this case Roger & Moreau[43] use

$$C_1 = \tilde{k} + k_1 - (\tilde{k}_2\tan(\psi) - kM)/(\beta^2 + \tan^2(\psi)) \quad (5.14)$$

where $\tilde{k}^2 > 0$, while to get the correct decay on the surface,

$$C_1 = -\tilde{k} + k_1 - (\tilde{k}_2\tan(\psi) - kM)/(\beta^2 + \tan^2(\psi)), \quad (5.15)$$

when $\tilde{k}^2 < 0$. Secondly, the Schwarzchild solution is only valid when $\tilde{k}$ does not equal zero. Thirdly, there is an extra term, $\mathrm{e}^{-\,\mathrm{i}C_2y_{2c}}$, in Equation 5.10 compared to Equation 2.128. This term comes from the shift theorem and accounts for a strip whose

centre line is not along $y_2 = 0$. Finally, the integral must be completed numerically, which is much more computationally expensive than assuming infinite span.

Figure 5.22, Figure 5.23 and Figure 5.24 compare far-field solutions for the finite and infinite-span implementations for different azimuthal angles, polar angles and chords, respectively. For each case, the strip theory solution matches the infinite span solution when the span to wavelength ratio is greater than 10^3. As the span is reduced, there comes a point at which the strip theory solution no longer matches the infinite span solution. In most cases the solution starts to vary in a sinusoidal pattern about the infinite span solution when the integral over k_2 includes the point where $\tilde{k} = 0$. Thus, it occurs at high ratios of d/k at azimuthal observer angles closer to the plane of the plate as the centre of the sinc function shifts towards this location. As the span is reduced, the variation increases further and the result can also become spiky. This is because the location $\tilde{k} = 0$ becomes more important to the integral, and at this location there is a singularity, arising from the term $\sqrt{\frac{C_1}{C_1 - C_3}}\,\mathrm{E}(c[C_1 - C_3])$ in $\Gamma(c, C_1, C_3)$. This behaviour is, however, suppressed when the chord to wavelength ratio, c/λ, is low because the error function now goes to zero more quickly than the denominator, $C_1 - C_3$, as $\tilde{k} \to 0$. A robust manner in which to overcome this singularity is needed if strip theory is to become useful for industrial application.

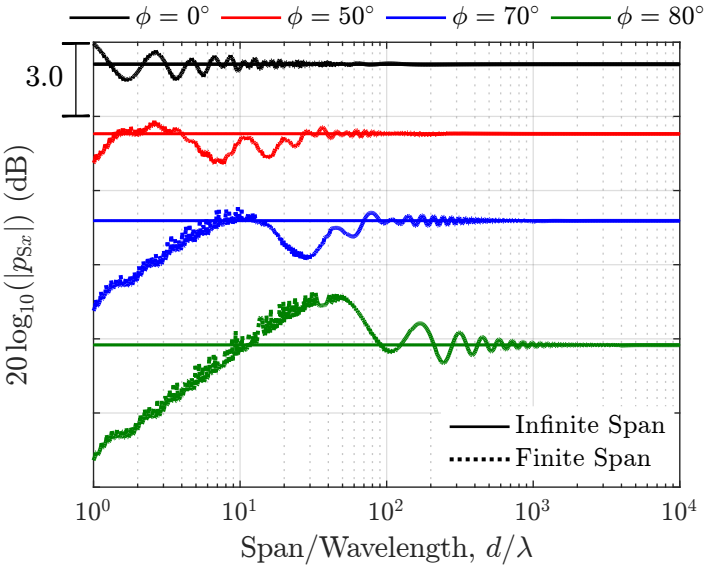

FIGURE 5.22: Comparison of the finite-span and infinite-span solutions at several azimuthal angles. $f = 1000$ Hz, $c = 3.4$, $\theta = 90°$ and $k_1 = 45$

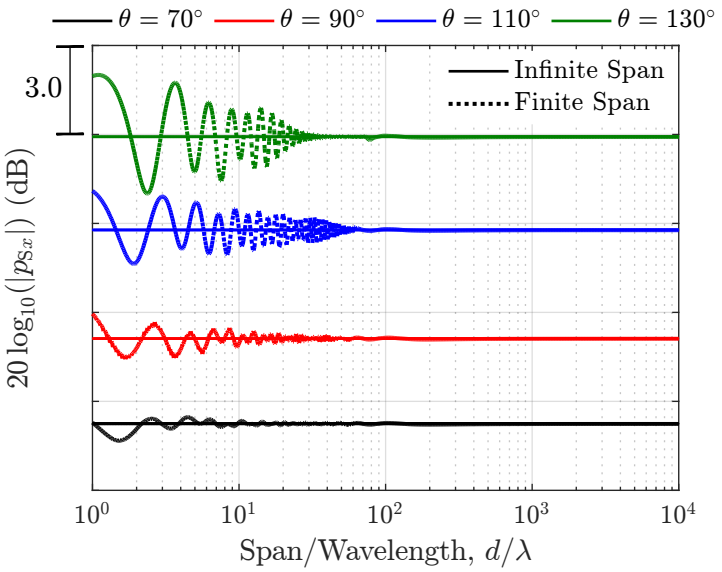

FIGURE 5.23: Comparison of the finite-span and infinite-span solutions at several polar angles. $f = 1000$ Hz, $c = 3.4$, $\phi = 0°$ and $k_1 = 45$

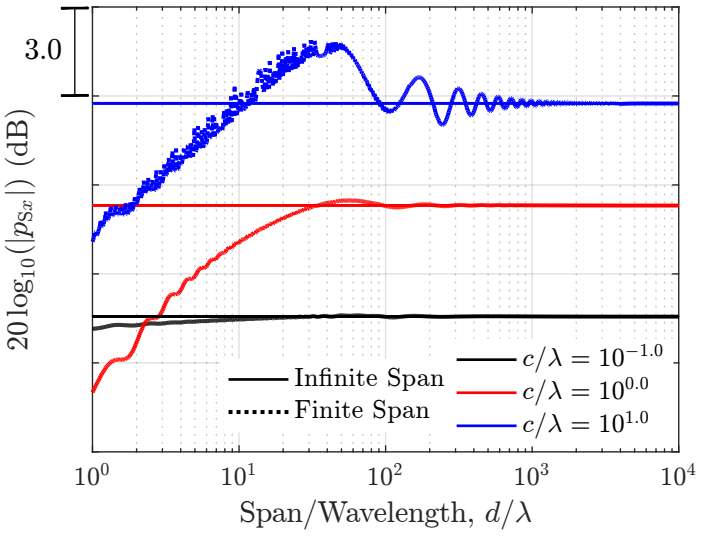

FIGURE 5.24: Comparison of the finite-span and infinite-span solutions at several plate chords.$f = 1000$ Hz, $\phi = 80°$, $\theta = 90°$ and $k_1 = 45$

As the noise from multiple strips is to be summed coherently, the total noise should converge on the infinite span solution as the number of strips is increased. This is demonstrated in Figure 5.25 with example spectra calculated using increasing numbers of strips. This is most evident at the lowest frequencies with the amplitude initially 8 dB below the infinite span solution. At high frequencies, there is not such an obvious change in amplitude but, by the time the number of strips reaches 32, the spectrum shows the same scalloped pattern as the infinite span solution. Additionally, Figure 5.25 demonstrates that, for each total number of strips, the spectrum matches that of a single strip with the same overall span.

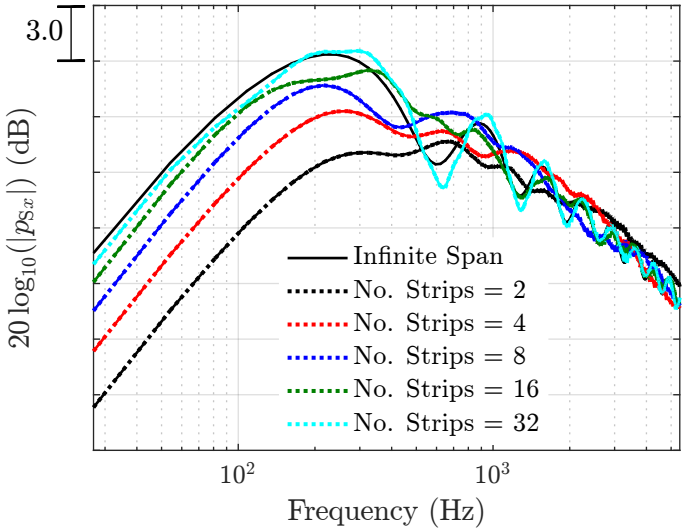

FIGURE 5.25: Convergence of strip theory model on the infinite span solution with increasing number of strips. $c = 0.1$, $d = c/8$, $\theta = 90°$, $\phi = 45°$. Dashed lines are single strips with the same overall span as combined $d = c/8$ strips.

As previously mentioned, the plate used in the JSI noise experiments has an aspect ratio of 1.44. At low frequencies and low jet velocities, therefore, the finite span may have an effect. In Figure 5.26, a comparison of the finite and infinite span models is shown with the far-field measurements of Lawrence at a jet Mach number of 0.3. In general there is little difference between the two models. The largest differences occur at polar angles $\theta = 110°$ and $\theta = 130°$. At these angles, the finite span model appears to more accurately predict some of the subtler features of the measured spectra. For instance, at $\theta = 110°$ (Figure 5.26c), there is a 'trough' in the spectra at approximately 500 Hz, which is not captured by the infinite span model, but is by the finite span model.

The trough in Figure 5.26c occurs at approximately 500 Hz in the experimental data but at approximately 600 Hz in the finite span model. This could be due to neglecting the effect of the span ends on the scattered surface pressure, as strip theory still assumes the span is infinite when calculating the scattered surface pressure on each strip. Roger et al[120] have demonstrated that including the span ends, via application of Schwarzchild's solution to each, can have a significant effect on the surface pressure and far-field directivity. Their results demonstrate that the effect on the scattered surface pressure can extend a wavelength into the plate. At 600 Hz, the span to wavelength ratio is approximately two, so the effect of the span ends could extend over a large portion of the plate.

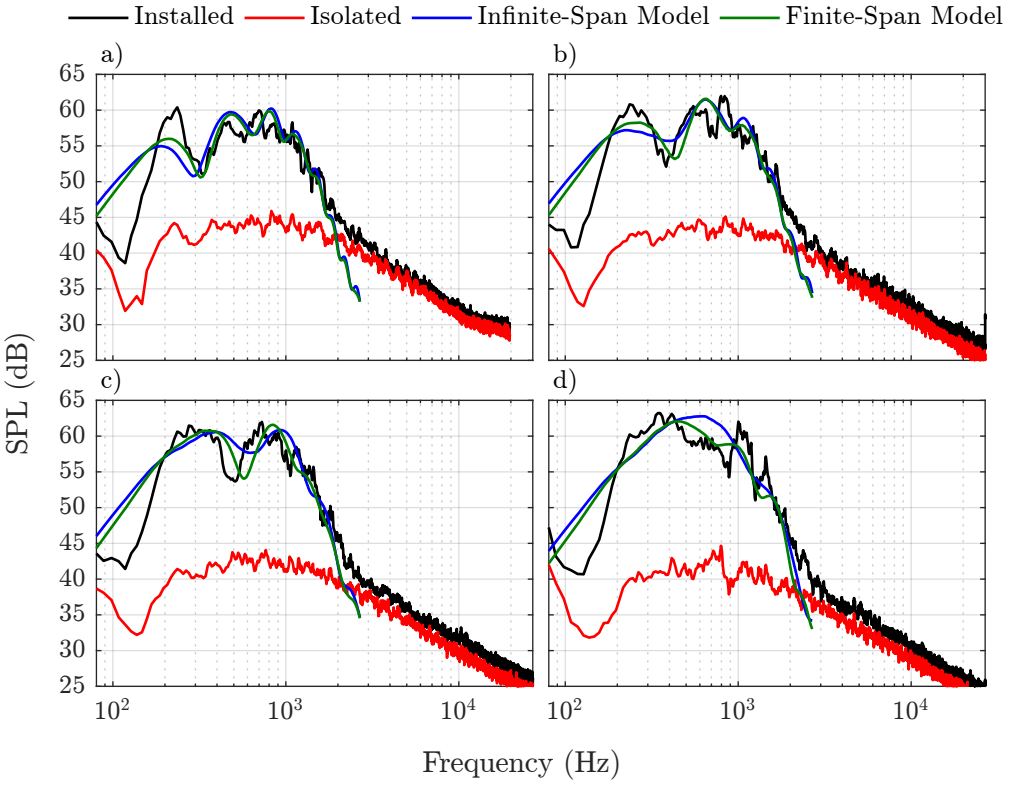

FIGURE 5.26: Comparison of finite and infinite span models with the measurements of Lawrence.[18] a) $\theta = 70°$; b) $\theta = 90°$; c) $\theta = 110°$; d) $\theta = 130°$. $M_\mathrm{j} = 0.3$, $M_\mathrm{f} = 0.0$, $l/D = 3$, $h/D = 1$ and $\phi = 180°$

In Figure 5.26 the difference between the infinite and finite span models was most noticeable at $\theta = 110°$. At this polar angle, Figure 5.27 displays comparisons between the models at different jet velocities. The same 'trough' can been seen in the measured and finite span model spectra at the same frequency for all jet velocities.

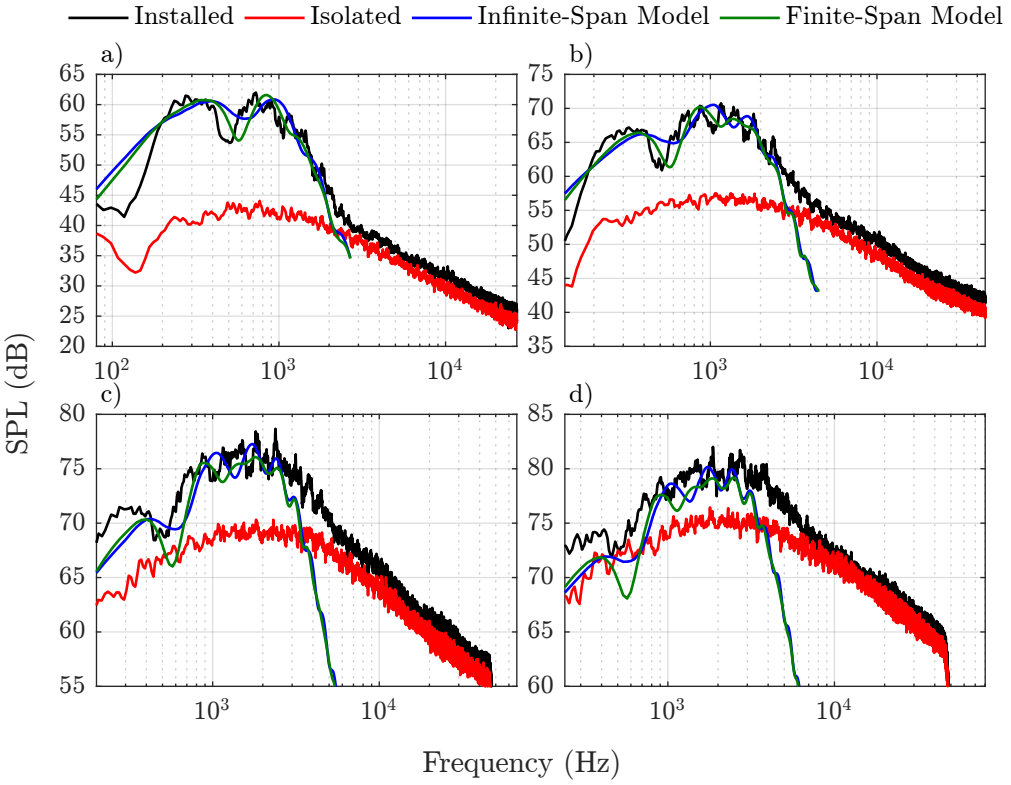

FIGURE 5.27: Comparison of finite and infinite span models with the measurements of Lawrence.[18] a) $M_j = 0.3$; b) $M_j = 0.5$; c) $M_j = 0.75$; d) $M_j = 0.9$. $M_f = 0.0$, $l/D = 3$, $h/D = 1$, $\theta = 110°$ and $\phi = 180°$

In Figure 5.22 the effect of finite span was shown to be greater towards the sideline. It would, therefore, be appropriate to test the finite span implementation of the JSI noise model against measured data at angles other than $\phi = 0°$. This comparison can be made using the $c/D = 7.5$ plate with the 40 mm Doak jet. However, the near-field measurements of this jet cannot be decomposed into modes as only one near-field microphone was used. Therefore, a comparison will be made of the OASPL directivity, and the near-field measurements of Lawrence will be used to includes modes of order greater $m = 0$.

In Figure 5.28 a comparison of the azimuthal OASPL directivities for the $c/D = 7.5$ plate at several jet velocities is presented. There is quite a large variation in the experimental directivities with jet velocity. At $M_j = 0.3$, the OASPLs at $\phi = \pm 60°$ are only 3 dB below the peak, while at $M_j = 0.8$, this increases to 6 dB and the directivity appears more 'peaked'. This change in directivity is captured well by the model, however it is clear that the model requires the hydrodynamic pressure field to be decomposed into at least modes of order $m = 0$ & 1.

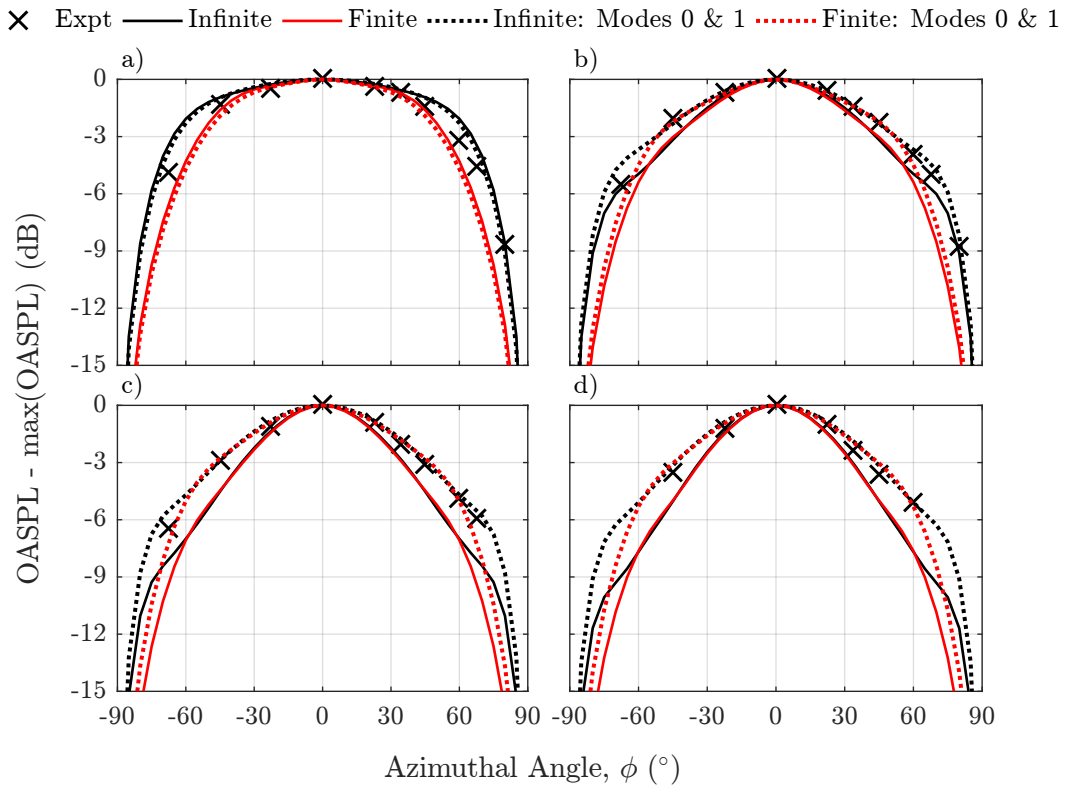

FIGURE 5.28: Azimuthal OASPL directivity of JSI noise. 'Infinite' and 'Finite' span model predictions use near-field pressure measurements of the 40 mm Doak jet and, therefore, only uses mode 0. 'Infinite: Modes 0 & 1' and 'Finite: Modes 0 & 1' span model predictions use near-field pressure measurements of the 38.1 mm Doak jet. $c/D = 2.5$, $\psi = 0°$ and $\theta = 90°$. a) $M_j = 0.3$; b) $M_j = 0.6$; c) $M_j = 0.75$; d) $M_j = 0.8$. $\theta = 90°$.

Comparing the finite and infinite span models, the results are almost identical up to $\phi = \pm 60°$. Beyond this angle, the gradient of the finite model increases and the infinite model initially decreases. When including mode $m = 1$, the finite span model still separates from the infinite span model beyond $\pm 60°$, but now the directivity of both models match that of the experiment up to approximately $\pm 60°$. Overall, the infinite span model shows the best comparison with the measured data, with the finite span model under-predicting.

It is possible that the under-prediction at azimuthal angles close to the plane of the plate is again due to neglecting the effect of the span ends on the surface pressure. To determine whether this is the case, the method of Roger et al[120] could be implemented within the current strip theory model. A numerical experiment could also be performed using BEM to determine the effect of the span ends on the surface pressure, and make a comparison with the analytical model.

For the shorter plate chords, the increased aspect ratio of the surface reduces the effect of the finite span. Figure 5.29 demonstrates that for the $c/D = 2.5$ plate the OASPL

directivities of finite and infinite span models are almost identical even for the lowest jet velocity.

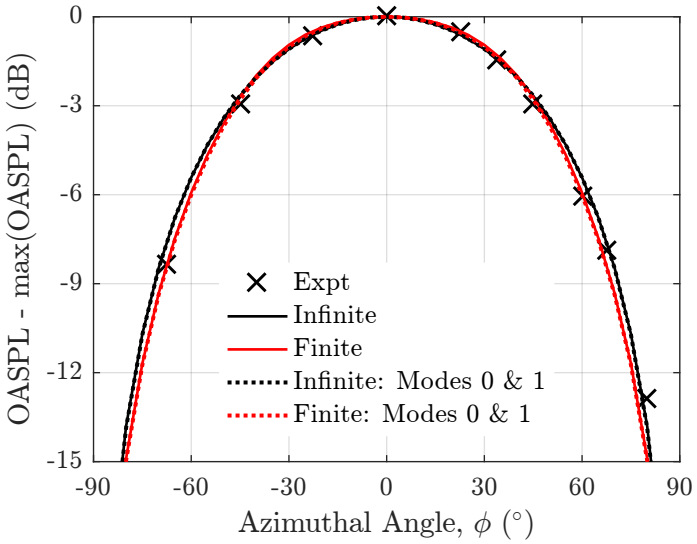

FIGURE 5.29: Azimuthal OASPL directivity of JSI noise. $c/D = 2.5$, $\psi = 0°$, $M_j = 0.3$ and $\theta = 90°$

Overall, it does not seem necessary to include the effect of finite span in JSI noise models for uniform scattering surfaces: At a polar observer angle of $\theta = 0°$ the effect of including finite span in the predictions was to include some subtler features of the spectra, but at Strouhal numbers and aspect ratios too low to be important for real aeroplanes. At angles close to the plane of the plate, where the finite span model showed the greatest difference to the infinite span model, it was the infinite span model whose directivity compared best with the experimental measurements. It will be demonstrated in the next section, however, that the use of strip theory, is still useful for estimating JSI noise for more representative wing geometries.

5.6 Swept Wings

Turbofan powered airliners, for which JSI noise is a concern, cruise in the transonic regime, where shock waves form along the wings. To reduce the drag created by these shock waves, the wings are swept backwards. This means that the wing trailing edge is not actually perpendicular to the jet axis, as considered thus far. Experiments[58,59] have shown that sweep alters the directivity of JSI noise, by shifting the peak in the azimuth 'outboard' for rearward sweep and reducing the JSI noise at 'inboard' azimuthal angles. This asymmetry in directivity comes about from the asymmetry in the axial wavenumber spectrum of the jet hydrodynamic pressure field, which is propagating downstream from the jet nozzle.[60]

Trailing edge sweep was included within the JSI noise model of Lyu & Dowling,[71,111,115] using a transform developed by Roger et al.[72] For the unswept infinite-span trailing edge, the spanwise wavenumber that propagated to the far-field was equivalent to a plane wave propagating towards the azimuthal angle of the observer. For the swept case, the spanwise wavenumber that propagates to the far-field is now given by

$$k_2 = \tilde{k}x_2/\tilde{r}_x - k_1\tan(\psi) - (k/\beta^2)\tan(\psi)(M - x_1/\beta\tilde{r}_x). \tag{5.16}$$

Thus, the spanwise wavenumber that propagates to the far-field is now also a function of axial wavenumber and wing sweep. This can also be demonstrated by using a rotation matrix to transform the problem (see Appendix C), such that $\tilde{y}_2$ is parallel to the trailing edge. The wavenumbers perpendicular and parallel to the trailing edge in the new coordinate system are

$$\tilde{k}_1 = k_1\cos(\psi) - k_2\sin(\psi) \tag{5.17}$$

and

$$\tilde{k}_2 = k_1\sin(\psi) + k_2\cos(\psi). \tag{5.18}$$

with the solution set in the new coordinate system identical to the unswept case.

To validate their swept trailing edge model, Lyu & Dowling use the experimental results of Piantanida et al.[58,59] The model shows very good agreement with the measured data, correctly predicting the peak azimuthal angle and the azimuthal directivity, despite the use of near-field spectra and axial wavenumbers measured with a different jet.

To verify the implementation of the swept wing model and to discuss key features of the JSI noise due to swept wings, a comparison to Piantanida's measurements has been repeated in Figure 5.30 and Figure 5.31. The methods for scaling the jet hydrodynamic pressure spectra and wavenumbers from Chapter 4 have been used to scale the Doak laboratory spectra to the diameter and velocity used by Piantanida. As with the comparison made by Lyu & Dowling, it was necessary to scale the far-field amplitude to match the unswept plate measurements at $\phi = 0°$.

Figure 5.30 displays a comparison between the experimental data of Piantanida and the swept wing model of Lyu & Dowling. There is good agreement between the peak angle and directivity across the four sweep angles. However, at a sweep angle of $\psi = 30°$, the peak amplitude is over predicted. Figure 5.30 demonstrates that the incorporation of higher order modes becomes increasingly important as sweep angle is increased.

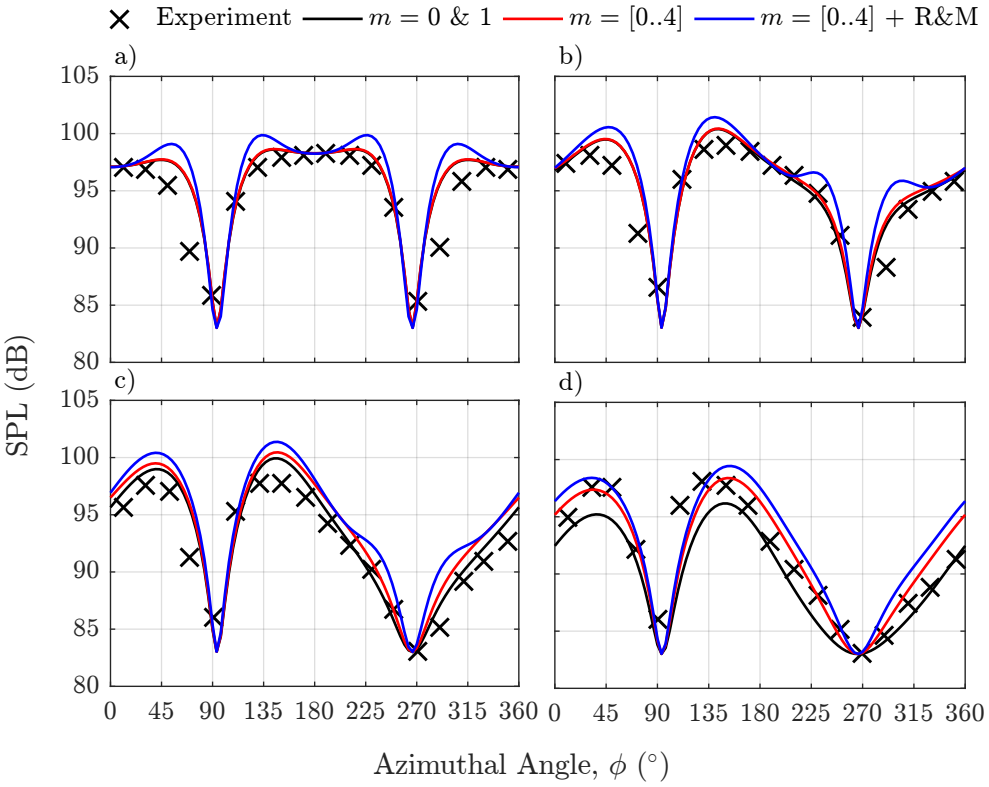

FIGURE 5.30: Comparison of the swept wing model of Lyu with the experimental data of Piantanida. $M_j = 0.4$, $l/D = 4$, $r/D = 1$, $\theta = 90°$ and St $= 0.2$. a) $\psi = 0°$; b) $\psi = 15°$; c) $\psi = 30°$; d) $\psi = 45°$.

At a Strouhal number of 0.2, the mean chords of the plates are less than the acoustic wavelength. Applying Roger & Moreau's backscattering theory, therefore should significantly affect the directivity. This is evidenced in Figure 5.30, however, it served to worsen the comparison with the experimental data, introducing double peaks, and further over predicting the peak amplitude.

Another comparison between the model and Piantanida's measurements is displayed in Figure 5.31 at the larger radial plate distance of $h/D = 1.5$. The same conclusions can be drawn as with the previous figure, however the over prediction of the peak amplitudes at sweep angles of $\psi = 15°$ and $\psi = 30°$ are now much more pronounced. There is also a discrepancy between the peak angles at $\psi = 45°$. Reasons for these discrepancies could include: a) the scaling method of Chapter 4 not accurately enough calculating the spectra and axial wavenumber of the jet used by Piantanida; b) modelling the plates as parallelograms, instead of the trapeziums used by Piantanida (only the trailing edge was swept), this would not however account for the double peak with the addition of back scattering to the model with the unswept trailing edge; and/or, c) the microphones being too close for the far-field assumption in the model to be valid (the microphones are on an array spaced $14.3D$ from the jet axis)

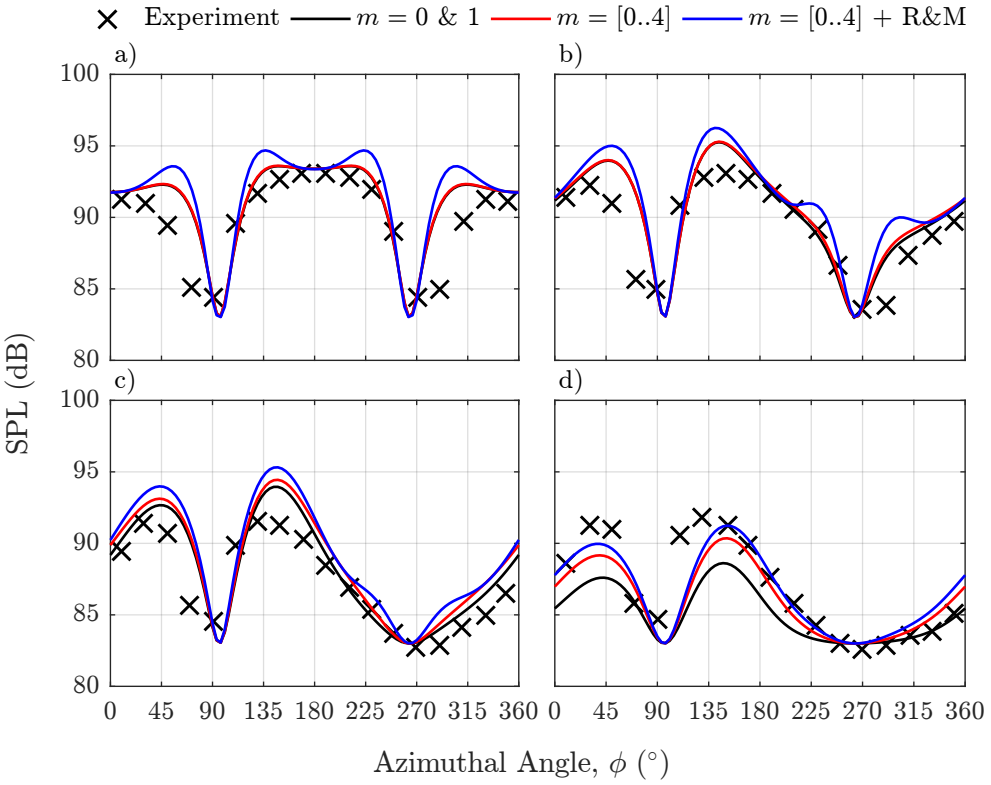

FIGURE 5.31: Comparison of the swept wing model of Lyu with the experimental data of Piantanida. $M_j = 0.4$, $l/D = 4$, $r/D = 1.5$, $\theta = 90°$ and St $= 0.2$. a) $\psi = 0°$; b) $\psi = 15°$; c) $\psi = 30°$; d) $\psi = 45°$;

In an attempt to overcome these issues, new installed jet noise measurements have been performed with a swept plate in the Doak Laboratory. A parallelogrammatic plate was used with chord $c/D = 2.5$ and sweep angle $\psi = 20°$. These values were deemed to be representative of commercial airliners. Furthermore, they allow comparison with the unswept $c/D = 2.5$ plate. Noise measurements were taken in the far-field on an azimuthal array, positioned at $\theta = 90°$, both statically and in flight. The near-field measurements of this jet (see Chapter 4) were taken with a single microphone, preventing an azimuthal modal decomposition which the comparison with Piantanida's measurements has shown to be necessary; and the model was shown in the previous section to overestimate the amplitude of the JSI noise at such a short chord.

Figure 5.32 displays a comparison of the JSI OASPL directivities measured in the experiment and calculated with the model. The simplified model uses the measured near-field spectra for the same jet (see Chapter 4), while the full model uses the near-field spectra measured by Lawrence. For the unswept plate, the full model appears to capture the measured directivity both statically and in flight. With the swept plate the simplified model captures the increase in the broadness of the peak as the flight-stream velocity increases. However, it appears that more modes are required to capture the correct directivity at angles below the peak. In-flight near-field pressure measurements with

multiple microphones would certainly improve this comparison. It would also be useful to ascertain whether there are changes to the azimuthal modal decomposition in flight.

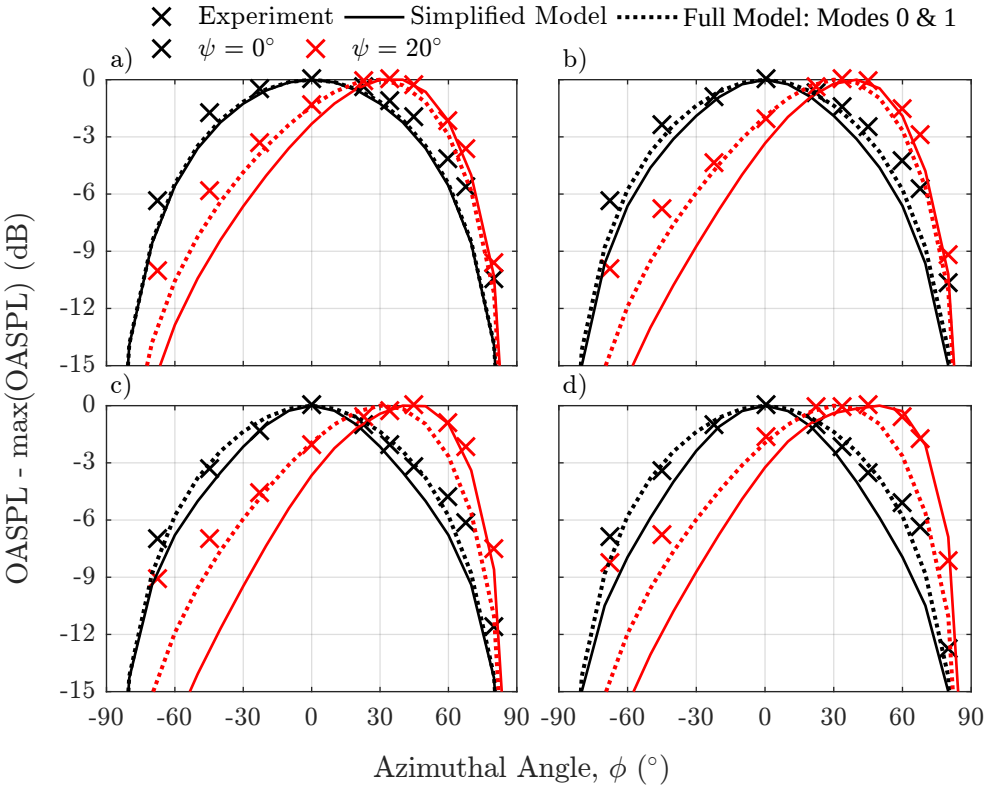

FIGURE 5.32: Comparison of swept wing model of Lyu & Dowling with installed jet noise measurements in the Doak Laboratory. $l/D = 3$, $h/D = 1$ and $\theta = 90°$. a) $M_j = 0.6$ $M_f = 0$; b) $M_j = 0.75$ $M_f = 0$; c) $M_j = 0.75$ $M_f = 0.1$; and, d) $M_j = 0.75$ $M_f = 0.2$.

The difference in measured JSI-noise OASPL between the swept and un-swept plate is displayed in Figure 5.33, without the flight stream, and in Figure 5.34, where flight-stream Mach number has been varied. These plots show that the difference between the swept and unswept wing is a function of jet and flight velocities, as well as sweep angle. The maximum (positive) difference occurs at the highest jet and flight Mach numbers. There are also angles of minimum and maximum difference, above/below which the difference heads back towards zero; because at observer angles in the plane of the plate theory says that the edge-scattered noise is zero, so the JSI noise of both plates goes to zero.

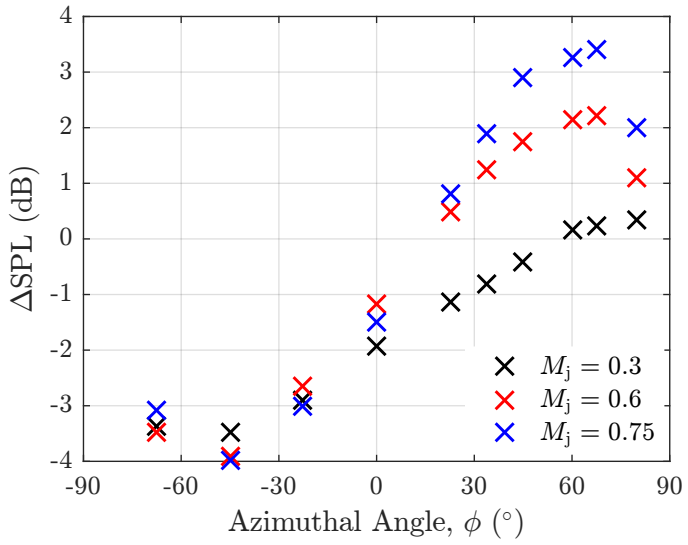

FIGURE 5.33: Difference between measured JSI noise OASPL with the unswept and swept wing. $M_f = 0$, $l/D = 3$, $h/D = 1$ and $\phi = 0°$

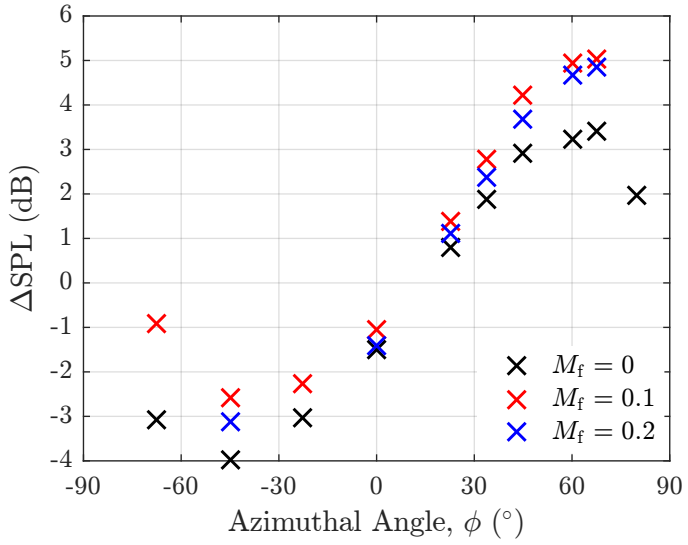

FIGURE 5.34: Difference between measured JSI noise OASPL with the unswept and swept wing. $M_f = 0$, $l/D = 3$, $h/D = 1$ and $\phi = 0°$

The overall change in JSI noise on an aeroplane due to sweep is, as this section has shown, going to be highly dependent on not only the geometry of the wing but jet and flight velocity as well. What should not be forgotten when looking at the graphs here is that effectively only one jet and 'wing' is shown. If one were to add a second jet and symmetrical plate, then everything else being equal: the difference at $\theta = 90°$ and $\phi = 0°$ in Figure 5.33 and Figure 5.34 would be preserved; ΔSPL about $\phi = 0°$ would be symmetric: and, the peak difference in the $\theta = 90°$ arc would be reduced, as the unswept SPL would increase by 3 dB but the swept SPL by less. For the results in Figure 5.33, the swept OASPL would be less than the unswept OASPL at all azimuthal

angles for $M_j = 0.3$, and at 60° and $M_j = 0.75$ the swept OASPL would only be slightly higher than the unswept OASPL.

5.6.1 Cranked Wings

While jet airliners have swept wings to reduce drag at their transonic cruising speeds, the trailing edges of the wings are generally not fully swept. Instead, the trailing edges are often cranked, with an unswept/low-sweep inboard section and a swept outboard section (see for example Figure 5.35). Reasons for the change in sweep angle can include improved aerodynamic and structural performance, increased performance of trailing-edge high-lift devices, and to allow for the suitable positioning of the main landing gear.[121–125]

FIGURE 5.35: View of the underside of an Airbus A220, displaying the unswept and swept portions of the wing trailing edge

As discussed in the previous section, trailing-edge sweep has a large effect on the azimuthal directivity of JSI noise. It is, therefore, to be expected that the crank will further change the directivity of the JSI noise. All else being equal, the unswept section would likely dominate at 'inboard' azimuthal angles (i.e. directly below the aircraft) and the swept section would dominate at outboard azimuthal angles (i.e. towards the sideline). It may, therefore, be necessary to model such a planform geometry.

To demonstrate the potential effect of a crank on JSI noise, the noise produced by a cranked wing has been modelled using strip theory, as discussed in Section 5.5. The wing planform is that of a narrow-body airliner,[18] with the exception that the chord at the position of the crank has been kept constant across the entire wing in the model (see Figure 5.39). The wing planform has an unswept inboard section and an outboard section swept at $\psi = 17.6°$, which is also approximately 63% longer than the inboard section. Using strip theory, the wing is split into two 'strips', one strip modelling the unswept section of the wing and the other modelling the swept section. For comparison, fully unswept and swept ($\psi = 0°$ and $\psi = 17.6°$ respectively) planforms with the same

chord and overall span have also been modelled. In all three cases, the spanwise position of the jet axis is the same as the crank.

The comparison has been conducted using a jet Mach number of 0.6, which is between approach and cut-back conditions,[18] and a flight Mach number of 0.2, the highest at which the model was found to work earlier in this chapter. The inputs, axial wavenumber and near-field amplitude, come from measurements taken in the Doak laboratory using a microphone within the flight-stream flow, as described in Chapter 3. Therefore, the entire spectrum is treated as mode of order 0.

Figure 5.36 displays a comparison of azimuthal directivity between the different planform geometries at a polar angle of $\theta = 90°$ and over four Strouhal numbers, covering the peak of the JSI noise spectrum. The figure shows that, for the most part, the amplitude of the cranked wing falls between that of the fully unswept and swept wings, though it is clear that the unswept and swept strips strongly influence different angle ranges. These directivity calculations were created using only mode 0, while it was shown earlier in this chapter that higher order modes are required to calculate the directivity of a swept wing. If higher modes were to be included then the amplitude due to the swept portion of the wing would likely increase around $\phi = 0°$ and $\phi = 180°$, reducing the influence of the unswept portion. It is therefore important for a calculation such as this that the modal content of the jet near-field pressure in flight is measured.

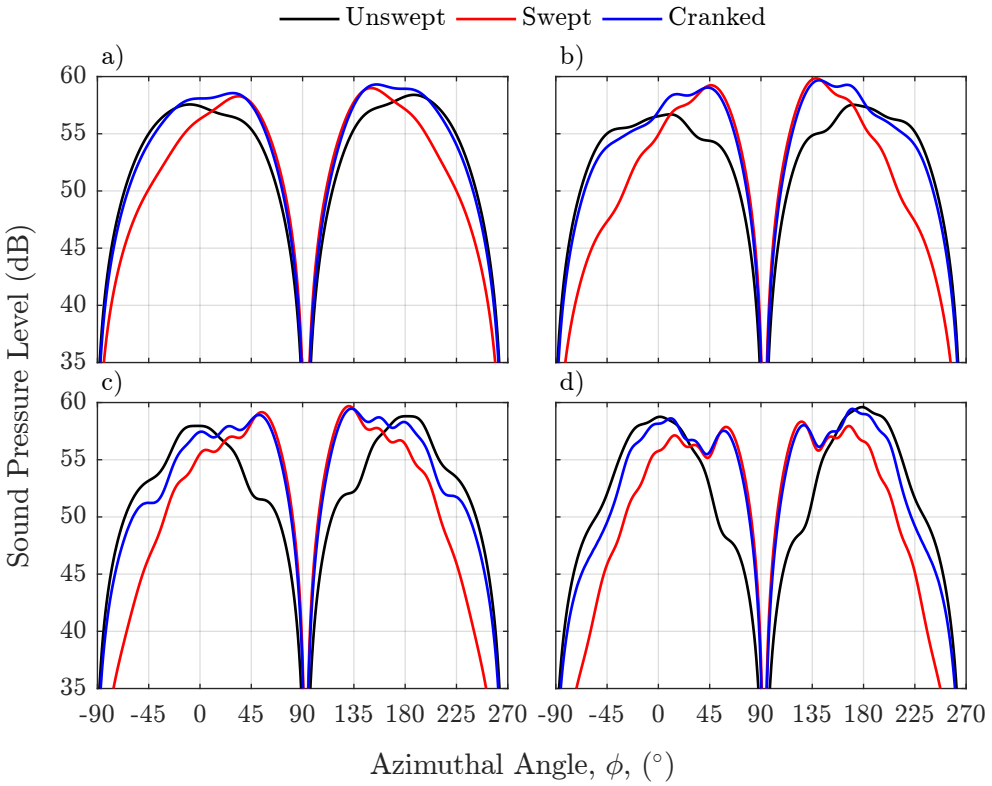

FIGURE 5.36: Comparison of azimuthal directivity for different planform geometries. $M_\mathrm{j} = 0.6$, $M_\mathrm{f} = 0.2$ & $\theta = 90°$. a) St $= fD_\mathrm{j}/(U_\mathrm{j} - U_\mathrm{f}) = 0.4$; b) St $= 0.6$; c) St $= 0.8$; and, d) St $= 1$.

The effect of the different planforms on the combined azimuthal and polar directivity is displayed in Figure 5.37. Comparing (a) and (b) the effect of sweep on the directivity is clear, pushing the peak rearward, towards the sideline, and reducing the amplitude. The directivity of the cranked wing combines the directivity of the fully unswept and swept planforms, as shown for the azimuthal directivity alone in Figure 5.36. This comparison has been made using a single wing, as one might measure in a laboratory, in reality an airliner has two symmetric wings. This means that the regions $\phi > 225°$ and $\phi < -45°$, in Figure 5.36, currently dominated by the unswept portion of the cranked wing would instead be dominated by the swept portion of the opposing wing. This means that the unswept portion of the wing would only influence the amplitude/directivity directly below the wing. However, Figure 5.37 shows that the noise scattered by the unswept portion would also be the main influence at far forward angles, such as $\theta > 130°$. This, therefore, also suggests that it may be necessary to consider the influence of the full wing geometry on JSI noise.

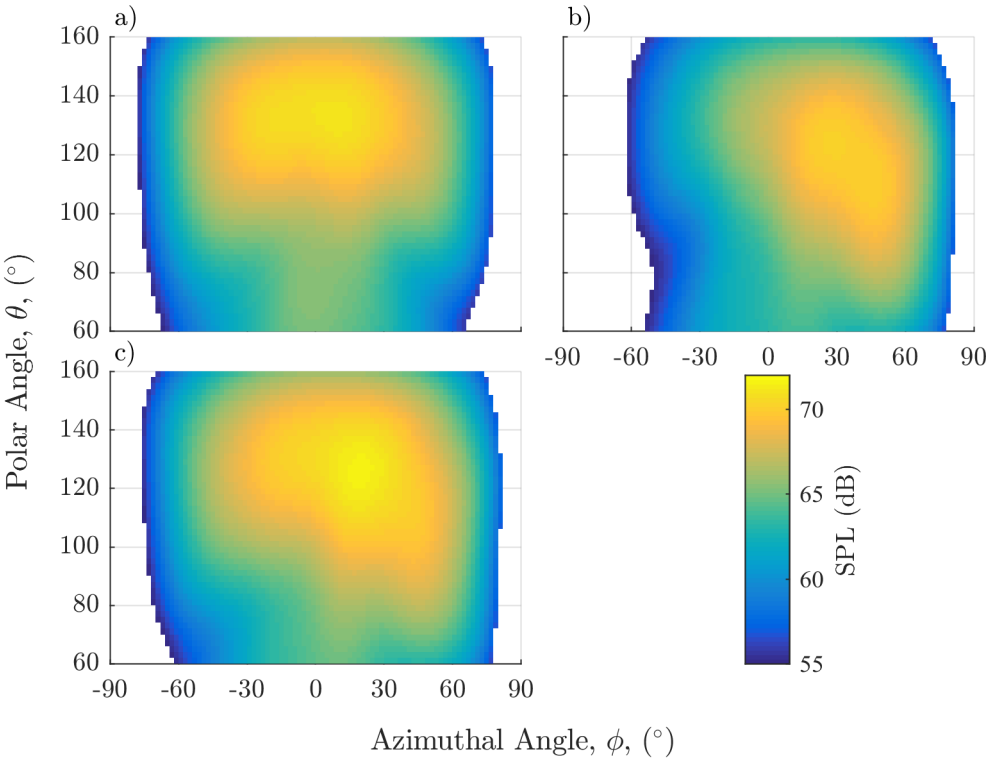

FIGURE 5.37: Comparison of polar and azimuthal directivity for different planform geometries. $M_\mathrm{j} = 0.6$, $M_\mathrm{f} = 0.2$ and $\mathrm{St} = fD_\mathrm{j}/(U_\mathrm{j} - U_\mathrm{f}) = 0.6$. a) Unswept; b) Swept; and, c) Cranked.

In both Figure 5.36 and Figure 5.37 the azimuthal directivity of the unswept plate is not symmetric about $\phi = 0°/180°$, as one might expect. This is due to the asymmetric placement of the wing relative to the jet axis, with the spanwise midpoint of the wing shifted in the positive y_2 ($\phi = 90°$) direction, and comes from the inclusion of the $\mathrm{e}^{-\mathrm{i}C_2 y_{2c}}$ term in Equation 5.10. The term $\mathrm{e}^{-\mathrm{i}C_2 y_{2c}}$ includes $\mathrm{e}^{-\mathrm{i}k_2 y_{2c}}$ that, if all the other terms

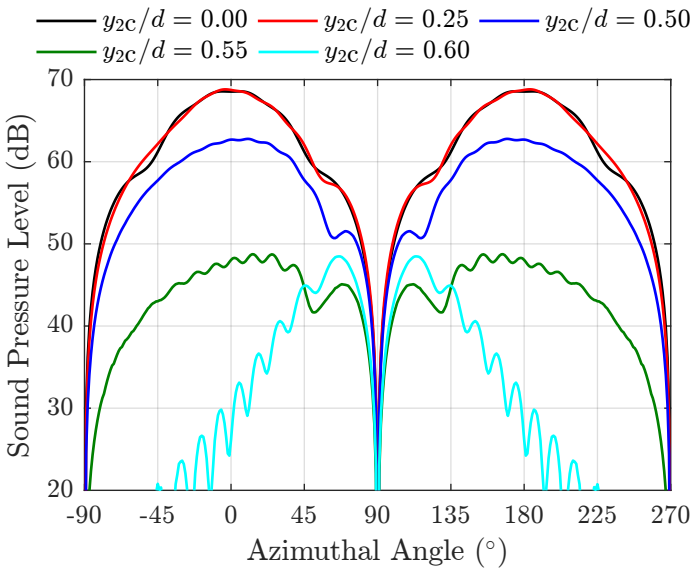

FIGURE 5.38: Example of the effect of plate midpoint location on azimuthal directivity. $d/c = 4.76$, $\psi = 0°$, $M_j = 0.6$, $M_f = 0.2$ and $\mathrm{St} = fD_j/(U_j - U_f) = 0.6$

bar $p_I'(\omega, m, k_2)$ were removed, would give an inverse Fourier transform that returned the incident pressure on the midpoint of the plate. Combined with the remaining terms in Equation 5.10, the effect of a shift in mid-point on the amplitude of the far-field scattered pressure is lessened relative to the effect on the mid-point pressure; but the peak amplitude shifts in the azimuthal direction associated with the shift in mid-point, as displayed in Figure 5.38. This effect is less noticeable for the swept wing as the directivity is already asymmetrical, but explains why the directivity of the cranked wing follows that of the swept wing (i.e. $45° < \phi < 135°$) more closely than that of the unswept wing (i.e. $-90° < \phi < 0°$ & $180° < \phi < 270°$).

One issue with the use of strip theory to model a cranked wing is that the trailing-edge scattered pressure from each strip is calculated independently. This leads to a sudden change in the scattered surface pressure solution either side of the crank (see, for example, Figure 5.39). Instead the solution for the surface pressure would have to match at the crank, modifying the surface pressure on either side of the crank from the infinite span solution. When propagated to the far-field this would modify the directivity pattern. If Amiet's condition for assuming infinite span were met on each strip, then the effect of the crank may be insignificant. However, if the conditions were not met, i.e. the aspect ratio of a strip was small, then the crank (and the opposing end of the strip) could have a significant effect on the directivity of that strip. Additionally, the crank tends to be close to the engines on twin engine airliners, meaning that the incident pressure on the wing due to the jet will be at its maximum very close to the crank, potentially increasing the effect of the crank of the scattered acoustic field.

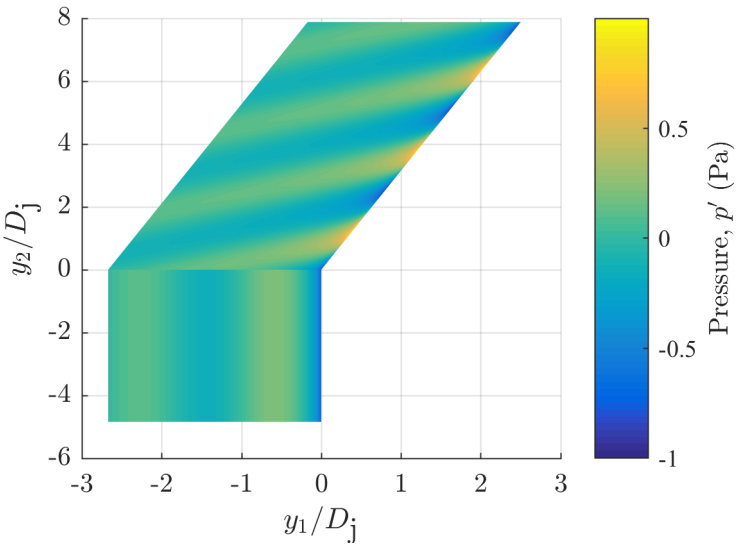

FIGURE 5.39: Scattered surface pressure on the cranked wing, as calculated using Equation 2.118 applied to two strips. St = 0.8, $k_2 = 0$, $U_s = 292$ m/s and $U_f = 102$ m/s.

5.7 Summary

The aim of this chapter has been to validate a jet-surface interaction noise model against laboratory measurements of installed jet noise at ambient flow conditions and with scattering-surface geometries closer to what is seen on current airliners. This has meant comparing to measurements with a co-axial 'flight stream' to simulate the effect of flight on the jet, and with plates with chord to nozzle diameter ratios and sweep angles in the range seen on current commercial airliners.

Comparing the model with the laboratory measurements utilising the flight stream, it was demonstrated that the model was able to accurately capture the amplitude and spectral shape of the jet-surface interaction noise up to a flight stream Mach number of 0.2. Beyond a Mach number of 0.2, at a Mach number of 0.3, the model was still capturing the peak frequency and spectral shape of the installed jet noise, but was however under-predicting the measured amplitude. Several hypothesis have been proposed for the cause of this under-prediction, but further work is required to determine the exact cause.

Next, the model has been compared to installed jet noise measurements taken with plates of differing chord length. The measurements show that, at low jet velocities, as the chord decreases the OASPL polar directivity transitions from a cardioid to a dipole shape, as would be expected from theory. The predicted spectra from the model compare very well to the measured data at the largest plate chord. However, the model tends to increasingly over-predict the measured spectra as chord decreases and jet velocity

increases. This is especially apparent in the rear polar arc. Roger & Moreau's back-scattering theory was added to the model to try to improve the prediction with short chords. While this addition did improve the spectral shape in the rear arc, it had no effect on the overall amplitude of the predicted spectra, which continued to over-predicted the measured level.

Finally, the model was extended with strip theory to model scattering surfaces with finite span and cranked wings. The strip theory model was found to improve the predicted spectral shape at low frequencies with a large plate with low aspect ratio. However, at azimuthal angles close to the plane of the plate the strip-theory model was found to under-predict, and the infinite span model gave the best comparison to the measured data. Using the strip theory model to calculate the noise from a cranked wing, showed the unswept section to dominate at angles close to directly above/below the plate, while the swept section dominated at angles closer to the sideline.

Chapter 6

Large Model-Scale Data

In Chapter 4, methods were discussed for scaling near-field hydrodynamic pressure spectra and wavenumbers for axisymmetric jets. Subsequently, in Chapter 5, the jet-surface interaction (JSI) model of Lyu & Dowling was validated using a co-flow to simulate the effect of flight. Methods were then discussed for using this jet-surface interaction noise model for more realistic finite chord, finite span and swept trailing edge geometries. In this chapter, the results of these two chapters are brought together to produce a semi-empirical jet-surface interaction noise prediction tool. The prediction tool is compared to installed jet noise measurements taken in QinetiQ's Noise Test Facility (NTF), to assess whether it can robustly predict large-scale realistic model jet-surface interaction noise spectra.

6.1 Jet-Surface Interaction Noise Prediction Tool

The aim of this prediction tool is to be able to produce fast, low-fidelity, far-field JSI noise spectra for realistic configurations of wings and jet nozzles. The tool should incorporate the effects of nozzle exit area, jet velocity, flight velocity, h/D, l/D, chord, sweep angle and crank location. Additionally, the prediction tool must work over a range of polar and azimuthal observer angles suitable for calculating aeroplane certification noise levels and noise contours.

The model relies on LES or experimental near-field pressure data as the input. In this chapter the 38.1 mm nozzle near-field ring-array measurements of Lawrence[18] at a jet Mach number of 0.3 are used. These measurements have been chosen because the ring of microphones allows the pressure to be decomposed into azimuthal modes and because they provide sufficient resolution along the jet axis. The pressure measurements have been decomposed into modes 0 to 4, which are then converted to PSD using Welch's method with a bandwidth of 10 Hz. Despite there being slight differences in the near-field spectra at different jet Mach numbers (see Chapter 4), the Mach 0.3 spectra is

to be used exclusively because the hydrodynamic field dominates the near-field spectra over the widest Strouhal number range.

In order to scale the hydrodynamic pressure measurements for a new jet, first an effective jet diameter is calculated based on the primary and secondary (if present) nozzle areas,

$$D_{\mathrm{e}} = \sqrt{4(A_{\mathrm{s}} + A_{\mathrm{p}})/\pi}. \tag{6.1}$$

This effective diameter is then used to scale the axial location of the trailing edge. Ideally one would scale the axial location by the potential core length of the isolated jet, to better capture the turbulence properties within the shear layer. However, the potential core length is unlikely to be known for a new jet without the help of hot-wire measurements or similar. For in-flight predictions, the stretching of the potential core in flight must be taken into account. The axial position of the trailing edge is, therefore, further scaled to calculate an equivalent static l/D. From the measurements performed by Proença[98] of the Doak 40 mm jet, the following empirical formula is used,

$$\frac{l_{\mathrm{e}}}{D_{\mathrm{e}}} = \frac{4.6}{16U_{\mathrm{f}}/340 + 4.6}\frac{l}{D_{\mathrm{e}}}. \tag{6.2}$$

The radial position of the trailing edge is also adjusted for cases where the wing is sufficiently close to the jet axis such that it distorts the flow field. This is based on the installed jet noise measurements of Lawrence,[18] which placed the trailing edge of a plate both outside and within the flow-field of the isolated jet (see Figure 6.1). The far-field measurements show that, for a flat plate, the increase in far-field OASPL with decreasing h reduces as the trailing edge enters the flow field of the isolated jet (see Figure 6.2). So, if

$$\frac{h}{D_{\mathrm{e}}} < \frac{l_{\mathrm{e}}}{D_{\mathrm{e}}}\tan(0.13) + 0.5 \tag{6.3}$$

then

$$\frac{h}{D_{\mathrm{e}}} = \frac{l_{\mathrm{e}}}{D_{\mathrm{e}}}\tan(0.13) + 0.5. \tag{6.4}$$

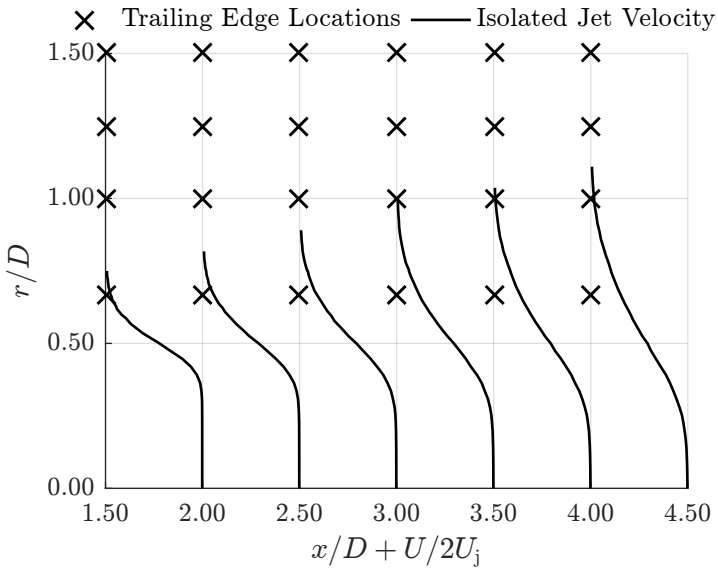

FIGURE 6.1: Trailing edge locations used in the JSI noise parametric study by Lawrence[18] in comparison to the isolated jet axial flow field calculated using LES by Wang.[106] The velocity profiles end at 1% of the jet velocity.

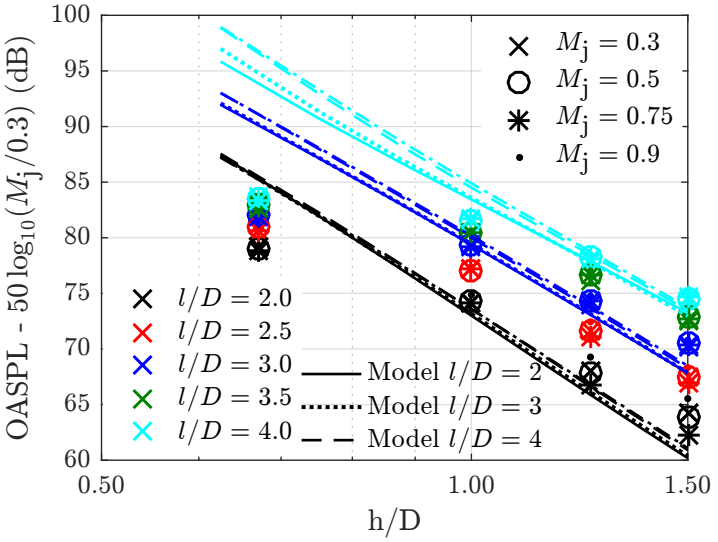

FIGURE 6.2: Velocity scaling of far-field JSI noise

The amplitude and radial locations of the measured near-field spectra are then linearly interpolated to the value of l_e/D_e, to set the spectral shape and to define r/D_e at the axial location of the wing. The spectrum is then scaled using

$$\text{PSD} = \text{PSD} + 10\log_{10}(D_e/D_{ref}) + 30\log_{10}([U_s - U_f]/U_{ref}) \tag{6.5}$$

to arrive at the amplitude of the incident hydrodynamic pressure spectra at the trailing edge axial location.

Next, the axial wavenumber of the hydrodynamic field is required both to compute the correct rate of propagation with radial location, r, and the correct JSI noise directivity. To calculate the axial wavenumber a straight line has been fitted through the peak axial wavenumbers for azimuthal modes of order 0 and 1 from the Doak Laboratory LES (see Figure 4.16), giving

$$k_1 = \frac{2\pi}{D_\mathrm{e}}\left(C_1 + C_2\frac{f_\mathrm{ref}D_\mathrm{ref}}{U_\mathrm{ref}}\right), \tag{6.6}$$

Where $C_1 = 0.1$ and $C_2 = 1.4$. The LES has been used, rather than calculating the axial wavenumber from the measured spectra, as both methods agree well initially, but the peak of the hydrodynamic field was apparent above the acoustic field over a greater Strouhal number range from the LES. The equivalent frequency at the desired jet nozzle and flow conditions is given by

$$f = \frac{f_\mathrm{ref}D_\mathrm{ref}}{U_\mathrm{ref}}\frac{U_\mathrm{s}}{D_\mathrm{e}}. \tag{6.7}$$

The next step is to calculate the transfer function between the near-field and the scattered far-field pressures using Amiet's theory. The UK TSB-funded SYMPHONY project tested a realistic airliner wing planform geometry with a cranked trailing edge, which can be approximated by applying Amiet's theory to two trapezoidal strips (Figure 6.3). However, at low frequencies leading-edge back scattering is likely to have an effect. Therefore, Roger & Moreau's back-scattering theory is then applied to each strip. To do this one must assume the leading and trailing edges of each strip are parallel. The chord, therefore, has been set to that at the crank directly above the jet axis (see Figure 6.3).

Both the observer and wing locations are defined in the reference frame of the aeroplane, while the model uses a reference frame based on the wing. Therefore, the azimuthal location of the observer, the radial wing locations and the spanwise wing location are all adjusted to account for the dihedral of the wing.

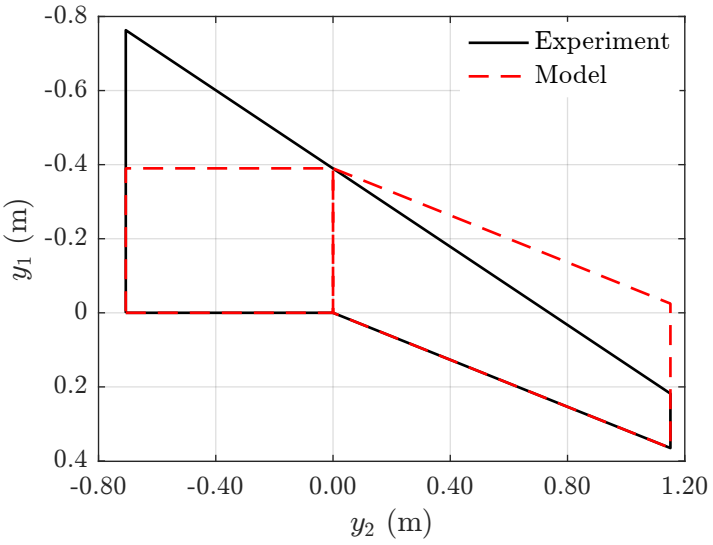

FIGURE 6.3: SYMPHONY wing planform

6.1.1 Model Sensitivity

The axial wavenumber in Equation 6.6 affects both the amplitude of the incident pressure on the trailing edge, and hence the amplitude of the JSI noise, and the directivity of the JSI noise. It is, therefore, important to understand the sensitivity of the calculated JSI noise to the empirical coefficients in Equation 6.6.

The propagation of the hydrodynamic pressure onto the plate is calculated using modified Bessel functions of the second kind, given the outward propagating waves and axial wavenumber greater than the acoustic wavenumber. Increasing the coefficients in Equation 6.6 increases the rate of decay of the hydrodynamic pressure field with r. For radial positions greater than the measurement location, the calculated pressure will therefore decrease, while at radial positions small than the measurement location the calculated amplitude will increase. The opposite would occur if the coefficients in Equation 6.6 were to be reduced.

For a plate location, h, greater than the radial measurement position, r, increasing/decreasing the coefficients in Equation 6.6 will decrease/increase the peak amplitude of the pressure incident on the trailing edge, and vice-versa for $h < r$. JSI noise, however, is also affected by the spanwise wavenumber distribution on the trailing edge, which is also affected by the axial wavenumber. For $h > r$ JSI noise will decrease with increasing C_1 and C_2. But for $h < r$ the amplitude of some frequencies will increase while the amplitude of JSI noise for other frequencies decreases.

Figure 6.4 displays how the OASPL of the JSI noise calculated in the manner described above is affected by variations in C_1 and C_2. The ranges of the coefficients cover those from measurements in Chapter 4 and the condition is one that will be used later in

this chapter. As expected the amplitude of the JSI noise increasingly diverges as h increases, and converges at an h lower than the measurement location of $r/D \approx 1$, with an increase in C_1 or C_2 decreasing JSI noise. The flattening of the OASPL at $h/D < 0.75$ is due to the simple way in which the JSI noise is modelled for trailing edge positions within the flow field of the equivalent isolated jet, as described above. The majority of wing positions used in this chapter are about or below the measurement location (for Figure 6.4 the measurement location is $r/D \approx 1$). The exception is when variations in h/D are specifically being considered, where values of h/D up to an equivalent of $h/D_\mathrm{j} = 1.4$ in Figure 6.4 are considered.

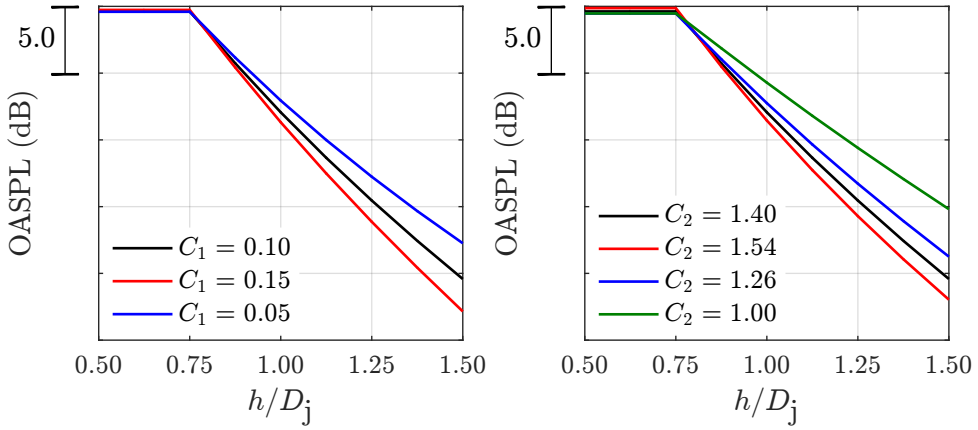

FIGURE 6.4: Effect of variation in axial wavenumber coefficients, C_1 and C_2, on reduction in OASPL with radial trailing-edge location h. $U_\mathrm{j} = 245$ m/s, $U_\mathrm{f} = 0$ m/s and $l/D = 1.94$

The effect of variations in C_1 and C_2 on the model JSI noise spectra is demonstrated in Figure 6.5 and Figure 6.6. At this position, the trailing edge position h is lower than the measurement location r, hence the amplitude increases at some frequencies and decreases at others as described previously. C_1 and C_2 can be seen to affect different regions of the spectra. C_1 affects low frequencies, where $\mathrm{St}C_2$ is not large relative to C_1, while C_2 has a greater effect at high frequencies, where $\mathrm{St}C_2$ is large relative to C_1.

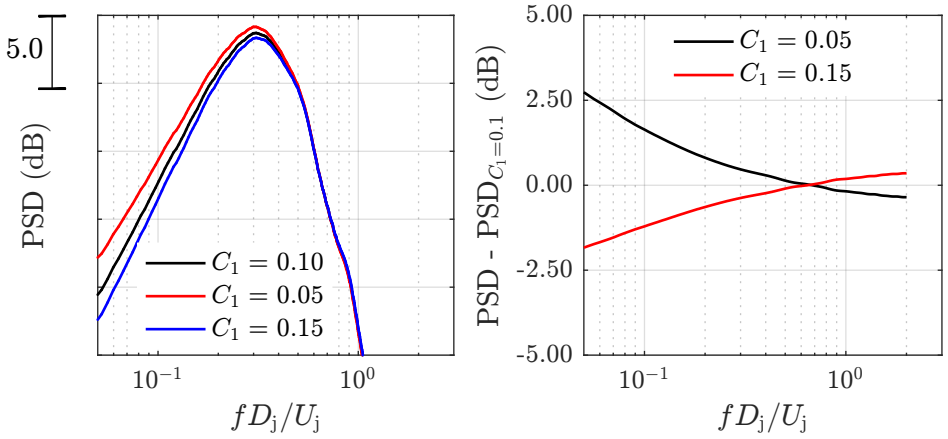

FIGURE 6.5: Variation in model spectrum with axial wavenumber coefficient C_1. $U_j = 245$ m/s, $U_f = 0$ m/s, $h/D = 0.88$, $l/D = 1.94$ and $c = 0.4$ m

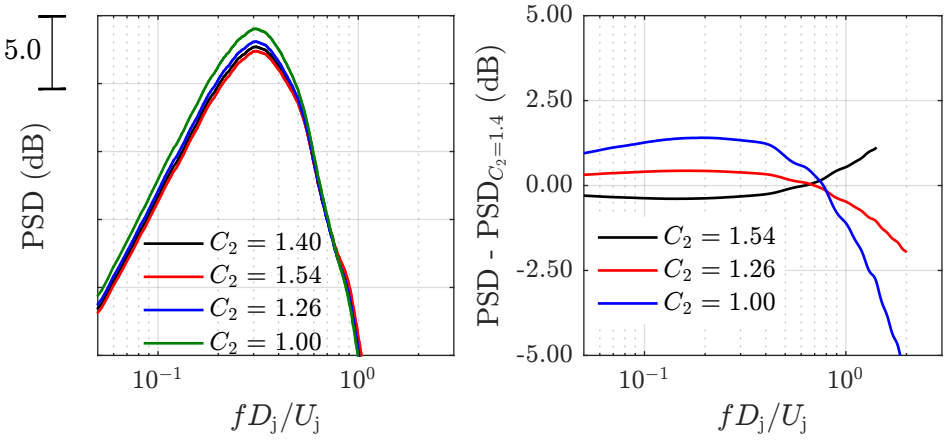

FIGURE 6.6: Variation in model spectrum with axial wavenumber coefficientC_2. $U_j = 245$ m/s, $U_f = 0$ m/s, $h/D = 0.88$, $l/D = 1.94$ and $c = 0.4$ m

Figure 6.7 and Figure 6.8 display examples of how the sensitivity of the calculated JSI noise varies with polar angle. JSI noise in the rear arc is more sensitive to changes in axial wavenumber than that in the forward arc.

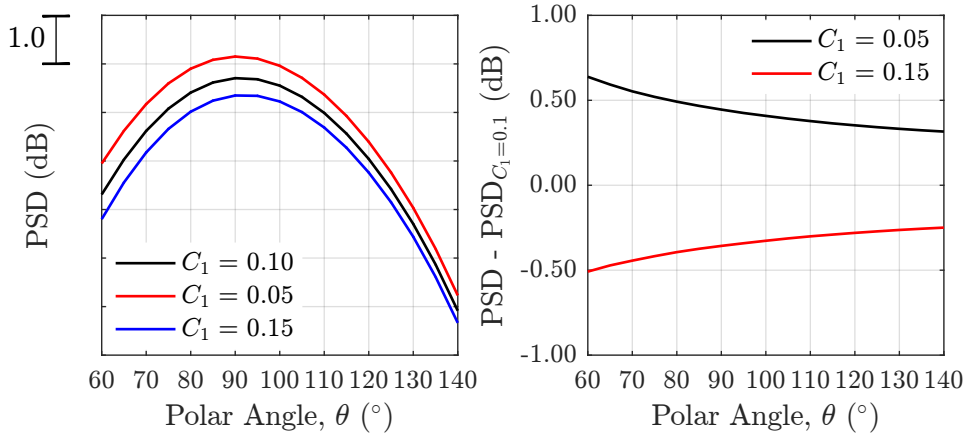

FIGURE 6.7: Variation in polar directivity with axial wavenumber coefficient C_1. St = 0.31, $U_\mathrm{j} = 245$ m/s, $U_\mathrm{f} = 0$ m/s, $h/D = 0.88$, $l/D = 1.94$ and $c = 0.4$ m

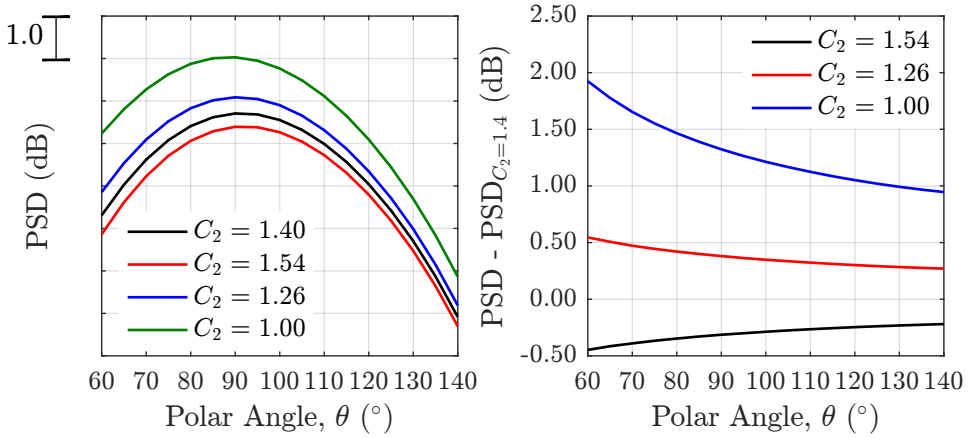

FIGURE 6.8: Variation in polar directivity with axial wavenumber coefficient C_2. St = 0.3, $U_\mathrm{j} = 245$ m/s, $U_\mathrm{f} = 0$ m/s, $h/D = 0.88$, $l/D = 1.94$ and $c = 0.4$ m

6.2 Large-Scale Tests

In order to validate the JSI noise prediction tool on a larger and more representative scale, installed jet noise measurements from the SYMPHONY and HARMONY projects are used. As part of the UK Technology Strategy Board funded projects SYMPHONY[137,139] (SYstem Manufacturing and Product design tHrough cOmponent Noise technologY) and HARMONY[138] (wHole AiRcraft Multidisciplinary nOise desigN sYstem), installed jet noise measurements were taken in QinetiQ's Noise Test Facility (NTF). The aim of SYMPHONY was to provide experimental data against which semi-empirical, analytical and numerical models for jet-airframe interaction noise could be validated. Both campaigns utilised a 1/10th scale jet nozzle and airframe representative of current 150 seater commercial narrow-body jet airliners. [1]

[1]The author played no role in these experiments

6.2.1 QinetiQ's Noise Test Facility

The Noise Test Facility (NTF) was a purpose built anechoic chamber for the measurement of noise produced by the exhaust from gas turbine engines. Originally commissioned in 1972[126] (and then decommissioned in 2016), the NTF comprised a chamber (see Figure 6.9) 26 m wide by 27 m long and 15 m high, lined with twenty-one thousand acoustic wedges, ensuring anechoic conditions down to 90 Hz. Initially, the facility was designed to allow the static testing of 1/10th scale subsonic jets, up to 18 inches in diameter.[126] However, in 2003, the NTF was improved to allow the simulation of forward flight with the installation of a co-axial 1.8 m-diameter 'flight stream' capable of simulating speeds up to Mach 0.33.[127] Additionally, the NTF was capable of testing hot jets by passing the core jet air through an Avon combustion can. Heat exchangers could also be used to remove the heat of compression to simulate unheated jets, such as a bypass jet. The chamber acoustic properties were kept stable by the use of extraction fans to prevent recirculation of the exhaust gases. Jet velocities and total temperatures, within 3 m/s and 5 K of the respective targets, were achieved through measurements of total temperature, pressure and mass flow rate upstream of the nozzles.[18] The jet operating conditions were adjusted to the chamber conditions to ensure that the desired acoustic Mach numbers were maintained.

FIGURE 6.9: View of the NTF showing jet nozzles, exhaust gas collector and microphone arrays

6.2.2 Nozzles

Three nozzles were used in the SYMPHONY and HARMONY test campaigns. First, the baseline nozzle, named S33-P51, was designed to be representative of current bypass engines used on narrow-body jet airliners. As such, it includes both primary and secondary flows, a pylon and nozzle bifurcations. This nozzle was used for a study of the effect of wing position and configuration, however only a handful of different wing locations were used with only small variations in location, due to the requirement to change the pylon for each wing location. Due to the cost involved in replacing the pylon for each wing location, a second nozzle was created. This nozzle, S33-A55, was an axisymmetric version of S33-P51-UL without the pylon and bifurcations. The S33-A55 nozzle had a 0.1857 m diameter, with a secondary nozzle exit area of 0.013828 m^2 and an area ratio between secondary and primary nozzles of 5.5, giving an effective diameter, D_e, of 0.147 m. With this nozzle, a much larger parametric study was conducted to ascertain the effect of wing location on far-field noise.

Finally, a single stream nozzle, S33-ASS, was used for direct comparison with the Doak Laboratory jet. The primary and secondary flows are matched and mixed before exiting the S33-ASS nozzle, and includes no centre body, bullet, pylon nor bifurcations. The outer diameter of this nozzle matches the outer diameter of the other two nozzles, at 0.1857 m, however, the exit area is increased to 0.02708 m^2.

6.2.3 Airframe

The airframe was a 1/10th-scale half-wing and fuselage model of a modern 150-seater commercial jet airliner. In order to capture the effects of lift on the jet, the wing was designed to create representative amounts of lift at take-off and landing with the use of angled flaps. A representative aerofoil was chosen for the wing, with modifications to the aerofoil only made to the suction surface, to ensure that the pressure surface remained representative with respect to the jet flow. To simulate conditions during take-off and landing, the trailing edge of the wing could be replaced by single slotted Fowler flaps (without flap track fairings) at 16° and 32° flap angles. The airframe was positioned relative to the jet nozzle using a rotating 'stinger' assembly. Linear actuators were used for fine adjustment of the axial, spanwise and radial position of the wing. The airframe was connected to the positioning system by a structural support (replacing the port wing with the jet nozzle beneath the wing on the starboard side of the fuselage) (see Figure 6.10).

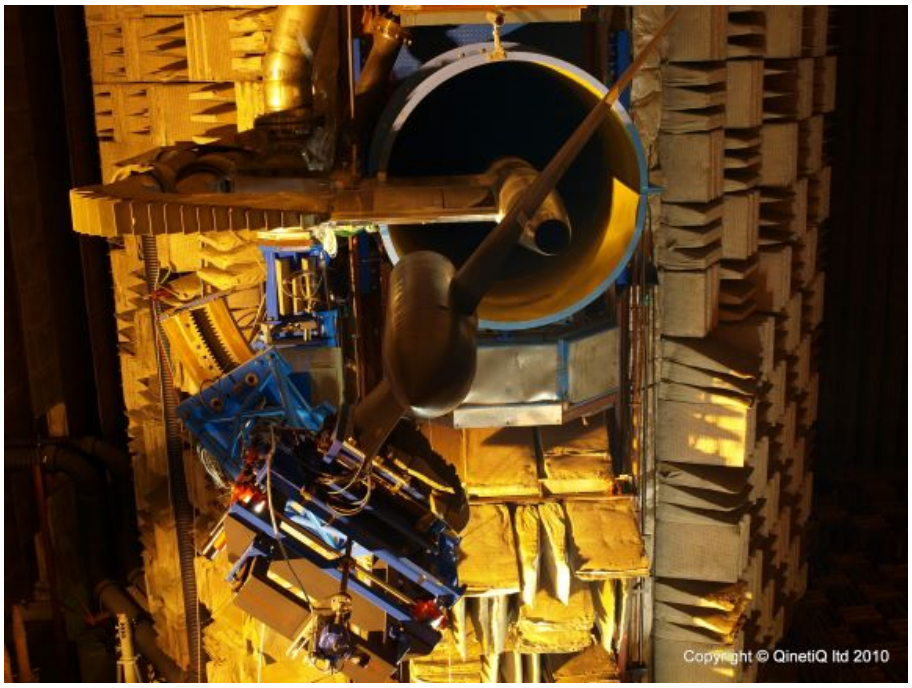

FIGURE 6.10: Close-up of the rig, showing fuselage, positioning system and S33-ASS nozzle

For the installed S33-P51 nozzle test, a sensor was installed in the pylon to ensure correct positioning of the wing. Without a pylon, no sensor could be installed with the S33-A55 and S33-ASS nozzles. In-flight, when the wing produces lift, it is therefore possible that the wing could move from the desired location with the S33-A55 and S33-ASS nozzles. It was, therefore, not possible to know the exact location of the wing in flight with the S33-A55 and S33-ASS nozzles.

6.2.4 Microphone Arrays

Two microphone arrays are used in the following analysis: the Flyover and Stargate arrays. The flyover array was a linear array of 1/4" free-field microphones positioned at an azimuthal angle of 0° directly below the airframe. The array was positioned parallel to the jet axis at a radial distance of 10.2 m from the jet centreline, placing it in the geometric far-field of the model jet at over 50 secondary jet diameters. The microphones were placed at polar angles between 50° and 130°, with spacings of 5° between the polar angles of 70° and 130° and 10° otherwise.

The Stargate array was a traversable circular array 4.5 m in diameter, centred on the jet axis. The array consists of 36 1/4" free-field microphones spaced every 10° azimuthally around the array, starting from 6° azimuth, and 9 1/2" free-field microphones spaced between the 1/4" microphones between 331° and 51° azimuth. The array was traversed between polar angles of 28° and 110°.

6.2.5 Test Conditions

The jet conditions used in the following analysis are labelled 8, 6a, 21 and 22. The velocities and temperatures associated with each condition are given in Table 6.1. Condition 8 relates to a maximum take-off thrust condition, 6a to a cutback condition and conditions 21 and 22 are matched jets, where the primary and secondary jets have the same properties, mimicking a single stream nozzle. When simulating flight, SYMPHONY and HARMONY used flight-stream speeds of 52 and 103 m/s, labelled respectively F1 and F8.

TABLE 6.1: Jet conditions, velocities and total temperatures used in the SYMPHONY and HARMONY test campaigns

Condition	U_p (m/s)	Θ_p (K)	U_s (m/s)	Θ_s (K)
6a	268	696	245	347
6b	244	288	243	346
8	378	729	292	359
21	255	320	255	320
22	187	305	187	305

6.2.6 Data Processing

Each time series recorded by the microphones during a test is processed into narrow and third-octave band spectra. These are then further corrected for various effects including measurement system calibration, background noise, atmospheric attenuation, spherical spreading and flight-stream shear-layer refraction. In this chapter, the narrow band data is used, corrected for all but shear layer refraction due to the low frequencies associated with JSI noise.

For OASPL analyses, OASPL has been calculated by integrating from $f = 200$ Hz, the lower limit of the NTF spectra, up to $f = 1.2(U + U_\mathrm{f})/D$, in an attempt to integrate over the low-frequency JSI noise hump, ignoring the high-frequency jet mixing noise.

6.3 Results

6.3.1 Diameter Scaling

In Chapter 5 the JSI noise model of Lyu & Dowling was validated against small installed jet noise measurements. The hydrodynamic pressure spectra used as the inputs to the model came from measurements of the jet from the nozzle used for the installed measurements. In this chapter these same near-field pressure measurements are used in

predicting the installed jet noise from nozzles almost five times the diameter. This should provide evidence for, or potentially against, the method for scaling the hydrodynamic pressure spectrum demonstrated in Chapter 4.

In Figure 6.11, a comparison is made between the prediction tool and measured installed jet noise spectra for the axisymmetric planar single-stream, S33-ASS, nozzle. This is the simplest of the three nozzles, without bullet, pylon, bifurcations nor primary and secondary streams, so is most comparable to the nozzle used for the near-field pressure measurements used as the input to the prediction tool. The comparison shows that there is good agreement between the measured and predicted spectra, especially at polar angle $\theta = 90°$.

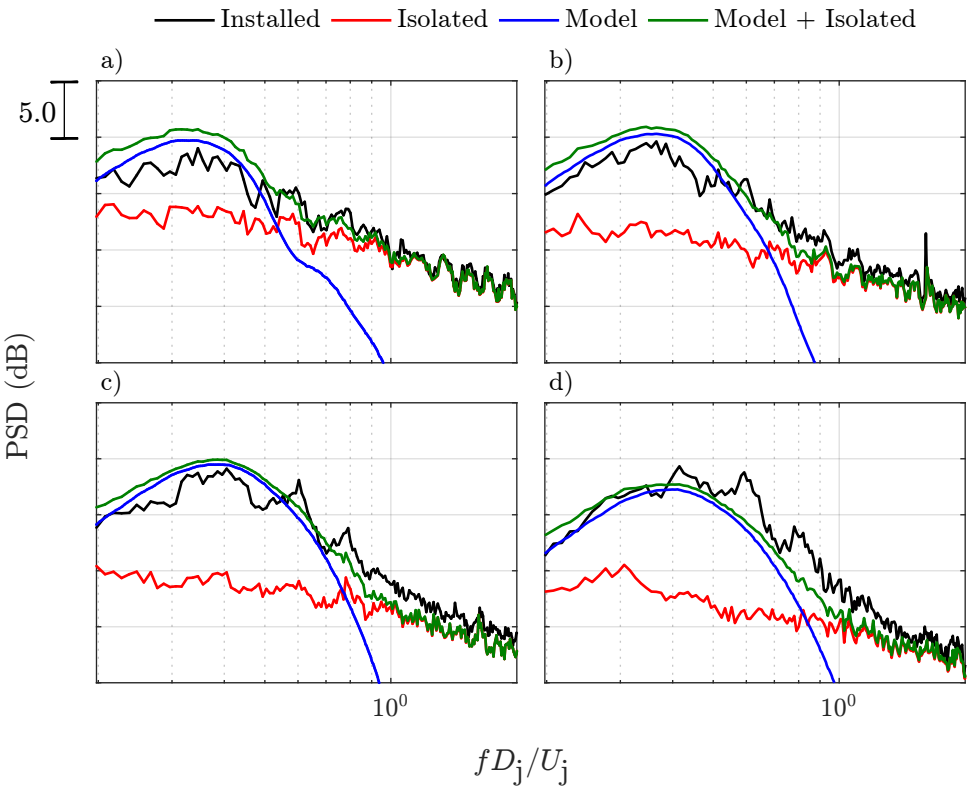

FIGURE 6.11: Comparison of measured installed jet noise with model prediction. Nozzle S33-ASS, $l/D = 1.94$, $h/D = 0.88$, $\phi = 0°$ and condition 22S ($U_j = 187$ m/s). a) $\theta = 70°$; b) $\theta = 90°$; c) $\theta = 110°$; d) $\theta = 130°$.

The comparison in Figure 6.11 displays an increasing overprediction as polar angle, θ, decreases. This is more obvious when comparing the polar OASPL directivity in Figure 6.12. This is not unexpected, as the same effect was observed with the Doak data, in Chapter 5. However, the polar directivities are very different, perhaps due to the increased complexity of the scattering surface. Given though that the overprediction was also seen with the Doak Laboratory measurements, the overall good agreement in Figure 6.11 would suggest that the effect of diameter is adequately captured by the model.

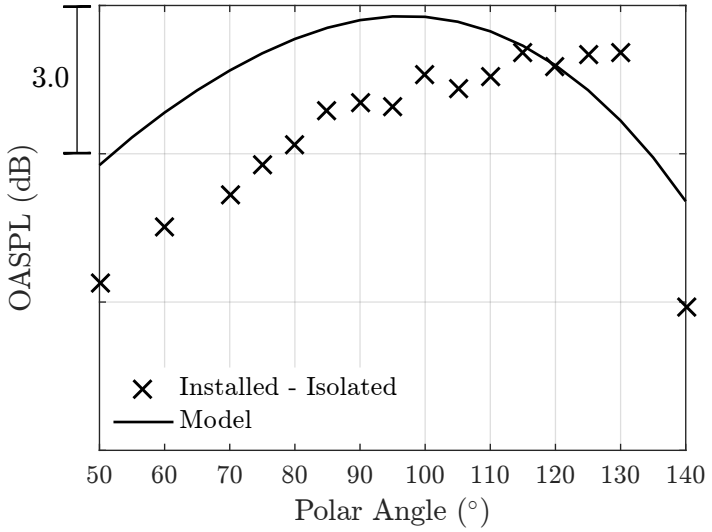

FIGURE 6.12: Comparison of polar OASPL directivity. Nozzle S33-ASS, $l/D = 1.94$, $h/D = 0.88$, $\phi = 0°$ and condition 22S ($U = 187$ m/s).

6.3.2 Flight Velocity

For aircraft certification it is important that JSI noise can be calculated in flight, as certification measurements are taken during approach and take off. Comparisons of the predicted and measured spectra at flight speeds of 52 m/s and 103 m/s are displayed in Figure 6.13 and Figure 6.14 respectively. At the lower flight velocity the model appears to adequately predict the spectra, however, at the highest flight velocity, Figure 6.14, the peak frequency range of the prediction is below that of the measured data, by as much as 50% in Figure 6.14d.

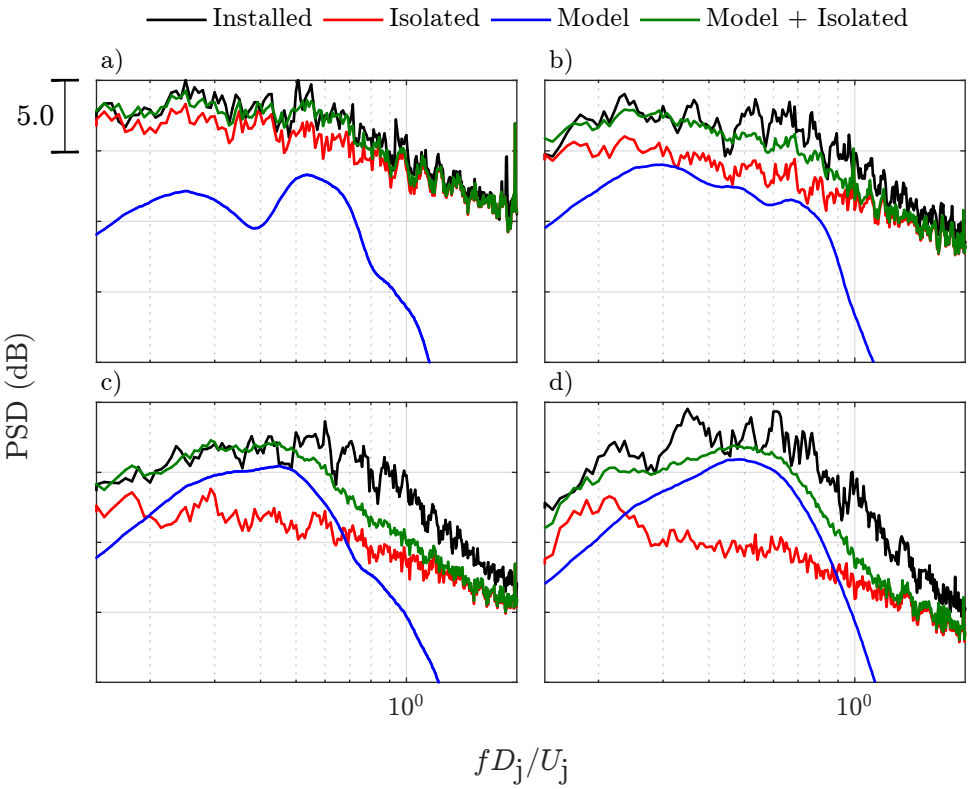

FIGURE 6.13: Comparison of measured installed jet noise with model prediction. Nozzle S33-ASS, $l/D = 1.94$, $h/D = 0.83$, $\phi = 0°$ and condition 21F1 ($U_j = 255$ m/s and $U_f = 52$ m/s). a) $\theta = 70°$; b) $\theta = 90°$; c) $\theta = 110°$; d) $\theta = 130°$.

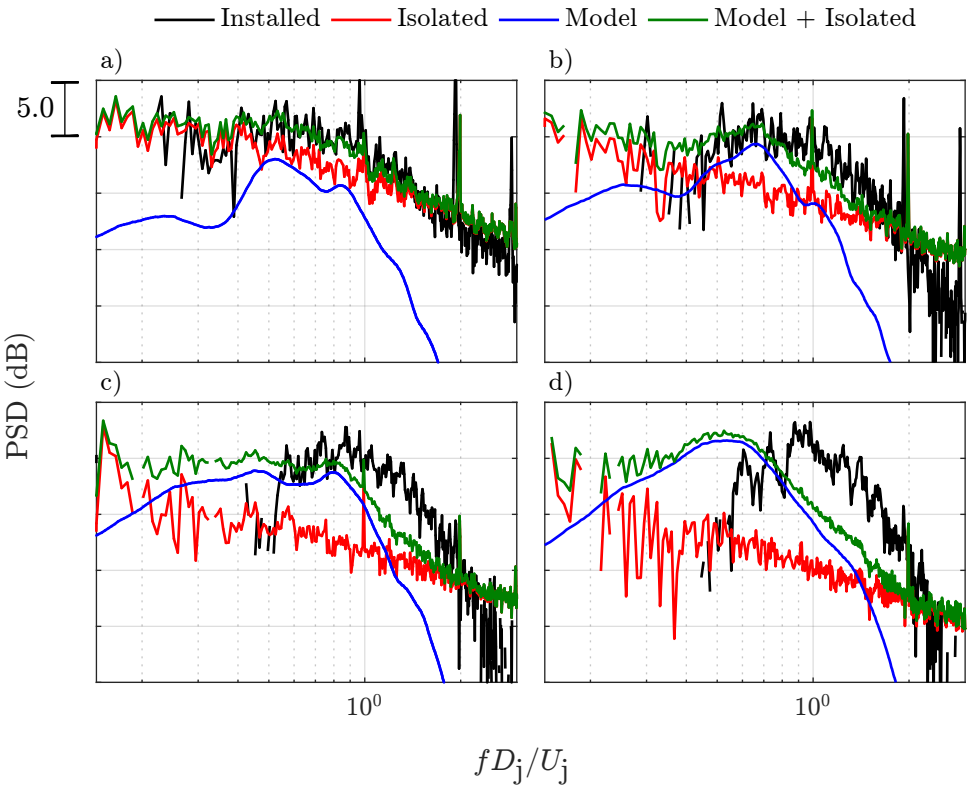

FIGURE 6.14: Comparison of measured installed jet noise with model prediction. Nozzle S33-ASS, $l/D = 1.94$, $h/D = 0.77$, $\phi = 0°$ and condition 21F8 ($U_j = 255$ m/s and $U_f = 103$ m/s). a) $\theta = 70°$; b) $\theta = 90°$; c) $\theta = 110°$; d) $\theta = 130°$.

The in-flight scaling methods are based on the near-field pressure measurements described in Chapter 4. These measurements demonstrated that the amplitude and frequency of the hydrodynamic pressure field scaled as $(U_j - U_f)^3$ and U_j, respectively, if the axial microphone location was kept constant relative to the potential core length. Using these scaling methods in the prediction tool has led to accurate prediction of the JSI amplitude, giving some confidence in this approach. However, peak frequency is noticeably underpredicted at a flight velocity of 103 m/s.

There are several reasons why this velocity scaling may be incorrect for capturing the correct frequency, at least for this case. Firstly, only one near-field measurement location relative to the potential core length was used in the Doak Laboratory, this may not be enough to draw a robust conclusion on the scaling of the near-field with flight velocity; Secondly, the static measurement was at $x/D = 3$, with the microphone traversed downstream as flight velocity increased. For JSI noise prediction, the trailing edge position remains constant and so the position relative to the potential core reduces in flight, it is possible the frequency scaling changes below a certain distance relative to the potential core length. Thirdly, the potential core length in flight may not be calculated correctly. Fourthly, the rate of attenuation decays with radial position increases with frequency; if the radial position of the trailing-edge or the axial wavenumbers are incorrect then

the amplitude of the peak frequency may be over attenuated. Finally, if the calculated directivity is incorrect then this could shift the peak frequency at a given angle away from that measured.

Near-field measurements in Chapter 4 suggested that if the microphone is shifted downstream as flight speed is increased then the peak frequency scales with jet velocity, as suggested by Miller.[54] However, the microphone position was based on the empirical potential core length equation from Proenca,[98] that was created with measurements at only one jet velocity, and hence is a function of flight speed only. This may have lead to inaccuracies in the positioning of the microphone for the different jet velocities, and hence the scaling of the near-field, as methods of scaling potential core length such as[128]

$$1 + C_1 \frac{U_\mathrm{f}}{U_\mathrm{j} - U_\mathrm{f}} \tag{6.8}$$

are a function of jet and flight velocity, and could perhaps have been used to correct the microphone position for the effect of jet velocity. Once corrected for the effect of the stretching of the potential core the scaling of frequency with jet velocity suggested by Miller is based on an eddy convection speed in the jet shear layer. However, convection velocity has also been proposed to be a function of flight velocity, such as[129]

$$U_\mathrm{c} = 0.65(U_\mathrm{j} - U_\mathrm{f}) + U_\mathrm{f}. \tag{6.9}$$

Finally, completely different frequency scaling methods have been proposed, with Vera[65] showing good results, in comparison to laboratory measurements with a flight stream, scaling a static model prediction to flight using $f \propto U_\mathrm{j} - U_\mathrm{f}$ which has also been used for jet-mixing noise.[130,131]

With the predictions based on near-field pressure measurements and potential core lengths measured within the Doak laboratory, the predictions could be affected by any differences in developments of the jets. For instance, the jet pipework within the Doak laboratory extends[98] for a greater distance within the flight stream than the stinger in the NTF.[127] This could lead to a greater boundary layer thickness-to-jet-diameter ratio at the lip of the Doak jet relative to that on the NTF nozzle. This could in turn affect the development of the jet and the near-field in flight.

When the spectrum of the incident pressure extends to wavelengths of a similar or greater size to the chord of the scattering surface, then the spectrum of the far-field scattered acoustic field will display an broad peak with peaks and troughs (see Figure 5.12 for example). If there are inaccuracies in the calculation, such as the incident axial wave number wing planform etc., then frequencies seeing constructive/destructive interference could change, leading to the peak occurring at a different frequency. This however, will have little effect on the upper end of the JSI spectrum, where the amplitude roll-off is very high, Figure 6.14c & d show a roll-off of greater than 30 dB/decade. While the

model and measurements show very similar gradients in these regions there is a frequency shift between them that is not due to an error in the calculation of the directivity.

Further, analysis of the peak frequency of the measured installed jet noise suggests a frequency scaling of $U_\mathrm{j} + U_\mathrm{f}$. This is close to what one might expect using a frequency scaling based on both position relative to the potential core length and convection velocity, if the convection velocity is a function of both jet and flight velocity. Replacing the U_j frequency scaling in the prediction tool with $U_\mathrm{j} + U_\mathrm{f}$, such that

$$f = \frac{f_\mathrm{ref} D_\mathrm{ref}}{U_\mathrm{ref}} \frac{U_\mathrm{s} + U_\mathrm{f}}{D_\mathrm{e}}, \tag{6.10}$$

both the in-flight predictions are greatly improved, with the spectral shape now a much better match for the measured data (see Figure 6.15 and Figure 6.16). This method to scale the frequency of the hydrodynamic field with flight velocity will, therefore, be used for the remainder of this chapter. Further in-flight near-field pressure measurements are certainly required to understand this discrepancy in scaling the near-field frequency with U_j and $U_\mathrm{j} + U_\mathrm{f}$.

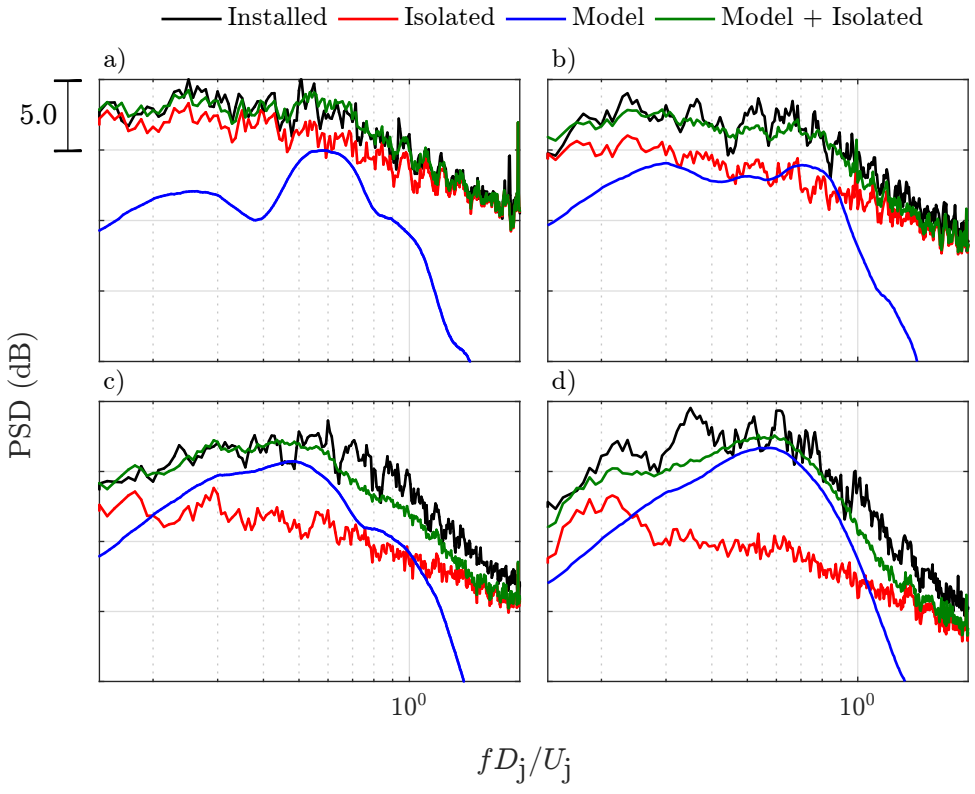

FIGURE 6.15: Comparison of measured installed jet noise with model prediction using $U_\mathrm{j} + U_\mathrm{f}$ frequency scaling. Nozzle S33-ASS, $l/D = 1.94$, $h/D = 0.83$, $\phi = 0°$ and condition 21F1 ($U_\mathrm{j} = 255$ m/s and $U_\mathrm{f} = 52$ m/s). a) $\theta = 70°$; b) $\theta = 90°$; c) $\theta = 110°$; and, d) $\theta = 130°$.

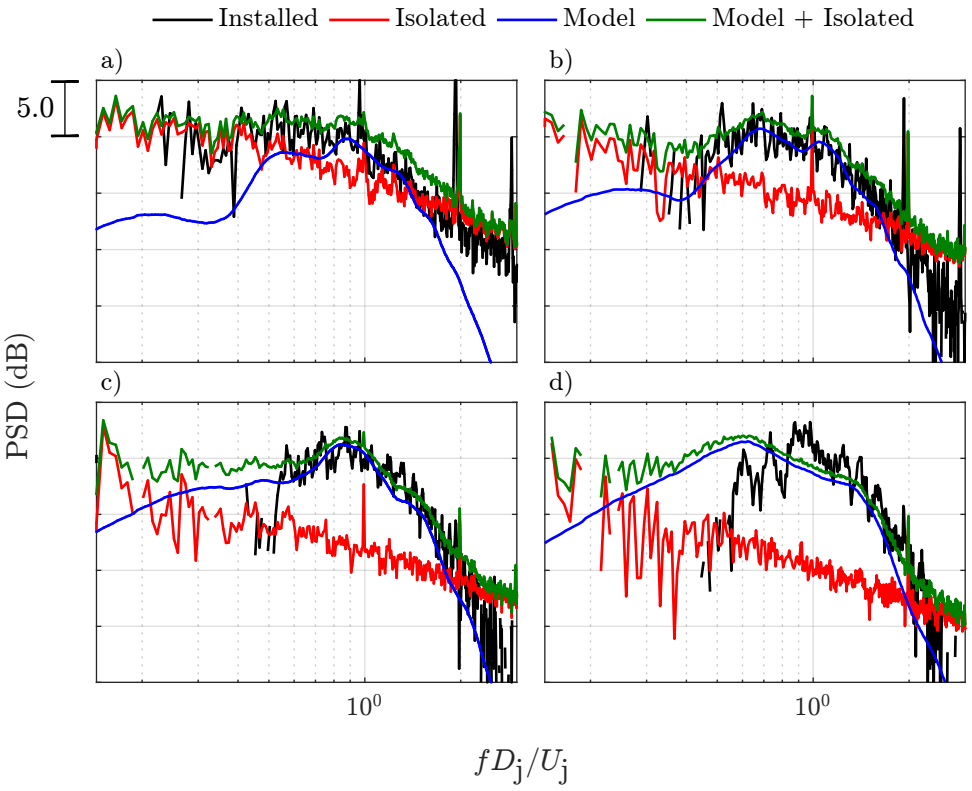

FIGURE 6.16: Comparison of measured installed jet noise with model prediction using $U_j + U_f$ frequency scaling. Nozzle S33-ASS, $l/D = 1.94$, $h/D = 0.77$, $\phi = 0°$ and condition 21F8 ($U_j = 255$ m/s and $U_f = 103$ m/s). a) $\theta = 70°$; b) $\theta = 90°$; c) $\theta = 110°$; and, d) $\theta = 130°$.

Strangely, the amplitude of the model spectra is in very good agreement with the measurements at all polar angles in Figure 6.15 and Figure 6.16. This is strange because the static data is showing the model to overpredict in the rear arc, as does comparisons to the Doak Laboratory data. Also, when validating the model in flight in Chapter 5 the model was found to underpredict for flight Mach numbers $M_f > 0.2$, while here the model appears to work well at a flight Mach number $M_f = 0.3$ ($U_f = 103$ m/s). Lastly, the model does not appear to properly capture the spectral shape at the polar angle $\theta = 130°$ and flight velocity $U_f = 103$ m/s. This may suggest that something is missing, or not correctly modelled, in scaling the hydrodynamic pressure spectrum in flight. However, it should also be noted that there is a large variety of spectral shapes in Figure 6.15 and Figure 6.16 and, other than in Figure 6.16d, these are very well predicted by the model.

With the frequency scaling in the prediction tool modified to include the flight velocity, the results of this section show that the prediction tool is capable of scaling up to large model-scale single stream circular jets. The model correctly accounts for the effects of diameter, jet velocity and flight velocity at observer positions and azimuthal angle of the flyover array. However, the overprediction in the rear arc seen in Chapter 5 is also shown to occur with the large model-scale data.

6.3.3 Axisymmetric Annular Nozzle

In Chapter 4, far-field installed jet noise measurements were presented to demonstrate the effect of bullets on JSI noise. Based on these measurements the model scales the position of the trailing edge, hydrodynamic pressure field frequency and amplitude with the effective diameter, D_e. Figure 6.17 compares these measurements with the JSI noise model. The model predicts the same amplitude for the nozzles with the same effective diameter. For both effective diameters, the sur-peak spectra matches between the model and the measurements. However, the model increasingly overpredicts at frequencies below the peak of the measured spectra. This is especially obvious for the effective diameter $D_e = 32$ mm, where the peak frequency is underpredicted by approximately 150 Hz.

The most likely reason for the overprediction of the model below the peak frequencies of the measured is displayed in Figure 4.1, which compares the near-field spectra of the 38.1 mm and 40 mm Doak jet nozzles. The near-field spectra of the two nozzles are shown to be equal at frequencies above the peaks. However, the 38.1 mm nozzle has a lower peak frequency, and the difference in amplitude between the two nozzles continues to increase as frequency decreases. As it is the near-field measurements of the 38.1 mm jet that are used as the input to the JSI noise model, one can expect the 40 mm installed jet noise measurements to be overpredicted at frequencies below the peak, as is likely the case for the other nozzles used in Figure 6.17.

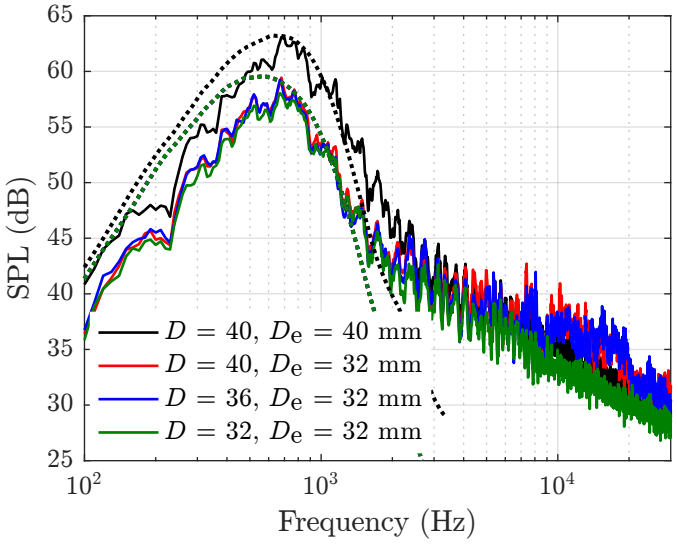

FIGURE 6.17: Comparison of the model prediction (dotted lines) with the installed jet noise measurements (solid lines) taken in the Doak Laboratory with round and annular jet nozzles. $h = 0.04$ m, $l = 0.12$ m, $c = 0.2$ m, $\theta = 90°$, $\phi = 0°$ and $M_j = 0.3$

The SYMPHONY and HARMONY campaigns used an axisymmetric annular nozzle, S33-A55, which includes a bullet. Unlike the nozzles used in the Doak Laboratory,

S33-A55 has primary and secondary streams. If the velocities of the two streams are different then this creates an internal shear layer that could modify the pressure seen by the trailing edge in comparison to a single stream nozzle. This internal shear layer can be avoided if the two streams are matched (i.e. having the same velocity and temperature), simulating a single stream nozzle. Three matched jet conditions were used during the campaign and can therefore be used to further validate the use of the effective diameter to calculate JSI noise.

Figure 6.18 and Figure 6.19 display comparisons of the prediction tool with the measured spectra using the effective diameter and secondary nozzle diameter respectively within the model. The matched jet condition 21 has been used to remove any effect of a secondary internal shear layer. This radial wing location, $h/D_{\mathrm{s}} = 0.76$, was chosen because, when non-dimensionalised by effective diameter, it is at the same location as the near-field microphone input data. Hence, errors in the wavenumber calculation should be small. In Figure 6.18 the amplitude of the model and measurements match at $\theta = 130°$ as with the single stream, S33-ASS, nozzle, although the overprediction in the rear arc seems to have increased. In comparison, the model overpredicts the measured data at all angles in Figure 6.19, including at $\theta = 130°$ where the amplitude of the prediction is three to four decibels greater than in Figure 6.18. This provides further evidence for the use of effective diameter to scale the hydrodynamic pressure spectra and trailing edge location for JSI noise prediction.

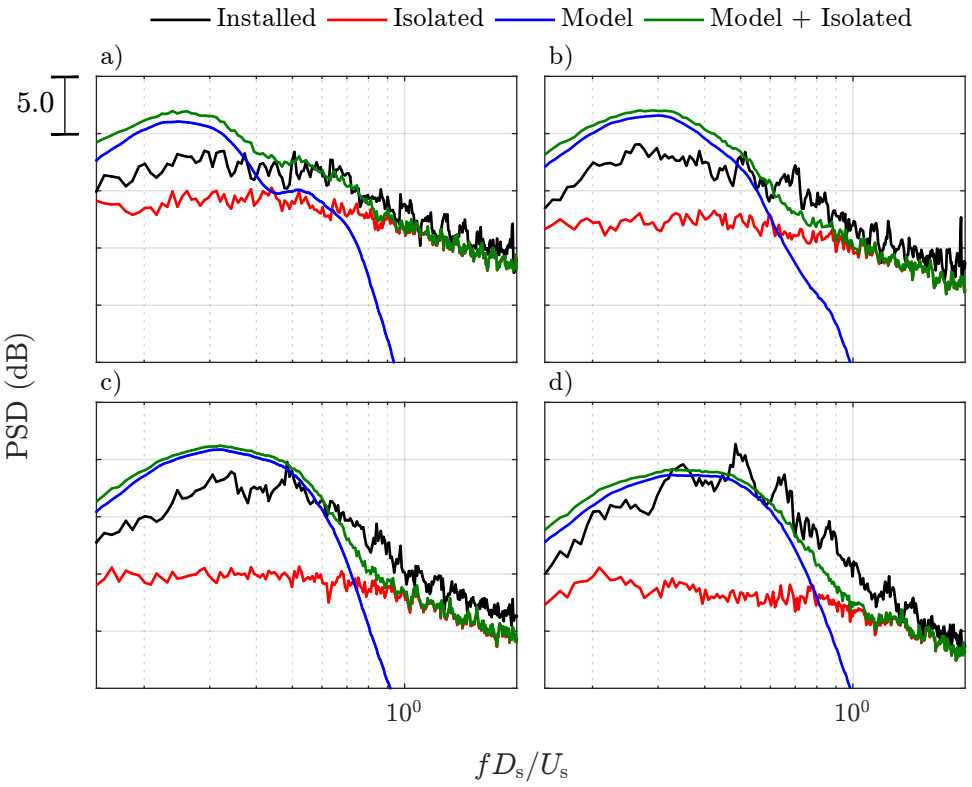

FIGURE 6.18: Comparison of measured installed jet noise with model prediction. Nozzle S33-A55, $l/D_s = 2.35$, $h/D_s = 0.76$, $\phi = 0°$ and condition 21S ($U_s = U_p = 255$ m/s and $U_f = 0$ m/s). a) $\theta = 70°$; b) $\theta = 90°$; c) $\theta = 110°$; and, d) $\theta = 130°$.

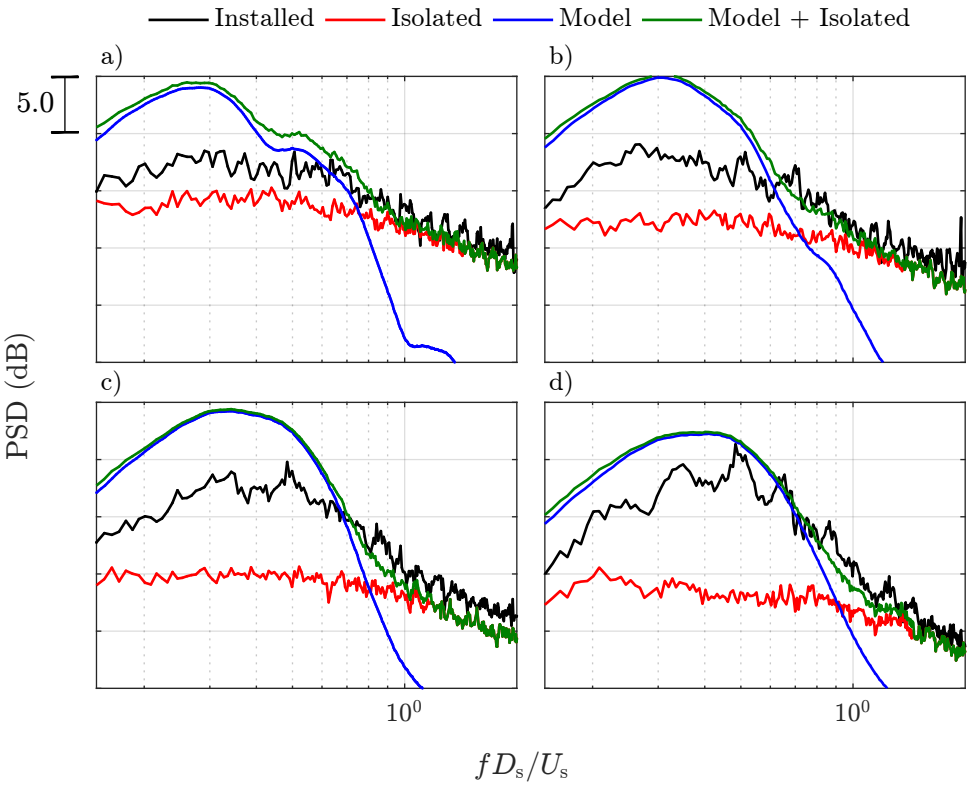

FIGURE 6.19: Comparison of measured installed jet noise with model prediction, however the nozzle outer, D_s, rather than effective, D_e, diameter has been used in the model. Nozzle S33-A55, $l/D_s = 2.35$, $h/D_s = 0.76$, $\phi = 0°$ and condition 21S ($U_s = U_p = 255$ m/s and $U_f = 0$ m/s). a) $\theta = 70°$; b) $\theta = 90°$; c) $\theta = 110°$; and, d) $\theta = 130°$.

In Figure 6.18 the model is in good agreement with the measured spectrum at polar angle $\theta = 130°$. However, the amplitude is increasingly overpredicted at decreasing polar angles, by a greater amount than seen with the round single stream nozzle. With the single stream nozzle the overprediction reduced in flight. Figure 6.20 demonstrates that this is also occurs with the annular jet, which continues to provide evidence for using effective diameter.

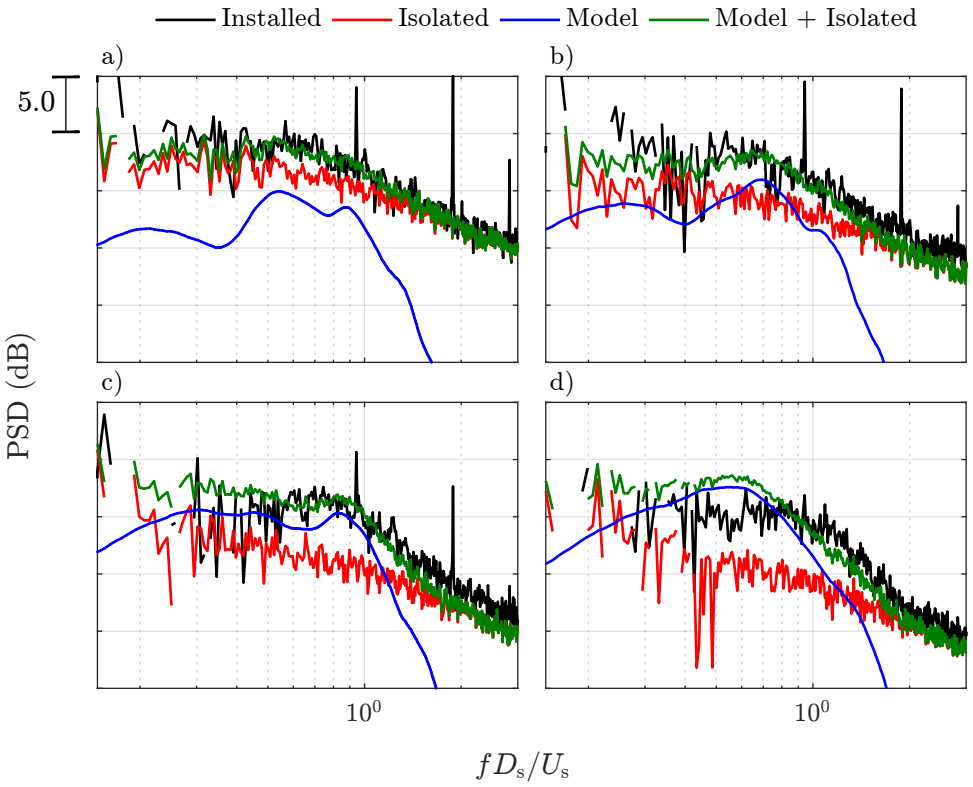

FIGURE 6.20: Comparison of measured installed jet noise with model prediction. Nozzle S33-A55, $l/D_s = 2.35$, $h/D_s = 0.76$, $\phi = 0°$ and condition 21F8 ($U_s = U_p = 255$ m/s and $U_f = 102$ m/s). a) $\theta = 70°$; b) $\theta = 90°$; c) $\theta = 110°$; and, d) $\theta = 130°$.

6.3.4 Radial Trailing Edge Location

The radial position, h, of the trailing edge has been shown to have a strong effect on the amplitude of JSI noise, at least when the trailing edge is outside the jet flow field (for one example see Figure 6.2). It is, therefore, important that the model is able to capture the effect of the radial location of the trailing edge. With the dual stream axisymmetric annular nozzle, S33-A55, a parametric study was conducted with jet condition, wing configuration and wing position, providing a range of radial trailing edge locations with which to compare.

The model uses cylindrical harmonics to propagate the hydrodynamic pressure radially. For a given frequency and mode, this relies on the axial wavenumber to give the correct rate of decay. Therefore, differences in the model and measurements as h is changed would indicate that the axial wavenumber is not adequately modelled. Currently, the axial wavenumber is modelled as a linear function with Strouhal number, which is constant with axial location and flight velocity.

Figure 6.21, Figure 6.22 and Figure 6.23 display a comparison of measured and predicted OASPL at flight velocities of 0, 51 and 102 m/s respectively. A polar angle of 130° and a jet velocity of 292 m/s (condition 8) have been chosen for this comparison. In all

three cases the amplitudes and gradients of the predicted and measured OASPL are very similar up to $h/D_s = 0.9$. In Figure 6.23 at greater values of h/D_s the JSI noise is masked by the jet mixing noise and further comparison is not possible. In Figure 6.21 and Figure 6.22 the measured and predicted data starts to diverge instead, with the gradient of the measured OASPL decreasing. Overall though, the decay of the JSI noise OASPL with radial trailing edge locations looks to be in agreement with the measurements.

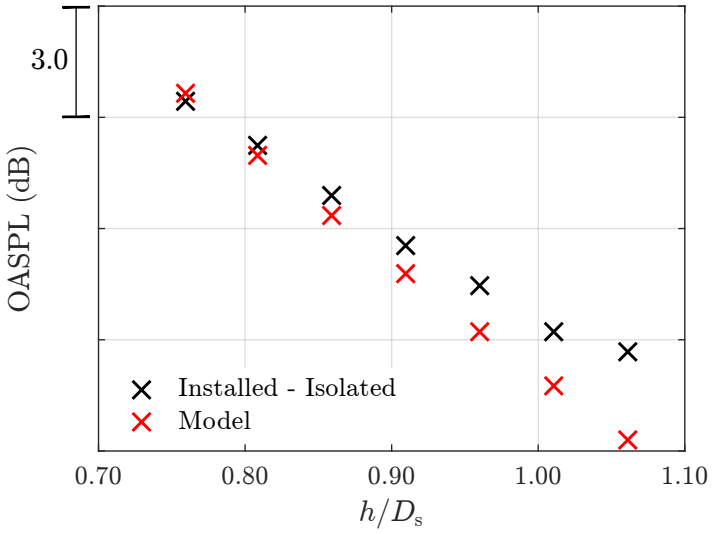

FIGURE 6.21: Comparison of measured installed jet noise with model prediction. Nozzle S33-A55, $l/D_s = 2.35$, $\theta = 130°$, $\phi = 0°$ and condition 8S ($U_s = 292$ m/s, $U_p = 378$ m/s and $U_f = 0$ m/s).

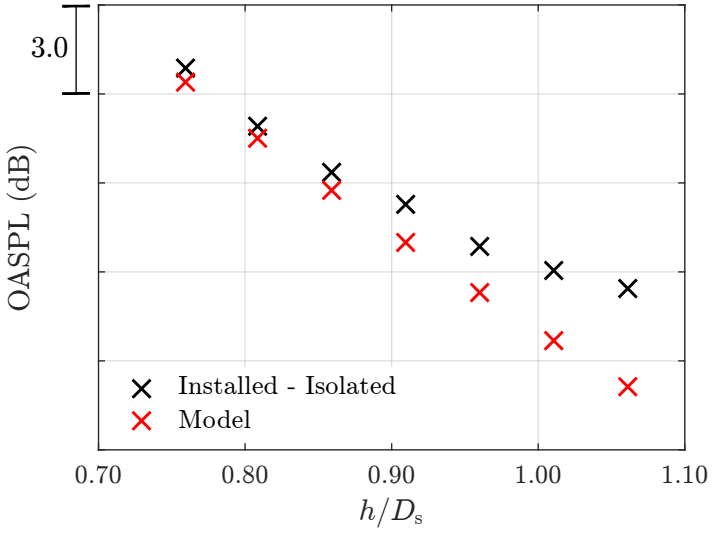

FIGURE 6.22: Comparison of measured installed jet noise with model prediction. Nozzle S33-A55, $l/D_s = 2.35$, $\theta = 130°$, $\phi = 0°$ and condition 8F1 ($U_s = 292$ m/s, $U_p = 378$ m/s and $U_f = 52$ m/s).

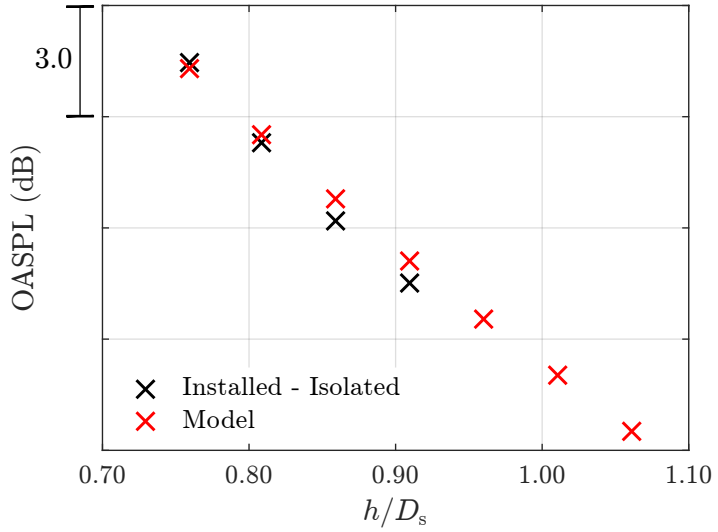

FIGURE 6.23: Comparison of measured installed jet noise with model prediction. Nozzle S33-A55, $l/D_s = 2.35$, $\theta = 130°$, $\phi = 0°$ and condition 8F8 ($U_s = 292$ m/s, $U_p = 378$ m/s and $U_f = 102$ m/s).

The comparison of the model and experimental data used measurements with jet condition 8, which has different primary and secondary jet velocities. This difference in primary and secondary velocities leads initially to a second shear layer (between the primary and secondary jets), in the 'initial' region. As both the inner and outer shear layers grow they will combine together in an intermediate zone before fully combining in the 'fully merged' zone.[132] The addition of a second shear layer, and its mixing with the outer shear layer, will make the near field develop differently to that of a single stream jet. Therefore, modelling the near field of a dual-stream jet by scaling measurements of a single-stream jet may only be possible under certain conditions.

Measurements by Ko & Kwan[132] of a coaxial jet with velocity ratio $U_s/U_p = 0.7$ have displayed similarity in non-dimensional velocity and turbulence profiles between single stream jets and the outer shear layer within the initial region of dual-stream jets. Beyond the initial region, the peak turbulence of the outer shear layer remains constant over a large portion of the 'intermediate zone' with the profile outside the peak continuing to display similarity with that of single stream jets. Furthermore, measurements of velocity and pressure spectra through the jet show that, for this high velocity ratio, the peak Strouhal number is associated with the outer shear layer, and the vortices in the outer shear layer continue to grow through the intermediate zone.

The S33-A55 and S33-P51-UL nozzles have a diameter ratio approximately 33% greater than the nozzles used by Ko & Kwan. The velocity ratios of conditions 8 and 6 are also greater than the highest ratio (0.7) used by Ko & Kwan at approximately 0.78 and 0.92. The axial positions of the trailing edge used with these nozzles likely falls statically in the intermediate zone, but with the high velocity ratios and high diameter

ratio, the near-field pressure external to the jet can still likely be approximated by that of a single-stream jet. In flight, the stretching of the outer shear layer likely places the axial position of the trailing-edge within the initial region, where the outer shear layer behaves as that of a single-stream jet and thus the near-field is likely also developing as such.

6.3.5 Azimuthal Directivity

In Chapter 5 it was suggested that strip theory could be used to model trailing edge scattering from the cranked wings used on commercial airliners. The SYMPHONY project used a realistic wing planform with a crank, and also used an azimuthal ring array of microphones. This allows the azimuthal directivities of the two scattering models (infinite span and strip theory) to be compared to the measured data, providing an indication of the suitability of strip theory for modelling cranked wings.

The Stargate azimuthal array was only deployed for jet condition 8 with $U_\mathrm{f} = 0$ and 102 m/s. In flight, the difference between the installed noise and isolated mixing noise is low. Thus, away from the peak, the JSI OASPL is quickly masked beneath the mixing noise. Statically, the prediction tool has been shown to overpredict in the mid and rear arcs. Therefore, a comparison of the OASPL directivity will first be performed at $U_\mathrm{f} = 102$ m/s and $\theta = 110°$. This will then be followed by a comparison for the static case. Unfortunately, the maximum polar angle at which the Stargate array could be positioned is $\theta = 110°$; a larger angle would have increased the difference between installed and isolated noise in flight, and allowed for a static comparison further into the forward arc. In order to compare the directivity, the amplitudes will be normalised to that of the peak on the shielded side of the wing, because the prediction tool does not account for reflection of jet mixing noise from the wing. To demonstrate the effect of strip theory, the directivity will also be calculated using the prediction tool for wings of the same chord and span, with and without sweep.

Figure 6.24 displays the OASPL measured on the Stargate array and predicted using the model at $U_\mathrm{f} = 102$ m/s and $\theta = 110°$. It is clear from looking at the measured data that the OASPL amplitude is higher on outboard (i.e. $0° < \phi < 180°$) side of the model than on the inboard side((i.e. $180° < \phi < 360°$)). The amplitude is also higher on the unshielded side of the wing ($-90° < \phi < 90°$) than on the shielded side ($90° < \phi < 270°$). The outboard shift has been shown[58–60, 71, 115] to be the effect of a backward-swept wing. The discrepancy in amplitude between the unshielded ($\phi = 0°$) and shielded ($\phi = 180°$) sides of the wing could be due to the corrupting presence of reflected jet mixing noise also in the spectra over the OASPL frequency integration range. In comparison, the model (using strip theory) and the swept (infinite span) directivities both show the same outboard shift and a good comparison to the measured

OASPL on the shielded side. The unswept (infinite span) prediction shows no shift at all, with the directivity peaking directly above and below the wing.

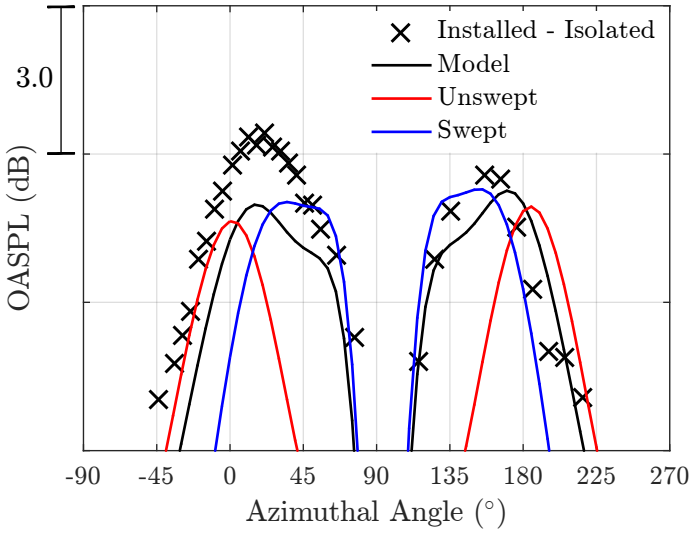

FIGURE 6.24: Comparison of measured installed jet noise with model prediction. Nozzle S33-A55, $l/D_s = 2.35$, $\theta = 110°$, $h/D_s = 0.81$ and condition 8F8 ($U_s = 292$ m/s, $U_p = 378$ m/s and $U_f = 102$ m/s.

Figure 6.25 displays comparisons of the directivity of the prediction tool with that of the experimental data without the flight stream. The same trends in the measured directivity discussed with Figure 6.24 are visible in Figure 6.25. Figure 6.25 does show, however, that the amplitude of the measured OASPL on the unshielded side of the wing increases relative to that on the shielded side as polar angle, θ increases. The predictions, on the other hand, have a higher amplitude on the shielded side of the wing, as the distance from trailing edge to the microphone is shorted compared the unshielded side. Of the three predictions, the model (using strip theory) directivity compares best with the measured data, the swept directivity now underpredicting the amplitude noticeably on the inboard side.

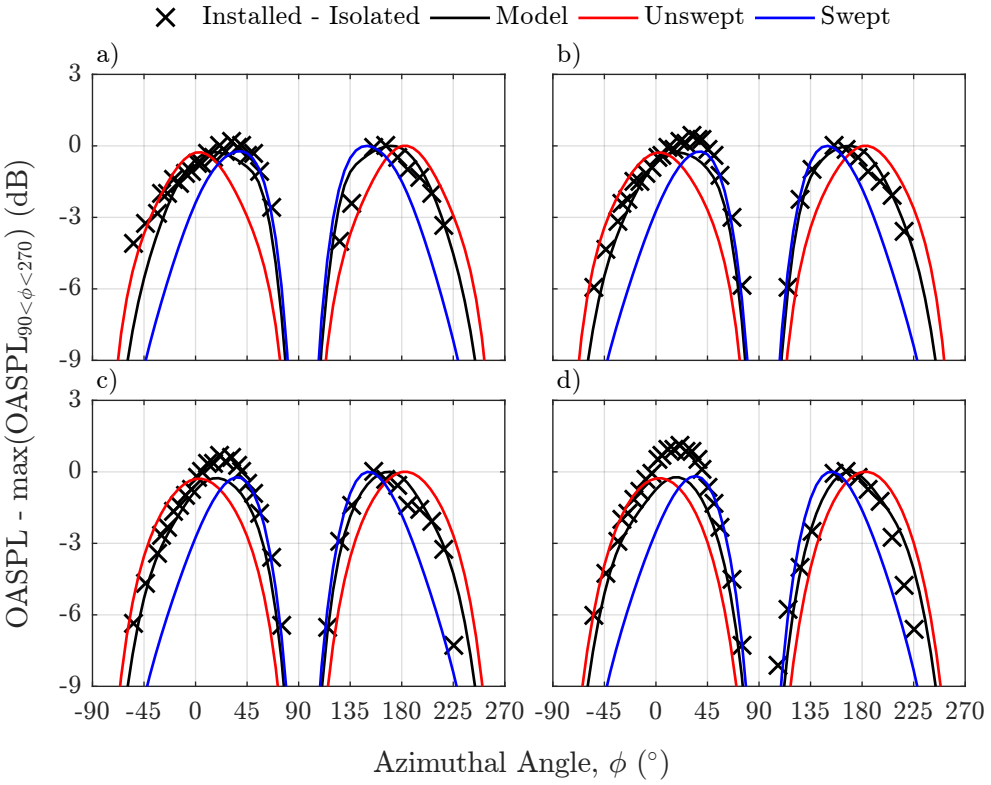

FIGURE 6.25: Comparison of measured installed jet noise with model prediction. Nozzle S33-A55, $l/D_s = 2.35$, $\theta = 110°$, $h/D_s = 0.81$ and condition 8S ($U_s = 292$ m/s, $U_p = 378$ m/s and $U_f = 0$ m/s).

Overall, the results show that strip theory can be used to improve JSI noise predictions for cranked wing geometries. However, it would appear that for cases displayed here one could assume the wing to be fully swept. If the span of the wing is also assumed to be infinite, then the scattering solution would be purely analytical, significantly reducing the calculation time for each observer location.

6.3.6 Flap Deployment

Nozzle S33-P51 is the most realistic of the three nozzles, with bullet, bifurcations and pylon. The bifurcations and pylon break the axisymmetry of the nozzle, which could affect the development of the hydrodynamic pressure field. This nozzle was also used with the most realistic wing locations, with the trailing edge within the flow field of the equivalent isolated jet. This close positioning of the wing could also distort the jet and hydrodynamic pressure field, which would in turn affect the JSI noise.

A comparison between the prediction tool and measurements is made in Figure 6.26 for a static condition. The overall trends are the same as for the axisymmetric nozzle(S33-A55), the amplitude and spectral shape match well at polar angle $\theta = 130°$, however at lower angles the model increasingly overpredicts. At this trailing edge location the

wing is likely to distort the jet. This is accounted for in the prediction tool very simply, by setting the radial trailing edge location to the edge of the shear layer (as described at the beginning of this chapter). Therefore, at lower radial trailing edge locations the amplitude of the JSI noise prediction will remain constant.

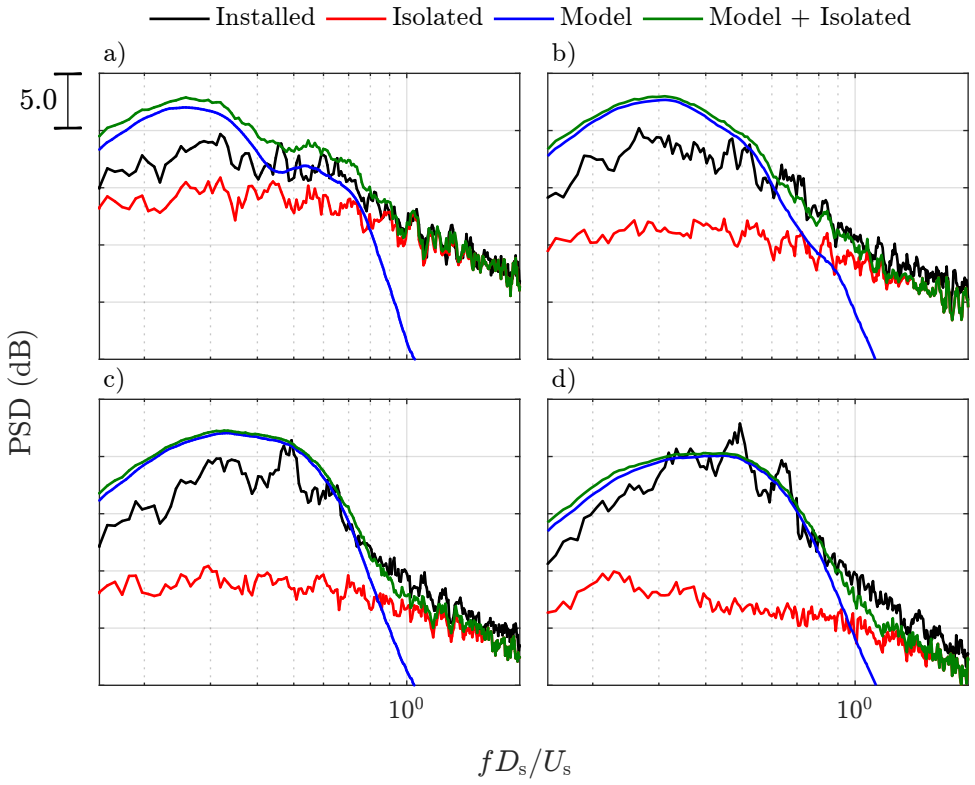

FIGURE 6.26: Comparison of measured installed jet noise with model prediction. Nozzle S33-P51, $l/D_s = 2.35$, $h/D_s = 0.66$ and condition 6aS ($U_s = 245$ m/s, $U_p = 268$ m/s and $U_f = 0$ m/s). a) $\theta = 70°$; b) $\theta = 90°$; c) $\theta = 110°$; and, d) $\theta = 130°$.

Introducing a co-flow has been shown to reduce the model overprediction observed in the rear arc for the axisymmetric nozzles. Additionally, the co-flow stretches the jet, reducing the width of the shear layer at the trailing edge location and hence reducing the potential for distortion of the jet by the trailing edge. In Figure 6.27 the model and measured spectra are compared at a flight velocity of 102 m/s. The overprediction in the rear arc has reduced and the spectral shapes display good agreement up to a polar angle of $\theta = 110°$. The amplitude does appear though to have reduced to the point where the amplitude is slightly underpredicted, and at $\theta = 130°$ the spectral shapes no longer match. Without information of the jet flow field it is difficult to understand why the amplitude is underpredicted, and spectral shape so different at $\theta = 130°$.

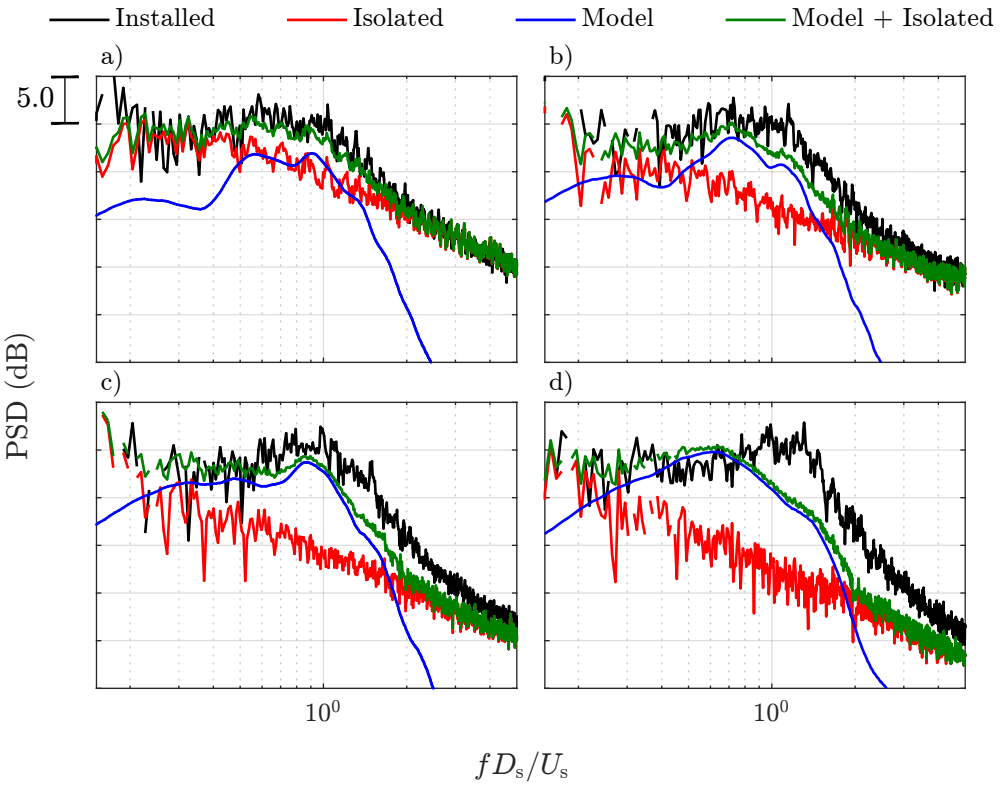

FIGURE 6.27: Comparison of measured installed jet noise with model prediction. Nozzle S33-P51, $l/D_s = 2.35$, $h/D_s = 0.66$, $\phi = 0°$ and condition 6aF8 ($U_s = 245$ m/s and $U_f = 102$ m/s). a) $\theta = 70°$; b) $\theta = 90°$; c) $\theta = 110°$; and, d) $\theta = 130°$.

During take off and landing, aeroplanes deploy flaps in order to increase the maximum amount of lift the wing can produce; this helps in lowering the take-off and landing speeds. Typically, modern airliners use single slotted fowler flaps that extend the wing trailing edge backwards and then tilt downwards. This positions the trailing edge closer to and at an angle to the nozzle axis, which can severely distort the jet.

In Figure 6.28 is displayed the measured and predicted spectra for a 32° flap deployment, placing the trailing edge inside the nozzle lip line, at a flight velocity of 102 m/s. There has clearly been a large increase in noise across the whole spectrum in comparison to the wing configurations used thus far. This will be due to a variety of reasons, such as an increase in wing self-noise, due to the washing of the underside of the wing by the jet, and changes to the mixing noise, due to the distortion of the shear layer. There are also tones in the spectra (they are more apparent in Figure 6.29 at a lower flight velocity), which have been studied by Lawrence[18, 133] and shown by Jordan et al.[134] to be due to trapped waves within the potential core of the jet.

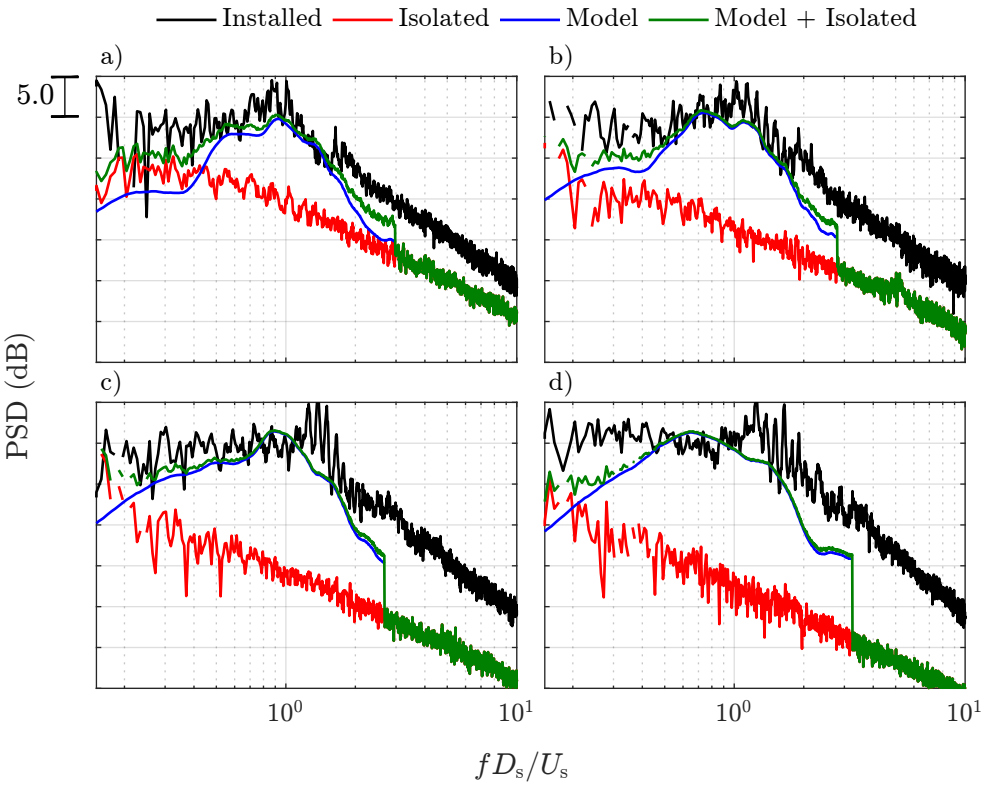

FIGURE 6.28: Comparison of measured installed jet noise with model prediction. Nozzle S33-P51, $l/D_s = 2.54$, $h/D_s = 0.36$, $\beta = 32°$ and condition 6aF8 ($U_s = 292$ m/s, $U_p = 268$ m/s and $U_f = 102$ m/s). a) $\theta = 70°$; b) $\theta = 90°$; c) $\theta = 110°$; and, d) $\theta = 130°$.

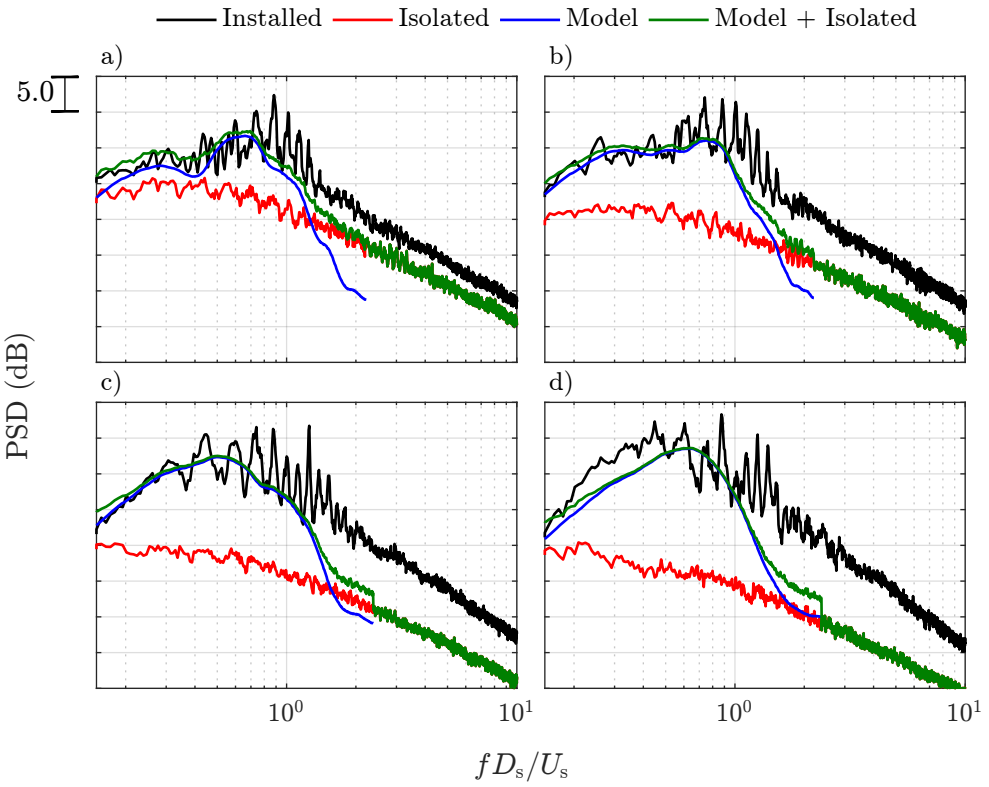

FIGURE 6.29: Comparison of measured installed jet noise with model prediction. Nozzle S33-P51, $l/D_s = 2.54$, $h/D_s = 0.36$, $\beta = 32°$, $\phi = 0°$ and condition 6aF1 ($U_s = 292$ m/s and $U_f = 52$ m/s). a) $\theta = 70°$; b) $\theta = 90°$; c) $\theta = 110°$; and, d) $\theta = 130°$.

The prediction tool, which uses the near-field pressure spectra of an isolated jet as the input, does not account for any of the aforementioned changes to the jet. Neither does the tool account for the change in shape of the wing, still assuming that the wing is in a plane parallel to the nozzle axis. Also, as previously mentioned, the tool assumes that the trailing edge is at the edge of the isolated jet flow field, not at the true trailing edge location. It is therefore surprising that the predicted spectra are in anyway comparable to the measurements, but below a Strouhal number of one there appears to be fair amount of agreement in shape and amplitude. It would be necessary to remove the noise due to the other new/enhanced sources before a better comparison could be made.

In Figure 6.28 the model prediction cuts off at a Strouhal number of approximately three, despite being above the level of the isolated jet mixing noise. This is due to the acoustic field contaminating the hydrodynamic pressure field in the near-field pressure spectra used as the input to the model at higher Strouhal numbers. If, as in this case, higher Strouhal numbers are required, the input would have to be modified in order to remove the acoustic field from the near-field pressure spectra.

6.4 Summary

A JSI noise prediction tool has been created based on (i) the scaling laws developed in Chapter 4, (ii) the jet near-field pressure measurements of Lawrence, and (iii) the JSI noise model (cylindrical harmonic propagation coupled with Amiet's trailing edge scattering theory) of Lyu & Dowling. The prediction tool has been verified against large model-scale installed jet noise measurements taken in QinetiQ's NTF using realistic dual stream nozzle and high-lift wing and fuselage surface geometries.

Comparison of the prediction tool with the axisymmetric single stream nozzle, S33-ASS, showed the ability to scale to much larger nozzle diameters. Also, while the U_j frequency scaling, found in Chapter 4, was seen not to work in flight, a $U_\mathrm{j} + U_\mathrm{f}$ correction showed the predictions to compare well with the measurements. However, the amplitude of the installed spectrum was increasingly overpredicted with decreasing polar in the rear arc for the static case. This is currently believed to be due to the assumption that the pressure incident on the trailing edge is stationary, however further study is necessary.

Next, the prediction tool was compared to measurements from an axisymmetric, coaxial bulleted nozzle, with primary and secondary flows. Other than the consistent overprediction in the rear arc for the static jet cases, the amplitude and spectral shapes of the predictions compared well with the measured data. This provides further evidence that the effective nozzle diameter should be used to scale the jet hydrodynamic pressure field of an annular bulleted jet. The good comparison of the spectra and the variation in OASPL with radial trailing edge location also gives confidence in the modelling of the axial wavenumber. Finally, a comparison of azimuthal OASPL directivities, with cranked, fully unswept and fully swept planform geometries successfully demonstrated the applicability of strip theory to model more representative airframes, particularly regarding cranked wings.

Finally, the model was compared to the most realistic nozzle geometry, including the engine-airframe pylon and internal nozzle bifurcations. In flight there was good agreement between the prediction tool and the measured data for the clean wing case. For the deployed flap cases, the flap distorts the jet, modifying and adding to the noise sources. For these cases the JSI noise model no longer captures the physics of the installed jet noise.

Chapter 7

Conclusions and Future Work

7.1 Conclusions

The aim of this thesis was to produce a semi-empirical jet-surface interaction noise model that could be used by industry. To this end, methods for scaling an isolated jet's hydrodynamic pressure field with jet velocity, flight velocity, core nozzle and secondary nozzle area have been evidenced. Combined with a database of jet near-field pressure measurements, the hydrodynamic axial wavenumber and spectrum make up the input to a jet-surface interaction noise model that incorporates cylindrical harmonic near-field propagation theory and acoustic edge scattering theory. The model has been validated against installed jet noise measurements using a co-flow to simulate the effect of flight. The model has then been extended with Roger & Moreau's back-scattering theory, to capture the physics of finite chord of real wings. Finally, strip theory has been used to describe the scattering from the sections of cranked wings on airliners. The resulting prediction tool is seen to compare well with large model-scale laboratory measurements of in-flight installed jet noise.

In Chapter 4, unsteady pressure measurements were taken in the near field of laboratory jets, both with and without a co-axial flight stream flow. These measurements were used to demonstrate various scaling laws for jet hydrodynamic pressure spectra and to create inputs for the jet-surface interaction noise calculations in the later chapters. The static spectra were used to provide further evidence of the manner in which the peak amplitude and frequency of the hydrodynamic pressure field scales. The former scaling with jet velocity cubed, and the latter with jet velocity. A comparison of large and small nozzle pressure spectra provided evidence of peak amplitude and frequency scaling with nozzle diameter and the reciprocal of nozzle diameter, respectively. Measurements of the jet near-field pressure within the flight stream were used to demonstrate that, if the axial location of the microphone relative to the potential core length is kept constant, then the amplitude of the hydrodynamic pressure spectra scales with $(U_\mathrm{j} - U_\mathrm{f})^3$. Using LES,

it was demonstrated that the peak axial wavenumber of the hydrodynamic pressure field could be approximated as a linear function of Strouhal number. Finally, far-field measurements of installed jet noise are used to show that an effective diameter based on flow area can be used to scale the hydrodynamic pressure spectra of bulleted nozzles.

In Chapter 5, far-field installed jet noise measurements were taken using a co-flow to simulate the effect of forward motion on the jet. These measurements were used to validate the jet-surface interaction noise model of Lyu & Dowling in flight. Additional measurements using plates with shorter, more realistic, chord lengths, have shown that the model increasingly overpredicts jet-surface interaction noise in the rear arc as jet velocity is increased. Roger & Moreau's back-scattering theory was also included to improve the predictions with the shorter chord lengths. This improved the prediction of the spectral shape and amplitude at very low frequencies but did not improve the over-prediction in the rear arc. It is then demonstrated that at least azimuthal modes 0 and 1 of the hydrodynamic field are required to produce the correct azimuthal directivity on the installed round laboratory jet. Finally, it is suggested that cranked wing geometries could be modelled by splitting the wing into strips, each with constant trailing edge sweep, retaining coherence between the strips. This is shown in the following chapter to improve the predicted azimuthal directivity of cranked wings, however the use of strip theory requires numeric integration, which increases the time and complexity required to converge on a solution. This integral also spans a singularity and a robust manner in which to deal with this is still required if it is to be used in industry.

Finally, in Chapter 6, a jet-surface interaction noise prediction tool has been assembled. The prediction tool is based on the jet near-field pressure measurements of Lawrence, the jet hydrodynamic pressure scaling methods presented in Chapter 4, cylindrical harmonic propagation for the near-field pressure, edge scattering theory and strip theory to represent realistic wing planforms. This prediction tool has then been compared with large-scale far-field installed jet noise measurements taken in QinetiQ's Noise Test Facility, using more realistic nozzle and airframe geometries. While the comparison has shown the model to overpredict the amplitude of the static jet in the mid to rear arcs, the prediction tool accurately captures the amplitude and spectral shape of the installed jets in flight.

7.2 Future Work

The next key aspect of the jet-surface interaction noise prediction tool that requires development is the prediction of the jet hydrodynamic source pressure field itself. Predictions are currently made using hydrodynamic pressure spectra from an isolated jet together with a crude empirical correction made wing locations likely to significantly distort the jet flow field. Work is therefore required to understand how the wing distorts

the jet, and what effect this has on the incident hydrodynamic pressure. Further in-flight near-field pressure investigations should also be taken to understand how the peak frequency of the hydrodynamic pressure field scales in flight. Ideally, in-flight azimuthal modal decompositions should be performed and used as the input to the jet-surface interaction noise model. This would serve to improve the predictions at angles closer to the sideline observer location or for wings with swept trailing edges.

Thus far, the effect of flight on jet-surface interaction noise has been included within Amiet's theory, for the trailing-edge scattering, and via an empirical scaling method for the incident hydrodynamic source pressure field. Additionally, for a full-scale installed jet, the wing would generate lift in flight. This lift force may bend or distort the jet modifying the hydrodynamic pressure field incident on the trailing edge. To model such an effect will require understanding of the lift produced by the wing and the effect this has on the jet both in the model-scale scenario, with a finite flight stream, and in the full-scale infinite flight stream situation.

The model has been seen to overpredict jet-surface interaction noise in the rear arc, especially at high jet velocities. This is thought to be due to the assumption that the pressure incident on the trailing edge is stationary. This assumption could be removed using the conical Greens function used by Vera, or the Gaussian near-field pressure distribution used by Bychkov & Faranosov. To further investigate whether the assumed incident pressure is the cause, numerical experiments could be conducted to understand how the incident pressure distribution affects the far-field pressure scattered by the surface.

Currently, the jet-surface interaction noise from a cranked wing is calculated by splitting the wing into several strips, each with constant trailing edge sweep, and applying Amiet's theory to each strip. With Amiet's theory the scattered surface pressure is first calculated assuming the surface to be semi-infinite, whereupon the far-field scattered pressure is calculated by applying Curle's theory to the finite region occupied by a strip. This means that the effect of the crank on the surface pressure is not accounted for. An analytical solution should, therefore, be sought to improve the model and to explore whether changes to the crank geometry can influence jet-surface interaction noise.

Airliner wings do not have constant chord and the planform can often be split into two trapezoid sections. Each section could then be modelled using Amiet's theory, without incorporating back-scattering. To include back-scattering, each wing section needs to be approximated with parallelograms to arrive at a fully analytical solution. Further research is required to determine whether there is a benefit to including back-scattering theory for such planforms, and, if so, what chord should be used to best represent the trapezoid sections as parallelograms.

Appendix A

Spanwise Fourier Transform

In order to calculate JSI noise, Lyu & Dowling take measurements of the unsteady near-field pressure of an isolated jet using a ring array of microphones. Assuming the near-field pressure to be stationary, cylindrical harmonics are used to propagate the near-field measurements, taken at the axial location of the trailing edge, onto the surface. Then, in order to make use of Amiet's theory, the incident pressure is decomposed in to spanwise wavenumber components by taking a Fourier transform along y_2,

$$p'_{\mathrm{I}}(\omega, m, k_2) = \frac{p'(\omega, m)}{2\pi} \int_{-\infty}^{\infty} \mathrm{K}_m \left(\iota_r \sqrt{h^2 + y_2^2} \right) \mathrm{e}^{\mathrm{i}m\phi} \, \mathrm{e}^{\mathrm{i}k_2 y_2} \, \mathrm{d}y_2 \tag{A.1}$$

where, using de Moivre's formula,

$$\mathrm{e}^{\mathrm{i}m\phi} = \left(\sum_{n=0}^{\lfloor |m|/2 \rfloor} (-1)^n \binom{|m|}{2n} \frac{h^{|m|-2n} y_2^{2n}}{(h^2 + y_2^2)^{|m|/2}} + \mathrm{i} \sum_{n=0}^{\lfloor (|m|-1)/2 \rfloor} (-1)^n \binom{|m|}{2n+1} \frac{m}{|m|} \frac{h^{|m|-(2n+1)} y_2^{2n+1}}{(h^2 + y_2^2)^{|m|/2}} \right). \tag{A.2}$$

The Fourier transform along y_2 can be completed using the following integral representation for the modified Bessel function of the second kind,

$$\mathrm{K}_m(z) = \frac{1}{2}\left(\frac{z}{2}\right)^m \int_0^\infty \frac{1}{t^{m+1}}\,\mathrm{e}^{-t-z^2/4t}\,\mathrm{d}t, \tag{A.3}$$

where the following identity has also been used

$$\mathrm{K}_{-m}(z) = \mathrm{K}_m(z). \tag{A.4}$$

Working through the real component of the incident pressure as an example, the following integral needs to be evaluated

$$\int_{-\infty}^{\infty} \frac{y_2^{2n}}{\sqrt{h^2+y_2^2}}\,\mathrm{e}^{\,\mathrm{i}k_2 y_2}\,\mathrm{K}_m(\iota_r\sqrt{h^2+y_2^2})\,\mathrm{d}y_2. \tag{A.5}$$

Substituting the integral representation of the Bessel function into the preceding integral leads to

$$\int_0^\infty \frac{\iota_r^m}{2^{m+1}t^{m+1}}\,\mathrm{e}^{-t-(\iota_r h)^2/4t}\int_{-\infty}^{\infty} y_2^{2n}\,\mathrm{e}^{\,\mathrm{i}k_2 y_2-(\iota_r y_2)^2/4t}\,\mathrm{d}y_2\,\mathrm{d}t. \tag{A.6}$$

The Fourier transform can be evaluated using standard identities,

$$\int_0^\infty \frac{\iota_r^m}{2^{m+1}t^{m+1}}\,\mathrm{e}^{-t-(\iota_r h)^2/4t}\,\mathrm{i}^{2n}\frac{\mathrm{d}^{2n}}{\mathrm{d}k_2^{2n}}\left[\frac{2\sqrt{\pi t}}{\iota_r}\,\mathrm{e}^{-(k_2/\iota_r)^2 t}\right]\mathrm{d}t, \tag{A.7}$$

which is then rearranged into the following form

$$\frac{\mathrm{i}^{2n}\sqrt{\pi}\iota_r^{m-1}}{2^m}\frac{\mathrm{d}^{2n}}{\mathrm{d}k_2^{2n}}\int_0^\infty \frac{1}{t^{m+1/2}}\,\mathrm{e}^{-t(1+[k_2/\iota_r]^2)-(\iota_r h)^2/4t}\,\mathrm{d}t. \tag{A.8}$$

Now, by using the transform

$$u = (1+[k_2/\iota_r]^2)t, \tag{A.9}$$

the integral form of the Bessel function can be returned

$$\frac{\mathrm{i}^{2n}\sqrt{2\pi}}{\iota_r^m h^{m-1/2}}\frac{\mathrm{d}^{2n}}{\mathrm{d}k_2^{2n}}\frac{1}{2}\left(\frac{h\sqrt{\iota_r^2+k_2^2}}{2}\right)^{m-1/2}[\iota_r^2+k_2^2]^{m/2-1/4}\int_0^\infty \frac{1}{u^{m+1/2}}\,\mathrm{e}^{-u-h^2[\iota_r^2+k_2^2]/4u}\,\mathrm{d}u, \tag{A.10}$$

and the result of the integral is

$$\frac{\mathrm{i}^{2n}\sqrt{2\pi}}{\iota_r^m h^{m-1/2}}\frac{\mathrm{d}^{2n}}{\mathrm{d}k_2^{2n}}\left[(\iota_r^2+k_2^2)^{m/2-1/4}\,\mathrm{K}_{m-1/2}\left(h^2\sqrt{\iota_r^2+k_2^2}\right)\right]. \tag{A.11}$$

Applying this method to the full equation Equation A.1 results in the following expression for the spanwise wavenumber spectrum

$$\begin{aligned} p'_{\mathrm{I}}(\omega,m,k_2) = \frac{p'(\omega,m)}{2\pi}\int_{-\infty}^{\infty}\mathrm{K}_m\left(\iota_r\sqrt{h^2+y_2^2}\right)\mathrm{e}^{\,\mathrm{i}m\phi}\,\mathrm{e}^{\,\mathrm{i}k_2y_2}dy_2 = \\ \frac{p'(\omega,m)}{\sqrt{2\pi}}\left(\sum_{n=0}^{\lfloor|m|/2\rfloor}\binom{|m|}{2n}h^{-2n+1/2}\iota_r^{-|m|}\frac{\mathrm{d}^{2n}}{\mathrm{d}k_2^{2n}}\left[(\iota_r^2+k_2^2)^{|m|/2-1/4}\,\mathrm{K}_{|m|-1/2}\left(h\sqrt{\iota_r^2+k_2^2}\right)\right]\right. \\ \left.-\frac{m}{|m|}\sum_{n=0}^{\lfloor(|m|-1)/2\rfloor}\binom{|m|}{2n+1}h^{-2n+1/2}\iota_r^{-|m|}\frac{\mathrm{d}^{2n}}{\mathrm{d}k_2^{2n}}\left[k_2(\iota_r^2+k_2^2)^{|m|/2-3/4}\,\mathrm{K}_{|m|-3/2}\left(h\sqrt{\iota_r^2+k_2^2}\right)\right]\right). \end{aligned} \tag{A.12}$$

While this solution is valid for all modes, to date, published results have only used azimuthal modes of orders 0 and 1, which have been shown to contain the majority of the energy in the hydrodynamic field for axisymmetric jets. This is fortunate, as it is not necessary to evaluate any derivatives in Equation A.12 for azimuthal modes of orders 0 and 1. However, it is possible that for non-axisymmetric jets, such as those with pylons or chevrons, significant amounts of energy may also be seen in higher-order modes. It may also be necessary to include higher-order modes for swept wings, or observer azimuthal angles near the plane of the scattering surface.

As mentioned, the form of the spanwise-wavenumber spectra in Equation A.12, is easy to evaluate for $|m| \leq 1$. However, for $|m| > 1$ derivatives with respect to k_2 need to be evaluated, which to do numerically would need very careful treatment. Instead, the derivatives can be evaluated

in Equation A.7, where

$$\frac{\mathrm{d}^{2n}}{\mathrm{d}k_2^{2n}}\,\mathrm{e}^{-(k_2/\iota_r)^2 t} = \mathrm{e}^{-(k_2/\iota_r)^2 t}\sum_{o=0}^{n}(-1)^{2n-o}\frac{(2n)!(2k_2)^{2n-2o}}{o!(2n-2o)!}\left(\frac{t}{\iota_r^2}\right)^{2n-o}. \tag{A.13}$$

Substituting this series back into Equation A.7 and continuing with the derivation, the solution becomes

$$\begin{aligned} p'_{\mathrm{I}}(\omega,m,k_2) = \frac{p'(\omega,m)}{2\pi}\int_{-\infty}^{\infty}\mathrm{K}_m\left(\iota_r\sqrt{h^2+y_2^2}\right)\mathrm{e}^{\mathrm{i}m\phi}\,\mathrm{e}^{\mathrm{i}k_2 y_2}\,\mathrm{d}y_2 = \\ \frac{p'(\omega,m)}{\sqrt{2\pi}}\left(\sum_{n=0}^{\lfloor|m|/2\rfloor}\binom{|m|}{2n}\frac{1}{\iota_r^{|m|}}\sum_{o=0}^{n}(-1)^{2n-o}\frac{(2n)!k_2^{2n-2o}}{o!(2n-2o)!2^o h^{o-1/2}}[\iota_r^2+k_2^2]^{|m|/2-1/4-n+o/2}\,\mathrm{K}_{|m|-1/2-2n+o}\left(h\sqrt{\iota_r^2+k_2^2}\right)\right. \\ \left.-\frac{m}{|m|}\sum_{n=0}^{\lfloor(|m|-1)/2\rfloor}\binom{|m|}{2n+1}\frac{1}{\iota_r^{|m|}}\sum_{o=0}^{n}(-1)^{2n+1-o}\frac{(2n+1)!k_2^{2n+1-2o}}{o!(2n+1-2o)!2^o h^{o-1/2}}[\iota_r^2+k_2^2]^{|m|/2-3/4-n+o/2}\,\mathrm{K}_{|m|-3/2-2n+o}\left(h\sqrt{\iota_r^2+k_2^2}\right)\right). \end{aligned} \tag{A.14}$$

This solution replaces the derivatives with series summations, and is thus much easier to evaluate numerically.

The solution, and implementation, was validated by comparison with a numerical calculation of the spanwise-wavenumber spectrum (Figure A.1). The numerical solution was created by calculating the incident pressure at points on a line along y_2 using Equation 2.99 with a single mode and axial wavenumber. A Discrete Fourier Transform (DFT) was then taken across the points on the line.

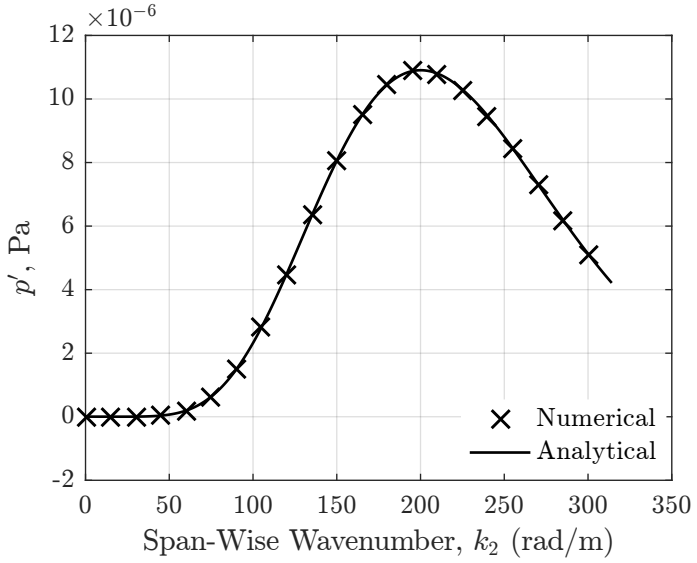

FIGURE A.1: Comparison of numerical and analytical solutions for the spanwise wavenumber spectrum along the trailing edge of a plate. Azimuthal mode order, m, is equal to nine.

Appendix B

Large-Eddy Simulation

Several sets of LES data (described below) were available to support the analysis of JSI noise in this thesis. The simulations were created by Zhong-Nan Wang and Iftehkar Naqavi at the University of Cambridge.

B.1 HARMONY

As part of the HARMONY project, a LES was created[112] of a cold jet, with a Mach number of 0.875, produced by an axisymmetric single-stream nozzle. During the simulation, flow properties were recorded on two FWH surfaces (Figure B.1) surrounding the jet and spaced $1D$ apart. Each FWH surface consists of rings of probes from $x/D = 0$ to $x/D = 10$ with an axial spacing of $0.25D$. Each ring consists of 17, 16 equally spaced and 1 repeated, probes, which combine to produce a cone about the jet with an angle of ten degrees, starting at $x/D = 0$, $r/D = 0.75$ on the lower surface.

The total sample time of the flow parameters on the FWH surface allows for a lower Strouhal number limit of 0.0085. The upper Strouhal limit is determined by the mesh resolution, which is dependent on the position of the probe. For the lower FWH surface the upper Strouhal limit is 3, while for the upper FWH the upper Strouhal limit is 2.

In order to compute the PSD and/or CPSD on the FWH surfaces, Welch's method has been used. A bandwidth equivalent to a Strouhal number of 0.034 has been used. With a 50% overlap this allows for 7 averages, which helps to improve the statistical significance of the results. Ideally more averages would be conducted, however, this would involve reducing the number of samples used for each Fourier transform, which increases the lowest resolved frequency and for JSI noise it is the low frequencies which are of most interest. Hamming windows were applied to the time series, in order to reduce the side lobes produced by the finite Fourier transform.

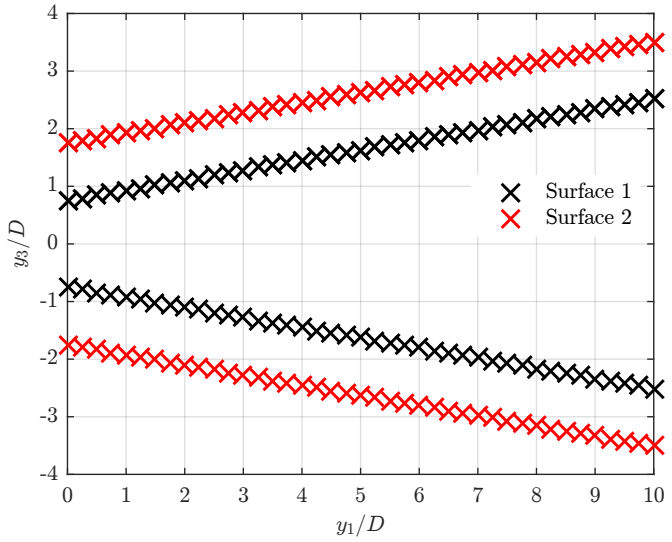

FIGURE B.1: Location of probes on the HARMONY LES FWH surfaces in the $y_2 = 0$ plane

B.2 Doak

A series of LESs[106, 107] have been run based on the geometry of the 38.1 mm Doak jet nozzle at a acoustic Mach number of 0.6. This choice of geometry and Mach number allows direct comparison with the acoustic measurements of Lawrence[18] and hot-wire velocity measurements of Proenca.[98, 135]

For the isolated jet LES, three FWH surfaces are available. Each consists of conical surface from $x/D = -1$ to $x/D = 20$ followed by a cylindrical surface up to $x/D = 30$. The surfaces are made up of rings of 129, 128 equally spaced and 1 repeated, probes spaced axially $0.2D$ apart. At $x/D = -1$ and $x/D = 30$ rings of probes were positioned radially to close off the upstream and downstream ends of the surfaces.

Also available are probes positioned on cylinders within and in the near-field of the jet. These probes are positioned in rings of 32 equally spaced microphones, with the rings positioned $0.25D$ apart radially and $0.5D$ axially, between $r/D = 0.5$ and $r/D = 4$.

The FWH surfaces have been sampled with a time step of $6\text{E}-6$ s for a total of 6000 samples. This gives a total simulation time of ≈36 ms and a Nyquist Strouhal number of ≈ 16. This Nyquist frequency is not realisable, however, as it is also affected by the mesh resolution, which is capable of computing Strouhal numbers up to two.

Appendix C

Alternate Swept Wing Derivation

As with the straight trailing edge case the scattered field is described by the convected Helmholtz equation

$$k^2 p' - 2ikM\frac{\partial p'}{\partial y_1} + (1-M^2)\frac{\partial^2 p'}{\partial y_1^2} + \frac{\partial^2 p'}{\partial y_2^2} + \frac{\partial^2 p'}{\partial y_3^2} = 0, \tag{C.1}$$

and the first part of the solution for the scattered surface pressure is, as before,

$$p_{\,\mathrm{S1}} = p'_{\mathrm{I}}(\omega, k_1, k_2)\,\mathrm{e}^{-\,\mathrm{i}k_1 y_1 - \,\mathrm{i}k_2 y_2}. \tag{C.2}$$

However, the boundary conditions for the second part of the solution are now given by

$$\frac{\partial p'_{\mathrm{S2}}}{\partial y_3} = 0, y_1 < y_2\tan(\psi) \tag{C.3}$$

and

$$p'_{\mathrm{S2}} = -p'_{\mathrm{I}}\,\mathrm{e}^{-\,\mathrm{i}k_1 y_1 - \,\mathrm{i}k_2 y_2}, y_1 \geq y_2\tan(\psi). \tag{C.4}$$

Now, in order to make use of Schwarzchild's solution,[41] the following transforms are required

$$\tilde{y}_1 = \frac{y_1}{\beta}\cos(\tilde{\psi}) - y_2\sin(\tilde{\psi}), \tag{C.5}$$

$$\tilde{y}_2 = \frac{y_1}{\beta}\sin(\tilde{\psi}) + y_2\cos(\tilde{\psi}), \tag{C.6}$$

$$\tilde{y}_3 = y_3 \tag{C.7}$$

and

$$p' = \tilde{p}'\,\mathrm{e}^{\,\mathrm{i}\tilde{k}M(\tilde{y}_1\cos(\alpha) + \tilde{y}_2\sin(\alpha))}, \tag{C.8}$$

where

$$\tan(\tilde{\psi}) = \tan(\psi)/\beta. \tag{C.9}$$

This leads to a static form of the Helmholtz equation

$$\tilde{k}^2\tilde{p}' + \frac{\partial^2\tilde{p}'}{\partial\tilde{y}_1^2} + \frac{\partial^2\tilde{p}'}{\partial\tilde{y}_2^2} + \frac{\partial^2\tilde{p}'}{\partial\tilde{y}_3^2} = 0. \tag{C.10}$$

The boundary conditions for the second part of the scattered surface pressure are now

$$\frac{\partial\tilde{p}'_{\mathrm{S2}}}{\partial\tilde{y}_3} = 0, \tilde{y}_1 < 0 \tag{C.11}$$

and

$$\tilde{p}'_{\mathrm{S2}} = -p'_{\mathrm{I}}\,\mathrm{e}^{-\mathrm{i}\tilde{y}_1(\tilde{k}_1+\tilde{k}M\cos(\tilde{\psi}))-\mathrm{i}\tilde{y}_2(\tilde{k}_2+\tilde{k}M\sin(\tilde{\psi}))}, \tilde{y}_1 \geq 0, \tag{C.12}$$

where

$$\tilde{k}_1 = \beta k_1\cos(\tilde{\psi}) - k_2\sin(\tilde{\psi}) \tag{C.13}$$

and

$$\tilde{k}_2 = \beta k_1\sin(\tilde{\psi}) + k_2\cos(\tilde{\psi}), \tag{C.14}$$

using

$$y_1 = \beta(\tilde{y}_1\cos(\tilde{\psi}) + \tilde{y}_2\sin(\tilde{\psi})) \tag{C.15}$$

and

$$y_2 = -\tilde{y}_1\sin(\tilde{\psi}) + \tilde{y}_2\cos(\tilde{\psi}). \tag{C.16}$$

Taking a Fourier transform along $\tilde{y}_2$ results in a 2D form of the Helmholtz equation to which Schwarzchild's solution can be applied

$$(\tilde{k}^2 - \tilde{k}_2^2)\tilde{p}' + \frac{\partial^2\tilde{p}'}{\partial\tilde{y}_1^2} + \frac{\partial^2\tilde{p}'}{\partial\tilde{y}_3^2} = 0, \tag{C.17}$$

resulting in

$$p'_{\mathrm{S2}} = p'_{\mathrm{I}}\,\mathrm{e}^{-\mathrm{i}\tilde{y}_1\tilde{k}_1-\mathrm{i}\tilde{y}_2\tilde{k}_2}[(1+\mathrm{i})\,\mathrm{E}(-\tilde{y}_1[\tilde{k}_1 + \tilde{k}M\cos(\tilde{\psi}) + \sqrt{\tilde{k}^2 - \tilde{k}_2^2}]) - 1]. \tag{C.18}$$

The next step is then to scatter this surface pressure to the far-field with Kirchoff/Curle's theory, this will be done in the transformed coordinates, because it allows the integrals to be separated. In the transformed domain the derivative of the free space Greens function normal to the surface is

$$\frac{\partial G}{\partial\tilde{y}_3} \approx \frac{\mathrm{i}\tilde{k}(x_3 - y_3)}{4\pi\beta\tilde{r}_x^2}\,\mathrm{e}^{-\mathrm{i}\tilde{k}(\tilde{r}_x-\tilde{y}_1\tilde{x}_1/\tilde{r}_x-\tilde{y}_2\tilde{x}_2/\tilde{r}_x)+i\tilde{k}M([\tilde{x}_1-\tilde{y}_1]\cos(\tilde{\psi})+[\tilde{x}_2-\tilde{y}_2]\sin(\tilde{\psi}))}. \tag{C.19}$$

First integrating along the spanwise direction

$$\int_{-\tilde{d}/2}^{\tilde{d}/2} \mathrm{e}^{-\mathrm{i}\tilde{y}_2(\tilde{k}_2+\tilde{k}M\sin(\tilde{\psi})-\tilde{k}\tilde{x}_2/\tilde{r}_x)}\,\mathrm{d}\tilde{y}_2 = \tag{C.20}$$

$$\frac{2\sin(\tilde{d}/2(\tilde{k}_2+\tilde{k}M\sin(\tilde{\psi})-\tilde{k}\tilde{x}_2/\tilde{r}_x)}{\tilde{k}_2+\tilde{k}M\sin(\tilde{\psi})-\tilde{k}\tilde{x}_2/\tilde{r}_x}, \tag{C.21}$$

where

$$\tilde{d} = d(\sin^2(\tilde{\psi})/\cos(\tilde{\psi})-\cos(\tilde{\psi})) \tag{C.22}$$

and which in the limit of $\tilde{d}/2 \to \infty$

$$\lim_{\tilde{d}/2\to\infty} \frac{2\sin(\tilde{d}/2(\tilde{k}_2+\tilde{k}M\sin(\tilde{\psi})-\tilde{k}\tilde{x}_2/\tilde{r}_x)}{\tilde{k}_2+\tilde{k}M\sin(\tilde{\psi})-\tilde{k}\tilde{x}_2/\tilde{r}_x} = \tag{C.23}$$

$$2\pi\delta(\tilde{k}_2+\tilde{k}M\sin(\tilde{\psi})-\tilde{k}\tilde{x}_2/\tilde{r}_x). \tag{C.24}$$

Integrating now along the chordwise direction, and applying Amiet's correction, leads to

$$\int_{-\tilde{c}}^{0} [\,\mathrm{E}(-\tilde{y}_1 C_1) - 1/(1+\mathrm{i})]\,\mathrm{e}^{-\mathrm{i}\tilde{y}_1 C_2}\,\mathrm{d}\tilde{y}_1 =$$

$$\frac{1}{\mathrm{i}C_2}\left[\mathrm{e}^{\mathrm{i}C_2\tilde{c}}\,\mathrm{E}(C_1\tilde{c}) - \sqrt{\frac{C_1}{C_1-C_2}}\,\mathrm{E}(\tilde{c}[C_1-C_2]) - \frac{\mathrm{e}^{\mathrm{i}C_2\tilde{c}}}{(1+\mathrm{i})}\right], \tag{C.25}$$

where

$$\tilde{c} = \cos(\tilde{\psi})c/\beta, \tag{C.26}$$

$$C_1 = \tilde{k}_1 + \tilde{k}M\cos(\tilde{\psi}) + \sqrt{\tilde{k}^2-\tilde{k}_2^2} \tag{C.27}$$

and

$$C_2 = \tilde{k}_1 + \tilde{k}M\cos(\tilde{\psi}) - \tilde{k}\tilde{x}_1/\tilde{r}_x. \tag{C.28}$$

Setting

$$\Gamma(\tilde{c}, C_1, C_2) = \mathrm{e}^{\mathrm{i}C_2\tilde{c}}\,\mathrm{E}(C_1\tilde{c}) - \sqrt{\frac{C_1}{C_1-C_2}}\,\mathrm{E}(\tilde{c}[C_1-C_2]) - \frac{\mathrm{e}^{\mathrm{i}C_2\tilde{c}}}{(1+\mathrm{i})} \tag{C.29}$$

the solution for the scattered pressure in the far-field then becomes

$$p'_{\mathrm{S}x} = \frac{(1+\mathrm{i})\tilde{k}x_3}{\tilde{r}_x^2}\,\mathrm{e}^{-\mathrm{i}\tilde{k}(\tilde{r}_x - Mx_1/\beta)} \int\int \frac{p'_{\mathrm{I}}}{C_2}\delta(\tilde{k}_2+\tilde{k}M\sin(\tilde{\psi})-\tilde{k}\tilde{x}_2/\tilde{r}_x)\Gamma(\tilde{c}, C_1, C_2)\,\mathrm{d}k_2\,\mathrm{d}k_1. \tag{C.30}$$

This simplifies to

$$p'_{\mathrm{S}x} = (1+\mathrm{i})\frac{\tilde{k}x_3 p'_{\mathrm{I}}}{\tilde{r}_x^2 C_2}\,\mathrm{e}^{-\mathrm{i}\tilde{k}(\tilde{r}_x - Mx_1/\beta)}\Gamma(\tilde{c}, C_1, C_2), \tag{C.31}$$

with

$$\begin{aligned} k_2 &= \frac{1}{\cos(\tilde{\psi})}[\tilde{k}\tilde{x}_2/\tilde{r}_x - \tilde{k}M\sin(\tilde{\psi}) - \beta k_1 \sin(\tilde{\psi})] \\ &= -k_1\tan(\psi) - \frac{kM\tan(\psi)}{\beta^2} + \frac{kx_1\tan(\psi)}{\beta^3\tilde{r}_x} + \frac{kx_2}{\beta\tilde{r}_x} \end{aligned} \tag{C.32}$$

Appendix D

Trapezium Wing

Commercial jet airliners tend to have wings with differing trailing- and leading-edge sweep. This will affect the scattering of jet noise from the trailing edge both by changing the scattered surface pressure and by changing the surface area which radiates to the far-field. The change to the surface pressure would need to be calculated using a leading-edge correction (and possibly further trailing- and leading-edge corrections), which is further complicated from Roger & Moreau's back-scattering correction by the difference in angle between the leading and trailing edges. However, the change in the radiation integral can be calculated using Amiet's theory alone.

The surface pressure from which the far-field pressure is to be calculated is given by

$$p_{S2} = \mathrm{e}^{-\mathrm{i}k_2 y_2 - \mathrm{i}k_1 y_1}[(1+\mathrm{i})\,\mathrm{E}(-[y_1 - y_2\tan(\psi)]C_1) - 1] \tag{D.1}$$

for a swept trailing edge, where

$$C_1 = \tilde{k} + k_1 - (\tilde{k}_2\tan(\psi) - kM)/(\beta^2 + \tan^2(\psi)). \tag{D.2}$$

Using Curle's theory, the far-field pressure is given by

$$p_{\mathrm{S}x}(\omega,k_1,k_2)=\int_{d_1}^{d_2}\int_{y_2\tan(\psi_{LE})-c}^{y_2\tan(\psi_{TE})}\mathrm{e}^{-\mathrm{i}k_2y_2-\mathrm{i}k_1y_1}[(1+\mathrm{i})\,\mathrm{E}(-[y_1-y_2\tan(\psi)]C_1)-1]\frac{\mathrm{i}\tilde{k}x_3}{4\pi\beta\tilde{r}_x^2}\,\mathrm{e}^{-\mathrm{i}\tilde{k}(\tilde{r}_x-y_1x_1/\beta^2\tilde{r}_x-y_2x_2/\tilde{r}_x)+\mathrm{i}\tilde{k}M(x_1-y_1)/\beta}\,\mathrm{d}y_1\,\mathrm{d}y_2 \quad \text{(D.3)}$$

where $\tilde{k}=k/\beta$ and $\tilde{r}_x=\sqrt{(x_1/\beta)^2+x_2^2+x_3^2}$. Now, because the sweep angles of the trailing edge and leading edge are different, the transform used for the swept wing can't be used alone to complete the integral. Instead, the transforms

$$\tilde{y}_1=y_1-y_2\tan(\psi_{\mathrm{TE}}) \quad \text{(D.4)}$$

and

$$\tilde{y}_2=y_2(\tan(\psi_{\mathrm{LE}})-\tan(\psi_{\mathrm{TE}}))-c \quad \text{(D.5)}$$

are used. Applying these transforms to the integral results in

$$p_{\mathrm{S}x}(\omega,k_1,k_2)=\frac{\mathrm{i}\tilde{k}x_3\tan(\tilde{\psi})\,\mathrm{e}^{-\mathrm{i}\tilde{k}(\tilde{r}_x-Mx_1/\beta)-\mathrm{i}cC_3}}{4\pi\beta\tilde{r}_x^2}\int_{\tilde{d}_1}^{\tilde{d}_2}\int_{\tilde{y}_2}^{0}\mathrm{e}^{-\mathrm{i}\tilde{y}_1C_2-\mathrm{i}\tilde{y}_2C_3}[(1+\mathrm{i})\,\mathrm{E}(-\tilde{y}_1C_1)-1]\,\mathrm{d}\tilde{y}_1\,\mathrm{d}\tilde{y}_2, \quad \text{(D.6)}$$

where $\tan(\tilde{\psi})=\tan(\psi_{\mathrm{LE}})-\tan(\psi_{\mathrm{TE}})$, $\tilde{d}=d\tan(\tilde{\psi})-c$,

$$C_2=k_1+\tilde{k}M/\beta-\tilde{k}x_1/\beta^2\tilde{r}_x \quad \text{(D.7)}$$

and

$$C_3=\frac{\tan(\psi_{\mathrm{TE}})k_1}{\tan(\tilde{\psi})}+\frac{k_2}{\tan(\tilde{\psi})}+\frac{\tan(\psi_{\mathrm{TE}})\tilde{k}M}{\beta\tan(\tilde{\psi})}-\frac{\tan(\psi_{\mathrm{TE}})\tilde{k}x_1}{\beta^2\tilde{r}_x\tan(\tilde{\psi})}-\frac{\tilde{k}x_2}{\tilde{r}_x\tan(\tilde{\psi})}. \quad \text{(D.8)}$$

Completing the first integral

$$p_{\mathrm{S}x}(\omega,k_1,k_2)=\frac{(1+\mathrm{i})\tilde{k}x_3\tan(\tilde{\psi})\,\mathrm{e}^{-\mathrm{i}\tilde{k}(\tilde{r}_x-Mx_1/\beta)-\mathrm{i}cC_3}}{4\pi\beta\tilde{r}_x^2C_2}\int_{\tilde{d}_1}^{\tilde{d}_2}\mathrm{e}^{-i\tilde{y}_2C_3}\left[\mathrm{e}^{-\mathrm{i}\tilde{y}_2C_2}\,\mathrm{E}(-\tilde{y}_2C_1)-\sqrt{\frac{C_1}{C_1-C_2}}\,\mathrm{E}(-\tilde{y}_2[C_1-C_2])+\frac{1-\mathrm{e}^{-\mathrm{i}\tilde{y}_2C_2}}{(1+\mathrm{i})}\right]\mathrm{d}\tilde{y}_2. \tag{D.9}$$

Had y_2 not been transformed, then the final integral would have been hard to complete analytically. However, the solution now fails when the trailing and leading edges are parallel.

Completing now the second integral, the solution for the far-field pressure becomes

$$p_{\mathrm{S}x}(\omega,k_1,k_2)=\frac{(1+\mathrm{i})\tilde{k}x_3\tan(\tilde{\psi})\,\mathrm{e}^{-\mathrm{i}\tilde{k}(\tilde{r}_x-Mx_1/\beta)-\mathrm{i}cC_3}}{4\pi\beta\tilde{r}_x^2C_2}\left[\Gamma(\tilde{y}_2,C_1,C_2,C_3)\right]_{\tilde{d}_1}^{\tilde{d}_2}, \tag{D.10}$$

where

$$\begin{aligned}\Gamma(\tilde{y}_2,C_1,C_2,C_3)=&-\frac{\mathrm{e}^{-\mathrm{i}\tilde{y}_2(C_2+C_3)}}{\mathrm{i}(C_2+C_3)}\,\mathrm{E}(-\tilde{y}_2C_1)-\frac{1}{\mathrm{i}(C_2+C_3)}\sqrt{\frac{C_1}{C_1-C_2-C_3}}\,\mathrm{E}(\tilde{y}_2[C_2+C_3-C_1])+\frac{\mathrm{e}^{-\mathrm{i}\tilde{y}_2C_3}}{\mathrm{i}C_3}\sqrt{\frac{C_1}{C_1-C_2}}\,\mathrm{E}(-\tilde{y}_2[C_1-C_2])\\&-\frac{1}{\mathrm{i}C_3}\sqrt{\frac{C_1}{C_1-C_2-C_3}}\,\mathrm{E}(-\tilde{y}_2[C_1-C_2-C_3])-\frac{1}{1+\mathrm{i}}\frac{\mathrm{e}^{-\mathrm{i}\tilde{y}_2C_3}}{\mathrm{i}C_3}+\frac{1}{1+\mathrm{i}}\frac{\mathrm{e}^{-\mathrm{i}\tilde{y}_2(C_2+C_3)}}{\mathrm{i}(C_2+C_3)}\end{aligned} \tag{D.11}$$

In order to implement this solution, a function is made to look like

$$\frac{\mathrm{E}(xt)}{\sqrt{t}}. \tag{D.12}$$

With this function, when $t=0$ L'Hopital's rule allows the solution to be found,

$$\lim_{t\to0}\frac{\mathrm{E}(xt)}{\sqrt{t}}=x\sqrt{\frac{2}{\pi}}, \tag{D.13}$$

where otherwise the $\frac{1}{\sqrt{t}}$ might make the solution appear singular. The solution will still, however, fail when the sweep angles of the leading and trailing edges are equal, as $\tan(\tilde{\psi}) = 0$. Additionally, this solution is computationally more expensive than for parallel leading and trailing edges, because the amount of Error functions that need evaluating have increased from two to eight.

Appendix E

Modified Back-Scattering Theory

In Chapter 5, the back-scattering theory of Roger & Moreau[43, 51] was shown to improve the JSI noise predictions, created using Amiet's theory, with realistic (in relation to the nozzle diameter) chord lengths. The plates used in that experiment were un-swept. Later on in Chapter 5, comparison was made between the model predictions and experimental measurements using a swept plate with a realistic chord length. Therefore, the back-scattering theory of Roger & Moreau needed to be extended to include swept wings.

The derivation of the swept back-scattering theory starts with the scattered surface pressure solution for a swept trailing edge, as derived by Lyu[71, 111, 115] using the transforms of Roger et al,[72]

$$p_{S2} = \mathrm{e}^{-\mathrm{i}k_2\tilde{y}_2 - \mathrm{i}k_1\tilde{y}_1}[(1+\mathrm{i})\,\mathrm{E}(-\tilde{y}C_1) - 1],$$

where

$$C_1 = \tilde{k} + k_1 - \frac{\tilde{k}_2\tan(\psi) - kM}{\beta^2 + \tan^2(\psi)},$$

$$\tilde{k} = \frac{\sqrt{k^2 - \tilde{k}_2^2 + (\tilde{k}_2 M - k\tan(\psi))^2}}{\beta^2 + \tan^2(\psi)}$$

and

$$\tilde{y}_1 = y_1 - \tan(\psi)y_2.$$

The derivation then follows the same procedure outlined in Section 2.2.2.1, with the exceptions that

$$\breve{y}_1 = -(\tilde{y}_1 + c)$$

and

$$\Phi' = \tilde{\Phi}'\,\mathrm{e}^{-\mathrm{i}k_2\tilde{y}_2 - \mathrm{i}\tilde{y}_1(\tilde{k}_2\tan(\psi) - kM)/(\tan^2(\psi)+\beta^2)}.$$

The far-field scattered pressure due to back scattering then becomes

$$p'_{Sx3} = \frac{p'_I k x_3 \, e^{-i k(\tilde{r}_x - M x_1/\beta)/\beta - 2 i c \tilde{k}}}{\beta^2 \tilde{r}_x^2 (k - M k_1)\sqrt{i\pi C_1 c}} \left[1 - \frac{M C_1}{M C_1 + k - M k_1}\right]$$
$$\left[M\left\{e^{2i\tilde{k}c}\left[1 - (1+i)\,E(2\tilde{k}c)\right]\right\}^c - M\,e^{icC_3} + i\left\{k - M\frac{\tilde{k}_2\tan(\psi) - kM}{\tan^2(\psi)+\beta^2} - M\tilde{k} + MC_3\right\}\left\{\right.\right.$$
$$\frac{1+\varepsilon}{C_3 - 2\tilde{k}}\,e^{ic[2\tilde{k}+C_3]/2}\sin(c[C_3 - 2\tilde{k}]/2) + \frac{1-\varepsilon}{C_3+2\tilde{k}}\,e^{ic[C_3-2\tilde{k}]/2}\sin(c[C_3+2\tilde{k}]/2)$$
$$+ \frac{(1-i)(1+\varepsilon)}{2(C_3-2\tilde{k})}\,e^{2ic\tilde{k}}\,E(2\tilde{k}c) - \frac{(1+i)(1-\varepsilon)}{2(C_3+2\tilde{k})}\,e^{-2ic\tilde{k}}\,E^*(2\tilde{k}c)$$
$$\left.\left. + \frac{1}{2}\,e^{icC_3}\sqrt{\frac{2\tilde{k}}{C_3}}\,E(cC_3)\left[\frac{(1+i)(1-\varepsilon)}{C_3+2\tilde{k}} - \frac{(1-i)(1+\varepsilon)}{C_3-2\tilde{k}}\right]\right\}\right] \quad \text{(E.1)}$$

with

$$C_3 = \tilde{k} + \frac{\tilde{k}_2\tan(\psi) - kM}{\tan^2(\psi)+\beta^2} + \frac{kM}{\beta^2} - \frac{kx_1}{\beta^3\tilde{r}_x}$$

and

$$k_2 = -k_1\tan(\psi) - (k/\beta)(\tan(\psi)[M/\beta - x_1/(\beta^2\tilde{r}_x)] - x_2/\tilde{r}_x).$$

In Roger & Moreau's back-scattering theory, once the surface potential scattered by the trailing edge has been calculated, Amiet's Error function is replaced by its asymptotic expansion. Applying the Schwarzchild solution, the following integral needs completing

$$\int_0^\infty \sqrt{-\frac{y_1}{\xi}}\,\frac{e^{-i\tilde{k}\xi}}{\xi - y_1}\,\frac{e^{-i\tilde{k}\xi}}{\sqrt{\xi}}\,d\xi. \quad \text{(E.2)}$$

This integral does not have an analytic solution,[43] therefore it is assumed that the incident potential on the leading edge is stationary, such that the integral becomes

$$\frac{1}{\sqrt{c}}\int_0^\infty \sqrt{-\frac{y_1}{\xi}}\,\frac{e^{-i\tilde{k}\xi}}{\xi - y_1}\,e^{-i\tilde{k}\xi}\,d\xi = \frac{\pi}{\sqrt{c}}\,e^{-2i\tilde{k}y_1}[1 - (1+i)\,E(-2ky_1)]. \quad \text{(E.3)}$$

Comparing a numerical implementation of Equation E.2 with the analytical solution, Equation E.3, Roger & Moreau demonstrate that there is an error in the imaginary part of the analytical solution. They then suggest correcting this error by multiplying the imaginary part of Equation E.3 by a correction factor,

$$\varepsilon = \left(1 + \frac{1}{2\tilde{k}c}\right)^{-1/2}. \quad \text{(E.4)}$$

This comparison is repeated in Figure E.1, with more values of $\tilde{k}c/2$. As Roger & Moreau state, there is an error in the imaginary part for all values of $\tilde{k}c/2$. However, there is also an increasing error in the real component as $\tilde{k}c/2$ reduces. Figure E.2 displays the imaginary component after the correction factor is applied. The correction factor of

Roger & Moreau improves the result significantly, but the error does still increase as $\tilde{k}c/2$ decreases. After some trial and error, and comparing with the correction factors of Santana et al.,[136] a improved correction is found in

$$\varepsilon = \left(1 + \frac{2}{3.3\tilde{k}c}\right)^{-1/3}. \tag{E.5}$$

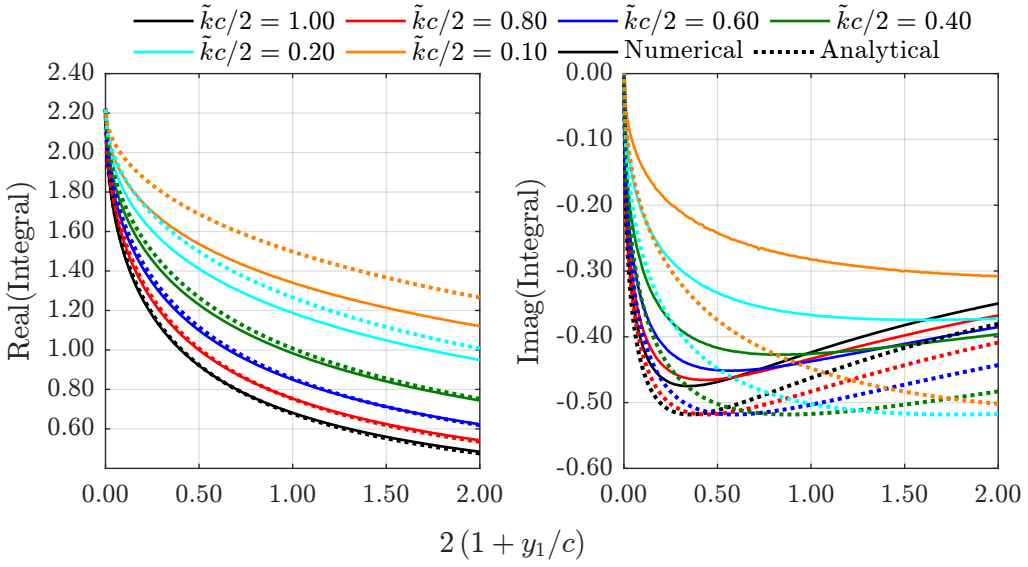

FIGURE E.1: Comparison of the numerical implementation of Equation E.2 with the simplified analytical solution Equation E.3. $\tilde{k}c/2$ is equivalent to $\bar{\mu}$ in Roger & Moreau's notation.

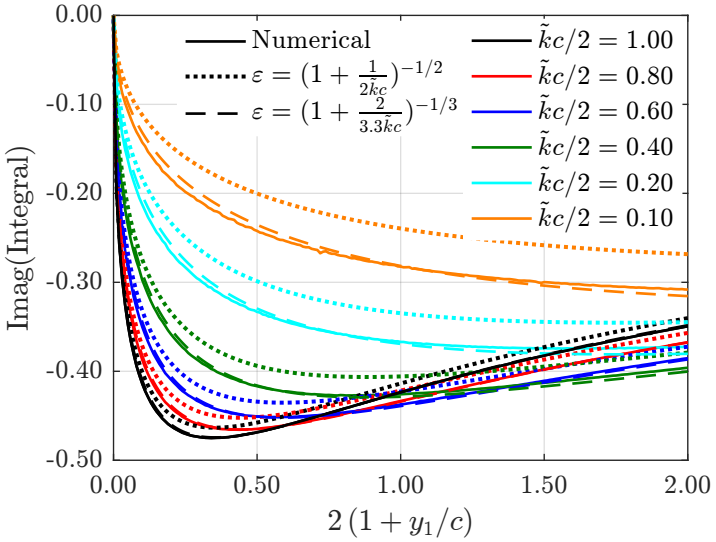

FIGURE E.2: Comparison of the numerical implementation of Equation E.2 with the simplified analytical solution Equation E.3 including correction factors. $\tilde{k}c/2$ is equivalent to $\bar{\mu}$ in Roger & Moreau's notation.

To get an analytical solution to the back scattering problem, Amiet's Error function is replaced with its asymptotic approximation, before also assuming that the pressure incident on the leading edge is stationary. Comparing the exact function with the asymptotic expansion (Figure E.3), the expansion works well when $|cC_1|$ is greater than 2. Below $|cC_1| = 2$, however, the asymptotic expansion diverges from the exact function, with the exact function becoming less sinusoidal and attaining a finite value at $|cC_1| = 0$. Because of the sinusoidal nature of the asymptotic approximation, the back-scattering solution of Roger & Moreau becomes questionable in this region. It is also debatable whether one would expect to be able to get a physical result using Amiet's theory in this region, given that the wavelength is larger than the chord.

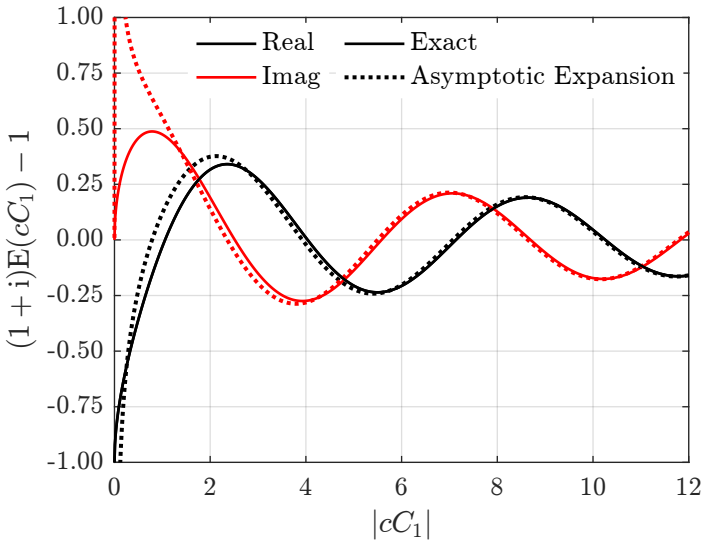

FIGURE E.3: Comparison of Amiet's Error function with its asymptotic expansion

Despite the questionable validity of applying Amiet's theory for $|cC_1| \leq 2$, Figure E.4 shows that the $1/\sqrt{cC1}$ decay can lead to the pressure on the leading edge being a significant proportion of that at the trailing edge. For context, with the $c/D = 0.7$ plate, $M_\mathrm{j} = 0.3$, $M_\mathrm{f} = 0$ and $k_2 = 0$, at Strouhal numbers of 0.2 and 0.5, $|cC_1|$ 2 and 6 respectively. So at these Strouhal numbers the scattered pressure amplitude incident on the leading edge is between 40 and 20 % of that at the trailing edge. The application of the back-scattering solution could therefore be expected to have a significant effect on the scattered far-field pressure.

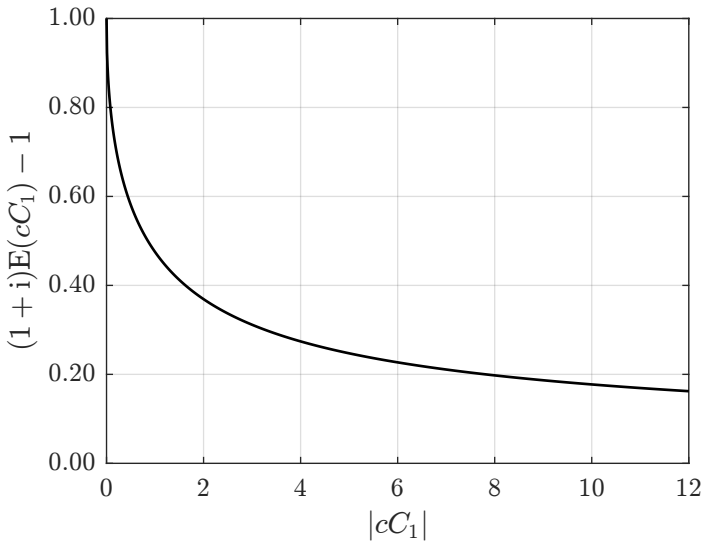

FIGURE E.4: Amplitude of Amiet's Error function

Figure E.5 displays the relative error between the asymptotic expansion and the exact function. The error is fairly significant for values of $|cC_1|$ less than three, above this values the relative error quickly drops below one percent, so is unlikely to have a significant effect on the result. There are, however, two fairly simple methods with which this error could be reduced. Firstly, the approximation

$$(1+\mathrm{i})\,\mathrm{E}(-\tilde{y}_1 C_1)-1 \approx -|(1+\mathrm{i})\,\mathrm{E}(cC_1)-1|\frac{\mathrm{e}^{\mathrm{i}\tilde{y}_1 C_1}}{\sqrt{\mathrm{i}}} \tag{E.6}$$

could be used. This gives the correct amplitude at the leading edge and preserves the phase of the asymptotic approximation, but gives the wrong phase at the leading edge for low values of $|cC_1|$. Secondly, the approximation

$$(1+\mathrm{i})\,\mathrm{E}(-\tilde{y}_1 C_1)-1 \approx [(1+\mathrm{i})\,\mathrm{E}(cC_1)-1]\,\mathrm{e}^{\mathrm{i}(\tilde{y}_1-c)C_1} \tag{E.7}$$

gives the correct amplitude and phase at the leading edge, but does not preserve the phase of the asymptotic approximation. In both cases the correct phases and amplitudes would be returned for large values of $|cC_1|$.

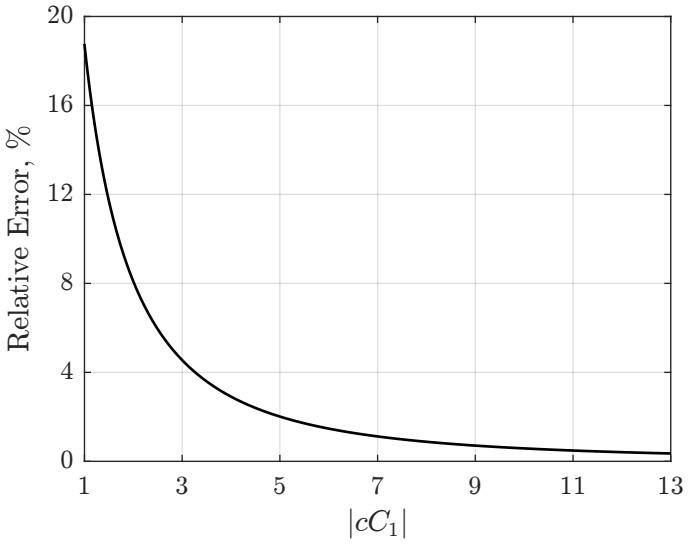

FIGURE E.5: Relative error between the absolute values of $(1 + \mathrm{i})\mathrm{E}(cC_1) - 1$ and its asymptotic expansion

For example, if there is no ambient flow nor sweep and $k_2 = 0$, then calculating the back-scattered surface pressure involves solving the integral

$$\int_0^\infty -\frac{1}{\pi}\sqrt{-\frac{\breve{y}_1}{\xi}}\,\frac{\mathrm{e}^{-\mathrm{i}k(\xi-\breve{y}_1)+\mathrm{i}k_1(\xi+c)}}{\xi-\breve{y}_1}\{(1+\mathrm{i})\,\mathrm{E}([\xi+c][k_1+k])-1\}. \tag{E.8}$$

Using Roger & Moreau's original approximation, the solution becomes

$$\frac{\mathrm{e}^{\mathrm{i}k\breve{y}_1-\mathrm{i}kc}}{\sqrt{\mathrm{i}\pi(k_1+k)c}}\{\,\mathrm{e}^{-2\,\mathrm{i}k\breve{y}_1}[1-(1+\mathrm{i})\,\mathrm{E}(-2k\breve{y}_1)]\}^{\mathrm{c}}, \tag{E.9}$$

while for the approximations above the solutions become, respectively,

$$\frac{\mathrm{e}^{\mathrm{i}k\breve{y}_1-\mathrm{i}kc}}{\sqrt{\mathrm{i}}}\{\,\mathrm{e}^{-2\,\mathrm{i}k\breve{y}_1}[1-(1+\mathrm{i})\,\mathrm{E}(-2k\breve{y}_1)]\}^{\mathrm{c}}|(1+\mathrm{i})\,\mathrm{E}(c[k_1+k])-1|, \tag{E.10}$$

and

$$-\,\mathrm{e}^{\mathrm{i}k\breve{y}_1+\mathrm{i}k_1c}\{\,\mathrm{e}^{-2\,\mathrm{i}k\breve{y}_1}[1-(1+\mathrm{i})\,\mathrm{E}(-2k\breve{y}_1)]\}^{\mathrm{c}}[(1+\mathrm{i})\,\mathrm{E}(c[k_1+k])-1]. \tag{E.11}$$

Comparing the approximate analytical solutions to a numerical implementation of Equation E.8 (Figure E.6 and Figure E.7), shows that Equation E.10 makes an almost negligible improvement on Equation E.9. On the other hand, Equation E.11 provides a better approximation of Equation E.8 for all the cases shown. If it is considered necessary, it would be fairly simple to include Equation E.11 in Equation E.1. This also serves to once again demonstrates that the in Amiet's theory (more specifically, the Schwarzchild solution) it is the pressure incident on the edge that is most important, not necessarily the overall shape of the incident pressure.

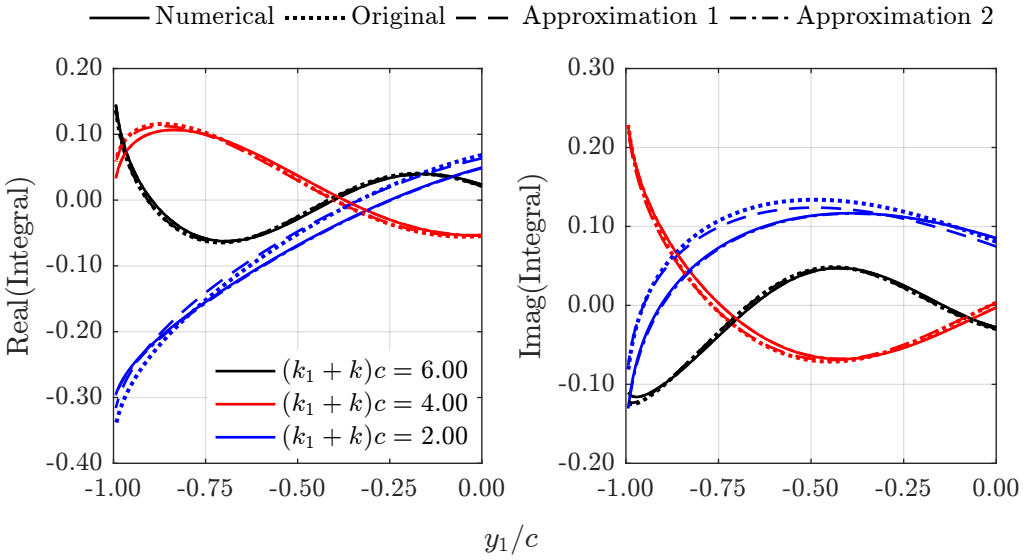

FIGURE E.6: Comparison of the numerical calculation of Equation E.8, with Roger & Moreau's original approximation (Equation E.9) and two modified solutions (1) Equation E.10 and 2) Equation E.11). $k_1 = 0$

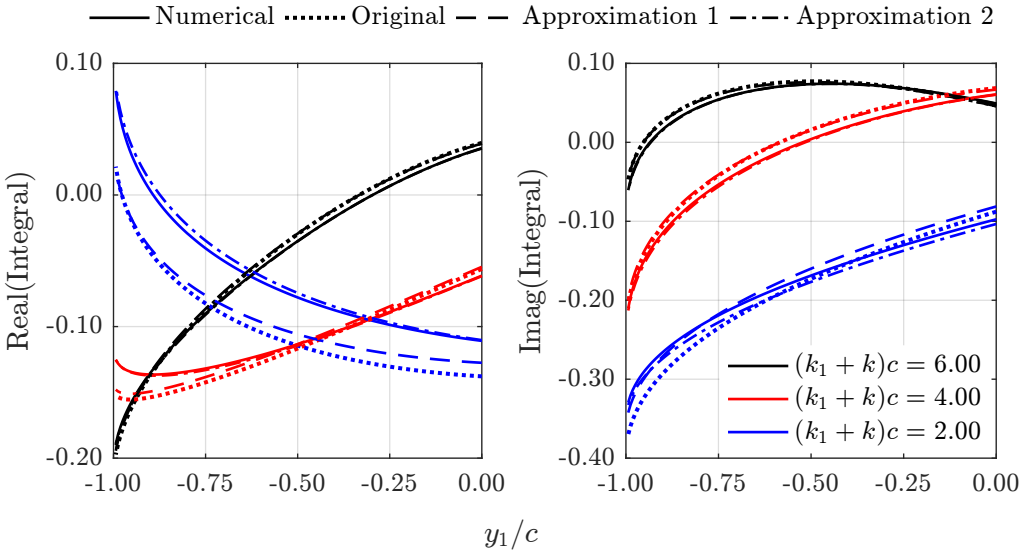

FIGURE E.7: Comparison of the numerical calculation of Equation E.8, with Roger & Moreau's original approximation (Equation E.9) and two modified solutions (1)Equation E.10 and 2) Equation E.11). $k_1 = 2k$

References

[1] J Lee, G Cebrian, L Edmonds, D Rhodes, and J Patel. Civil Aviation Authority ERCD REPORT 1601 Noise Exposure Contours for Heathrow Airport 2015. Technical report, 2017.

[2] ICAO. On Board a Sustainable Future: ICAO Environmental Report 2016, 2016.

[3] M J T Smith. *Aircraft Noise*. Cambridge University Press, Cambridge, 1989.

[4] N Dickson. ICAO Noise Standards, 2013.

[5] ICAO. Reduction of Noise at Source. icao.int/environmental-protection/pages/reduction-of-noise-at-source.aspx.

[6] Department for Transport. Night Flying Restrictions at Heathrow, Gatwick and Stanstead. Technical report, Department for Transport, London, 2014.

[7] R Baker. Decision-2018 Airport Charges. Technical report, Heathrow, 2017.

[8] Department for Transport. Night Flying Restrictions at Heathrow, Gatwick and Stanstead Stage 1 Consultation. Technical report, Department for Transport, London, 2013.

[9] M Darecki, C Edelstenne, T Enders, E Fernandez, P Hartman, J-P Herteman, M Kerkloh, I King, P Ky, M Mathieu, G Orsi, G Schotman, C Smith, and J-D Wörner. Flightpath 2050 - Europe's Vision for Aviation. Technical report, European Commission, Luxembourg, 2012.

[10] W R Graham, C A Hall, and M Vera Morales. The potential of future aircraft technology for noise and pollutant emissions reduction. *Transport Policy*, 34:36–51, 2014.

[11] Rolls-Royce plc. *The Jet Engine*. Wiley, 5th edition, 2005.

[12] H Cohen, GFC Rogers, and HIH Saravanamuttoo. *Gas Turbine Theory*. Pearson Education, fourth edition, 1996.

[13] M Goldstein. *Aeroacoustics*. McGraw-Hill International Book Company, 1976.

[14] M J Lighthill. On Sound Generated Aerodynamically I. General Theory. *Proceedings of the Royal Society A Mathematical, Physical and Engineering Sciences*, 211(1107):564–587, 1952.

[15] M J Lighthill. On Sound Generated Aerodynamically. II. Turbulence as a Source of Sound. *Proceedings of the Royal Society A Mathematical, Physical and Engineering Sciences*, 222(1148), 1954.

[16] P Jordan and T Colonius. Wave Packets and Turbulent Jet Noise. *Annual Review of Fluid Mechanics*, 45(1):173–195, 2013.

[17] Rolls-Royce. *The Jet Engine*. Rolls-Royce, 2nd edition, 1966.

[18] J L T Lawrence. *Aeroacoustic interactions of installed subsonic round jets*. PhD thesis, University of Southampton, 2014.

[19] M Daly, editor. *Jane's Aero-Engines 2017-2018*. IHS, Coulsdon, 2017.

[20] D Way and B Turner. Model tests demonstrating under-wing installation effects on engine exhaust noise. In *6th Aeroacoustics Conference*, pages 1–14, Reston, Virigina, jun 1980. AIAA Paper 1980-1048.

[21] G Sengupta. Analysis of jet-airframe interaction noise. In *8th Aeroacoustics Conference*, pages 1–10, Reston, Virigina, apr 1983. AIAA Paper 1983-0783.

[22] J G Shearin. Investigation of jet-installation noise sources under static conditions. Technical report, NASA, 1983.

[23] C Mead and P Strange. Under-wing installation effects on jet noise at sideline. In *4th AIAA/CEAS Aeroacoustics Conference*, pages 1–15, Reston, Virigina, jun 1998. AIAA Paper 1998-2207.

[24] D. J. Way. On the correction of noise data measured outside an airstream used for flight simulation. Technical report, NGTE Note 1018, 1976.

[25] C A Brown. Jet-Surface Interaction Test: Far-Field Noise Results. *Journal of Engineering for Gas Turbines and Power*, 135(7):071201, 2013.

[26] J A Stratton. *Electromagnetic Theory*. McGraw-Hill International Book Company, 1941.

[27] J Anderson. *Fundamentals of Aerodynamics*. McGraw-Hill Education, 6 edition, 2016.

[28] P. A. Lush. Measurements of subsonic jet noise and comparison with theory. *Journal of Fluid Mechanics*, 46(3):477–500, 1971.

[29] W A Olsen, A Gutierrez, and R G Dorsch. The Effect of Nozzle Inlet Shape, Lip Thickness, and Exit Shape on Subsonic Jet Noise. Technical report, National Aeronautics and Space Administration, Cleveland, Ohio, 1973.

[30] R. J. Gaeta and K. K. Ahuja. Subtle differences in jet-noise scaling with narrow-band spectra compared to 1/3-octave band. In *9th AIAA/CEAS Aeroacoustics Conference and Exhibit*, pages 1–14. AIAA Paper 2003-3124, 2003.

[31] M Harper-Bourne. Jet Noise Measurements: Past and Present. *International Journal of Aeroacoustics*, 9(4-5):559–588, 2010.

[32] R H Self. Jet noise prediction using the Lighthill acoustic analogy. *Journal of Sound and Vibration*, 275(3-5):757–768, aug 2004.

[33] C R S Ilário, M Azarpeyvand, V Rosa, R H Self, and J R Meneghini. Prediction of jet mixing noise with Lighthill's Acoustic Analogy and geometrical acoustics. *The Journal of the Acoustical Society of America*, 141(2):1203–1213, 2017.

[34] V Rosa. *RANS-based prediction of noise from isothermal and hot subsonic jets*. PhD thesis, University of Southampton, 2018.

[35] J E Ffowcs-Williams and L H Hall. Aerodynamic sound generation by turbulent flow in the vicinity of a scattering half plane. *Journal of Fluid Mechanics*, 40(04):657, 1970.

[36] H M Macdonald. A Class of Diffraction Problems. *Proceedings of the London Mathematical Society*, s2_14(1):410–427, 1915.

[37] N Curle. The Influence of Solid Boundaries upon Aerodynamic Sound. *Proceedings of the Royal Society A: Mathematical, Physical and Engineering Sciences*, 231(1187):505–514, sep 1955.

[38] D S Jones. Aerodynamic Sound Due to a Source Near a Half-Plane. *IMA Journal of Applied Mathematics*, 9(1):114–122, 1972.

[39] S. W. Rienstra. Sound diffraction at a trailing edge. *Journal of Fluid Mechanics*, 108:443–460, 1981.

[40] R K Amiet. Noise due to turbulent flow past a trailing edge. *Journal of Sound and Vibration*, 47(3):387–393, 1976.

[41] K Schwarzschild. Die Beugung und Polarisation des Lichts durch einen Spalt. I. *Mathematische Annalen*, 55(2):177–247, jun 1901.

[42] R K Amiet. Effect of the incident surface pressure field on noise due to turbulent flow past a trailing edge. *Journal of Sound and Vibration*, 57(2):305–306, 1978.

[43] M Roger and S Moreau. Back-scattering correction and further extensions of Amiet's trailing-edge noise model. Part 1: theory. *Journal of Sound and Vibration*, 286(3):477–506, sep 2005.

[44] M. J. Fisher, M. Harper-Bourne, and S. A.L. Glegg. Jet Engine Noise Source Location: The Polar Correlation Technique. *Journal of Sound and Vibration*, 51(1):23–54, 1977.

[45] S A L Glegg. *Jet Noise Source Location*. PhD thesis, University of Southampton, 1979.

[46] M Harper-Bourne. On Modelling the Hydrodynamic Field of High-Speed Jets. In *10th AIAA/CEAS Aeroacoustics Conference*, pages 1–11. AIAA Paper 2004-2830, 2004.

[47] O P Bychkov and G A Faranosov. On the possible mechanism of the jet noise intensification near a wing. *Acoustical Physics*, 60(6):633–646, 2014.

[48] O P Bychkov and G A Faranosov. An Experimental Study and Theoretical Simulation of Jet-Wing Interaction Noise. *Acoustical Physics*, 64(4):437–452, 2018.

[49] M T Landahl. *Unsteady Transonic Flow*. Cambridge University Press, 1989.

[50] R K Amiet. Acoustic radiation from an airfoil in a turbulent stream. *Journal of Sound and Vibration*, 41(4):407–420, aug 1975.

[51] S Moreau and M Roger. Back-scattering correction and further extensions of Amiet's trailing-edge noise model. Part II: Application. *Journal of Sound and Vibration*, 323(1-2):397–425, 2009.

[52] A Depitre. EPNdB Metric: Why is it used in Aircraft Noise Certification? How is it Calculated? In *Noise Certification Workshop*, Bangkok, 2006. ICAO.

[53] R K Amiet. High frequency thin-airfoil theory for subsonic flow. *AIAA Journal*, 14(8):1076–1082, aug 1976.

[54] W R Miller. Flight effects for jet-airframe interaction noise. In *8th AIAA Aeroacoustics Conference*, pages 1–9. AIAA Paper 1983-0784, 1983.

[55] M Yildiz and O K Mawardi. On the Diffraction of Multipole Fields by a SemiInfinite Rigid Wedge. *The Journal of the Acoustical Society of America*, 32(12):1685–1691, dec 1960.

[56] A V G Cavalieri, P Jordan, W R Wolf, and Y Gervais. Scattering of wavepackets by a flat plate in the vicinity of a turbulent jet. *Journal of Sound and Vibration*, 333(24):6516–6531, 2014.

[57] A V G Cavalieri, P Jordan, T Colonius, and Y Gervais. Axisymmetric superdirectivity in subsonic jets. *Journal of Fluid Mechanics*, 704:388–420, 2012.

[58] S Piantanida, V Jaunet, P Jordan, J Huber, A V Cavalieri, and W Wolf. Scattering of turbulent-jet wavepackets by a swept trailing edge. In *21st AIAA/CEAS Aeroacoustics Conference*, pages 1–16, Reston, Virginia, jun 2015. AIAA Paper 2015-2998.

[59] S Piantanida, V Jaunet, J Huber, W R. Wolf, P Jordan, and A. V. G. Cavalieri. Scattering of turbulent-jet wavepackets by a swept trailing edge. *The Journal of the Acoustical Society of America*, 140(6):4350–4359, 2016.

[60] P A S Nogueira, A V G Cavalieri, and P Jordan. A model problem for sound radiation by an installed jet. *Journal of Sound and Vibration*, 391:95–115, mar 2017.

[61] P A S Nogueira, J R L N Sirotto, R F Miotto, A V G Cavalieri, J A Cordioli, and W R. Wolf. Acoustic radiation of subsonic jets in the vicinity of an inclined flat plate. *The Journal of the Acoustical Society of America*, 146(1):50–59, 2019.

[62] J Huber, P Jordan, M Roger, Y Gervais, and D Lizarazu. Exploring Flight Effects for Installed Jet Noise using a Wavepacket Sound-Source Model. In *23rd AIAA/CEAS Aeroacoustics Conference*, pages 1–14, Reston, Virginia, jun 2017. AIAA Paper 2017-3382.

[63] J V Vera, J Lawrence, R H Self, and M Kingan. The prediction of the radiated pressure spectrum produced by jet-wing interaction. In *21st AIAA/CEAS Aeroacoustics Conference*, pages 1–14, Reston, Virginia, jun 2015. AIAA Paper 2015-2216.

[64] J Vera, S Sinayoko, R H Self, M J Kingan, and J L T Lawrence. Hydrodynamic pressure field propagation model for the prediction of the far-field sound produced by jet-wing interaction. In *22nd AIAA/CEAS Aeroacoustics Conference*, pages 1–12. AIAA Paper 2016-2859, 2016.

[65] J Vera. *Modelling Jet Noise Installation Effects Associated with Close-coupled, Wing-mounted, Ultra High Bypass Ratio Engines.* PhD thesis, University of Southampton, 2019.

[66] R Reba, S Narayanan, and T Colonius. Wave-packet models for large-scale mixing noise. *Aeroacoustics*, 9(4):533–558, 2010.

[67] B Lyu and A Dowling. Noise Prediction for Installed Jet. In *22nd AIAA/CEAS Aeroacoustics Conference*, pages 1–15. AIAA Paper 2016-2986, 2016.

[68] B Lyu, A P Dowling, and I Naqavi. Prediction of installed jet noise. *Journal of Fluid Mechanics*, 811:234–268, 2017.

[69] B Lyu and A P Dowling. On the Mechanism and Reduction of Installed Jet Noise. In *23rd AIAA/CEAS Aeroacoustics Conference*, pages 1–15. AIAA Paper 2017-3523, 2017.

[70] B Lyu and A P Dowling. Experimental validation of the hybrid scattering model of installed jet noise. *Physics of Fluids*, 30(8):085102:1–19, aug 2018.

[71] B Lyu and A P Dowling. Prediction of installed jet noise due to swept wings. In *2018 AIAA/CEAS Aeroacoustics Conference*, volume 811, pages 234–268, Reston, Virginia, jun 2018. AIAA Paper 2018-2980.

[72] M Roger, C Schram, and L De Santana. Reduction of Airfoil Turbulence-Impingement Noise by Means of Leading-Edge Serrations and/or Porous Material. In *19th AIAA/CEAS Aeroacoustics Conference*, pages 1–20, Reston, Virginia, may 2013. AIAA Paper 2013-2108.

[73] O Bychkov, S Denisov, G Faranosov, and N Ostrikov. Theoretical modeling of the excess noise due to jet-wing interaction. In *22nd AIAA/CEAS Aeroacoustics Conference*, pages 1–21. AIAA Paper 2016-2932, 2016.

[74] M Z Afsar, S J Leib, and R F Bozak. Effect of de-correlating turbulence on the low frequency decay of jet-surface interaction noise in sub-sonic unheated air jets using a CFD-based approach. *Journal of Sound and Vibration*, 386:177–207, 2017.

[75] M Z Afsar. Improved trailing edge noise prediction using CFD data within a generalized Rapid-distortion theory approach. In *25th AIAA/CEAS Aeroacoustics Conference*, Delft, may 2019. AIAA Paper 2019-2712.

[76] G Faranosov, O P Bychkov, V Kopiev, L F Soares, and AV Cavalieri. The Modeling of Jet-Plate Interaction Noise in the Presence of Co-Flow. In *25th AIAA/CEAS Aeroacoustics Conference*, number May, pages 1–17, Delft, Netherlands, may 2019. AIAA Paper 2019-2492.

[77] M Harper-Bourne. Jet Near-Field Noise Prediction. In *5th AIAA/CEAS Aeroacoustics Conference*, pages 236–249, Seattle, 1999. AIAA 1999-1838.

[78] M Harper-Bourne. ADP014103: Prediction the Jet Near-Field of Combat Aircraft. Technical report, 2003.

[79] M Harper-Bourne. On Modelling the Acoustic Forcing Functions of the Near-Field Noise of High-Speed Jets. In *11th AIAA/CEAS Aeroacoustics Conference*, pages 23–25. AIAA Paper 2005-2994, 2005.

[80] C Tam, M Golebiowski, and J Seiner. On the two components of turbulent mixing noise from supersonic jets. In *Aeroacoustics Conference*, Reston, Virigina, may 1996. American Institute of Aeronautics and Astronautics.

[81] R E A Arndt, D F Long, and M N Glauser. The proper orthogonal decomposition of pressure fluctuations surrounding a turbulent jet. *Journal of Fluid Mechanics*, 340:1–33, jun 1997.

[82] A Guitton, P Jordan, E Laurendeau, and J Delville. Velocity dependence of the near pressure field of subsonic jets: understanding the associated source mechanisms. In *13th AIAA/CEAS Aeroacoustics Conference (28th AIAA Aeroacoustics Conference)*, pages 1–9, Reston, Virigina, may 2007. AIAA Paper 2007-3661.

[83] S A E Miller. Prediction of Near-Field Jet Cross Spectra. *AIAA Journal*, 53(8):2130–2150, 2015.

[84] I V Belyaev, M Y Zaytsev, V F Kopiev, N N Ostrikov, and G A Faranosov. Studying the effect of flap angle on the noise of interaction of a high-bypass jet with a swept wing in a co-flow. *Acoustical Physics*, 63(1):14–25, 2017.

[85] E Mollo-Christensen. Measurements of Near Field Pressure of Subsonic Jets. Technical report, Massachusetts Institute of Technology, 1963.

[86] G K Batchelor and A E Gill. Analysis of the stability of axisymmetric jets. *Journal of Fluid Mechanics*, 14(04):529, 1962.

[87] M Lessen and P J Singh. The stability of axisymmetric free shear layers. *Journal of Fluid Mechanics*, 60(03):433, sep 1973.

[88] G E Mattingly and C C Chang. Unstable waves on an axisymmetric jet column. *Journal of Fluid Mechanics*, 65(3):541–560, 1974.

[89] A V G Cavalieri, D Rodríguez, P Jordan, T Colonius, and Y Gervais. Wavepackets in the velocity field of turbulent jets. *Journal of Fluid Mechanics*, 730:559–592, 2013.

[90] J E Ffowcs-Williams and A J Kempton. The noise from the large-scale structure of a jet. *Journal of Fluid Mechanics*, 84(4):673–694, 1978.

[91] O de Almeida. Semi-empirical methods for coaxial jet noise prediction. Technical Report 326, Institute of Sound and Vibration Research; University of Southampton, Southampton, 2008.

[92] C B Chinoy. Estimation of Subsonic Far-Field Jet Mixing Noise from Single-Stream Circular Nozzles, ESDU 89041, 1989.

[93] C B Chinoy. ESDU 11002: The Prediction of the Far-Field Mixing Noise from Coaxial Subsonic Jets Based on a Database for Stationary Coplanar Nozzles. Technical report, ESDU, 2011.

[94] ARP 876, Gas Turbine Exhaust Noise Prediction. Technical Report 724, Society of Automotive Engineers, 1978.

[95] J R Stone and F J Montegani. An Improved Prediction Method for the Noise Generated in Flight by Circular Jets. In *99th Meeting of the Acoustic Society of America*, Atlanta, 1980. NASA.

[96] J R Stone, E A Krejsa, B J Clark, and J J Berton. Jet Noise Modeling for Suppressed and Unsuppressed Aircraft in Simulated Flight, Technical Report CR 215524. Technical Report March, 2009.

[97] T Dassen, H Holthusen, and M Beukemat. Design and Testing of a Low Self-Noise Aerodynamic Microphone Forebody. In *2nd AIAA/CEAS Aeroacoustics Conference*, State College, PA, 1996. AIAA Paper 1996-1711.

[98] A R Proenca. *Aeroacoustics of Isolated and Installed Jets under Static and In-Flight Conditions*. PhD thesis, University of Southampton, 2018.

[99] Anderson Proenca and Jack Lawrence. Blockage Effects on the Pressure Field of 3D-Printed Small-Scale Jet Nozzles. In *AIAA AVIATION 2021 FORUM*, Reston, Virginia, aug 2021. AIAA Paper 2021-2305.

[100] P D Welch. The Use of Fast Fourier Transform for the Estimation of Power Spectra: A Method Based on Time Averaging Over Short, Modified Periodograms. *IEEE Transactions on Audio and Electroacoustics*, 15(2):70–73, 1967.

[101] Fredric J. Harris. On the Use of Windows for Harmonic Analysis with the Discrete Fourier Transform. *Proceedings of the IEEE*, 66(1):51–83, 1978.

[102] H E Bass, L C Sutherland, A J Zuckerwar, D T Blackstock, and D M Hester. Atmospheric absorption of sound: Further developments. *Journal of the Acoustical Society of America*, 97(1):680–683, 1995.

[103] H. E. Jr Plumblee. Effects of Forward Velocity on Turbulent Jet Mixing Noise. Technical report, NASA, 1976.

[104] R K Amiet. Refraction of sound by a shear layer. *Journal of Sound and Vibration*, 58(4):467–482, jun 1978.

[105] C. L. Morfey and P. F. Joseph. Shear layer refraction corrections for off-axis sources in a jet flow. *Journal of Sound and Vibration*, 239(4):819–848, 2001.

[106] Z N Wang, A Proenca, J Lawrence, P G Tucker, and R H Self. Large-Eddy Simulation of Installed Jet Flows and Acoustics. In *25th AIAA/CEAS Aeroacoustics Conference*, number May, pages 1–11, Delft, Netherlands, may 2019. AIAA Paper 2019-2453.

[107] Z-N Wang, A Proenca, J Lawrence, P G Tucker, and R Self. Large-Eddy-Simulation Prediction of an Installed Jet Flow and Noise with Experimental Validation. *AIAA Journal*, pages 1–10, mar 2020.

[108] J Jacques. Wind-Tunnel Simulation of the Effects of Flight on Radiated Sound. Technical report, Engineering Department, University of Cambridge, 1976.

[109] H K Tanna, B J Tester, and C L Morfey. Effects of Forward Velocity on Turbulent Jet Mixing Noise. Technical report, Lockheed-Georgia Company, 1976.

[110] P O Witze. Centerline Velocity Decay of Compressible Free Jets. *AIAA Journal*, 12(4):417–418, 1974.

[111] B Lyu. *Installed jet noise*. PhD thesis, University of Cambridge, 2018.

[112] I Z Naqavi, Z N Wang, P G Tucker, M Mahak, and P Strange. Far-field noise prediction for jets using large-eddy simulation and Ffowcs WilliamsHawkings method. *International Journal of Aeroacoustics*, 15(8):757–780, 2016.

[113] N W M Ko and F C Chu. Annular Jets of Different Diameter Ratios. *Aeronautical Quarterly*, 34(3):163–196, aug 1983.

[114] N W M Ko and W T Chan. Similarity in the initial region of annular jets: three configurations. *Journal of Fluid Mechanics*, 84(4):641–656, 1978.

[115] B Lyu and A P Dowling. Modelling installed jet noise due to the scattering of jet instability waves by swept wings. *Journal of Fluid Mechanics*, 870:760–783, 2019.

[116] J Christophe, J Anthoine, and S Moreau. Amiet's Theory in Spanwise-Varying Flow Conditions. *AIAA Journal*, 47(3):788–790, mar 2009.

[117] L D Santana. *Semi-analytical methodologies for airfoil noise prediction*. PhD thesis, KU Leuven, 2015.

[118] R F Miotto, W Wolf, L D de Santana, and C H Venner. Application of Amiet's theory for noise prediction of general airfoil profiles subjected to spanwise-varying inflow conditions. In *2018 AIAA/CEAS Aeroacoustics Conference*, pages 1–13, Reston, Virginia, jun 2018. AIAA Paper 2018-3143.

[119] R F Miotto, W R Wolf, and L D de Santana. Leading-Edge Noise Prediction of General Airfoil Profiles with Spanwise-Varying Inflow Conditions. *AIAA Journal*, 56(5):1711–1716, may 2018.

[120] M Roger, C Schram, and S Moreau. On vortex-airfoil interaction noise including span-end effects, with application to open-rotor aeroacoustics. *Journal of Sound and Vibration*, 333(1):283–306, 2014.

[121] D McRae. The Aerodynamic Development of the Wing of the A 300B. *The Aeronautical Journal*, 77(751):367–379, 1973.

[122] J P Fielding. *Introduction to Aircraft Design*. Cambridge University Press, Cambridge, oct 1999.

[123] E Obert. *Aerodynamic Design of Transport Aircraft*. IOS Press, Amsterdam, 2009.

[124] A K Kundu. *Aircraft Design*. Cambridge University Press, Cambridge, 2010.

[125] E Torenbeek. *Advanced Aircraft Design*. John Wiley & Sons, Ltd, Oxford, UK, jun 2013.

[126] D L Martlew, J M Hawkins, R L Brooking, and A S Kennedy. The design , construction and operation of the noise test facility at the National Gas Turbine Establishment. *The Aeronautical Journal*, 80(781):1–19, 1976.

[127] R A Pinker. The enhancement of the QinetiQ Noise Test Facility for larger-scale exhaust systems. In *10th AIAA Aeroacoustics Conference*, pages 1–14. AIAA Paper 2004-3019, 2004.

[128] A. Michalke and U. Michel. Prediction of jet noise in flight from static tests. *Journal of Sound and Vibration*, 67(3):341–367, dec 1979.

[129] M. J. Fisher and G. A. Preston. A modelling of the noise from simple co-axial jets part II - in a simulated flightstream. Technical Report 226, Institute of Sound and Vibration Research, 1993.

[130] J. R. Stone. Flight effects on exhaust noise for turbojet and turbofan engines: comparison of experimental data with prediction. Lewis Research Center, NASA, NASA TM-X-73552, 1976.

[131] H Y Lu. An Empirical Model For Prediction of Coaxial Jet Noise in Ambient Flow. In *10th Aeroacoustics Conference*, Seattle, Washington, jul 1986. AIAA Paper 1986-1912.

[132] N W M Ko and A S H Kwan. The initial region of subsonic coaxial jets. *Journal of Fluid Mechanics*, 73(02):305–332, 1976.

[133] J L T Lawrence and R H Self. Installed jet-flap impingement tonal noise. In *21st AIAA/CEAS Aeroacoustics Conference*, pages 1–12. AIAA Paper 2015-3118, 2015.

[134] P Jordan, V Jaunet, A Towne, A V G Cavalieri, T Colonius, O Schmidt, and A Agarwal. Jet-flap interaction tones. *Journal of Fluid Mechanics*, 853:333–358, 2018.

[135] A Proenca, J L T Lawrence, and R Self. A Survey of the Turbulence Statistics of a Model-Scale Installed Jet at Low and Moderate Mach Numbers. In *23rd AIAA/CEAS Aeroacoustics Conference*, number June, pages 1–16, Reston, Virginia, jun 2017. AIAA Paper 2017-3705.

[136] L D Santana, C Schram, and W Desmet. Low-frequency extension of Amiet's theory for compact airfoil noise predictions. *Journal of Sound and Vibration*, 372:342–356, 2016.

[137] C M Wrighton and J L T Lawrence, Test Conduct Report SYMPHONY WP3.2 Installation Effects - Acoustic Tests, QinetiQ Report 10/02682, November 2010

[138] C Wrighton, Test Conduct Report for the Harmony IFX Test Programme at the QinetiQ Noise Test Facility, QinetiQ Report 16/00353, March 2016

[139] S Nauri, Symphony WP3.3 Diagnostics Tests Conduct Report, QinetiQ Report 10/02588, November 2010